Optimisation of positron accumulation in the GBAR experiment and study of space propulsion based on antimatter

Samuel Niang

To cite this version:

Samuel Niang. Optimisation of positron accumulation in the GBAR experiment and study of space propulsion based on antimatter. Accelerator Physics [physics.acc-ph]. Université Paris-Saclay, 2020. English. NNT : 2020UPASP075 . tel-03163848

HAL Id: tel-03163848
https://theses.hal.science/tel-03163848

Submitted on 9 Mar 2021

Optimisation of positron accumulation in the GBAR experiment and study of space propulsion based on antimatter

Thèse de doctorat de l'université Paris-Saclay

École doctorale n°576
Particules, hadrons, énergie et noyau : instrumentation, imagerie, cosmos et simulation (Pheniics)

Spécialité de doctorat : Physique des particules

Unité de recherche: Université Paris-Saclay, CEA, Département de Physique des Particules, 91191, Gif-sur-Yvette, France.
Référent: Faculté des sciences d'Orsay

Thèse présentée et soutenue en visioconférence totale, le 8 Décembre 2020 par

Samuel Niang

Composition du jury:

Réza Ansari Professeur, LAL, Université Paris-Saclay	Président
David Cassidy Professeur, University College London	Rapporteur & Examinateur
Alexandre Obertelli Professeur, HDR, Darmstadt University	Rapporteur & Examinateur
Gerda Neyens Professeure, KU Leuven et EP Department au CERN	Examinatrice
Martina Knoop Doctoresse, CNRS et Université d'Aix-Marseille	Examinatrice
Roland Lehoucq Docteur, CEA-E7, IRFU, Université Paris-Saclay	Examinateur
Boris Tuchming Docteur, HDR, CEA-E6, IRFU, Université Paris-Saclay	Directeur de thèse
Patrice Pérez Docteur d'État, CEA-E6, IRFU, Université Paris-Saclay	Co-directeur de thèse
Dirk Peter van der Werf Professeur, Swansea University	Co-encadrant de thèse

Thèse de doctorat

NNT: 2020UPASP075

"Of course I dream", I tell her. "Everybody dreams".
"But what do you dream about?", she'll ask.
"The same thing everybody dreams about", I tell her. "I dream about where I'm going". She always laughs at that.
"But you're not going anywhere, you're just wandering about".
That's not true. Not anymore. I have a new destination. My journey is the same as yours, the same as anyone's. It's taken me so many years, so many lifetimes, but at last I know where I'm going. Where I've always been going. Home. The long way around.

The Day of the Doctor

To Sonia and Alissa.

Résumé de la thèse en français

Chapitre 1 : Introduction

L'antimatière fut découverte mathématiquement par Dirac en 1928 et expérimentalement par Anderson en 1932 et son étude est encore de nos jours un champ de recherche à part entière, comme au CERN avec le décélérateur d'antiprotons. La particularité des antiparticules étant qu'elles peuvent s'annihiler avec leurs particules jumelles de matière et un photon peut se décomposer en une paire particule-antiparticule. Les recherches sur l'antimatière sont particulièrement intéressantes car elles pourraient être la source d'une brèche dans le modèle standard de la physique, ce qui ouvrirait de nouveaux champs de recherche.

Par ailleurs, d'après le modèle standard de la cosmologie basé sur le modèle standard de la physique des particules, il y avait autant de matière que d'antimatière au début de l'histoire de l'univers. Cependant, notre univers semble être constitué uniquement de matière. Il est alors possible qu'une rupture de symétrie dans les réactions d'annihilation-créations se soit produite. La violation de la symétrie CP, pourrait expliquer en partie cette différence, mais n'est pas la réponse au problème. C'est pour cela que des expériences telles que GBAR étudient d'autres paramètres comme la gravitation au niveau des particules élémentaires. Une différence dans le comportement gravitationnel entre la matière et l'antimatière mènerait ainsi à une percée dans notre connaissance de l'univers.

L'utilisation de l'antimatière dans le domaine du transport spatial sera également abordée durant cette thèse. En effet, la réaction d'annihilation a comme avantage de produire des particules légères voyageant à des vitesses proches de celle de la lumière et cette énorme quantité d'énergie cinétique ainsi dégagée pourrait être utilisée pour propulser une fusée. L'antimatière serait donc le carburant ayant le meilleur rendement énergétique et rendrait possible le voyage spatial proche de la vitesse de la lumière. Cette idée prometteuse a cependant plusieurs limitations. La première étant qu'il n'y a tout simplement pas de quantité macroscopique d'antimatière à notre disposition. À l'heure actuelle, il est possible d'en produire mais dans des quantités infinitésimales comparées à ce qui serait nécessaire pour un voyage spatial. Aussi, il n'existe pas pour l'heure de méthodes pour stocker de façon efficace une telle quantité d'antimatière. Enfin, de telles réactions d'annihilation produisent de grandes quantités de rayons gamma, dont il faudrait protéger la fusée et ses possibles occupants, ce qui n'est pas un problème trivial. Mais l'idée d'une telle application de l'antimatière demeure quelque chose d'assez attirant pour l'étudier.

Chapitre 2 : L'expérience GBAR

Le but de l'expérience GBAR est de déterminer le comportement gravitationnel de l'antimatière au repos en étudiant la chute libre d'un atome d'antihydrogène. Les deux composants de cet anti-atome sont les antiprotons, fournis par le décélérateur d'antiprotons ELENA, et les positons fournis par un accélérateur linéaire (LINAC). Le LINAC accélère des électrons jusqu'à 9 MeV qui percutent une cible de tungstène provocant la création de paires positons-électrons. La cible est équipée d'un modérateur biaisé à 50 V.

Le point clé de l'expérience est la création d'un ion antihydrogène $\overline{\mathrm{H}}^+$. Pour ce faire, un antiproton réagit deux fois dans un nuage de positronium (état lié d'un électron et d'un positon) suivant la réaction

$$\begin{aligned} \overline{p} + \mathrm{Ps} &\rightarrow \overline{\mathrm{H}} + e^-, \\ \overline{\mathrm{H}} + \mathrm{Ps} &\rightarrow \overline{\mathrm{H}}^+ + e^-. \end{aligned}$$

La création du positronium passe par la conversion de 10^{10} positons, à l'aide de silice nano-poreuse. Le LINAC fournissant 3×10^7 positons par seconde, ces derniers doivent être accumulés dans des pièges de Penning, comme présenté dans les chapitres 3, 4 et 5. Un piège sera installé pour accumuler les paquets d'antiprotons fournis par le décélérateur ELENA.

Une fois l'anti-ion créé, il est stabilisé à l'aide d'un champ électrique dans la chambre de chute libre. Le positon excédentaire est enlevé à l'aide d'un faisceau laser, et la chute libre peut être alors observée. Pour le moment, aucun antiproton n'a pu être piégé car le piège à antiproton est encore en cours d'installation. Le piégeage des antiprotons commencera lors du redémarrage d'ELENA en 2021. La chambre de chute libre est toujours en construction et sera installée également en 2021.

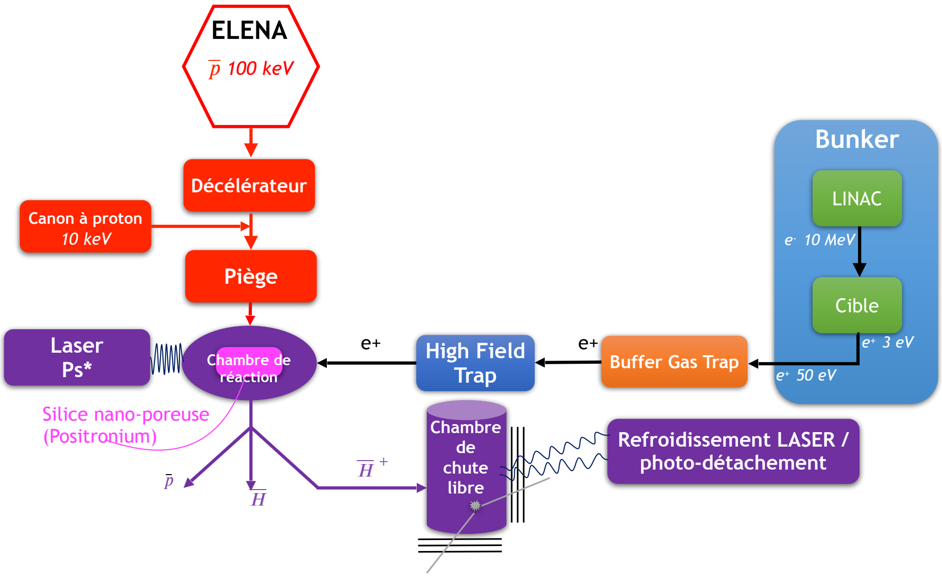

Schéma de l'expérience GBAR.

Chapitre 3 : Piégeage et transport d'une particule chargée

Le piégeage de particules chargées se fait à l'aide de pièges électromagnétiques nommés pièges de Penning-Malmberg. Dans le modèle du piège de Penning, un champ magnétique uniforme parallèle à l'axe principal est responsable du confinement radial des particules tandis qu'un potentiel parabolique est responsable du confinement axial.

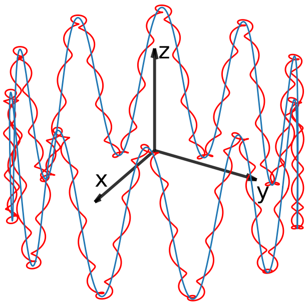

Mouvement d'une particule dans un piège de Penning-Malmberg. Dans le plan (x, y), le mouvement est composé de deux mouvements circulaires. Suivant l'axe z (parallèle au champ magnétique), il s'agit d'une oscillation.

Pour un grand nombre de particules, on parle de plasma quand la longueur de Debye est petite devant la longueur caractéristique du piège. Dans ce cas, les charges écrantent le champ électrique du piège. La longueur de Debye est définie par

$$\lambda_D = \sqrt{\frac{\epsilon_0 k_B T}{n_0 e^2}},$$

avec ϵ_0 la permittivité du vide, k_B la constante de Boltzmann, n_0 la densité de particules et e la charge des particules dans le plasma.

Un autre paramètre important est le paramètre de corrélation

$$\Gamma = \frac{e^2}{4\pi\epsilon_0 a k_B T} \propto \frac{a^2}{\lambda_D^2},$$

avec $a \equiv n_0^{-1/3}$, la distance moyenne entre les particules. En effet, un plasma faiblement corrélé pourra être considéré comme un fluide continu. Dans le cas contraire, il faudra prendre en compte les interactions entre chaque particule. Aussi, dans le cas d'un plasma, il est démontré qu'il existe une densité maximale nommée limite de Brillouin qui est proportionnelle au champ magnétique B:

$$n_B = \frac{B^2/(2\mu_0)}{mc^2},$$

avec μ_0 la perméabilité du vide, m la masse des particules et c la vitesse de la lumière.

Pour comprimer radialement le paquet de particules chargées dans le piège, la méthode du “Rotating Wall” est utilisée. Un potentiel oscillant est appliqué sur une électrode coupée en 4 et sur chaque partie, le champ oscillant appliqué a une phase de 90° par rapport au champ appliqué sur les électrodes voisines, créant ainsi un dipôle oscillant. Avec l'amplitude et la fréquence appropriée, la collection de charge est compressée.

Dans le cas de particules voyageant dans des zones où le champ magnétique change, il faut prendre en compte l'effet de miroir magnétique. En effet, si une particule chargée se déplace d'une région avec un champ magnétique B_i à un champ magnétique B_f (parallèles à l'axe principal) avec $B_f > B_i$, elle sera repoussée si l'angle entre son impulsion et l'axe principal est supérieur à

$$\theta_{i\mathrm{max}} = \arcsin\left(\sqrt{\frac{B_i}{B_f}}\right).$$

Pour franchir ce miroir magnétique, il est possible d'accélérer une particule d'énergie totale E, suivant l'axe principal, en ajoutant une énergie cinétique $\mathcal{E}$. L'angle maximal devient donc

$$\theta_{i,\mathrm{max}} = \arcsin\left(\sqrt{\frac{B_i}{B_f}\frac{E+\mathcal{E}}{E}}\right) > \arcsin\left(\sqrt{\frac{B_i}{B_f}}\right).$$

Chapitre 4 : Piège à gaz tampon

Le piège à gaz tampon (abrégé en BGT pour Buffer Gas Trap) utilisé dans l'expérience GBAR est un accumulateur à positons basé sur le principe du piège de Greaves-Surko. Il s'agit d'un piège de Penning à trois étages dans lequel des gaz (N_2 et CO_2) à très faibles pressions ont été injectés. Les positons en provenance du LINAC y perdent de l'énergie grâce aux collisions inélastiques avec le gaz, permettant le piégeage (grâce au N_2) et le refroidissement des particules (grâce au CO_2). Le paquet de positons ainsi accumulé peut être compressé radialement grâce à la technique du "Rotating Wall".

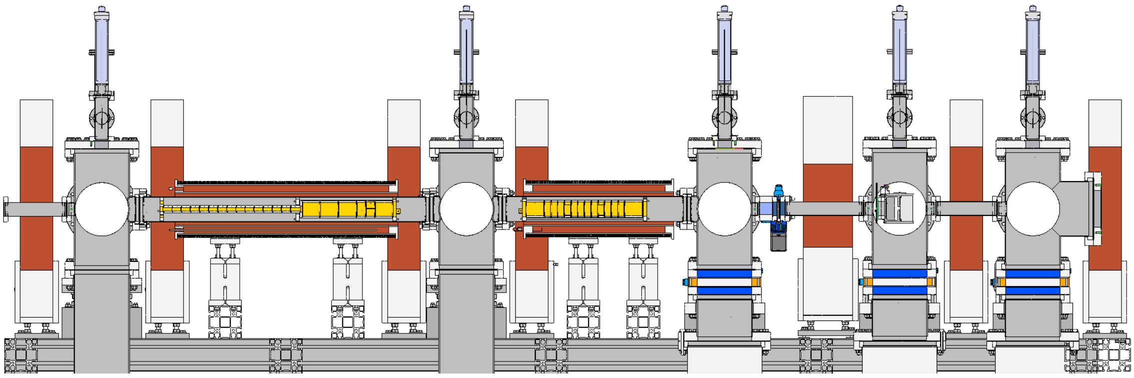

Schéma du piège à gaz tampon.

Les positons sont d'abord accumulés dans le second étage pendant 100 ms. Avec les paramètres définis dans ce chapitre, le temps de vie des positons dans cet étage est d'environ 0.6 s pour un taux de piégeage de $1.7 \times 10^6\ \mathrm{e}^+\ \mathrm{s}^{-1}$. Ici, le "Rotating Wall" a un rôle essentiel dans l'efficacité du piégeage et dans la compression radiale.

Après cela, le paquet de positons est comprimé axialement en changeant la forme du puits de potentiel électrique, dans l'optique de re-piéger les positons dans le troisième étage du piège. Le temps de vie des positons dans ce troisième étage ($\sim$ 10 s) est assez grand pour commencer un empilement des paquets de positons dans le troisième étage. 10 paquets correspondant à 10 × 100 ms d'accumulation dans le second étage sont ainsi transférés dans le troisième étage et y sont une fois de plus comprimés radialement à l'aide du "Rotating Wall".

A l'heure actuelle, le BGT fournit un paquet de $\sim 1.5 \times 10^6\,e^+$ chaque seconde (il y a une perte durant la procédure d'empilement dans le troisième étage). Ce paquet va être alors transféré dans le second piège de l'expérience où une nouvelle procédure d'empilement va avoir lieu afin de piéger le plus de positons possible.

Chapitre 5 : Piège à fort champ électro-magnétique

Le second piège de l'expérience est appelé "Piège à fort champ électro-magnétique" (abrégé en HFT pour High Field Trap). Il s'agit d'un piège de Penning-Malmberg disposant d'un électro-aimant refroidi permettant d'obtenir un champ uniforme de 5 T et il est possible d'appliquer des différences de potentiel de 2 kV entre chaque électrode (0.05 T et 140 V pour le précédent piège), ce qui permet le confinement d'un grand nombre de particules.

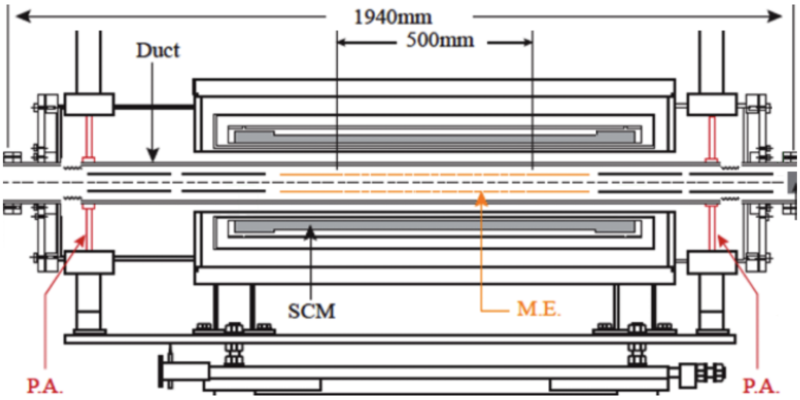

Schéma du piège. Les positons arrivent de la gauche et son éjectés vers la droite. La partie grisée (SCM) correspond à l'électro-aimant. Les électrodes représentées en orange (M.E.) permettent de créer un puits long de 500 mm.

Il a été en effet démontré dans un premier temps qu'il était possible de stocker plus de 10^9 électrons en provenance d'un canon à électron installé en amont du piège. Cependant, les expériences menées avec les électrons ont mis en avant qu'il y avait probablement un problème d'alignement entre les électrodes et le champ magnétique. Le même problème apparaît lors du re-piégeage des positons en provenance du BGT, ce qui amène à une perte d'environ un tiers des positons.

Néanmoins, un empilement des positons provenant du BGT dans le HFT a pu être effectué, ce qui a mené à un nouveau record concernant le piégeage de positons au sein de l'expérience GBAR avec 10^9 positons accumulés en 1100 s. Ce nombre peut être comparé au record mondial détenu par la collaboration ATRAP qui est de 4×10^9 en 14 400 s, montrant ainsi que notre résultat est encourageant. Les expériences effectuées avec ce piège ont été réalisées sans utiliser le “Rotating Wall”, ce qui devra être la prochaine étape du développement de la partie piégeage de positons. Après cela, il est envisagé de remplacer le BGT par un refroidissement des positons à l'aide d'un nuage d'électrons à l'entrée du HFT.

Chapitre 6 : Futur du piégeage de positons chez GBAR

Dans ce chapitre, une revue rapide des possibilités d'optimisation du piégeage est effectuée. Le problème actuel étant que le taux final de piégeage des positons est 100 fois inférieur à ce que nous souhaiterions pour produire des $\overline{\mathrm{H}}^+$.

Ainsi, des améliorations à court terme telles que celles prévues sur le LINAC sont à venir mais ce ne sera pas suffisant (un facteur autour de 3 est attendu). C'est pour cela que de plus profondes modifications sont à venir telles que l'utilisation d'un re-modérateur au Si-C dans le BGT ou le refroidissement par des électrons dans le HFT.

Au final, ces optimisations pourraient nous permettre d'avoir un taux de piégeage 50 fois supérieur au taux actuel. Ainsi, au lieu de créer un $\overline{\mathrm{H}}^+$ toutes les 100 s, ce serait toutes les 200 s (en accumulant les positons 200 s au lieu de 100 s).

Chapitre 7 : Équations de la fusée

Une partie de cette thèse a été dévolue à l'étude de la propulsion spatiale à antimatière. Dans notre modèle, des antiprotons sont annihilés sur une cible d'hydrogène et les particules produites chargées sont redirigées à l'aide d'un miroir magnétique pour propulser la fusée. Les particules neutres quant à elles quittent le centre d'interaction de façon isotropique, ne participant donc pas à l'accélération de la fusée. Si l'on considère qu'une fraction ξ des particules produites sont chargées, l'équation de déplacement de la fusée dans le cadre de la mécanique newtonienne est

$$v(t) = -\xi w \ln\left(\frac{m(t)}{m(t_0)}\right) + v(t_0),$$

avec v la vitesse, m la masse de la fusée et w la vitesse d'éjection des particules chargées. Le paramètre habituellement utilisé est l'impulsion spécifique définie dans notre cas comme

$$I_{\mathrm{sp}} = \frac{\xi w}{g},$$

avec g l'accélération de pesanteur sur Terre. À l'heure actuelle, les fusées couramment utilisées ont une I_{sp} de l'ordre de 400 s et comme démontré dans le chapitre suivant, on pourrait espérer une I_{sp} allant jusqu'à 10^7 s dans le cas d'une propulsion par antimatière. Cela permettait alors d'atteindre des vitesses proches de la vitesse de la lumière. C'est pourquoi l'équation du mouvement dans le cadre de la relativité restreinte a été présentée dans ce chapitre

$$v(t) = c\frac{\left(\frac{m(t)}{m(t_0)}\right)^{\frac{-2\xi w}{c}}\left(\frac{c+v(t_0)}{c-v(t_0)}\right) - 1}{\left(\frac{m(t)}{m(t_0)}\right)^{\frac{-2\xi w}{c}}\left(\frac{c+v(t_0)}{c-v(t_0)}\right) + 1},$$

avec c la vitesse de la lumière.

Chapitre 8 : Exemple de moteur à antimatière

Nous avons étudié dans ce chapitre le modèle du "Beamed core engine" pour propulser une fusée à l'aide d'antimatière, l'idée étant de diriger un faisceau de particules dans une direction précise pour accélérer la fusée. Dans notre cas, il s'agit d'envoyer un faisceau d'antiprotons sur une cible d'hydrogène et de rediriger les produits de réaction à l'aide d'un miroir magnétique. L'interaction proton-antiproton peut être simplifiée en moyenne par la réaction

$$p\bar{p} \rightarrow 1.5\pi^+ + 1.5\pi^- + 2\pi^0,$$

ainsi, environ 2/5 de l'énergie est perdue sous forme de particules neutres, les pions π^0 se désintégrant en γ qui devront être stoppés pour protéger l'intégrité de la fusée.

Une simulation basée sur la bibliothèque GEANT4 a été développée, et nous avons trouvé qu'il est possible d'obtenir une impulsion spécifique de 1.5×10^7 s, à l'aide d'un champ magnétique de 30 T dans la géométrie appropriée. Cependant, notre simulation est basée sur la présence d'un canon à antiproton, ce qui pour l'instant n'est pas quelque chose de réaliste.

Une autre limitation est due à la production de rayon γ. En effet, une telle fusée devrait être protégée par un bouclier assez dense pour absorber l'énergie et disposer de radiateurs assez larges pour évacuer toute la chaleur. Notre étude montre que dans ce cas, il serait très difficile pour une fusée propulsée par antimatière de dépasser une vitesse de $0.05c$.

Acknowledgements

During this PhD, I received different kinds of support and I would like to thank all of these people who helped me during this three years.

I would first like to thank my three supervisors, Boris Tuchming, Patrice Pérez, Dirk van der Werf who guided me a lot and gave me all the opportunities to improve myself as a person and as a scientist. I could say the same from all the members of GBAR collaboration. This team has been a big part of my life recently and working with them has been a pleasure. I would like to mention Pauline Comini and Bongho Kim who made my life happier in the control room as well as Jean-Yves Rousse and Sandrine Javello who made my life easier at CERN. Also, I would like to thank Laszlo Liszkay and Christian Regenfus for their assistance during my experiments and also Bruno Mansoulié for his substantial help in the correction of my manuscript.

In addition, I would like to thank all the interns who worked with me: Annalies M. Kleyheeg, Judith Gafriller, Romain Meriot and Benoit Garneret. They worked and helped me a lot and I hope they enjoyed this time together and I wish them to succeed in their studies.

All this work would not have been possible without CEA and CNES (represented by Stéphane Oriol, Frédérique Masson) which supported my thesis financially and administratively. I would like to thank these two remarkable institutions which believed in me enough to give me this great opportunity and I would like to thank all the people who had to deal with my case (Gautier Hamel de Monchenault, Georges Vasseur, Martine Oger, Béatrice Guyot, Florian Bauer and more).

It is also important for me to deeply thank the members of the jury: Réza Ansari, David Cassidy, Alexandre Obertelli, Gerda Neyens, Martina Knoop, and Roland Lehoucq. They took time to read and bring corrections or asked questions to help me to improve my manuscript. Thanks a lot again.

Furthermore, during my PhD, my friends supported me as much as I needed and for sure this period of my life would not have been the same without them. This is why I would like to thank Szabolcs, Riccardo, Shudhashil, McPherlain, Matheus, Jillo, Nick and Julien.

Unfortunately, it is impossible to thank everyone. Therefore, to conclude this long list, I would like to thank Filippo, my grandparents who supported me a lot during my long studies and the rest of my family. And finally, my sister Sonia, who supported me during my entire life.

Contents

List of Figures

List of Tables

Chapter 1

Introduction

> When I was a young man, Dirac was my hero. He made a new breakthrough, a new method of doing physics. He had the courage to simply guess at the form of an equation, the equation we now call the Dirac equation, and to try to interpret it afterwards.
>
> Richard Feynman, 1986

Contents

1.1 Discovery of antimatter

Before the Dirac theory of quantum electrodynamics, the state of the art to determine the behaviour of a particle was the Schrödinger equation within the framework of quantum mechanics. However, the Schrödinger equation had two shortcomings. Firstly, this equation was not relativistic, and considering that it is easy for an electron to reach an energy of several hundred keV, i.e., comparable to its rest mass-energy, it appeared that a relativistic equation to govern its behaviour had to be found. Secondly, the spin did not appear naturally and was an ad-hoc element of the quantum theory. Thus Dirac decided to work on a relativistic theory of the electron with a spin, and provided in 1928 [1], what is now called the Dirac equation (see more in Appendix B.3):

$$\left(i\hbar\gamma^{\mu}\partial_{\mu} - mc\right)\psi = 0, \tag{1.1.1}$$

where ψ is the wave function, m the mass of the particle, c the speed of light, γ^{μ} the Dirac matrices (defined in Appendix B.3). This equation led to a first solution (Appendix B.4):

$$\psi_s^{(+)}(p^{\mu}, x^{\mu}) = u_s(\overrightarrow{p})e^{-ip^{\mu}x_{\mu}}, u_s(\overrightarrow{p}) = \sqrt{\frac{E+mc^2}{2E}}\begin{pmatrix}\phi_s \\ \frac{\overrightarrow{p}\cdot\overrightarrow{\sigma}}{E+mc^2}c\phi_s\end{pmatrix}, \tag{1.1.2}$$

$$\phi_s = \begin{pmatrix}1 \\ 0\end{pmatrix} \text{ or } \begin{pmatrix}0 \\ 1\end{pmatrix}, \tag{1.1.3}$$

describing naturally the electron as a particle with two possible states corresponding to the spin (Appendix B.5). Thereby, the goal of Dirac in finding a relativistic theory of the electron with a spin was achieved.

However, a non expected solution, describing a particle of "negative" energy and with a reversed charge also appeared:

$$\psi_s^{(-)}(p^{\mu}, x^{\mu}) = v_s(\overrightarrow{p})e^{ip^{\mu}x_{\mu}}, v_s(\overrightarrow{p}) = \sqrt{\frac{E+mc^2}{2E}}\begin{pmatrix}\frac{\overrightarrow{p}\cdot\overrightarrow{\sigma}}{E+mc^2}c\phi_s \\ \phi_s\end{pmatrix} \tag{1.1.4}$$

In order to explain this negative energy solution, Dirac emitted the theory of a "sea" of electrons. When an electron escapes from this sea it creates a "hole" considered as a negative-energy state and when an electron falls into that "hole", it annihilates and the energy is released in the form of electromagnetic radiation. In 1931, he postulated that the "hole" could be a particle of the same mass as the electron, but with an opposite charge, and able to annihilate with an electron. The hypothetical particle was named "anti-electron" [2].

Considering that such a particle had never been observed, Pauli wrote in 1932: "Recently Dirac attempted the explanation [...] of identifying the holes with anti-electrons, particles of charge $+|e|$ and same mass as that of the electrons. The experimental absence of such particles [...] We do not believe, therefore, that this explanation can be seriously considered" [3].

In 1932, Anderson discovered experimentally this particle [4, 5], nowadays called the positron (see Figure 1.1), validating the Dirac theory in the process.

This breakthrough of Dirac and Anderson paved the way for modern particle physics as we know it, leading to the Standard Model of particle physics [6, 7, 8, 9, 10, 11], which is now a well established theory successfully describing a large amount of experimental results.

1.2 Why does antimatter matter?

1.2.1 CPT symmetry

The study of antimatter is an exciting field of research because it might be an opportunity to find a breach in the Standard Model. This is what we briefly explain now.

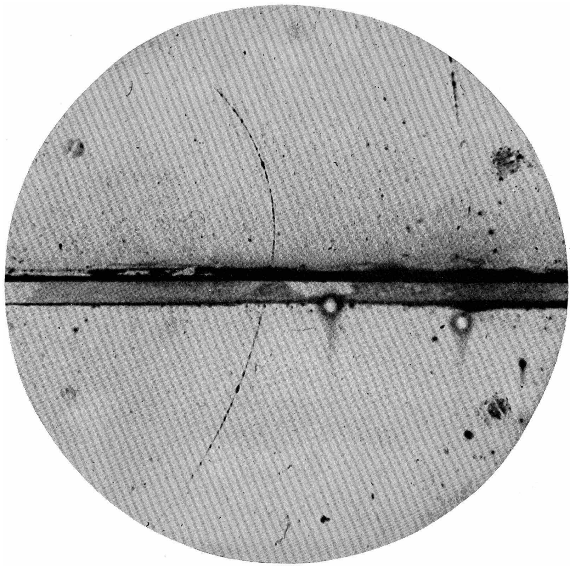

Figure 1.1 – Extracted from Ref. [5]. “A 63 million volt positron passing through a 6 mm lead plate and emerging as a 23 million volt positron. The length of this latter path is at least ten times greater than the possible length of a proton path of this curvature”. The particle comes from below the lead plate, and a magnetic field perpendicular to the plane bends the trajectory of the charged particles. The trajectory of the particle in this configuration shows that the charge is positive.

In physics, three fundamental symmetries are defined. They are associated to three fundamental transforms: charge conjugation (C), parity transformation (P) and time reversal (T). These symmetries are not necessarily fulfilled, but it has been demonstrated that the combination of the three transforms, named CPT transform, is a symmetry of a relativistic quantum theory.

The consequence of CPT symmetry is that each particle has a corresponding antiparticle with opposite electric charge, opposite spin, opposite internal quantum numbers, the same lifetime and inertial mass. The idea is to look for a CPT symmetry violation, because any asymmetry would be a clue to new physics.

Moreover, in the primordial universe, right after the Big Bang, according to the Standard Model of Cosmology, the amount of matter was equal to the amount of antimatter [12]. However our visible universe, as far as we know, is made of matter. This fact leads to at least two questions: why is the universe made of matter? What happened to antimatter? A small violation of CPT, in addition to a breakthrough in physics, could help in solving this problem [13].

Considering that the hydrogen atom is one of the most well known systems, the study of the antihydrogen atom, which again, according to the CPT theorem, should have the same quantum levels as those of hydrogen, is a relevant lead for CPT violation. Also, the antihydrogen atom is by far the easiest anti-atom to make. This explains why many experiments are working on it, as presented below.

1.2.2 Some important experiments

An important step on the way to antihydrogen production (antihydrogen being made of antiprotons and positrons) was the Bevatron experiment, which detected in 1955, sixty antiprotons [14]. This result was obtained by colliding a $\sim 5.6\,\text{GeV}$ proton beam on a copper target and deflecting the antiprotons. This was a major result, because it was the experimental proof that the Dirac theory of the electron could be extended to the proton.

Another step was the production and detection of 11 antihydrogen atoms at CERN in 1996 by the PS210 experiment [15] using the Low Energy Antiproton Ring (LEAR). Antiprotons $\overline{p}$ were sent on a target to collide with a nucleus (Z) in order to create an e^+e^- pair coming from a two-photon mechanism or from virtual Bremsstrahlung photons. Occasionally, the positron e^+ could bind with the antiproton to yield an antihydrogen atom $\overline{\text{H}}$:

$$\overline{p}Z \to \overline{p}\gamma\gamma Z \to \overline{p}e^+e^-Z \to \overline{\text{H}}e^-Z, \tag{1.2.1a}$$

$$\overline{p}Z \to \overline{p}\gamma^* Z \to \overline{p}e^+e^-Z \to \overline{\text{H}}e^-Z. \tag{1.2.1b}$$

This result was corroborated by a group working at Fermi Lab [16].

This last encouraging result led CERN in 1997 to build the Antiproton Decelerator (AD) [17] in order to provide slow antiprotons to different experiments, the antiprotons resulting from the collision of a $26\,\text{GeV}$ proton beam arising from the PS accelerator, colliding with a target and cooled to $5.3\,\text{MeV}$. Then in 2015 the Extra Low ENergy Antiproton ring (ELENA, see Figure 1.2) [18] was developed to decelerate the antiproton coming from the AD to $100\,\text{keV}$.

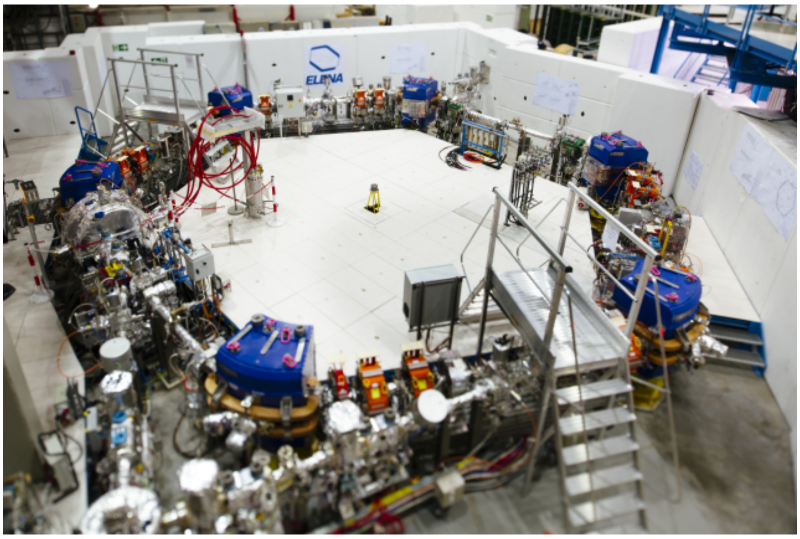

Figure 1.2 – Picture of the ELENA ring.

Nowadays, the AD hall (also named Antimatter Factory) is the major place were different collaborations (ALPHA [19], ATRAP [20], ASACUSA [21], BASE [22], AEGIS [23], ALPHA-G [24], and GBAR [25]) perform experiments on antimatter, with the objective of looking for CPT violation and also violation of the Weak Equivalence Principe (see Section 2.1).

Thanks to the AD, huge steps in the study of antimatter occurred over the last two decades. For example in 2002, the ATHENA [26] and ATRAP [27] collaborations were the first to produce and observe about 100 cold antihydrogen atoms. Then, the ALPHA collaboration managed to trap antihydrogen atoms for more than 1000 s [28]. In 2015, CPT invariance with baryonic antimatter was tested by the BASE collaboration in the measurement of the antiproton-to-proton charge-to-mass ratio with 2×10^{-10} relative precision [29]. Recently, at the end of 2016, the ALPHA collaboration observed the 1S-2S transition in magnetically trapped atoms of antihydrogen, with results consistent with CPT invariance at a relative precision of about 2×10^{-10} [30].

All these experiments have shown that for now, the predictions of the Standard Model are correct within the accuracy of these measurements. Also, other experiments, like AEGIS, ALPHA-G and of course GBAR, which is presented in the next chapter, investigate on the effect of gravity on antimatter.

1.3 Antimatter, the future of space travel?

Using antimatter as a vector of energy is a very appealing idea because 100% of the mass could annihilate with matter to obtain energy. For example, there is 9×10^{10} MJ of usable energy per kilogram of antimatter (if there is the same mass of matter for the annihilation). As an element of comparison, one kilogram of diesel represents 48.1 MJ by combustion and the global production of energy in 2018 is estimated to 6×10^{14} MJ[1].

This huge amount of energy per mass unit is obviously interesting for space travel. As will be presented in Chapter 7, for a single stage rocket, the variation of the velocity ΔV of the rocket (if $\Delta V \ll c$, where c is the speed of light) is described by

$$\Delta V = w \ln \frac{M_i}{M_f}, \tag{1.3.1}$$

where w is the velocity of ejection of the propellant relative to the rocket frame, M_i and M_f respectively the total initial and final masses of the rocket. Therefore, a high energy per mass unit leads to a possibility to increase the mass of the payload or to increase the final speed of the rocket. Figure 1.3 presents different payloads for different final speeds and different specific impulses I_{sp} ($I_{\mathrm{sp}} = \mathrm{w/g}$, more details in Section 7.1).

About the specific impulse, it is shown in Chapter 8 that it is possible to imagine an engine using antimatter and providing a specific impulse in the order of 10^7 s (because the products of the $p\bar{p}$ reactions are ejected with a speed close to the speed of light). To compare, the Vulcain engine, propelling currently the Ariane 5 rocket, has an I_{sp} of 434 s. It means that with the same specifications concerning the masses, the final speed of the rocket can be multiplied by a factor of 100 000.

However, there is a non negligible issue: there are no tons of antimatter available (not even nano-grams) and still no technology to produce and store macroscopic amounts of antimatter (see more in Section 8.4).

---

[1] 14 421 151 kilo ton of oil equivalent according to the International Energy Agency

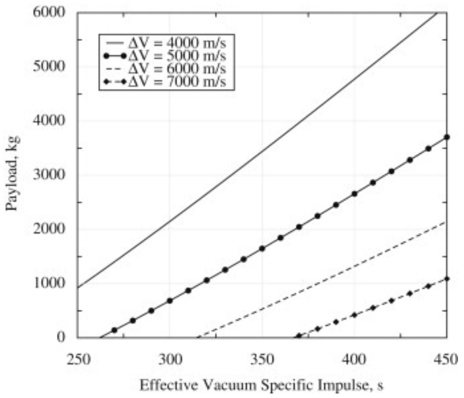

Figure 1.3 – Extracted from Ref. [31]. Payload for a single-staged rocket as a function of the effective specific impulse in vacuum. Launcher has an inert mass of 2 t, a propellant load of 12 t. Different ΔV mission requirements are reported.

1.4 Conclusion

Antimatter, discovered mathematically by Dirac in 1928 and experimentally by Anderson in 1932 is nowadays a very active field of research especially at CERN with the Antiproton Decelerator facility. It is also especially interesting because it could be a way to find a breach in the Standard Model of Physics, and open new fields of research.

Furthermore, the experiments such as the GBAR experiment studying the gravitation at the level of the elementary particles, would lead to a new breakthrough in our knowledge on the universe if it is shown that the gravitational behaviour of antimatter is different from that of matter.

The interest in antimatter for space propulsion comes from the annihilation reaction. Indeed, if a matter particle meets its twin antimatter particle, they annihilate each other into lighter particles that have a speed close to the speed of light. The huge amount of kinetic energy coming from the annihilation reaction could be used to have a propellant with a very high specific impulse when it is ejected from the rocket and with the highest possible energy density, making possible to reach speeds close to that of light.

Of course, this attractive idea is limited by two huge issues. First of all: there is no antimatter on Earth! For now, we know how to produce it, but in ridiculously small quantities compared to the required amount for a spatial trip. Secondly, we do not have for now a device able to store efficiently a large amount of antimatter. But it remains an exciting idea, which can be at least seriously studied.

Chapter 2

The GBAR experiment

> Gravity is a contributing factor in nearly 73 percent of all accidents involving falling objects.
>
> Dave Barry

Contents

2.1 Context and aim of the GBAR experiment

A simple way to determine a gravitational field is to do the analogy with an electric field. Indeed, if the charge density ρ is replaced by the mass density, the equation on the electric field E

$$\nabla \cdot E = \frac{\rho}{\epsilon_0} \tag{2.1.1}$$

becomes for the gravitational field g

$$\nabla \cdot g = -4\pi G \rho. \tag{2.1.2}$$

The main difference being that in the case of the electric field, two opposites charges are attracted and two similar charges are repelled and in the case of the gravitational field, two positives masses are attracted. Therefore, is it possible to have a negative mass (with antimatter for example)? Can we speak about antigravity for antimatter?

The Weak Equivalence Principle (WEP) states that the trajectory of a particle is independent of its composition and internal structure when it is only submitted to the gravitational force. In other words, it means that the gravitational mass is equal to the inertial mass. The inertial mass being positive, with the WEP, gravitational masses are also positive and attract each other.

The WEP has been tested with high accuracy in the case of matter. One generally defines the Eötvös parameter as

$$\eta_{1,2} = \frac{a_1 - a_2}{(a_1 + a_2)/2} = \frac{(m_g/m_i)_1 - (m_g/m_i)_2}{\left((m_g/m_i)_1 + (m_g/m_i)_2\right)/2} \tag{2.1.3}$$

with a_1, a_2 the accelerations of two different bodies in the same gravitational field, and m_g, m_i, the gravitational and inertial masses. If the WEP is valid, one should expect $\eta_{1,2} = 0$.

		Be-Ti	Be-Al
$\eta_{\oplus}$	(10^{-13})	0.3 ± 1.8	-0.7 ± 1.3
$\eta_{\odot}$	(10^{-13})	-3.1 ± 4.7	-5.2 ± 4.0
η_{DM}	(10^{-5})	-4.2 ± 6.2	-2.4 ± 5.2

Table 2.1 – Extracted from Ref. [32]. Eötvös parameters $\eta_{\oplus}$, $\eta_{\odot}$ and η_{DM} were calculated using the horizontal gravitational accelerations of Earth, Sun and galactic dark matter in comparing accelerations of Beryllium and Titanium, and Beryllium and Aluminium.

The torsion-balance tests already performed [32] show that in the case of matter, the WEP can be legitimately accepted, with $|\eta| < 10^{-12}$ (except for the measurement with dark matter, see Table 2.1).

Finally, wondering about gravity means wondering if the WEP is still valid for antimatter. Indeed, one idea to understand the matter dominance observed in the universe, is that with antimatter WEP is not fulfilled [33]. The GBAR experiment (Gravitational Behaviour of Antihydrogen at Rest [25]) arises from an idea of J. Walz and T. Hänsch [34], to study the free fall acceleration of the antihydrogen atom $\overline{\mathrm{H}}$.

If we take into account Morrison's argument [35], it is not possible to observe antigravity because this would lead to a non-conservation of energy with our current way to understand the gravitational interaction. Moreover, if we accept antigravity how to explain the fall of a photon in a gravitational field considering that the photon is its own antiparticle?

This is why the result of the GBAR experiment is awaited, knowing that if a relative difference of $\sim 1\%$ is found between the inertial mass of antimatter and the gravitational mass of antimatter, it will be the proof that there is something to change in our current models.

2.2 Scheme of the GBAR experiment

In the GBAR scheme (general layout shown in Figure 2.1), one first produces $\overline{\mathrm{H}}^+$ ions (one antiproton and two positrons) using the following reactions [36]

$$\overline{p} + \mathrm{Ps} \rightarrow \overline{\mathrm{H}} + e^-, \tag{2.2.1a}$$

$$\overline{\mathrm{H}} + \mathrm{Ps} \rightarrow \overline{\mathrm{H}}^+ + e^-, \tag{2.2.1b}$$

where $\overline{p}$ is an antiproton and Ps is an positronium atom. Ps consists of the bound state of a positron and an electron (e^+, e^-).

The antiprotons, provided by the ELENA decelerator at CERN [18], are decelerated, trapped and cooled (see Section 2.3) before being sent in the reaction chamber.

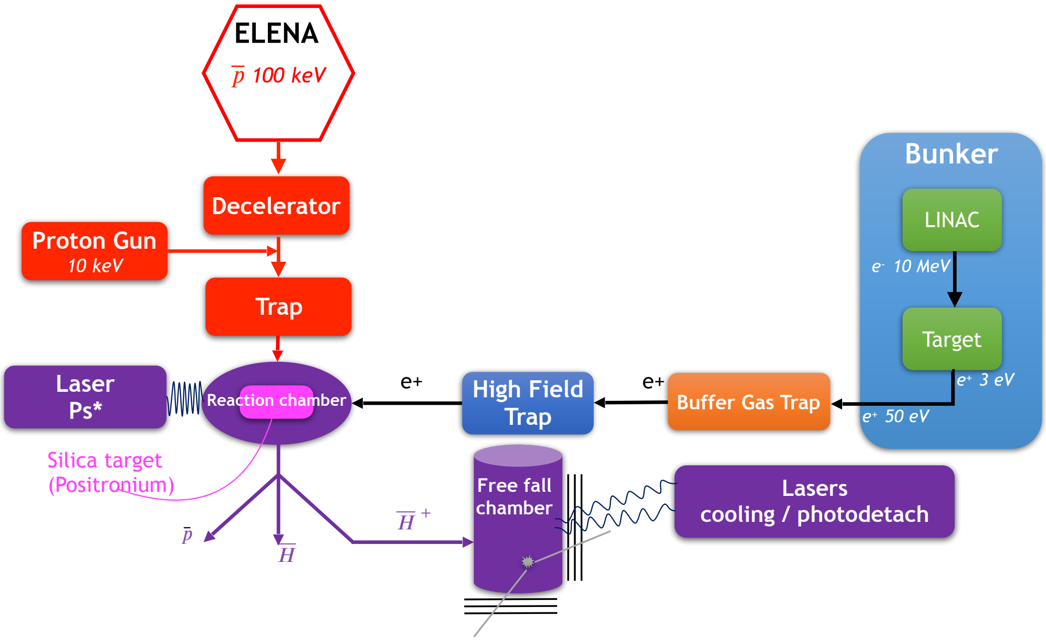

Figure 2.1 – Overall scheme of the GBAR experiment.

The positrons required for the positronium formation originate from an electron linear accelerator (LINAC), after the collision between the electrons and the target. The positrons are first accumulated in a Buffer Gas Trap (a modified Penning-Malmberg trap used to cool the positrons) and transferred into a High Field Trap (a 5 T Penning-Malmberg trap used to store a large amount of positrons). This trapping step will be detailed in this thesis.

The positronium target is produced by implantation of about 10^{10} positrons into a nanoporous silica film at a kinetic energy of 4 keV [37].

After the $\overline{\mathrm{H}}^+$ ion has been formed it is guided into a Paul trap where it is subsequently sympathetically cooled using laser cooled Be$^+$ ions [34]. When the anti-ion is cold enough, the extra positron is ripped off using laser pulses. The acceleration of the resulting neutral $\overline{\mathrm{H}}$ in Earth's gravitational field is determined from the Free Fall time of the $\overline{\mathrm{H}}$ atoms inferred from the time between the start of the fall given by the laser pulse and their annihilations on the wall of a free fall chamber.

2.3 Antiproton trapping

The antiprotons are provided by the ELENA decelerator at CERN [18] with the following beam parameters [38]:

- beam intensity: $5 \times 10^6 \overline{p}$ per pulse,
- beam energy: 100.0(1) keV,
- pulse shape: 1.3 m, 300 ns,
- beam emittance: 4π mm mrad.

The first stage of the GBAR antiproton line is a decelerator [39] inspired by the ISOLTRAP heavy ion decelerator [40] whose central element is a Pulsed Drift Tube (PDT) as shown in Figure 2.2. The incoming antiprotons, with an energy $E_i = 100\,\text{keV}$, are slowed by the high electric potential applied at the entrance of the PDT, $V_{\text{PDT}} = -99\,\text{kV}$. When the antiprotons are inside the PDT, the tube is switched from V_{PDT} to ground. Then, the antiprotons exit the tube with an energy $E_r = E_i - |V_{\text{PDT}}| = 1\,\text{keV}$ and can be trapped in order to be cooled and compressed.

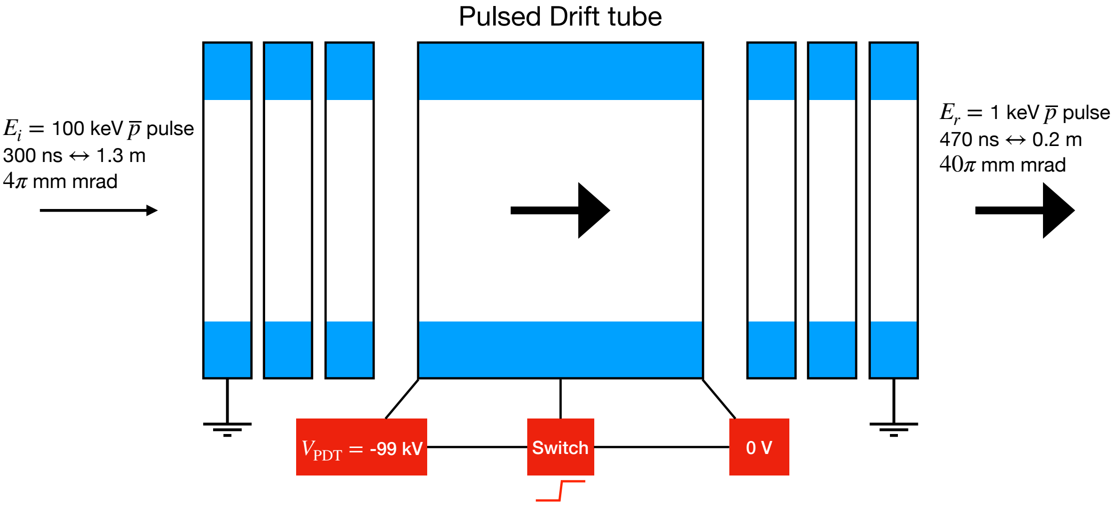

Figure 2.2 – Extracted from Ref. [39, 38]. Schematic of the Pulsed Drift Tube principle.

A 7 T Penning-Malmberg trap [41] (pictures in Figure 2.3) is used under ultra-high vacuum. The capture of antiprotons with a Penning-Malmberg trap has been firstly performed in 1986 [42], this is then a well known technique. While potential barriers confine the few keV antiprotons axially, the strong magnetic field confines them radially. Then, electrons trapped in a harmonic potential well cool the antiprotons to a few eV. Applying a rotating electric field generated by an azimuthally segmented electrode, the antiproton cloud is radially compressed. The antiprotons are trapped every 110 s (corresponding to the time between two ELENA pulses).

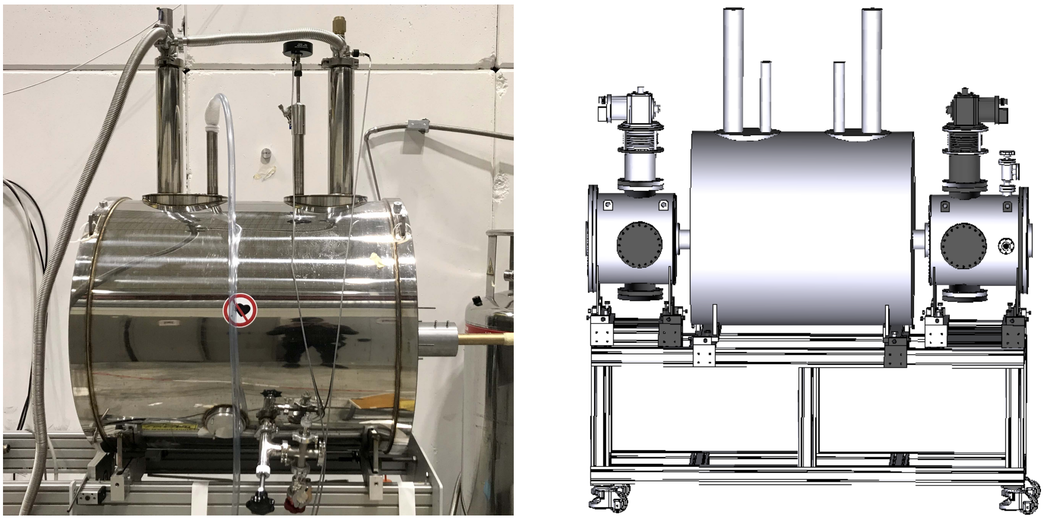

Figure 2.3 – Left: pictures of the antiproton trap magnet. Right: drawing of the magnet equipped with the cryogenic system to cool the electrodes.

2.4 Positronium production

As explained in section 2.1, the reactions to produce antihydrogen ions $\overline{\mathrm{H}}^+$ presented in Equations 2.2.1 require the creation of positronium (bound state of e^+e^-), and consequently, before that, of positrons. The $\overline{\mathrm{H}}^+$ production is dependent on the square of the positron number (linear dependence on the $\overline{p}$ number) because the formation is using positronium twice. This is why being able to trap positrons as much as possible is an important part of the GBAR experiment.

2.4.1 Positron source

The positrons are generated with a linear accelerator (LINAC) [43, 44] (scheme in Figure 2.4). The LINAC accelerates electrons up to an energy of 9 MeV, after which they impinge on a tungsten target where positrons are created through Bremsstrahlung radiation ($\gamma \rightarrow e^+e^-$).

The choice of a LINAC compared to ^{22}Na radioactive sources is based on:

- the beam intensity, 3×10^8 e^+ per second for the GBAR LINAC when it will be fully operating vs a maximum of 10^7 e^+ per second for a 50 mCi radioactive source;
- the reproducibility in the number of positrons produced, whereas the beam intensity decreases in time for ^{22}Na (^{22}Na has a lifetime of 2.7 years);
- with less than 10 MeV electron energy, there is no persistent radioactivity.

The mean kinetic energy of positrons generated using 9 MeV electrons is about 1 MeV. This energy is too large to allow positron trapping and has to be reduced. So, the positrons have to be moderated [44, 45] (scheme of the moderator in Figure 2.5).

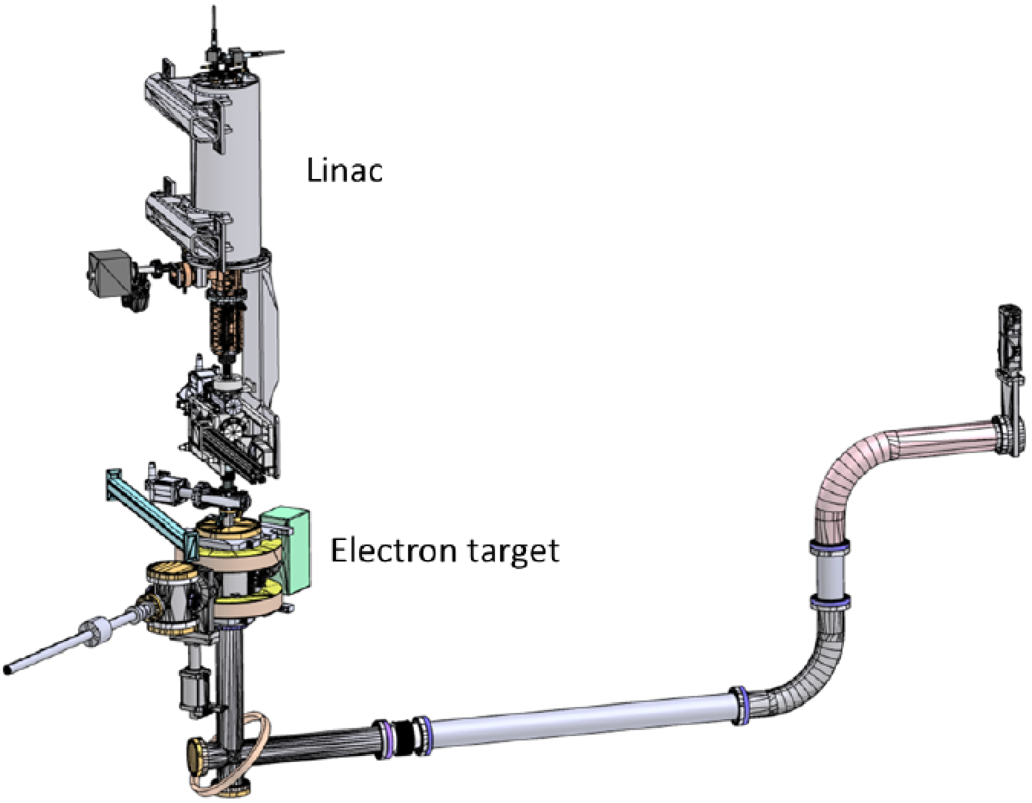

Figure 2.4 – Extracted from Ref. [44]. Scheme of the linac (vertical structure on the left) and the positron transfer line. The transfer magnetic field is generated by a solenoid wound around the beam pipe and larger coils.

The principle of a moderator is to implant positrons into a crystal lattice where they lose energy until they reach thermal equilibrium with the lattice. In the case of tungsten and some other materials, the work function of positrons is negative, i.e., the particles gain energy when they leave the metal. In our case the moderator is made of 12 layers of 20 µm thick tungsten mesh [44]. At the end of the process, the positrons that exit the moderator at 3 eV are accelerated to a kinetic energy of 50 eV due to the biasing of the moderator and a spread of energy of a few eV.

Once moderated, the positrons are ready to be accumulated in the Buffer Gas Trap (Chapter 4) and, subsequently in the High Field Trap (Chapter 5).

2.4.2 Positron trapping

In the aforementioned scheme it is estimated that a bunch of 10^{10} compressed and cooled positrons is required to produce a single $\overline{\mathrm{H}}^{+}$. The production of $\sim 10^{8} e^{+}\mathrm{s}^{-1}$ provided by the LINAC is not enough and an accumulation of $\sim 100\,\mathrm{s}$ is required.

The Buffer Gas Trap (BGT) is a Penning-Malmberg trap based on the Surko-Greaves scheme [46, 47] (originally developed by Surko and subsequently modified by Greaves). The BGT was developed at CEA Saclay [48]. It uses N_2 as trapping gas and CO_2 as cooling gas. The trap is constructed from 3 sets of electrodes. In the

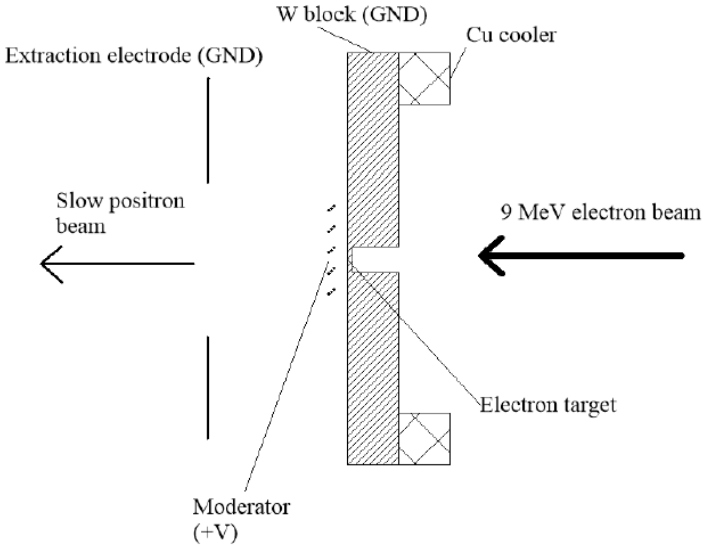

Figure 2.5 – Extracted from Ref. [44]. Cross section of the electron target. The potential of the moderator is $+V$, the rest of the structure is at ground. The copper block (“Cu cooler”) is water cooled. A magnetic field of 9.7 mT is parallel to the electron beam.

first stage, inelastic collisions occur under a typical N_2 pressure of 10^{-3} mbar, whilst the second one is used for the accumulation at a typical N_2 pressure of 10^{-4} mbar, with the final stage used to store positrons for a dozen of seconds with a typical CO_2 pressure of 10^{-6} mbar. The magnetic field in this trap is ~ 0.05 T and an electric potential between -140 V and 140 V is applied to the electrodes, as appropriate.

The High Field Trap [49, 50, 51, 52] is a 5 T Penning-Malmberg trap with 27 electrodes each able to hold potentials between -4 kV and 4 kV. The base pressure is lower than 10^{-9} mbar. This trap is used for long time storage and accumulation.

Both these traps are detailed in Chapters 4 and 5.

2.4.3 Positronium formation

The required positronium for reactions 2.2.1 is produced by positron implantation in a nanoporous silica film target (pictures of the nanoporous film in Figure 2.6), which is placed inside a cavity in the reaction chamber. When the positrons enter the nanopores, they detach electrons with which they can form bound states of positronium. The density of the nanopores is so high that they percolate to produce channels of tubes that reach the surface of the film. The negative work function of the positronium atoms with respect to the silica allows them to bounce inside those tubes until they are expelled in vacuum and produce a positronium cloud [53, 54] in the reaction cavity (see Figure 2.7).

The positron and the electron being two spin-$\frac{1}{2}$ particles, positronium exists in two forms. The singlet (spin 0, corresponding to the state $\frac{1}{\sqrt{2}}\left(|\uparrow,\downarrow\rangle - |\downarrow,\uparrow\rangle\right)$), named para-positronium has a lifetime of 125 ps, which is too short to combine with

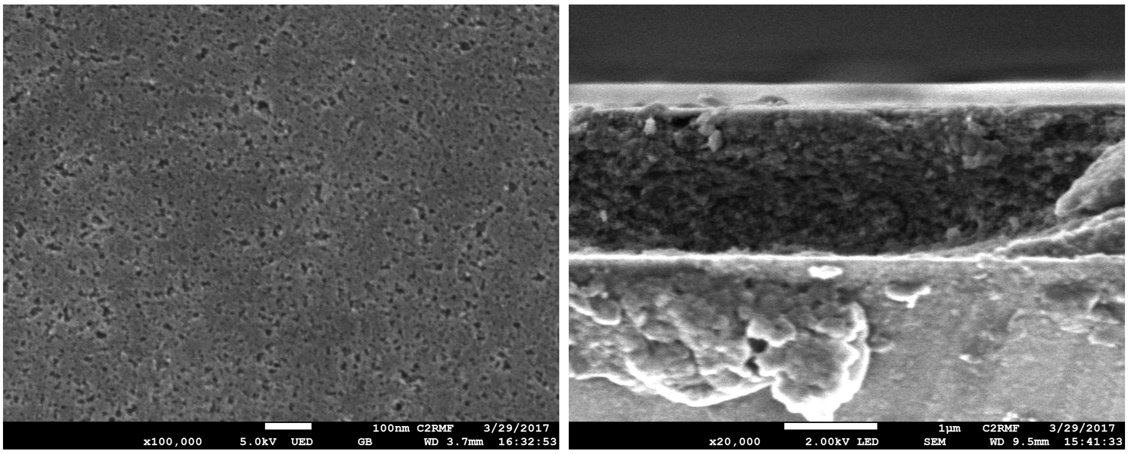

Figure 2.6 – Pictures of the nanoporous silica target obtained by Scanning Electron Microscopy. Left: picture from the top of the target (the positron entrance), one can clearly see the nanopores. Scale: 100 nm. Right: side of the target. One can see the imperfections at the surface. Scale: 1 µm. – Source: C2RMF / P. Lehuédé.

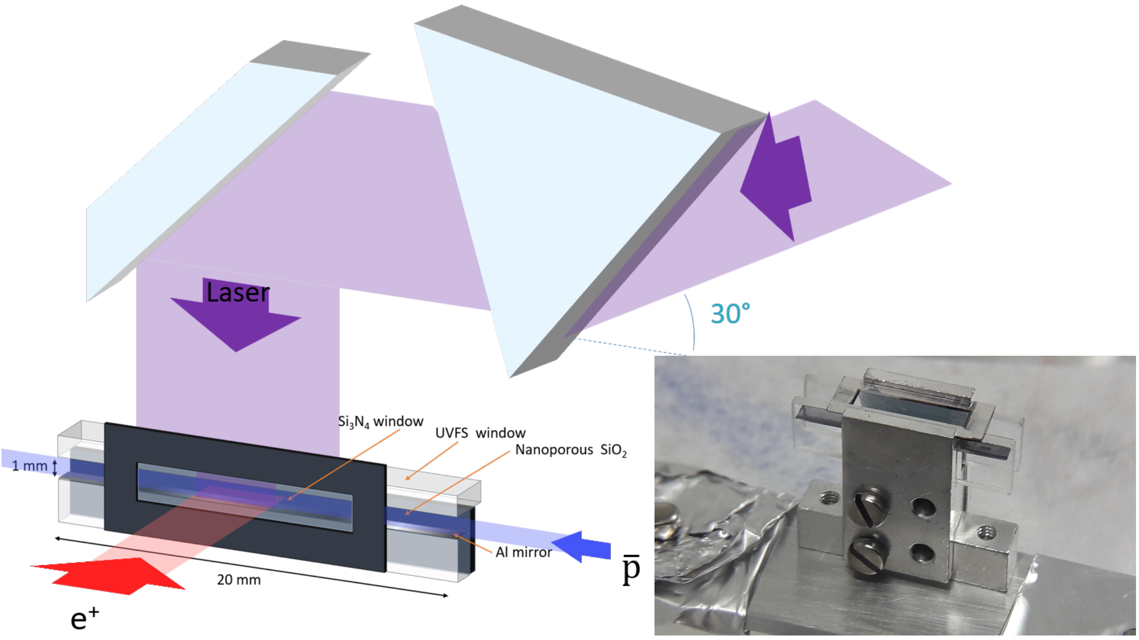

Figure 2.7 – The positrons go through a Si_3N_4 window to enter the nanoporous silica. They are expelled from it under the form of positronium $Ps = (e^+, e^-)$ and remain in the reaction cavity (volume of $1 \times 1 \times 20\text{mm}^3$). The positronium is excited to optimise the reaction rate with the incoming antiprotons. Source: P. Comini / GBAR Collaboration.

antiprotons to create antihydrogen. Thankfully, the triplet (spin 1 corresponding to the states $|\uparrow,\uparrow\rangle, |\downarrow,\downarrow\rangle, \frac{1}{\sqrt{2}}(|\uparrow,\downarrow\rangle + |\downarrow,\uparrow\rangle)$, named ortho-positronium has a lifetime of 142 ns [55, 56, 57], which is long enough to undergo the reactions described in 2.2.1. The efficiency to produce ortho-positronium atoms and eject them outside the film is estimated to be $\sim 30\%$.

The magnetic field inside the reaction cavity has to be low enough ($< 100\,\mathrm{G}$, the effect being strong above $2000\,\mathrm{G}$) to avoid ortho-positronium quenching [58], which means a spin-flip of the particles in the presence of a magnetic field, which has for consequence to turn some ortho-positronium into para-positronium (the maximum being one third).

Positronium measurements have been already performed at the GBAR experiment as presented in Ref. [59]. Once extracted from the HFT, the positron bunch is accelerated by a drift tube and focused by Einzel lenses to implant the positrons in the target. This target can be moved to let the positrons hit a MCP detector (see section 4.4.1, basically, it is a device to image the radial projection of the bunch). The annihilated positrons are detected using $PbWO_4$ crystals. The crystals convert the γ resulting from the annihilation into scintillating signals and a photomultiplier converts these signals into an electric signal. The experimental set up is presented in Figure 2.8.

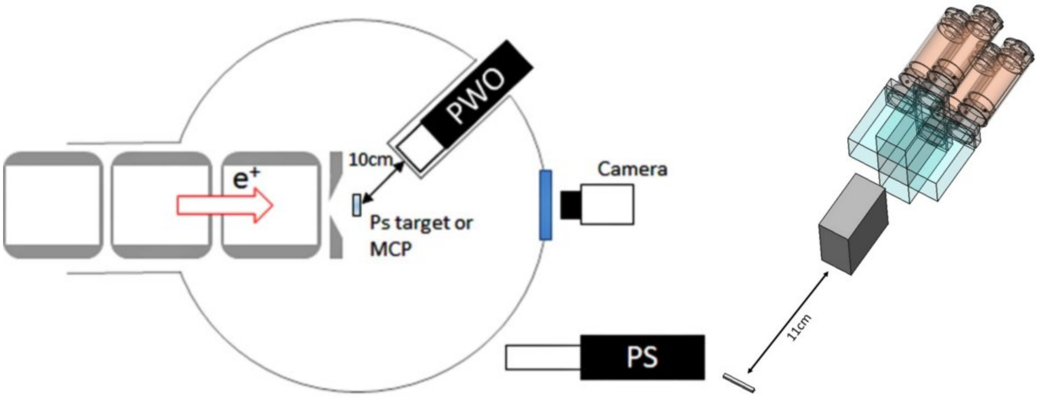

Figure 2.8 – Extracted from Ref. [59]. Left: Schematic view of the target area. The gray coloured tubes show the Einzel lenses aimed at focusing the positron beam. The circular line represents the reaction chamber area. The positronium converter and the MCP assembly are translated by a linear drive to the center of the chamber. A camera is located downstream of the MCP assembly to determine the positron beam profile. The $PbWO_4$ detector and a plastic scintillator (PS) are located at the backside of the target region for the gamma ray measurement. Right: Drawing of the detector assembly. The photomultiplier tubes are connected to the $PbWO_4$ crystals. The rectangle corresponds to the target cavity.

Positrons entering the Ps converter yield detected signals in the $PbWO_4$ detector. The distribution of the signal arrival time in the $PbWO_4$ detector shows two components: one peaking contribution arises from direct annihilation and $p-\mathrm{Ps}$ decay, while a decreasing exponential component corresponds to the decay of $o-\mathrm{Ps}$, whose lifetime is $142\,\mathrm{ns}$ (Figure 2.9).

2.5 $\overline{\mathrm{H}}^{+}$ production

Once the ortho-positronium cloud (section 2.4.3) is created in the reaction cavity (pictures in Figure 2.7), the antiprotons are sent from their storage trap and

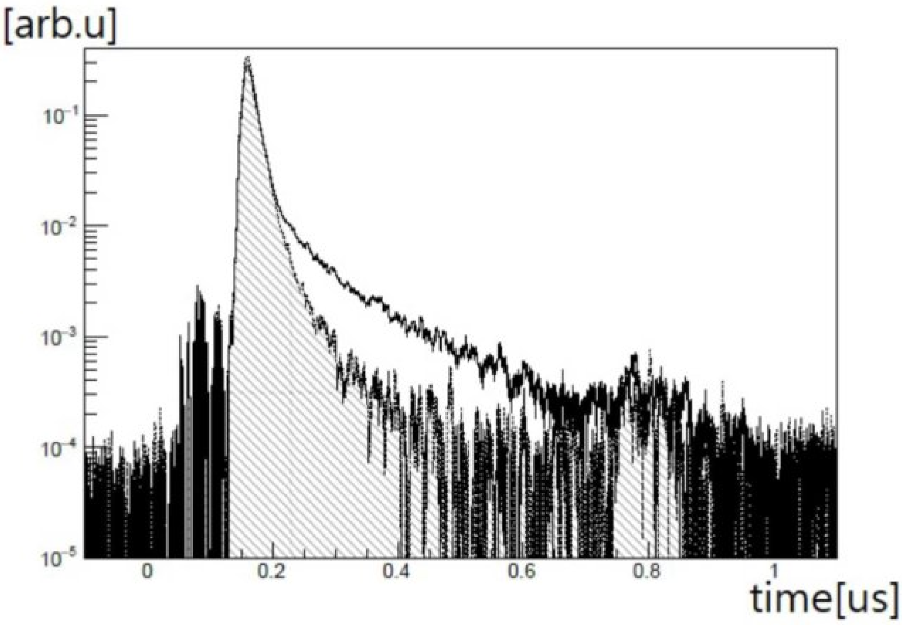

Figure 2.9 – Extracted from Ref. [59]. Raw signal distribution from the $PbWO_4$ detector (averaged data sample). The hatched histogram shows the signal arising from the e^+ beam hitting the MCP while the solid line histogram corresponds to the e^+ beam hitting the positronium converter.

positronium is excited with lasers in order to form antihydrogen atoms and ions.

According to the results presented in Figure 2.10, the cross-section (computed using the perturbative method Continuum Distorted Wave-Final State, CDW-FS) for the reaction $\overline{p}+\mathrm{Ps} \to \overline{\mathrm{H}}+e^-$ is optimal for Ps excited to level $2p$ with a $\overline{p}$ incident energy of 2 keV. For $\overline{\mathrm{H}}^+$ formation, Ps($2p$) is also required with an $\overline{\mathrm{H}}$ incident energy below 2 keV.

This first theoretical result highlights the interest of using excited positronium. Other studies on the topic are ongoing to confirm this result and optimise the $\overline{\mathrm{H}}^+$ production at the GBAR experiment.

At the exit of the reaction chamber, a beam composed of $\overline{p}$, $\overline{\mathrm{H}}$ and $\overline{\mathrm{H}}^+$ is obtained. An electrostatic switchyard (Figure 2.11) separates the charged beams, and the $\overline{\mathrm{H}}^+$ are sent to the free fall chamber.

2.6 $\overline{\mathrm{H}}^+$ cooling and $\overline{g}$ measurement

One to a few $\overline{\mathrm{H}}^+$ ions are expected every 100 s, corresponding to the period between two antiproton bunches coming from ELENA. A high capture efficiency is required to measure the antimatter gravitational acceleration $\overline{g}$. In a first trap, called ITO trap (Figure 2.12), a large Be^+ ion optical crystal is loaded ($\sim 10^6$ ions). Then the $\overline{\mathrm{H}}^+$ ions are captured in this trap to be sympathetically cooled by Coulomb interaction through the laser cooled Be^+ ion crystal. This process allows to cool the $\overline{\mathrm{H}}^+$ ions to mK temperatures [60, 61].

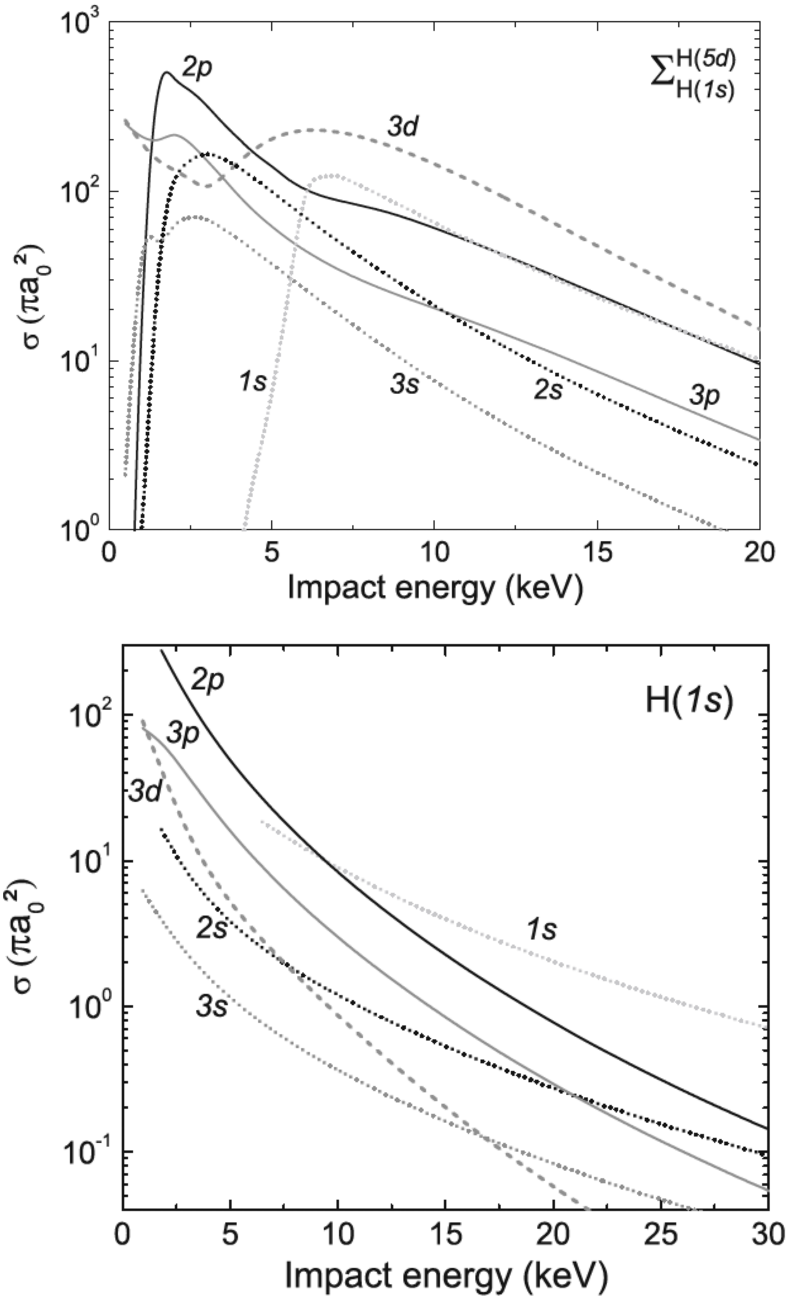

Figure 2.10 – Extracted from Ref. [36]. Top: Cross sections for antihydrogen production from different states of positronium (Ps(1s) to Ps(3d)). These cross sections correspond to the sum of the antihydrogen states up to $\overline{\mathrm{H}}$(5d). Bottom: Cross sections for $\overline{\mathrm{H}}^+$ ion production for Ps(1s) to Ps(3d). Only the $\overline{\mathrm{H}}$ ground state is taken into account, the contribution of the other states being negligible.

The $\overline{\mathrm{H}}^+$ ions are then transferred into a RF Paul trap named "precision trap", where they are cooled to µK temperatures using Raman cooling [62].

A laser pulse is sent to remove the extra positron, and the free fall of the neutral anti-atoms starts. The absorption of the photon and the emission of the positron give an initial velocity v_0 to the ions. The position z can be written as a function

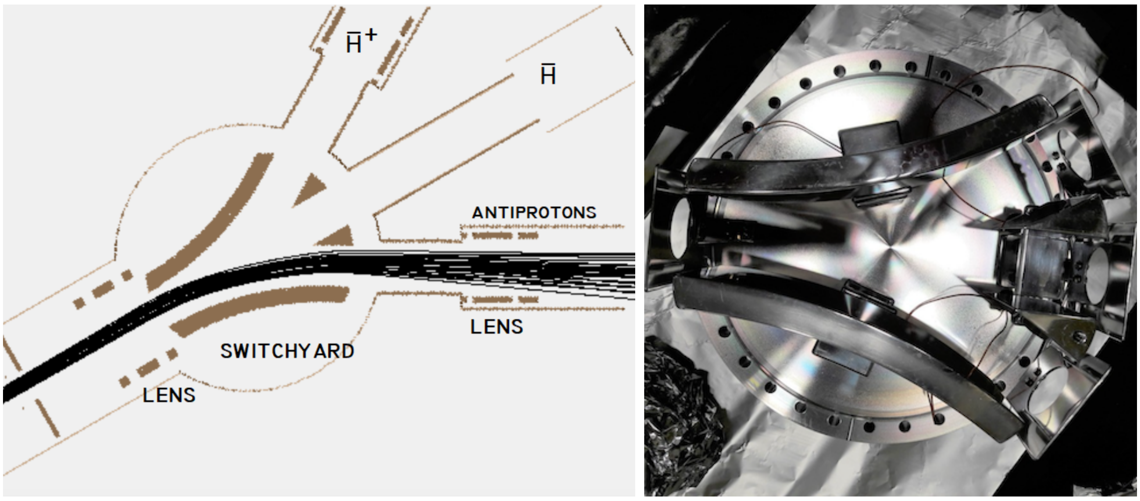

Figure 2.11 – Extracted from Ref. [38]. Left: Simulation of the switchyard. Right: Photograph of the switchyard.

of time:

$$z = \frac{1}{2}\overline{g}t^2 + v_0 t, \overline{g} = \frac{m_g}{m_i} g \tag{2.6.1}$$

The gravity measurement will be performed by detecting the $\overline{\mathrm{H}}$ annihilations on the vacuum chamber walls. In order to eliminate the cosmic-ray background and to determine precise trajectories of the charged particles coming from the annihilation, the free fall chamber (Figure 2.13) will be surrounded by Micromegas tracking detectors. Also, plastic scintillators will be used to detect the charged pions and provide the annihilation time with high precision [61].

The uncertainty on $\overline{g}$ can be written as [63]:

$$\frac{\Delta\overline{g}}{\overline{g}} = 2\sqrt{\left(\frac{\Delta z}{2h}\right)^2 + \left(\frac{\Delta v}{\sqrt{2\overline{g}h}}\right)^2} \tag{2.6.2}$$

with h the height the fall, Δz and Δv the position and velocity dispersions in the vertical direction.

Heisenberg's uncertainty principle $m\Delta z\Delta v \geq \hbar/2$ limits the relative precision of $\left(\frac{\Delta\overline{g}}{\overline{g}}\right)_{\text{opt}} = 1.7 \times 10^{-4}$ if $\overline{g} = g$ and $h = 1\,\text{m}$ [60]. However, if we take into account the recoil due to the absorption of the detachment photon, one can assume an uncertainty of $\Delta v \sim 1\,\text{m}\,\text{s}^{-1}$ [60], Equation 2.6.2 can be approximated with

$$\frac{\Delta\overline{g}}{\overline{g}} = \sqrt{2}\frac{\Delta v}{\sqrt{\overline{g}h}} = 0.4 \tag{2.6.3}$$

per detected atom. So, the 1% resolution can be obtained with about 1600 detected events. If we have an event every 100 s, two days of continuous detection are required.

2.7 Conclusion

The purpose of the GBAR experiment is to determine, as said by its name, the Gravitational Behaviour of Antimatter at Rest. The corner stone of the experiment

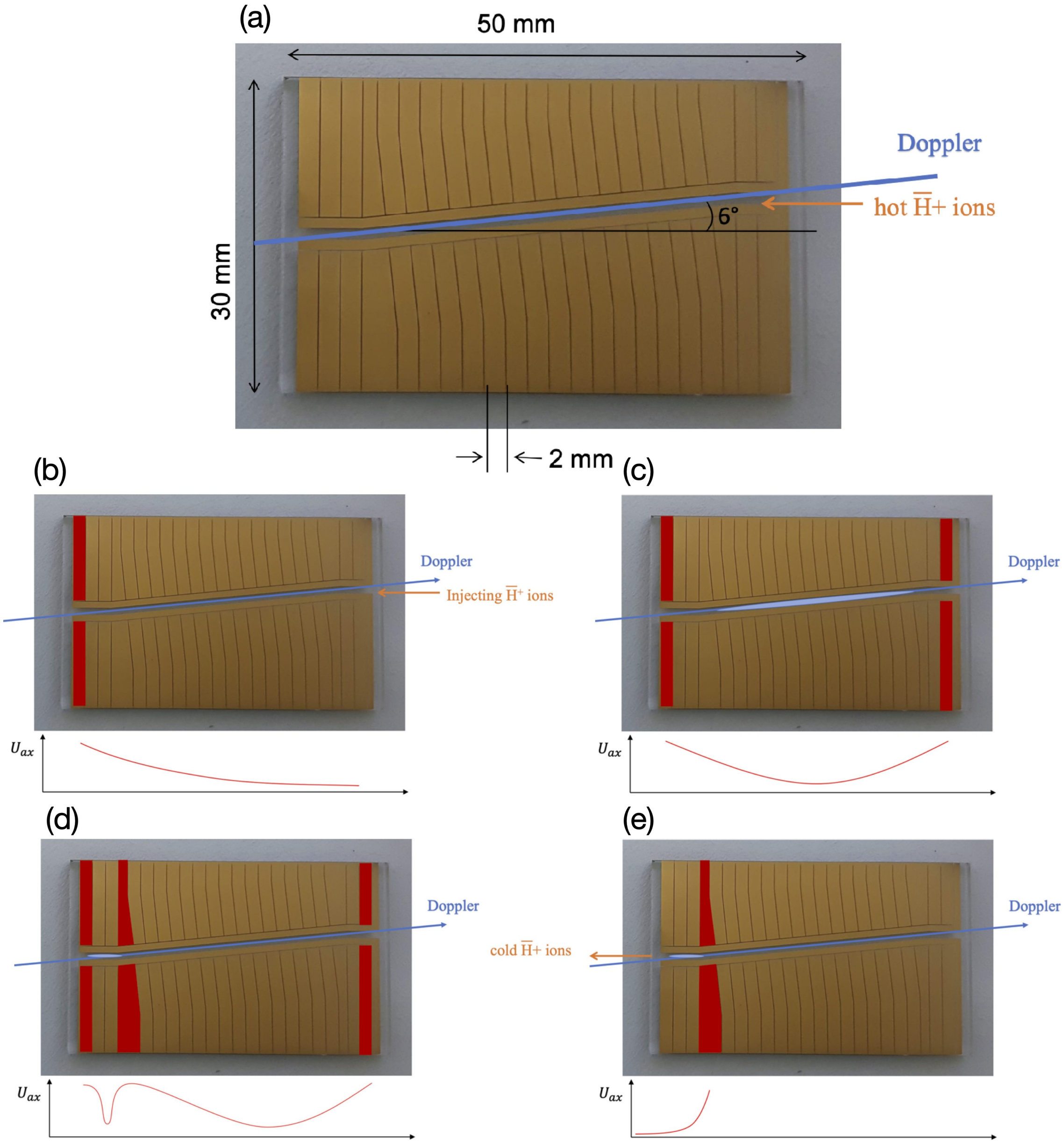

Figure 2.12 – (a) ITO trap (indium tin oxide). (b) $\overline{\mathrm{H}}^+$ ions injected at 0°, laser beam at 6°. (c) Doppler cooling light pressure does not act on $\overline{\mathrm{H}}^+$ ions thus they accumulate at the left side. (d) Double potential well to separate $\overline{\mathrm{H}}^+$ ions. (e) $\overline{\mathrm{H}}^+$ ions extraction toward precision trap. Source: A. Wilzewski, S. Wolf and F. Schmidt-Kaler.

is the creation of an antihydrogen ion $\overline{\mathrm{H}}^+$. Then ions will be stabilised in the Free Fall Chamber. Then using photo-detachment, the neutral $\overline{\mathrm{H}}$ atoms fall under the action of the Earth's gravitational field.

The two components of the antihydrogen atoms are the antiprotons and the positrons. The antiprotons are provided by the ELENA decelerator. The positrons by a 9 MeV LINAC accelerating electrons into a tungsten target equipped with a mesh moderator biased at 50 V.

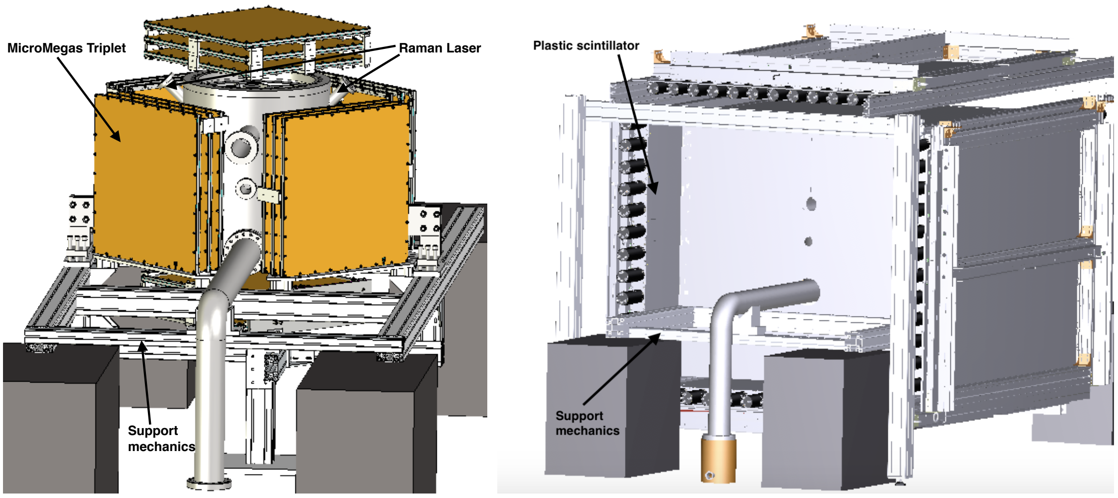

Figure 2.13 – Left: Schematic of the Free Fall Chamber. Right: The FFC surrounded by plastic scintillator.

These resulting low energy positrons are accumulated in a Buffer Gas Trap, and a High Field Trap. This step of positron trapping is presented in Chapters 4 and 5.

For the time being, antiprotons have not been trapped yet, because the antiproton trap will be delivered during the CERN Long Shut Down. This trapping will be performed right after the restarting of the ELENA decelerator in 2021. The Free Fall Chamber is under construction and should be delivered beginning 2021.

Chapter 3

Charged particle trapping and transport

> I have an equation, do you have one too?
>
> What would have said P. Dirac to
> R. Feynman in 1946

Contents

Penning-Malmberg traps, used to trap charged particles, are made of several cylindrical electrodes (to create an electrostatic field) and electromagnets (to create a magnetostatic field). They are major elements of many experiments on antimatter. Indeed, antimatter cannot be stored as easily as regular matter, as it has to be kept far away from any matter component to prevent its annihilation.

We will examine in this chapter the theory of this kind of traps (Section 3.1) and determine useful parameters for the traps of the GBAR experiment (Section 3.2). Also the presentation of a way to compute the electric field in a realistic Penning Trap and some details about the Rotating Wall technique are presented in Section 3.3. Finally, we will explain and determine in Section 3.4 the effect of the magnetic mirroring.

3.1 Penning-Malmberg trap

3.1.1 Electric field

As represented in Figure 3.1, an Penning-Malmberg trap is made of 3 cylindrical and concentric electrodes, aligned with a uniform magnetic field **B**.

To compute the electrostatic field **E**, we use the electric potential Φ as

$$\nabla.\mathbf{E} = 0, \tag{3.1.1a}$$
$$\mathbf{E} = -\nabla\Phi, \tag{3.1.1b}$$
$$\triangle\Phi = 0. \tag{3.1.1c}$$

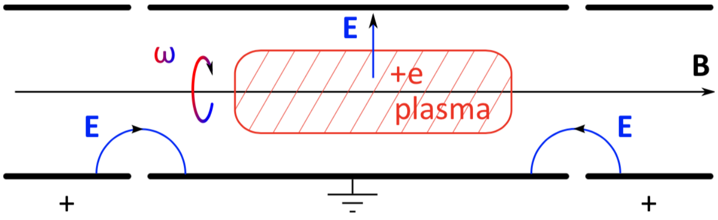

Figure 3.1 – Representation of a Penning-Malmberg trap.

Due to the symmetries of the problem, the electric and magnetic fields in the cylindrical coordinates r, θ, z can be written:

$$\mathbf{E} = \mathbf{E_r} + \mathbf{E_z} = E_r(r,z)\mathbf{e_r} + E_z(r,z)\mathbf{e_z}, \tag{3.1.2a}$$
$$\mathbf{B} = B\mathbf{e_z}, \tag{3.1.2b}$$

with $(\mathbf{e_r}, \mathbf{e_\theta}, \mathbf{e_z})$ the unit vectors. We obtain a differential equation for the potential:

$$\frac{1}{r}\frac{\partial}{\partial r}\left(r\frac{\partial\Phi}{\partial r}\right) + \frac{\partial^2\Phi}{\partial z^2} = 0 \tag{3.1.3}$$

It can be shown that a quadratic potential in r and z is a solution of the equation. If we impose the boundary conditions $\Phi(r, \pm L) - \Phi(r, 0) = \Delta V$ we obtain:

$$\Phi = \frac{\Delta V}{2L^2}\left(2z^2 - r^2\right) + c, \tag{3.1.4}$$

with c an arbitrary constant. The expression of the electric field is found by using the definition of the potential:

$$\mathbf{E} = -\frac{\Delta V}{L^2}\left(2z\mathbf{e_z} - r\mathbf{e_r}\right). \tag{3.1.5}$$

This potential can be modelled [41] by an ideal Penning trap as shown in Figure 3.2 using 3 electrodes. The two first (denoted end-cap in Ref. [41]) correspond to an equipotential of the form

$$z^2 = z_0^2 + \frac{r^2}{2}, \tag{3.1.6}$$

and the third (“ring”) corresponds to an equipotential of the form

$$z^2 = \frac{1}{2}\left(r^2 - r_0^2\right), \tag{3.1.7}$$

choosing z_0 and r_0 so as to have,

$$L^2 = \frac{1}{2}(2z_0^2 + r_0^2). \tag{3.1.8}$$

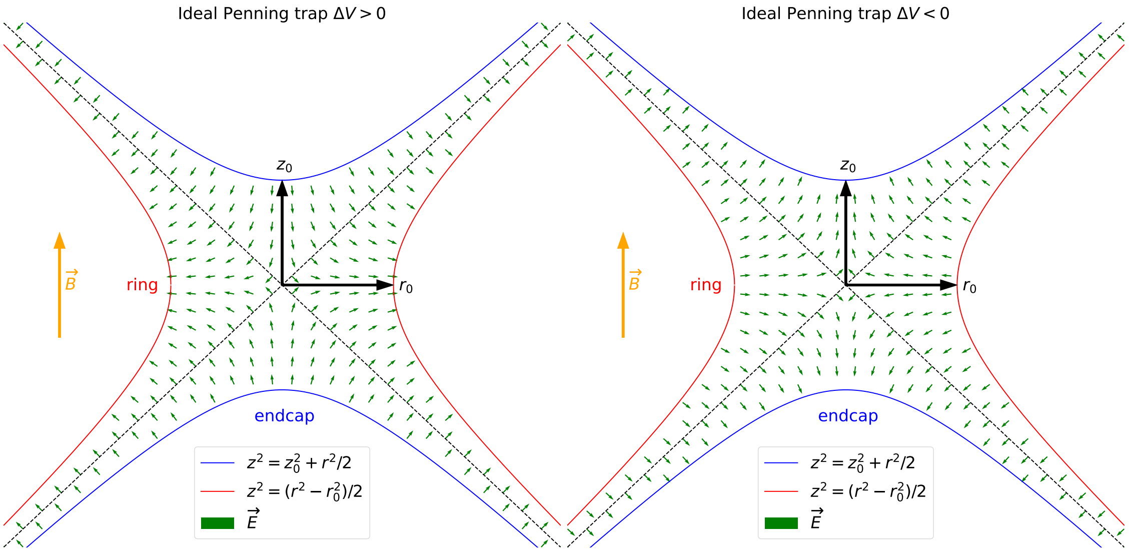

Figure 3.2 – Sectional diagrams of the electrodes of an ideal Penning trap used to produce a quadratic potential of the same form as given to the equation 3.1.4 (red and blue lines). Left: $\Delta V > 0$. Right: $\Delta V < 0$. In green, the electrostatic field.

3.1.2 Classical motion of a particle in the trap

In this section, we discuss the classical motion of a single particle in a Penning trap. The discussion is interesting because it allows to define parameters that are useful in other sections.

To generalise the problem, the variable ϵ will be used, with $\epsilon = +1$ for an electron and $\epsilon = -1$ for a positron, then the electric charge is $-\epsilon e$ to obtain the equation of motion, we use the expression of the Lorentz force:

$$m\mathbf{a} = -\epsilon e \left(\mathbf{E} + \mathbf{v} \times \mathbf{B}\right), \tag{3.1.9}$$

with m the mass of the positron, and $\mathbf{v}$ its velocity.

The result of the cross product having no component along the z axis, this previous equation is decomposed into the (x, y) plane and along the z axis to find a calculation similar to that presented for example in the article of Lowell S. Brown and Gerald Gabrielse [41]:

$$\ddot{\rho} + \frac{\epsilon e}{m} \left(\mathbf{E_r} + \dot{\rho} \times \mathbf{B}\right) = \mathbf{0}, \tag{3.1.10a}$$

$$\ddot{z} + w_z^2 z = 0, \tag{3.1.10b}$$

with $w_z^2 = -2\frac{\epsilon e}{m}\frac{\Delta V}{L^2}$ and $\rho = r\mathbf{e_r}$.

In particular, Equation 3.1.10b shows that to confine the particle along the z axis we need $w_z^2 > 0$, which means having $\Delta V > 0$ for a positron and $\Delta V < 0$ for an electron. So, along this axis, the motion of the particle is described by

$$z(t) = z_0 \cos\left(w_z t + \phi_0\right). \tag{3.1.11}$$

Equation 3.1.10a, which describes the motion in the (x, y) plane can also be written

$$\ddot{\rho} - \epsilon \omega_{\mathbf{c}} \times \dot{\rho} - \frac{1}{2}\omega_z^2 \rho = \mathbf{0}, \tag{3.1.12}$$

with $\omega_c = \frac{eB}{m} > 0, \omega_{\mathbf{c}} = \omega_c \mathbf{e_z}$.

For a positron ($e = 1.602 \times 10^{-19}\,\mathrm{C}, m = 9.109 \times 10^{-31}\,\mathrm{kg}$), with a magnetic field of 5 T, $\Delta V = 1\,\mathrm{kV}$ and with $L = 15\,\mathrm{cm}$:

$$\omega_c = 880\,\mathrm{GHz}, \tag{3.1.13a}$$

$$\omega_z = 125\,\mathrm{MHz}. \tag{3.1.13b}$$

A first way to solve this differential equation is proposed in the book *Trapped Charged Particles* [64] and is about writing the relationship 3.1.12 in Cartesian coordinates:

$$\ddot{x} + \epsilon \omega_c \dot{y} - \frac{1}{2}\omega_z^2 x = 0, \tag{3.1.14a}$$

$$\ddot{y} - \epsilon \omega_c \dot{x} - \frac{1}{2}\omega_z^2 y = 0. \tag{3.1.14b}$$

Defining $u = x + iy$, we get the differential equation:

$$\ddot{u} - i\epsilon \omega_c \dot{u} - \frac{1}{2}\omega_z^2 u = 0, \tag{3.1.15}$$

whose characteristic equation $w^2 - i\epsilon\omega_c w - \frac{1}{2}\omega_z^2 = 0$ has $w = i\epsilon\left(\frac{\omega_c}{2} \pm \omega_1\right)$ as solutions with:

$$\omega_1 \equiv \sqrt{\frac{\omega_c^2}{4} - \frac{\omega_z^2}{2}}. \tag{3.1.16}$$

Both frequencies ω_c' and ω_m, named respectively reduced cyclotron frequency and magnetron frequencies are defined as:

$$\omega_c' \equiv \frac{\omega_c}{2} + \omega_1 = \frac{\omega_c}{2} + \sqrt{\frac{\omega_c^2}{4} - \frac{\omega_z^2}{2}}, \tag{3.1.17a}$$

$$\omega_m \equiv \frac{\omega_c}{2} - \omega_1 = \frac{\omega_c}{2} - \sqrt{\frac{\omega_c^2}{4} - \frac{\omega_z^2}{2}}, \tag{3.1.17b}$$

to get the general solution of Equation 3.1.15:

$$u = \alpha \exp\left(i\epsilon\omega_c' t\right) + \beta \exp\left(i\epsilon\omega_m t\right), \tag{3.1.18}$$

with $\alpha, \beta \in \mathbb{C}$. This leads to the general form of the motion:

$$x = \Re(u) = a\cos\left(\epsilon\omega_c' t + \phi_1\right) + b\cos\left(\epsilon\omega_m t + \phi_2\right), \tag{3.1.19a}$$

$$y = \Im(u) = a\sin\left(\epsilon\omega_c' t + \phi_1\right) + b\sin\left(\epsilon\omega_m t + \phi_2\right), \tag{3.1.19b}$$

with $a, b, \phi_1, \phi_2 \in \mathbb{R}$.

So in the (xy) plane, the positron has a trajectory composed of two circular trajectories in the clockwise direction (in the counter clockwise for an electron), with frequencies ω_m and ω_c' (illustration in Figure 3.3).

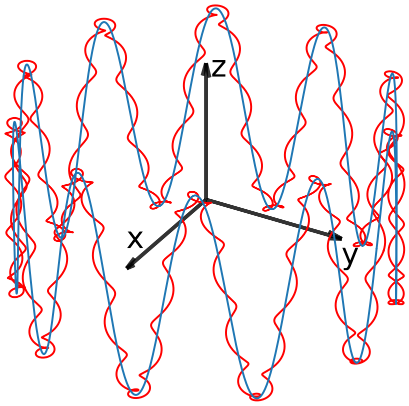

Figure 3.3 – Illustration of the motion of a charged particle in a Penning-Malmberg trap. In the (x, y) plane the motion composed of two circular motions. Along the z axis, there is an oscillation.

It is interesting to notice that the previous definitions impose to fulfil the condition: $\frac{\omega_c^2}{4} - \frac{\omega_z^2}{2} > 0$, otherwise we would bring up terms in $\exp\left(\pm\omega_1 t\right)$, then the confinement would be impossible. It is also important to notice that if ΔV is too large, then it is not possible to trap. The values in Equation 3.1.13 show that in a general use, $\omega_c \gg \omega_z$. In that case, $\frac{\omega_c^2}{4} - \frac{\omega_z^2}{2} > 0$ is fulfilled and the reduced cyclotron frequency becomes $\omega_c' = \omega_c - \frac{\omega_z^2}{2\omega_c}$ and the magnetron frequency becomes $\omega_m = \frac{\omega_z^2}{2\omega_c}$.

As a complement, one can notice that the article of Lowell S. Brown and Gerald Gabrielse [41] presents another method to solve the case of the electron, this method is interesting for a quantum treatment of the particle. To adapt this calculation to the case of a particle with a charge $-\epsilon e$ we have to define the vectors $\mathbf{V}^{(+)}$ and $\mathbf{V}^{(-)}$

as well as the frequency ω_+ (ω_c' in the previous calculation) and ω_- (ω_m) by these relationships:

$$\mathbf{V}^{(\pm)} = \epsilon\dot{\rho} - \omega_{\mp}\mathbf{e_z} \times \rho \tag{3.1.20a}$$

$$\omega_{\pm} = \frac{1}{2}\left(\omega_c \pm \sqrt{\omega_c^2 - 2\omega_z^2}\right) \tag{3.1.20b}$$

These vectors also verify the following differential equation:

$$\dot{\mathbf{V}}^{(\pm)} = \epsilon\omega_{\pm}\mathbf{e_z} \times \mathbf{V}^{(\pm)} \tag{3.1.21}$$

This equation represents two vectors rotating at frequencies $\omega_{\pm}$ in the counter clockwise for an electron, and clockwise for a positron. Then we obtain the ρ vector using the definition 3.1.20a:-

$$\rho = -\frac{\mathbf{e_z} \times \left(\mathbf{V}^{(+)} - \mathbf{V}^{(-)}\right)}{\omega_+ - \omega_-}, \tag{3.1.22}$$

which gives us a vector ρ in the (xy) plane, composed of two rotating vectors at frequencies $\omega_+ \equiv \omega_c'$ and $\omega_- \equiv \omega_m$, as in the previous calculation.

3.2 Non neutral plasma

3.2.1 Conditions to fulfill

A plasma is a collection of charged particles moving under the influence of an external electric field. In order to know if the studied system is a plasma, we have to focus on a characteristic scale called the Debye length λ_D beyond which the external electric field is screened:

$$\lambda_D = \sqrt{\frac{\epsilon_0 k_B T}{n_0 e^2}}, \tag{3.2.1}$$

where ϵ_0 is the vacuum permittivity, k_B the Boltzmann constant, n_0 the particle density and e the charge of the particles in the plasma. If we consider L, the characteristic length of our trap, we need to verify this first condition:

$$L \gg \lambda_D. \tag{3.2.2}$$

To understand this, we can use the example given in the book *Trapped Charged Particles* [65]. It is about a neutral plasma made of ions (charge $+e$) and electrons (charge $-e$) between two ideal electrodes, one with a potential $V > 0$ and the other connected to the ground, and separated by a distance L. In the absence of ions and electrons, the electric potential between the two electrodes is $\phi(x) = V\left(1 - \frac{x}{L}\right)$. The electrons are attracted by the electrodes at the V potential and the ions by the other, creating a Boltzmann distribution of charges (n_e for the electrons, n_i for the ions) if we suppose a thermal equilibrium at the temperature T:

$$n_e(x) = n_0 \exp\left(\frac{e\phi(x)}{k_B T}\right), \tag{3.2.3a}$$

$$n_i(x) = n_0 \exp\left(\frac{-e\phi(x)}{k_B T}\right). \tag{3.2.3b}$$

The Poisson equation gives us a differential equation for the electric potential thereby modified by the charges distribution:

$$\frac{\partial^2\phi}{\partial x^2} = \frac{e}{\epsilon_0}\left(n_e(x) - n_i(x)\right). \tag{3.2.4}$$

If we assume $|e\phi/(k_BT)| \ll 1$ et $L \gg \lambda_D$, we obtain:

$$\phi(x) = V\exp\left(-\sqrt{2}x/\lambda_D\right), \tag{3.2.5}$$

and we find that the field becomes zero for $x \gg \lambda_D$, in other words, the electric field is screened by the plasma beyond a characteristic length λ_D as expected.

Numerically, if we want to trap with a density $n_0 \sim 10^{17}\,\mathrm{m}^{-3}$ and a temperature $k_BT \sim 1\,\mathrm{eV}$ [52], we can estimate λ_D as:

$$\begin{aligned}\lambda_D &= 7.4\times10^3\sqrt{\frac{k_BT[\mathrm{eV}]}{n_0[\mathrm{m}^{-3}]}} && (3.2.6a)\\ &= 7.4\times10^3\sqrt{\frac{1}{10^{17}}} && (3.2.6b)\\ &= 20\,\mu\mathrm{m}. && (3.2.6c)\end{aligned}$$

Also, if we want to consider the plasma as a continuous fluid, the density must evolve slowly within the average inter-particle space $a \equiv n_0^{-1/3}$. Since the density evolves with a characteristic scale λ_D, we must observe $\lambda_D \gg n_0^{-1/3}$, or otherwise written:

$$n_0\lambda_D^3 = \left(\frac{k_BT}{e^2/(\epsilon_0 a)}\right)^{\frac{3}{2}} \gg 1. \tag{3.2.7}$$

By observing that the numerator can be related to the kinetic energy and the denominator to the potential energy of the mean interaction between two particles of the fluid, one can interpret the previous relation differently: the interactions between particles of the fluid are negligible compared to thermal agitation. In an equivalent way, one generally finds in the literature the coupling parameter Γ defined as:

$$\Gamma = \frac{e^2}{4\pi\epsilon_0 a k_BT} \propto \frac{a^2}{\lambda_D^2}. \tag{3.2.8}$$

To summarise, for a strongly correlated plasma (i.e., $\Gamma \gg 1$), $\lambda_D \ll a$ which means that the collection of charges cannot be considered as a continuous fluid, then all the interactions between particles have to be taken into account . If our plasma is weakly correlated (i.e., $\Gamma \ll 1$), fluid mechanics laws can be used to study the plasma and the Boltzmann distribution can describe the thermodynamic equilibrium as done previously.

As an example, let's see the coupling parameter in the required conditions for GBAR experiment. The density is estimated by $n_0 \sim 10^{17}\,\mathrm{m}^{-3}$ (then $a \sim 2\times10^{-6}\,\mathrm{m}$) and a temperature by $k_BT \sim 1\,\mathrm{eV}$. Then the coupling parameter is:

$$\begin{aligned}\Gamma &= \frac{(1.6\times10^{-19}[\mathrm{C}])^2}{4\pi\times8.85\times10^{-12}[\mathrm{C}^2\,\mathrm{s}^2\,\mathrm{kg}^{-1}\,\mathrm{m}^{-3}]\times2\times10^{-6}[\mathrm{m}]\times1.6\times10^{-19}[\mathrm{J}]} && (3.2.9a)\\ &= 7\times10^{-4} \ll 1. && (3.2.9b)\end{aligned}$$

In that case, the plasma is weakly correlated.

3.2.2 Plasma in the Penning-Malmberg trap

Let's take a look at the case of a plasma only composed of positrons [65].

As explained previously we can use the fluid mechanics to study the behaviour of our plasma if the relations 3.2.2 and 3.2.7 are respected. To establish the Euler equation presented in Equation 3.2.10, we work in the cylindrical basis $(\mathbf{e_r}, \mathbf{e_\theta}, \mathbf{e_z})$ and we consider three forces:

- an electrostatic force, $-en\nabla\phi$, with e the charge of the particles in the plasma, n the density and ϕ the total electric potential;
- magneto-static force, $qn\mathbf{v}\times\mathbf{B}$, with $\mathbf{B} = B\mathbf{e_z}$, the magnetic field and $\mathbf{v}$ the velocity of the fluid;
- the pressure force, $-\nabla p$, with p the pressure in the fluid.

This gives us the following equation:

$$mn\left(\frac{\partial \mathbf{v}}{\partial t} + (\mathbf{v}.\nabla)\,\mathbf{v}\right) = en\left(-\nabla\phi + \mathbf{v}\times\mathbf{B}\right) - \nabla p, \tag{3.2.10}$$

with m the mass of a particle.

Considering we are at the thermal equilibrium, we can affirm that the fluid is in rotation around the z axis with a frequency of $-\omega_{\text{rot}}$ (i.e., $\nabla\times\mathbf{v} = -2\omega_{\text{rot}}\mathbf{e_z}$). The $-$ sign comes from the fact that the positrons turn clockwise as shown by Equation 3.1.19 and keeping in mind that this rotation is a mean behaviour of all the single particles. The speed therefore is written in cylindrical coordinates:

$$\mathbf{v} = -\omega_{\text{rot}} r\mathbf{e}_\theta. \tag{3.2.11}$$

Let's begin by the component along the z axis of relation 3.2.10. Because we consider the plasma as a perfect gas, we can use the relation $p = k_B T n$, which gives:

$$-en\frac{\partial\phi}{\partial z} - k_B T\frac{\partial n}{\partial z} = 0. \tag{3.2.12}$$

This relation 3.2.12 can be partially integrated, leaving an r dependent constant of integration, N.

$$n(r,z) = N(r)\exp\left(-\frac{e\phi(r,z)}{k_B T}\right). \tag{3.2.13}$$

The component along $\mathbf{e}_\theta$ of relation 3.2.10 being zero, let's have a look at the relation along $\mathbf{e_r}$:

$$-mn\omega_{\text{rot}}^2 r = -en\left(\frac{\partial\phi}{\partial r} + B\omega_{\text{rot}} r\right) - k_B T\frac{\partial n}{\partial r}. \tag{3.2.14}$$

We can also inject Equation 3.2.13 in 3.2.14, which gives a new differential equation for N:

$$k_B T\frac{\partial N}{\partial r} = -m\omega_{\text{rot}}\left(\omega_c - \omega_{\text{rot}}\right) rN, \tag{3.2.15}$$

with $\omega_c \equiv \frac{eB}{m}$. This equation can be integrated to get $N(r)$ with a multiplicative constant:

$$N(r) = C\exp\left(-\frac{1}{k_B T}\omega_{\text{rot}}(\omega_c - \omega_{\text{rot}})\frac{r^2}{2}\right). \tag{3.2.16}$$

Thus we obtain the expression of $n(r, z)$:

$$\omega_{\text{rot}} n(r, z) = C \exp\left(-e\frac{\phi(r, z) + \phi_{\text{eff}}(r)}{k_B T}\right), \tag{3.2.17}$$

by defining an effective potential ϕ_{eff} as :

$$e\phi_{\text{eff}}(r) \equiv \frac{1}{2} m\omega_{\text{rot}} \left(\omega_c - \omega_{\text{rot}}\right) r^2. \tag{3.2.18}$$

This effective potential allows the radial confinement of the plasma. Equation 3.2.17 shows that the effective potential has to fulfil $\phi(r, z) + \phi_{\text{eff}}(r) > 0, \forall (r, z)$ to make the confinement possible. However, because for some z position we may have $\phi(r, z) = 0$, the condition to fulfil is $\phi_{\text{eff}} > 0, \forall r$. This leads to the following relations for the frequencies:

$$0 < \frac{\omega_{\text{rot}}}{\omega_c} < 1. \tag{3.2.19}$$

Another way to understand the problem would be to consider that the plasma is not confined by the magnetic field but by virtual negative charges of density n_0 whose electric potential would be ϕ_{eff}. Thereby, by using the Poisson equation ($\triangle\phi_{\text{eff}} = en_0/\epsilon_0$), we obtain the density of charge:

$$n_0 = \frac{2m\epsilon_0}{e^2}\omega_{\text{rot}}(\omega_c - \omega_{\text{rot}}). \tag{3.2.20}$$

In the article of Malmberg and O'Neil [66], it is explained that the density of the real particles matches with the uniform density of virtual particles up to a certain radius (cylindrical symmetry). If we assume that the Debye length (Equation 3.2.1) is smaller than the radius of the cylinder, the density of positrons (electrons in the article) falls sharply beyond this radius. Indeed, if we consider that the virtual charges neutralise the charge of our positrons, there is a radius where the supply of positrons is exhausted, because there is a finite amount of them.

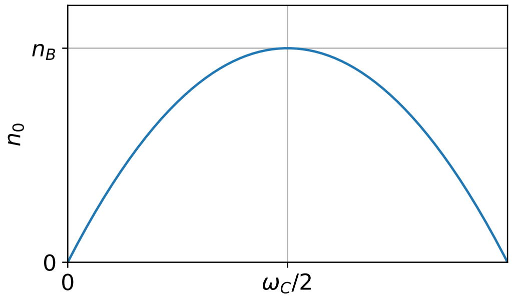

Figure 3.4 – Density of positrons as a function of the rotation frequency of the plasma. This density is maximal for $\omega_{\text{rot}} = \omega_c/2$, the so-called Brillouin limit.

Now we have a relation between the density of particles in the trap, the rotation frequency and the magnetic field (represented at Figure 3.4):

$$n = \frac{2m\epsilon_0}{e^2}\omega_{\text{rot}}(\omega_c - \omega_{\text{rot}}). \tag{3.2.21}$$

This relation also indicates that a maximal density of positrons called the Brillouin limit appears for $\omega_{\text{rot}} = \omega_c/2$ ($\omega_c = eB/m$):

$$n_B = \frac{m\epsilon_0\omega_c^2}{2e^2} = \frac{\epsilon_0 B^2}{2m} = \frac{B^2/(2\mu_0)}{mc^2}, \tag{3.2.22}$$

with μ_0 vacuum permeability and c the speed of light.

3.3 Realistic traps

3.3.1 Main electric field

As shown in Section 3.1.1, in the case of the ideal Penning-Malmberg trap, the potential is quadratic. However, in practice the potential cannot be quadratic because it cannot be infinite. Besides, the traps are made of more than 3 electrodes to be able to manipulate the particles. Then in this section, we describe how to compute analytically the electric potential for a set of cylindrical electrodes. This section is mostly inspired by the work presented in the thesis of Christopher Aled Isaac [67].

First of all, only one electrode is taken into account, and the effect of the other electrodes will be added using the superposition principle. Therefore, let's consider a cylindrical electrode of radius R and of half-length z_0 with a potential $V = 1\,\text{V}$. Let's also consider that there are two infinite cylindrical electrodes of radius R on both sides of the considered electrode, with a potential $V = 0$, then the potential at $r = R$ is $\phi(R, z) = H(z + z_0) - H(z - z_0)$, with H the Heaviside function (see Figure 3.5). L_0 is an integration limit with $L_0 \gg z_0$ and we impose $\phi(r, L_0) = 0, \forall r$.

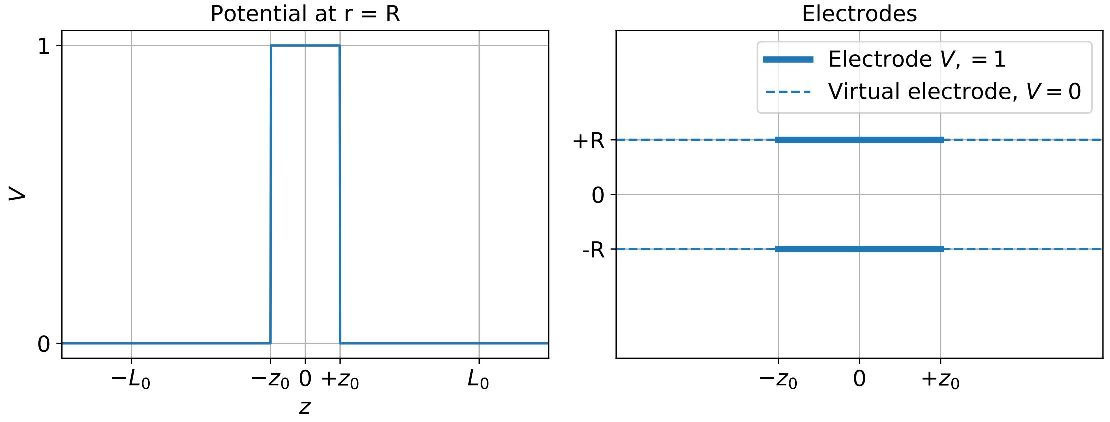

Figure 3.5 – Left: the boundary conditions for one electrode at $r = R$. Right: representation of the electrode on the (r, z) plane: the real electrode is between $-z_0$ and $+z_0$, the rest is a virtual electrode with the potential 0 on it.

To solve the Poisson equation (Equation 3.1.3) it is first assumed that the solution has the form:

$$\phi(r, z) = f(r)g(z). \tag{3.3.1}$$

The Poisson equation becomes

$$\frac{1}{f(r)}\left(\frac{1}{r}\frac{\mathrm{d}f}{\mathrm{d}r}+\frac{\mathrm{d}^2 f}{\mathrm{d}r^2}\right)+\frac{1}{g(z)}\frac{\mathrm{d}^2 g}{\mathrm{d}z^2}=0, \tag{3.3.2}$$

where the two terms depend on two separate variables. This implies, the first term is equal to a constant $\pm k^2$ and the second to the opposite:

$$\frac{1}{f(r)}\left(\frac{1}{r}\frac{\mathrm{d}f}{\mathrm{d}r}+\frac{\mathrm{d}^2 f}{\mathrm{d}r^2}\right)=-\frac{1}{g(z)}\frac{\mathrm{d}^2 g}{\mathrm{d}z^2}=\pm k^2 \tag{3.3.3}$$

The physical equation has to be the one with $+k^2$ otherwise g would be a hyperbolic function, which is impossible in our case because we cannot have an infinite potential. Then we obtain the two following equations

$$r^2\frac{\mathrm{d}^2 f}{\mathrm{d}r^2}+r\frac{\mathrm{d}f}{\mathrm{d}r}-(kr)^2 f(r)=0, \tag{3.3.4a}$$

$$\frac{\mathrm{d}^2 g}{\mathrm{d}z^2}+k^2 g(z)=0. \tag{3.3.4b}$$

The solution of the first equation is a modified Bessel function, then $f(r)=I_0(kr)=\sum_{m=0}^{\infty}=\frac{1}{m!\Gamma(m+1)}\left(\frac{kr}{2}\right)^{2m}$. The second equation can be integrated as $g(z)=A_k\cos(kz)+B_k\sin(kz)$. Because the function has to be even, $B_k=0$. Moreover, the boundary conditions give $g(L_0)=0=A_k\cos(kL_0)$. Then, the general solution will be

$$\phi(r,z)=\sum_{m\geq 0}A_m I_0(k_m r)\cos(k_m z), \tag{3.3.5}$$

with $k_m=\left(m+\frac{1}{2}\right)\frac{\pi}{L_0}$.

Now, to determine A_m we use the fact that we know $\phi(R,z)$:

$$\begin{aligned}
\int_{-L_0}^{L_0}\mathrm{d}z\cos(k_{m'}z)\phi(R,z) &= \sum_{m\geq 0}A_m I_0(k_m R)\int_{-L_0}^{L_0}\mathrm{d}z\cos(k_{m'}z)\cos(k_m z),\\
\int_{-z_0}^{z_0}\mathrm{d}z\cos(k_{m'}z) &= \sum_{m\geq 0}A_m I_0(k_m R)L_0\delta_{m,m'},\\
A_m &= \frac{2\sin(k_m z_0)}{L_0 k_m I_0(k_m R)}.
\end{aligned}$$

Then, the potential can be written:

$$\phi(r,z,z_0)=\sum_{m\geq 0}\frac{2}{L_0 k_m}\sin(k_m z_0)\cos(k_m z)\frac{I_0(k_m r)}{I_0(k_m R)} \tag{3.3.6}$$

To compute numerically the potential, we have to determine a limit for the summation. For the computations presented in this document, an algorithm similar to Algorithm 1 has been written.

Algorithm 1 Computation of $\phi(r, z, z_0)$

```
Require: $z_0, R, r, z$
  $\phi = 0$
  $i = 0$
  $\epsilon = 10^{-10}$
  $e = 1$
  $L_0 = 20z_0$
  while $|e| \geq \epsilon$ do
    $k = (i + \frac{1}{2})\frac{\pi}{L_0}$
    $e = \frac{2}{L_0 k} \sin(kz_0) \cos(kz) \frac{I_0(kr)}{I_0(kR)}$
    $\phi = \phi + e$
    $i = i + 1$
  end while
```

Thanks to the superposition principle, it is now straightforward to obtain the electric potential created by N cylindrical and concentric electrodes of same radii. If the electrode n of length $2z_{0,n}$ is placed at z_n under a potential V_n, one writes:

$$\phi(r, z) = \sum_{n=1}^{N} V_n \phi(r, z - z_n, z_{0,n}). \tag{3.3.7}$$

An illustration of the computation of the potential at $r = 0$ using Algorithm 1 is presented in Figure 3.6. As one can imagine, the smaller the radius of the electrode is compared to its length, the closer to the potential of the electrode the potential at r=0 is. It is also interesting to see that one can fit the potential with a quadratic function when $z \ll z_0$.

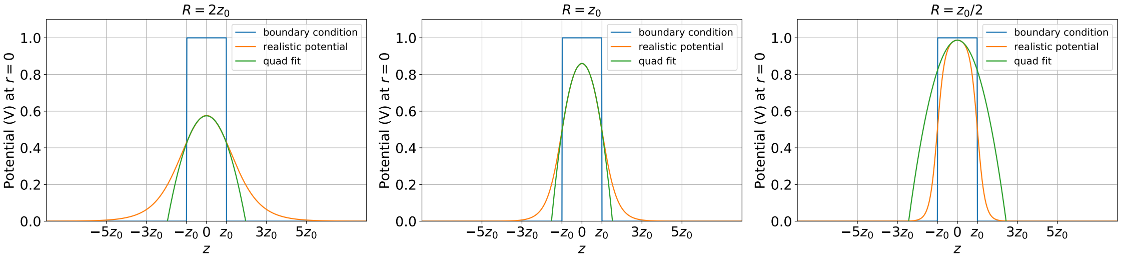

Figure 3.6 – Illustration of the computation of the electric potential for a trap made of 3 electrodes of 1 cm length.

However, there are two restrictions for this computation. The first one is that we have to ensure that $L_0 \gg z_{0,n}$ for all the electrodes, and the second one is that, as said before, all the electrodes must have the same radius, because the boundary conditions would be incompatible for the different electrodes. In the case of different radii, it would be better to use a simulation by finite element of the potential.

3.3.2 The rotating wall technique

The principle of the rotating wall technique [68], is to add an angular momentum to the plasma to compress it and to compensate the defects of the trap. Indeed, a spatially uniform positron plasma has a canonical angular momentum $P_\theta = Nm(\omega_c/2 - \omega_{\text{rot}}) < r^2 >$ [69], where N is the total number of positrons of mass m, ω_{rot} is the rotation frequency, ω_c the cyclotron frequency as introduced in Section 3.1.2 and $< r^2 >$ is the mean square radius of the plasma fluid. If one can apply the drift approximation (i.e. $\omega_{\text{rot}} \ll \omega_c$), we clearly have $P_\theta > 0$, and this is why adding a negative torque decreases the angular momentum, i.e., decreases $< r^2 >$ and compresses the plasma.

To add a negative torque, we use a split electrode and apply an oscillating signal of same frequency on each part of the cylindrical electrode, with a constant phase shift between two neighbour parts. In our case the cylindrical electrode is split in 4 and the phase is 90°. This section is a re-explanation of what can be found in Isaac's thesis [67].

To solve the Poisson equation in that case, we consider the potential on the electrode is $\Phi(\theta)$, as shown in Figure 3.7. Similarly to what has been done in Section 3.3.1, $\phi(r = R, \theta, z) = \Phi(\theta)$ only on the electrode, i.e. for $z \in [-z_0, z_0]$ and the potential is null outside this limit. Also, integration limit $L_0 \gg z_0$ such as $\phi(r, \theta, z = L_0) = 0$ needs to be set.

$$\Phi(\theta) = \begin{cases} -V_a & \frac{3\pi}{4} \leq \theta < -\frac{3\pi}{4} \\ -V_b & -\frac{3\pi}{4} \leq \theta < -\frac{\pi}{4} \\ V_a & -\frac{\pi}{4} \leq \theta < \frac{\pi}{4} \\ V_b & \frac{\pi}{4} \leq \theta < \frac{3\pi}{4} \end{cases} \tag{3.3.8}$$

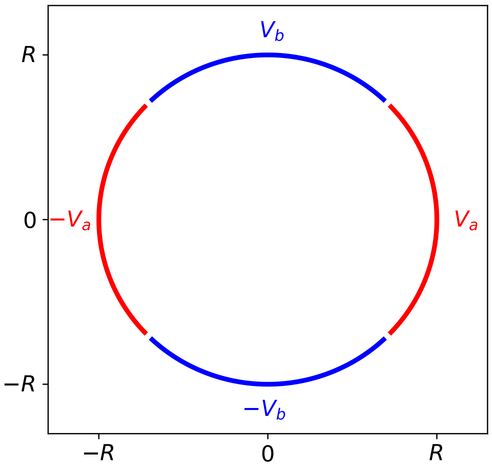

Figure 3.7 – Boundary conditions for an electrode split in four.

As in Section 3.3.1, one can assume that the potential is a product of three independent functions:

$$\phi(r,\theta,z) = f(r)g(z)h(\theta), \tag{3.3.9}$$

therefore, the Poisson equation leads to

$$\frac{\triangle\phi}{\phi} = \frac{1}{fr}\frac{\mathrm{d}}{\mathrm{d}r}\left(r\frac{\mathrm{d}f}{\mathrm{d}r}\right) + \frac{1}{hr^2}\frac{\mathrm{d}^2h}{\mathrm{d}\theta^2} + \frac{1}{g}\frac{\mathrm{d}^2g}{\mathrm{d}z^2} = 0. \tag{3.3.10}$$

The same argument as the one used in the previous section can be used again to find the general expression for g:

$$g_m(z) = A\cos(k_m z), k_m = \left(m + \frac{1}{2}\right)\frac{\pi}{L_0}, m \in \mathbb{N}. \tag{3.3.11}$$

For the angular part h, again, the fact that the variables are separated leads to:

$$\frac{1}{h}\frac{\mathrm{d}^2h}{\mathrm{d}\theta^2} = \pm n^2. \tag{3.3.12}$$

To keep the potential finite at large distances, the only physical equation is the one with $-n^2$, which gives us the general form for h:

$$h_n(\theta) = a\cos(n\theta) + b\sin(n\theta). \tag{3.3.13}$$

In order to find a condition on n, we use the fact that in cylindrical coordinates any function of θ must be 2π-periodic, i.e. $h(\theta + 2\pi) = h(\theta)$, which leads to the coupled equations:

$$\begin{cases} a\left(\cos(2n\pi) - 1\right) + b\sin 2n\pi & = 0, \\ a\sin 2n\pi + b\left(1 - \cos(2n\pi)\right) & = 0. \end{cases}$$

A non trivial solution $(a \neq 0, b \neq 0)$ requires the determinant of the system to be null, which leads to $\cos(2n\pi) = 1$, and then the condition on n is: $n \in \mathbb{N}$.

Inserting the previous result in Equation 3.3.10, the previous results leading to

$$\frac{r}{f}\frac{\mathrm{d}}{\mathrm{d}r}\left(r\frac{\mathrm{d}f}{\mathrm{d}r}\right) - \left(k_m^2 r^2 + n^2\right) = 0, \tag{3.3.14}$$

the solution for the radial part is then the modified Bessel functions of the first kind of order n:

$$f_{n,m}(r) = I_n(k_m r) \tag{3.3.15}$$

All of this gives the general solution of the equation which is:

$$\phi(r,\theta,z) = \sum_{n,m\geq 0} I_n(k_m r)A_{mn}\cos(k_m z)\left(a_{mn}\cos(n\theta) + b_{nm}\sin(n\theta)\right). \tag{3.3.16}$$

Now to determine the coefficients, the boundary condition $\phi(R,\theta,z) = \Phi(\theta), z \in [-z_0, z_0]$ is used as follows:

$$\int_{-L_0}^{L_0} \phi(R,\theta,z)\cos(k_l z)\mathrm{d}z =$$

$$\sum_{n,m\geq 0} I_n(k_m R)A_{mn}\left(a_{mn}\cos(n\theta) + b_{nm}\sin(n\theta)\right)\int_{-L_0}^{L_0}\cos(k_m z)\cos(k_l z)\mathrm{d}z \tag{3.3.17}$$

$$\Phi(\theta)\int_{-z_0}^{z_0}\cos(k_l z)\mathrm{d}z = \sum_{n,m\geq 0} I_n(k_m R)A_{mn}\left(a_{mn}\cos(n\theta)+b_{nm}\sin(n\theta)\right)L_0\delta_{m,l},$$

and then the following expression for Φ is obtained:

$$\Phi(\theta) = \frac{k_m}{2\sin(k_m z_0)}\sum_{n\geq 0} A_{mn}I_n(k_m R)L_0\left(a_{mn}\cos(n\theta)+b_{nm}\sin(n\theta)\right). \tag{3.3.18}$$

By developing Φ as Fourier series:

$$\Phi(\theta) = \sum_{n=1}^{\infty}\frac{4}{n\pi}\left(V_a\sin\left(\frac{n\pi}{2}\right)\cos\left(\frac{n\pi}{4}\right)\cos\left(n\theta\right)+V_b\sin\left(\frac{n\pi}{2}\right)\sin\left(\frac{n\pi}{4}\right)\sin\left(n\theta\right)\right) \tag{3.3.19}$$

one can identify a_{mn} and b_{mn}, which become now a_n and b_n.

Finally, the potential can be written as:

$$\phi(r,\theta,z) = \sum_{n,m\geq 0} I_n(k_m r)A_{mn}\cos(k_m z)\left(a_n\cos(n\theta)+b_n\sin(n\theta)\right) \tag{3.3.20}$$

with

$$a_n = \frac{4V_a}{n\pi}\left(\sin\left(\frac{n\pi}{2}\right)\cos\left(\frac{n\pi}{4}\right)\right) \tag{3.3.21a}$$

$$b_n = \frac{4V_b}{n\pi}\left(\sin\left(\frac{n\pi}{2}\right)\sin\left(\frac{n\pi}{4}\right)\right) \tag{3.3.21b}$$

$$A_{mn} = 0 \qquad n = 0 \tag{3.3.21c}$$

$$A_{mn} = \frac{2\sin(k_m z_0)}{k_m L_0 I_n(k_m R)} \qquad n \neq 0 \tag{3.3.21d}$$

As said before, we will apply an oscillating potential on each part on the electrode with a phase of 90° between adjacent parts. Then, V_a and V_b are defined as:

$$V_a = V_{\mathrm{RW}}\cos\left(\omega_r t\right) \tag{3.3.22a}$$

$$V_b = V_{\mathrm{RW}}\cos\left(\omega_r t+\frac{\pi}{2}\right) = -V_{\mathrm{RW}}\sin\left(\omega_r t\right) \tag{3.3.22b}$$

An illustration of the potential is presented in Figure 3.8 where it is possible to see that the equipotentials rotate with the same frequency as the oscillating potential.

However, it is not necessary to use such a complicated expression to predict what is happening in the trap. Indeed, if it is assumed that the plasma radius is much smaller than the radius of the electrode, then a limited expansion can be done. Let's start with the limited expansion of I_n:

$$I_n(x) = \sum_{l\geq 0}\frac{1}{l!\Gamma(n+l+1)}\left(\frac{x}{2}\right)^{(2l+n)}. \tag{3.3.23}$$

In that case, $x = k_m r$, with $x \ll 1$, because $r \ll R, L_0$, and then, the expansion at the first order in x is $I_n(x) = I_n(0) + I_n'(0)x + o(x)$. For this computation, the derivative is then required:

$$I_n'(x) = \frac{1}{2}\sum_{l\geq 0}\frac{2l+n}{l!\Gamma(n+l+1)}\left(\frac{x}{2}\right)^{(2l+n-1)}. \tag{3.3.24}$$

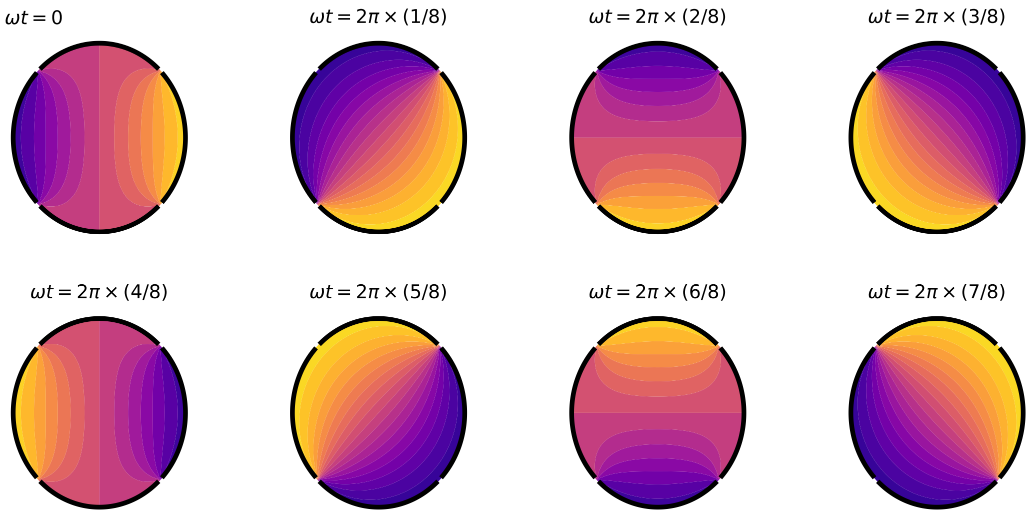

Figure 3.8 – Representation of the potential produced by a rotating wall with a frequency ω_r according to Equation 3.3.20 and Equation 3.3.22. The yellow areas represent a potential of $+V_r$ and the blue of $-V_r$.

It is clear that at $x = 0$, all the terms are null except when $2l + n - 1 = 0$, and knowing that $n \geq 1$, the only possibility is when $n = 1$ and $l = 0$. Then at first order, only n=1 gives a non null contribution to the total expansion and with $I_1'(0) \approx \frac{1}{2\Gamma(2)} = \frac{1}{2}$, we get $I_1(k_m r) \approx \frac{1}{2} k_m r$. Finally, the recombination of the terms leads to $a_1 \cos(\theta) + b_1 \sin(\theta) = \frac{2\sqrt{2}}{\pi} V_{\mathrm{RW}} \cos(\omega_r t + \theta)$.

In the end, with this approximation, the potential is the one of a rotating dipole:

$$\phi(r \ll R, \theta, z) \approx V_{\mathrm{RW}} r \cos(\omega_r t + \theta) \left(\frac{2\sqrt{2}}{\pi L_0} \sum_{m \geq 0} \frac{\cos(k_m z) \sin(k_m z_0)}{I_1(k_m R)} \right) \tag{3.3.25}$$

Isaac also showed in his thesis [67] that by using a quadratic potential and a oscillating dipole

$$\phi(z, r, \theta) = \frac{V_0}{2d^2} \left(z^2 - \frac{r^2}{2} \right) + \frac{m}{q} azr \cos(\theta + \omega_r t) \tag{3.3.26}$$

in the motion equations of a particle (which is correct according to what has been shown before), and adding a viscosity drag force $\mathbf{F} = -\kappa \mathbf{v}$, a compression rate Γ is obtained and defined as

$$\Gamma = \frac{\kappa}{4} \left(1 - \left| \frac{\tilde{\omega}}{\sqrt{1 + \tilde{\omega}^2}} \right| \right), \tag{3.3.27}$$

where

$$\tilde{\omega} = \frac{\omega_r + (\omega_z + \omega_-)}{\delta}, \tag{3.3.28a}$$

$$\delta = \frac{a}{\sqrt{\omega_c \omega_z}}, \tag{3.3.28b}$$

$\omega_c, \omega_z, \omega_-$ defined in Section 3.1.2. In that case, the maximal compression is for $\tilde{\omega} = 0$.

3.4 Magnetic mirroring

In particle physics experiments such as the GBAR experiment, particles have to travel through different spatial regions, each of them being influenced by a different source of magnetic field. These variations in the magnetic field may create what is named magnetic mirroring. As a more specific example, if a positron following a magnetic field line approaches a Penning-Malmberg trap with a stronger magnetic field, the positron may be repelled. In this section, the conditions to cross a magnetic mirror are presented.

Let's consider a positron following a magnetic field line. Locally, the field can be approximated along the z-axis (as presented in Figure 3.9). In the cylindrical frame where the main axis is the one whose the particle is wrapping around, $\mathbf{e_r}, \mathbf{e}_\theta, \mathbf{e_z}$, the velocity vector can be written:

$$\mathbf{v} = -v_\perp \mathbf{e}_\theta + v_\parallel \mathbf{e_z}, \tag{3.4.1}$$

with $v_\perp = r\omega_c = r\frac{eB}{m}$, the minus sign coming from the fact that a positron would go clockwise.

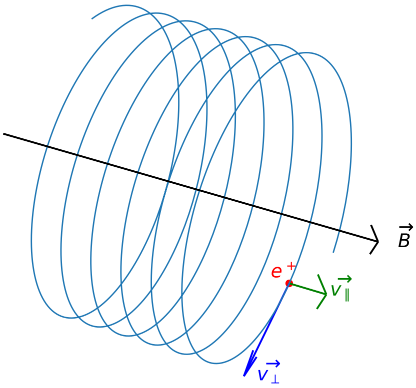

Figure 3.9 – Illustration of a positron following a magnetic field line.

For the rest of the demonstration of the magnetic mirroring effect, we need to introduce the magnetic moment of the positron. In the case of the positron with a circular trajectory with the frequency $\omega_c = \frac{eB}{m}$, the magnetic moment is:

$$\mu = \frac{mv_\perp^2}{2B} \tag{3.4.2}$$

Instead of solving the complete dynamic equation in order to know what happens when the particle goes from a region with $\mathbf{B_i} = B_i\mathbf{e_z}$ to a region with $\mathbf{B_f} = B_f\mathbf{e_z}$, the problem can be simplified. If the field evolves slowly compared to characteristic durations and lengths of the particle motion, the magnetic moment μ remains constant. This is what is called the adiabatic approximation.

A way to determine if this approximation is fulfilled is to compare with the characteristic duration $1/\omega_c = \frac{m}{qB}$ and characteristic length $r_c = \frac{v_\perp}{\omega_c} = \frac{mv_\perp}{qB}$. This leads to write

$$\left|\frac{1}{\mathbf{B}}\frac{\partial \mathbf{B}}{\partial t}\right| \ll \omega_c, \tag{3.4.3a}$$

$$\left|\frac{\nabla \mathbf{B}}{\mathbf{B}}\right|^{-1} \gg r_c. \tag{3.4.3b}$$

A particle of $\sim 50\,\mathrm{eV}$ energy has a speed of $4\,\mathrm{m\,\mu s^{-1}}$. It travels $\delta x = 10\,\mathrm{cm}$ in $\delta t = 25\,\mathrm{ns}$. In a magnetic field of $\sim 10\,\mathrm{mT}$, the cyclotron frequency is $\omega_c = 1.8\,\mathrm{GHz}$ and if we assume $\frac{1}{2}mv_\perp^2 \sim 1\,\mathrm{eV}$, $r_c = 0.3\,\mathrm{mm}$. We consider that during this travel, the variation of the magnetic field does not exceed $\frac{1}{B}\delta B = 30\,\%$ (as presented in Figure 4.7 of the Buffer Gas Trap chapter, see the variation on 10 cm at the level of a cross). With all these parameters, we obtain:

$$\left|\frac{1}{\mathbf{B}}\frac{\partial \mathbf{B}}{\partial t}\right| = \frac{\delta B/B}{\delta t} = 0.012\,\mathrm{GHz} \ll \omega_c \tag{3.4.4a}$$

$$\left|\frac{\nabla \mathbf{B}}{\mathbf{B}}\right|^{-1} = \frac{\delta x}{\delta B/B} = 30\,\mathrm{mm} \gg r_c \tag{3.4.4b}$$

So can consider now that we can use the adiabatic approximation.

3.4.1 Magnetic moment conservation

To prove the adiabatic approximation, let's first consider a magnetic field with a cylindrical invariance (such as the one created by a coil or solenoid). In that case, the magnetic field is written as $\mathbf{B} = B_r\mathbf{e_r} + B_z\mathbf{e_z}$. The Maxwell-Gauss equation $\nabla \cdot \mathbf{B} = 0$ leads to

$$B_r = -r\left(\frac{\partial B_r}{\partial r} + \frac{\partial B_z}{\partial z}\right). \tag{3.4.5}$$

If we consider that we stay close of the axis, a limited expansion gives

$$B_r = r\frac{\partial B_r}{\partial r}. \tag{3.4.6}$$

Combined with Equation 3.4.5 written $r\frac{\partial B_r}{\partial r} = -B_r - r\frac{\partial B_z}{\partial z}$, we obtain

$$B_r = -\frac{1}{2}r\frac{\partial B_z}{\partial z}. \tag{3.4.7}$$

Then, the component along the main axis of the magnetic force is $\mathbf{F} = e\mathbf{v} \times \mathbf{B}$ is $F_z = -e\frac{rv_\perp}{2}\frac{\partial B_z}{\partial z}$, which can be written

$$F_z = -\mu\frac{\partial B}{\partial z}. \tag{3.4.8}$$

This expression can be generalised in 3-dimension as

$$\mathbf{F}_\parallel = -\mu\frac{\mathrm{d}B}{\mathrm{dl}}, \tag{3.4.9}$$

with $\mathrm{d}\mathbf{l}$ an infinitesimal line element along $\mathbf{B}$.

We now have all the elements to prove the adiabatic approximation. Starting from the Newton equation

$$m\frac{\mathrm{d}\mathbf{v}}{\mathrm{d}t} = \mathbf{F}, \tag{3.4.10}$$

By multiplying this expression by $v_{\|}$

$$\left(m\frac{\mathrm{d}v_{\|}}{\mathrm{d}t} = F_{\|}\right) v_{\|},$$

and considering that $v_{\|} = \frac{\mathrm{d}s}{\mathrm{d}t}$, the line element can be removed as

$$\frac{m}{2}\frac{\mathrm{d}v_{\|}^2}{\mathrm{d}t} = -\mu\frac{\mathrm{d}B}{\mathrm{d}s} = -\mu\frac{\mathrm{d}B}{\mathrm{d}s}\frac{\mathrm{d}s}{\mathrm{d}t}.$$

The following expression is obtained

$$\frac{m}{2}\frac{\mathrm{d}v_{\|}^2}{\mathrm{d}t} = -\mu\frac{\mathrm{d}B}{\mathrm{d}t}. \tag{3.4.11}$$

To obtain the evolution of μ during the travel of the particle, we have to take into account that the kinetic energy is conserved, then $\frac{m}{2}\frac{\mathrm{d}v_{\|}^2}{\mathrm{d}t} + \frac{m}{2}\frac{\mathrm{d}v_{\perp}^2}{\mathrm{d}t} = \frac{m}{2}\frac{\mathrm{d}v_{\|}^2}{\mathrm{d}t} + \frac{\mathrm{d}\mu B}{\mathrm{d}t} = 0$ and the expression of the magnetic moment brings

$$\frac{m}{2}\frac{\mathrm{d}v_{\|}^2}{\mathrm{d}t} = -\frac{\mathrm{d}\mu B}{\mathrm{d}t}. \tag{3.4.12}$$

Finally, the combination of Equation 3.4.11 and Equation 3.4.12 gives

$$\frac{\mathrm{d}\mu}{\mathrm{d}t} = 0 \tag{3.4.13}$$

which means that the magnetic moment is conserved along the trajectory.

3.4.2 Mirroring conditions

Starting from the adiabatic approximation

$$\mu = \frac{mv_{\perp}^2}{2B} = \text{constant}, \tag{3.4.14}$$

the relationship between the perpendicular velocity and the magnetic field is obtained:

$$\frac{v_{\perp\mathrm{i}}^2}{B_i^2} = \frac{v_{\perp\mathrm{f}}^2}{B_f^2}, \tag{3.4.15}$$

for a particle initially in an area with a magnetic field B_i travelling to an area with B_f. If we name θ the angle between the velocity vector and the field line (see Figure 3.10), then Equation 3.4.15 can be rewritten:

$$\frac{\sin^2(\theta_i)}{B_i} = \frac{\sin^2(\theta_f)}{B_f} \tag{3.4.16}$$

$$\Leftrightarrow \sin^2(\theta_f) = \frac{B_f}{B_i}\sin^2(\theta_i) \tag{3.4.17}$$

To obtain the mirroring condition, we use the fact that for all θ_f the condition, $\sin^2(\theta_f) \leq 1$ has to be fulfilled if the particle goes across the magnetic mirror. So the maximal angle $\theta_{i\max}$ is given by

$$\theta_{i\max} = \arcsin\left(\sqrt{\frac{B_i}{B_f}}\right). \tag{3.4.18}$$

Here, it is implicit that $B_i < B_f$, in the opposite case, there is no magnetic mirroring and the condition $\sin^2(\theta_i) \leq 1$ can be used to obtain the maximal angle of the particles in the B_f field

$$\theta_{f\max} = \arcsin\left(\sqrt{\frac{B_f}{B_i}}\right). \tag{3.4.19}$$

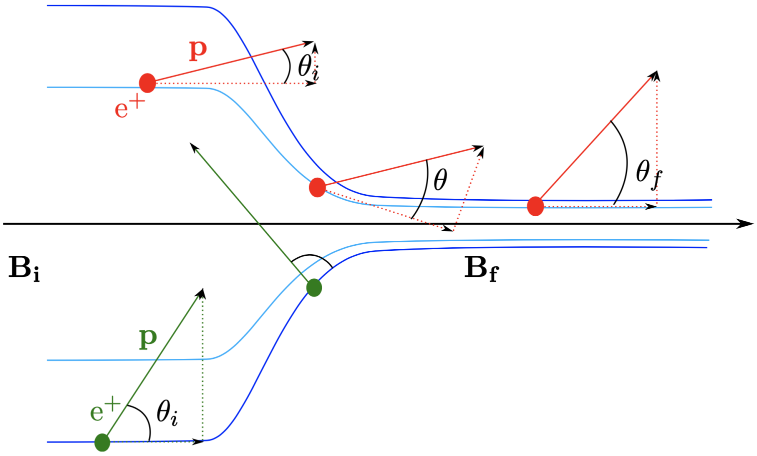

Figure 3.10 – Extracted from Ref. [52]. On this schematic four magnetic field lines are represented as well as two particles with different initial conditions. The cyclotron motion is not represented. In the case of the red positron, we have $\theta_i < \theta_{i\max}$, then the particle can go across the magnetic mirror and we get a positron with $\theta_f > \theta_i$. For the green positron, $\theta_i > \theta_{i\max}$ and we see that θ is increasing during the travel to reach the point where the particle can only go backward: this is the magnetic mirror.

As an example, let's see what is happening with the traps of the GBAR experiment. We want to send the positrons arising from the moderator (see Figure 2.5 and Ref. [44]) into one of the traps. The magnetic field is $B_i = 10\,\text{mT}$ from the moderator. If the positrons are sent straight to the Buffer Gas Trap (BGT), the magnetic field is $B_f = 0.02\,\text{T}$. In the case of positrons sent straight to the High Field Trap (HFT) the magnetic field is $B_f = 5\,\text{T}$. Then, the maximal angle at the exit of the moderator is

$$\theta_{i,\text{BGT}} = 0.79\,\text{rad}, \tag{3.4.20}$$

when the positrons are sent to the BGT and

$$\theta_{i,\text{HFT}} = 4.5 \times 10^{-2}\,\text{rad}, \tag{3.4.21}$$

when the positrons are sent to the HFT. One can conclude here that only the positrons with a momentum almost parallel to the magnetic field can enter inside the HFT, and in the case of the BGT, a larger angular distribution is accepted.

It is also interesting to compute the efficiency of the positron transfer. If we consider that the angular distribution is uniform after the moderator [44], the angular distribution is written $f(\theta, \phi) = \frac{1}{2\pi}$ (see Figure 3.11), then the transfer efficiency is

$$\epsilon = \int_{\phi=0}^{\phi=2\pi} \int_{\theta=0}^{\theta=\theta_{i\max}} \frac{\sin(\theta)\, \mathrm{d}\theta \mathrm{d}\phi}{2\pi} = 1 - \cos(\theta_{i\max}) = 1 - \cos\left(\arcsin\left(\sqrt{\frac{B_i}{B_f}}\right)\right), \tag{3.4.22}$$

noticing that $\cos(\arcsin x) = \sqrt{1 - x^2}$, the efficiency can be written as:

$$\epsilon = 1 - \sqrt{1 - \frac{B_i}{B_f}}, \tag{3.4.23}$$

and the numerical application for the trap gives

$$\epsilon_{\mathrm{BGT}} = 0.30, \tag{3.4.24}$$

$$\epsilon_{\mathrm{HFT}} = 1.0 \times 10^{-3}. \tag{3.4.25}$$

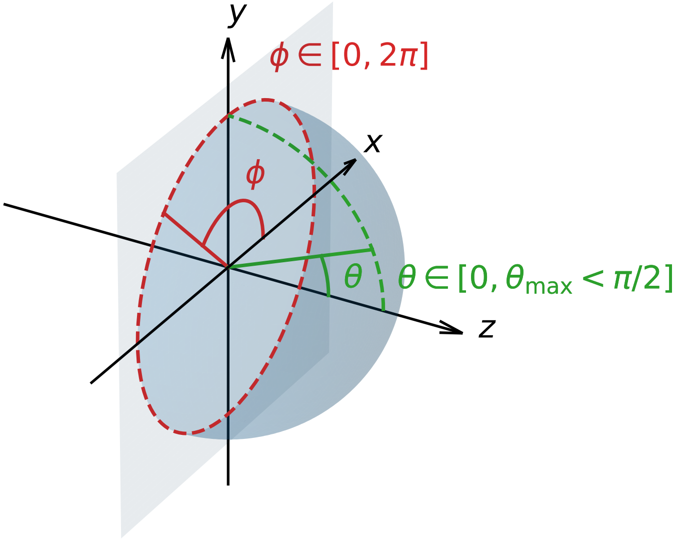

Figure 3.11 – Illustration of uniform angular distribution of momenta after the moderator.

We clearly see that for the BGT, the efficiency is relatively low but at least we can transfer a significant part of the positrons. If we try to send the positrons directly inside the HFT, the efficiency is drastically low. Thankfully, there is a way to improve this transfer efficiency in giving extra energy to the particles, this is what we will demonstrate in the next paragraph.

3.4.3 Crossing the magnetic mirror

A way to cross a magnetic mirror is to give extra momentum along the magnet axis to the particle thanks to an electric potential. To see how it works, let's consider a positron with a total energy E, a velocity v, and an angle between the momentum and the main axis θ_i. In this case, we define the "perpendicular" and the "parallel" energy such as

$$E_\perp = \frac{1}{2}mv_\perp^2 = \frac{1}{2}mv^2\sin^2(\theta_i) = E\sin^2(\theta_i), \tag{3.4.26}$$

$$E_\parallel = \frac{1}{2}mv_\parallel^2 = \frac{1}{2}mv^2\cos^2(\theta_i) = E\cos^2(\theta_i). \tag{3.4.27}$$

If we give to the particle momentum along the parallel axis using an electric field, corresponding to an energy $\mathcal{E}$, it is equivalent to add $\mathcal{E}$ to the parallel energy thereby written

$$E'_\parallel = E\cos^2(\theta_i) + \mathcal{E} = E + \mathcal{E} - E\sin^2(\theta_i). \tag{3.4.28}$$

Consequently the total energy being now $E + \mathcal{E}$, the parallel energy can also be written

$$E'_\parallel = (E+\mathcal{E})\cos^2(\theta'_i) = (E+\mathcal{E}) - (E+\mathcal{E})\sin^2(\theta'_i). \tag{3.4.29}$$

So the new angle between the momentum and the main axis after acceleration is expressed as

$$\sin^2(\theta'_i) = \frac{E}{E+\mathcal{E}}\sin^2(\theta_i), \tag{3.4.30}$$

and Equation 3.4.17 becomes

$$\sin^2(\theta_f) = \frac{B_f}{B_i}\frac{E}{E+\mathcal{E}}\sin^2(\theta_i). \tag{3.4.31}$$

This is similar to increasing the initial magnetic field from B_i to B'_i with

$$B_i \to B'_i = B_i\frac{E+\mathcal{E}}{E}, \tag{3.4.32}$$

and if $B'_i \geq B_f$, the magnetic mirror is counterbalanced.

Finally, to know what is the maximal angle allowing to cross the magnetic mirror, we look for the angle such as $\sin^2(\theta_f) = 1$, leading to

$$\theta_{i,\max} = \arcsin\left(\sqrt{\frac{B_i}{B_f}\frac{E+\mathcal{E}}{E}}\right), \tag{3.4.33}$$

and the efficiency for an original uniform distribution becomes,

$$\epsilon = 1 - \sqrt{1 - \frac{B_i}{B_f}\frac{E+\mathcal{E}}{E}}. \tag{3.4.34}$$

If $B'_i > B_f$, we have $\epsilon = 1$ and

$$\theta_{f,\max} = \arcsin\left(\sqrt{\frac{B_f}{B_i}\frac{E}{E+\mathcal{E}}}\right) \tag{3.4.35}$$

In the case of the Buffer Gas Trap in the GBAR experiment, the positrons have an energy of $E = 3\,\text{eV}$ (see Figure 2.5 and Ref. [44]) and are accelerated to $\mathcal{E} = 50\,\text{eV}$. The magnetic fields are still $B_i = 10\,\text{mT}$ and $B_f = 20\,\text{mT}$. The computation giving $B'_i = 176\,\text{mT} > B_f$, all the positrons go through the magnetic mirror with

$$\theta_{f,\text{max}} = 0.34\,\text{rad} \tag{3.4.36}$$

If we wanted to send the positrons directly into the HFT, the magnetic field being $B_f = 5\,\text{T}$ we would obtain

$$\theta_{i,\text{max}} = 0.19\,\text{rad}, \tag{3.4.37}$$

$$\epsilon = 0.018. \tag{3.4.38}$$

With an extra-energy of $\mathcal{E} = 1\,\text{kV}$, as it was the case during the first tests of the GBAR experiment at CEA Saclay [52], we would have

$$\theta_{i,\text{max,HFT}} = 0.96\,\text{rad}, \tag{3.4.39}$$

$$\epsilon = 0.42. \tag{3.4.40}$$

3.5 Conclusion

In this chapter, it has been shown how to compute the electric field produced by a Penning-Malmberg trap and the behaviour of charged particles trapped in it. Two interesting parameters have been introduced, the Debye length (Equation 3.2.1) which has to be small compared to the characteristic length of the trap if we want to consider the collection of particles as a plasma, and the coupling parameter (Equation 3.2.8) which is a scale of correlation of the plasma. A weakly correlated plasma can be considered as a continuous fluid. Otherwise, the interactions between particles have to be considered. Also, it has been seen that there is a maximal density of particles in a non neutral-plasma, the Brillouin limit (Equation 3.2.22) which is proportional to the magnetic field.

Furthermore, the rotating wall technique was presented, which is used in the positron traps of the GBAR experiment. An oscillating potential is added on an electrode split in 4, and on each part, there is a 90° phase shift with respect to its neighbours, which creates an oscillating dipole. With the appropriate rotating wall frequency, the plasma is compressed.

Finally, a complete description of the concept of magnetic mirror was presented and how to cross this barrier.

Chapter 4

The Buffer Gas Trap

> It's a trap!
>
> Admiral Ackbar, Return of the Jedi

Contents

In this chapter will be presented the experiments performed with the first Penning trap of the GBAR experiment. This trap, named Buffer Gas Trap (BGT), is a clone of the Swansea's trap [70], itself based on the Surko-Greaves Trap [46, 47].

The purpose of this BGT is to accumulate positrons coming from the linear accelerator (LINAC) of the experiment, using N_2 gas for the capture and CO_2 to reduce the energy spread. The positron bunch thus prepared must also be radially compressed. This is obtained using the rotating wall technique (principle presented in Section 3.3.2).

The LINAC provides positrons in pulses. It is used currently with a frequency of 200 Hz. In the future, this frequency is planned to be increased to 300 Hz. When enough positrons are accumulated in the first and second stage of the BGT they are transferred into a third stage to overcome the trap saturation, and a short lifetime ($\tau < 1\,\mathrm{s}$) due to the gas pressure ($10^{-3} - 10^{-4}$mbar). In this third stage, the pressure is lower ($\sim 10^{-6}$ mbar), so positrons can be stored for a longer time ($\tau \sim 10\,\mathrm{s}$). The sequence of accumulation in the first and second stage followed by the transfer to the third stage is repeated until the maximum amount of positrons in the third stage is reached. In the rest of the document, the transfer operation of positron bunches from one stage to another is named stacking.

Once the positron number in the third stage is large enough, the positrons are sent into another trap named High Field Trap (HFT), that has a higher capacity to store positrons: this is a stacking procedure which has to be repeated to trap more and more positrons.

The principle of a Surko-Greaves Trap is presented in Section 4.1, then a complete description of the BGT is detailed in Section 4.2 as well as the control of the trap in Section 4.3. Then, in Section 4.4 are explained the main concepts of the devices used to detect the trapped the positrons. Also, a study on the electron repeller placed upstream of the BGT is presented in Section 4.5 because this repeller will have an importance on the trapping efficiency. Finally, the experimental results concerning the positrons trapping are shown in Section 4.6 and Section 4.7.

4.1 Principle of the Surko-Greaves Trap

The Surko-Greaves Trap (originally developed by Surko and subsequently modified by Greaves) has been developed in order to accumulate positrons from radioactive sources and to deliver a positron beam, well focused and with a small energy spread [46, 71].

In the Surko-Greaves scheme, the trap is made of three long electrodes and two short electrodes at the entrance and exit as presented in Figure 4.1. N_2 gas is injected into the system so that inelastic collisions with the positrons make them loose enough energy to be trapped. The pressure decreases from the entrance to the exit to allow a long term storage in the last stage of the trap.

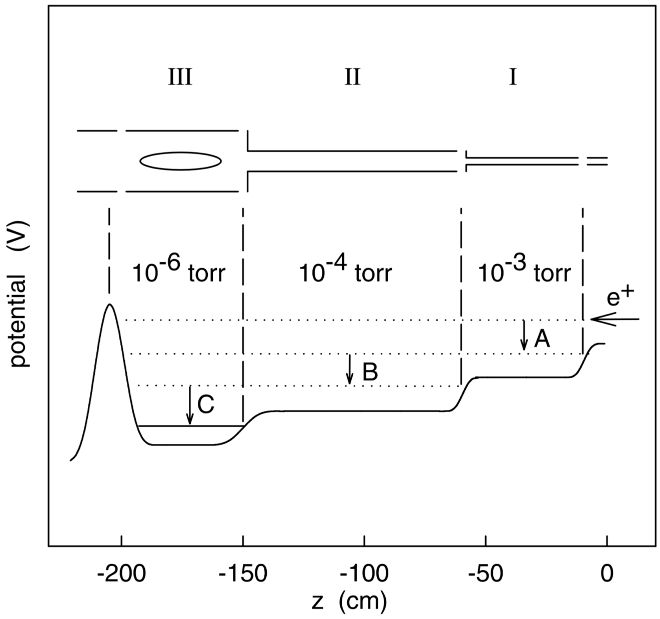

Figure 4.1 – Extracted from Ref. [47]. Schematic diagram of a Surko-Greaves positron accumulator, showing the three stages of differential pumping and the electrostatic potential. A represents the energy loss by inelastic collisions, B and C represent lower energy collisions. The electrostatic potential is set to maximise the positron trapping efficiency (between stages $\Delta V \sim 9 - 10\,\mathrm{V}$).

The choice of trapping gas is a compromise between its slowing power and the rate of positron annihilation. According to the results [47] presented in Table 4.1, N_2 is the best choice among all the possible tested gases.

Gas	Formula	Trapping efficiency (%)
Nitrogen	N_2	100
Carbon monoxide	CO	68
Oxygen	O_2	43
Sulfur dioxide	SO_2	33
Hydrogen	H_2	30
Nitrous Oxide	NO_2	20
Carbon dioxide	CO_2	16
Sulfur hexafluoride	SF_6	7
Carbonyl sulfide	OCS	4

Table 4.1 – Extracted from Ref. [47]. Summary of trapping efficiencies, normalised to nitrogen for a selection of gases.

As presented in Table 4.2, several reactions can happen between N_2 and positrons. In particular, we have to focus on electronic excitation and positronium formation. Electronic excitation makes the positrons lose about 10 eV of kinetic energy which is suitable for trapping in a $\sim 10\,\mathrm{V}$ well. However, its energy threshold of 8.59 eV is close to the energy threshold of positronium formation, 8.78 eV, which has to be avoided. Even if by varying the difference of potentials between electrodes, one can give more or less energy to favour one of the reactions it is impossible to trap positrons without losing some of them by annihilation.

Name	Reaction	Energy threshold
Annihilation	$e^+ + N_2 \rightarrow {N_2}^+ + 2\gamma$	-
Electronic scattering	$e^+ + N_2 \rightarrow N_2 + e^+$	-
Rotational excitation	$e^+ + N_2 \rightarrow {N_2}^{rot} + e^+$	$\sim 1\,\mathrm{meV}$
Vibrational excitation	$e^+ + N_2 \rightarrow {N_2}^{vib} + e^+$	$\sim 0.3\,\mathrm{eV}$
Electronic excitation	$e^+ + N_2 \rightarrow {N_2}^* + e^+$	8.59 eV
Positronium formation	$e^+ + N_2 \rightarrow {N_2}^+ + Ps$	8.78 eV
Ionisation	$e^+ + N_2 \rightarrow {N_2}^+ + e^+ + e-$	15.6 eV

Table 4.2 – Extracted from Ref. [48, 72]. Positron interactions with a nitrogen molecule and respective threshold energies.

Fortunately, as shown in Figure 4.2 there is an energy range of $\sim 3\,\mathrm{eV}$ for which electronic excitation is more important than positronium formation. Therefore, trapping is possible by fine-tuning the potential well.

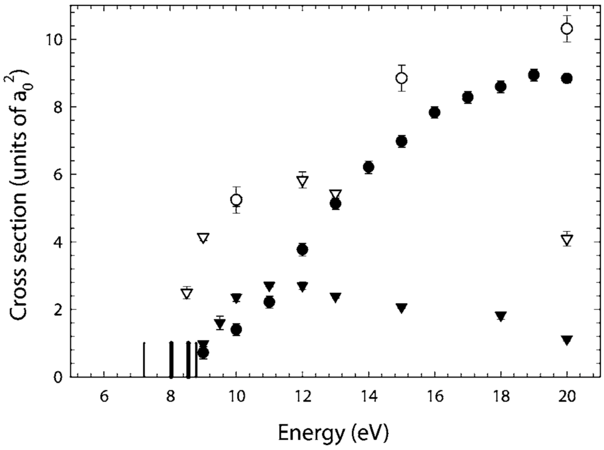

Figure 4.2 – Extracted from Ref. [72]. Comparison between the impact excitation of the electronic state (triangles) and positronium formation (circles) cross sections (a_0 is the Bohr radius) of N_2 (solid) and CO (open). The vertical bars on the x-axis mark the threshold values for Ps formation in CO (7.21 eV), electronic excitation in CO (8.07 eV), electronic excitation in N_2 (8.59 eV), and Ps formation in N_2 (8.78 eV).

Now that the positrons are trapped, the goal is to cool them. In this situation, we are more interested by the rotational and vibrational excitations. The optimal gas would be the one giving the shortest cooling time with a long lifetime. According to the results [47] presented in Table 4.3 (if the RW technique is used), N_2 is a poor cooling gas, and SF_6 would be the best but it has bad trapping properties (see Table 4.1). This is why generally in the experiments using buffer gas traps, both gases are used.

However, in the case of GBAR experiment, for the time being, it has been decided to not use SF_6, because it is a corrosive gas, which could destroy other sensitive parts of the experiment. Moreover, SF_6 is a greenhouse gas and special permissions need to be obtained. This is why we use CO_2 , which is the best cooling gas without fluorine.

Gas	τ_a (s)	τ_c (s)	E_{v} (eV)	$\dot{n}/n_{\text{max}}$ (s^{-1})
SF_6	2190	0.36	0.076, 0.188	10
CF_4	3500	1.2	0.157	10
CO_2	3500	1.3	0.291, 0.083	4
CO	2400	2.1	0.266	< 0.2
N_2	6300	115	0.292	< 0.2

Table 4.3 – Reprinted from [47]. Measured positron cooling times, τ_c and calculated annihilation times, τ_a, for selected molecules at a pressure of 2×10^{-8} Torr (2.7×10^{-8} mbar). Plasma compression rates, $\dot{n}/n_{\text{max}}$; are also shown, using the rotating wall technique and these gases for cooling. E_{v} are the vibrational energy quanta for each gas.

4.2 Description of the trap

The Buffer Gas Trap (BGT) of the GBAR experiment is a Surko-Greaves trap, based on Swansea's BGT [70], and developed for CEA Saclay [48]. It is now installed at CERN (April 2018, Figure 4.3).

The purpose of the BGT is to trap the positrons at the exit of the beam line coming from the LINAC thanks to inelastic collisions with N_2 and to cool them thanks to inelastic collisions with CO_2 gas. The magnitude of the magnetic field inside this trap is about 4×10^{-2} T, the maximum absolute electric potential is 140 V.

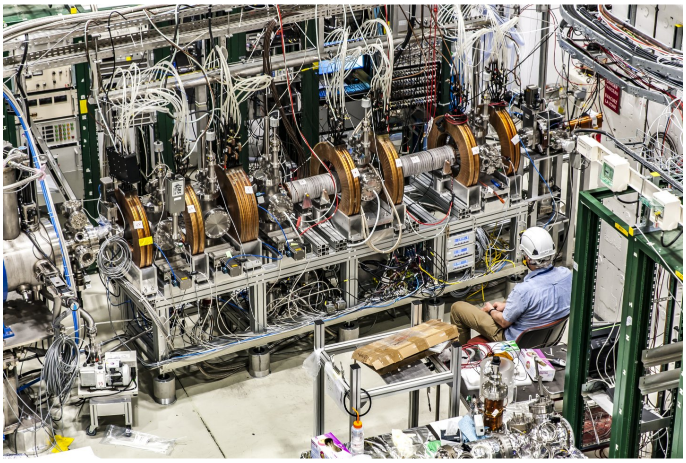

Figure 4.3 – Picture of the Buffer Gas Trap in the GBAR experiment at CERN (Picture by Ciaran McGrath).

4.2.1 Sets of electrodes

All the schematics of the BGT electrodes are presented in Appendix C. The first stage starts with a grounded ring (Figure C.1). The purpose of this ring is to ensure a ground potential at the entrance of the trap, but also, to support the electrodes.

Then, there are 15 cylindrical electrodes of length 24 mm, 16 mm inner diameter and 24 mm outer diameter (Figure C.2). Also, each electrode has a male and female tip so that they fit into one another. The last electrode is different from the other electrodes composing the first stage. This electrode has two male tips, to be embedded in a transition ring connecting the first and the second stage (Figure C.3). Both of these transition parts are in contact to be set at the same electric potential. The last electrode is also surrounded by a grounded ring (Figure C.4), in order to support the stage.

The Buffer Gas Trap second stage composed of 5 cylindrical electrodes of length 49 mm, 41 mm inner diameter and 49 mm outer diameter. Similarly to the first stage electrodes, they have both male and female tips to be easily embedded, except for the last one (Figure C.5). The fourth electrode (Figure C.6), is split in two electrodes of length 24 mm, one of them being split in four sections along the circumference for the Rotating Wall technique (see Section 3.3.2). The fifth and last electrodes of the second stage have 3 supports to embed a grounded support ring. The schematics of the electrode and the ring are presented in Figure C.7.

At both ends of the third stage there are two electrodes of length 49 mm. The entrance electrode is the same as the exit electrode of the second stage (Figure C.7). The exit electrode is similar to the long electrodes of the second stage (Figure C.5). In-between, there are twelve electrodes of length 18.4 mm, all of 41 mm inner diameter and 49 mm outer diameter. Two of them are split in four sections for the Rotating Wall technique (Figure C.8). The stage ends with a grounded ring, supporting the electrodes and insuring a potential of 0 V at the exit of the system.

All electrodes are assembled using small sapphire balls to prevent the contact between the electrodes as presented in Figure 4.4. The nitrogen gas is delivered in the first stage thanks to an inlet adapter on the first stage's ninth electrode and the CO_2 in the cross between the second and the third stage.

4.2.2 Electric potential

The electric potential is created using High Voltage Amplifiers (HVA), converting an analog signal into a high voltage. These amplifiers are limited to a maximal voltage of 140 V. Some electrodes have to be at the same potential so it is not necessary to have one amplifier per electrode. Moreover, some electrodes have to be set at 0 V extremely quickly (order of few ns) in order to eject a positron cloud or to re-trap one. In that case, fast switches are connected between the HVA and the electrodes. A summary of the electrode connection is presented in table 4.4. All the electrodes of the first stage are at the same potential except the first one.

The electrodes used for the RW technique are not directly connected to HVA. As explained in Section 3.3.2, we want to apply on each part of the electrode split in four a potential $V_0 + V_r \cos \omega t + \phi_i$ with V_0 provided by the HVA and the oscillating part with waveform generators and splitters, with $\phi_i = \{0°, 90°, 180°, 270°\}$. In

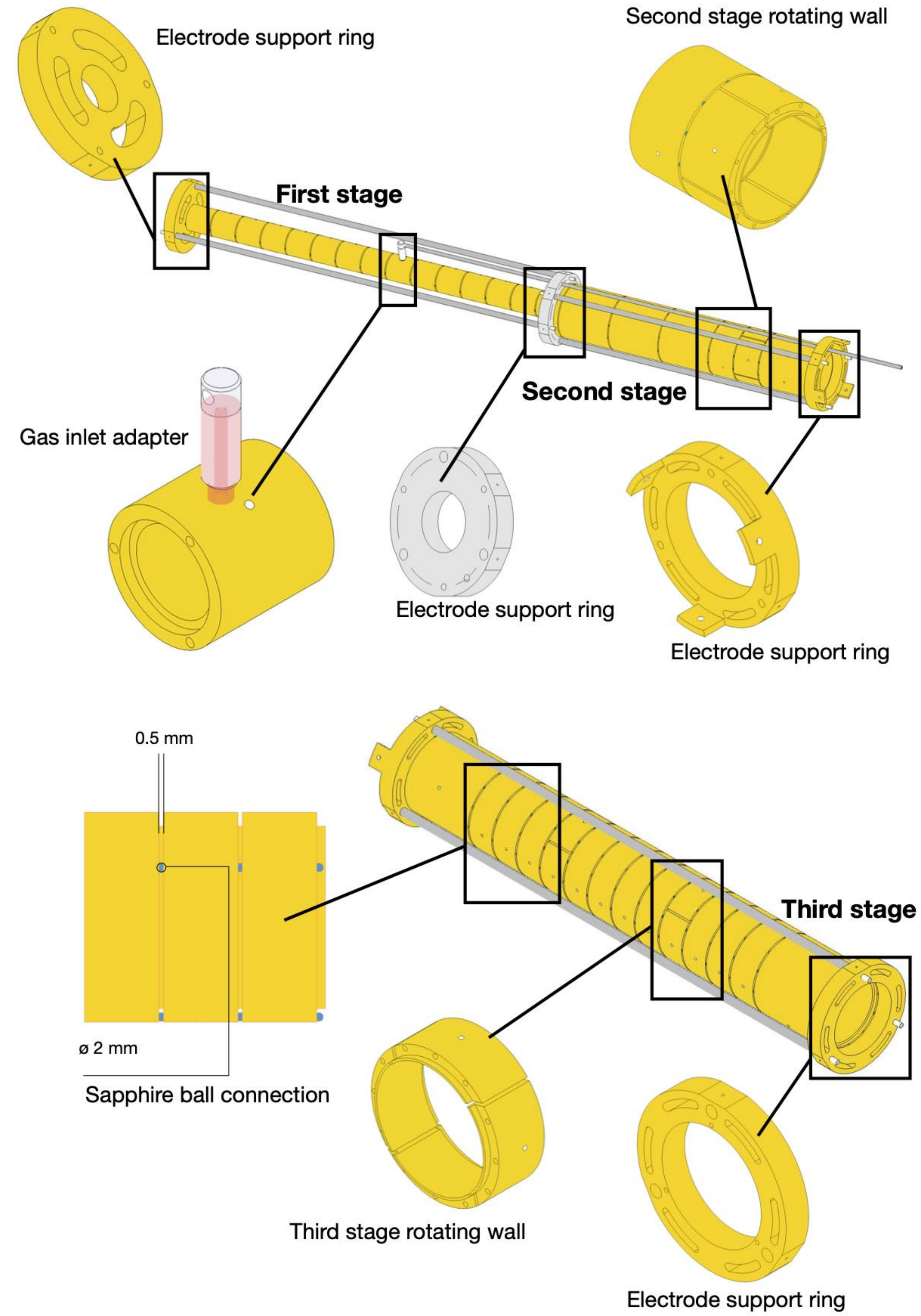

Figure 4.4 – Buffer Gas Trap electrodes assembled in stages.

practice one generator is associated to one RW electrode. The generator provides

Stage	Electrode	Name	Function
1st	1	E_0	Entrance
	2 to 15, same HVA	E_F	Inelastic collisions
2nd	1, 2, 3, same HVA	E_1, E_2, E_3	Accumulation well
	4	E_4	Accumulation well + RW
	5	E_5	Exit of the accumulation well, with fast switch
3rd	1	E_6	Trapping well entrance
	2, 3, 4, 6	E_7, E_8, E_{10}, E_{11}	First well
	5	E_9	First well + RW
	7	E_{12}	First well exit, with fast switch
	8, 9, 11, 12, 13	$E_{13}, E_{14}, E_{16}, E_{17}, E_{18}$	Second well
	10	E_{15}	Second well + RW
	14	E_{19}	Second well exit, with fast switch

Table 4.4 – Summary of the electrode connections for the Buffer Gas Trap

two oscillating signals phase-shifted by 90°. Each of these signals is connected to a splitter, giving two signals with a 180° shift, so four signals with the same amplitude and frequency, but with the desired phases, are obtained. Each signal is added to the static potential provided by the HVA using a RC circuit and finally connected to the corresponding part of the electrode.

To determine the overall electric potential at different space locations, it is not possible to use the analytic expressions presented in Equations 3.3.6 and 3.3.7 because the electrodes do not have all same radii, therefore the potential has been obtained using the SIMION simulation software [73] (see Figure 4.5).

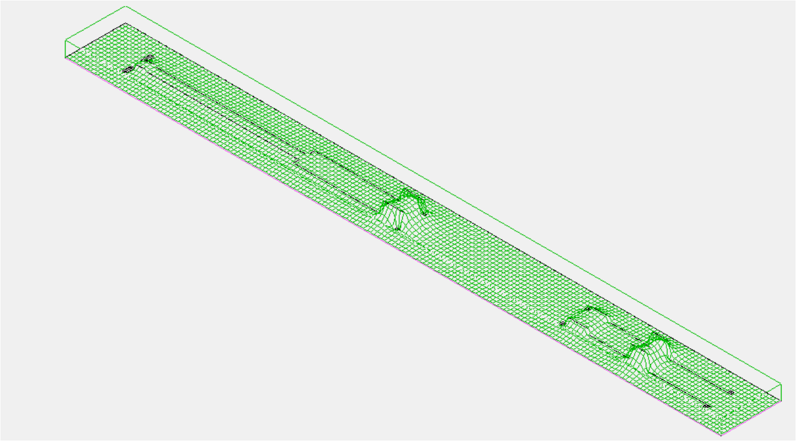

Figure 4.5 – Electric potential vs x and y (for a fixed for $z = 0$), where x is the beam axis and y is one of the radial direction. Computation obtained by SIMION [73] with the parameters of the BGT described in Section 4.2.1.

4.2.3 Magnetic Field

As explained in Section 3.2.2, a constant and uniform magnetic field is required to radially confine the positron cloud. This is why two solenoids surrounding the electrodes have been positioned ((a) in Figure 4.6). The solenoid surrounding the first and second stages is 620 mm long and the one surrounding the third stage is 420 mm long.

The adiabatic approximation implying that $\mu_B = \frac{mv_\perp^2}{2B}$ remains constant if B evolves “slowly” (with $v_\perp$ the orthogonal component of the particle speed), the following expression is obtained for a particle going from a region where the magnetic field is B_i to another one where it is B_f:

$$\frac{v_{\perp,\mathrm{f}}^2}{v_{\perp,\mathrm{i}}^2} = \frac{B_f}{B_i}. \tag{4.2.1}$$

To prevent the magnetic mirroring effects discussed in Section 3.4, that would occur if $\frac{B_f}{B_i} \gg 1$, the magnetic field has be sufficiently high outside of the solenoids. Moreover, we have to ensure that the beam is compressed enough to avoid annihilation. Indeed, we would like to let the beam travel inside a tube to be sent downstream into the HFT. If we consider that the orthogonal component of the speed is proportional to the magnetic field (indeed $v_\perp = r\omega_c = r\frac{qB}{m}$), equation 4.2.1 leads to the following equation of the radius of the circular movement of the particles:

$$\frac{r_f}{r_i} = \sqrt{\frac{B_i}{B_f}}, \tag{4.2.2}$$

which shows that an increase of the magnetic field decreases the radius of the beam.

To ensure a better compression of the beam, we need to increase the magnetic field around the tube, and this is the purpose of the larger circular coil, with a 135 mm width placed right after the cross after the third stage ((c) in Figure 4.6). In order to guide positrons, six circular coils of 90 mm width are placed on the sides of the crosses and the stages ((b) in Figure 4.6). The field map of the trap and the magnetic field of each coils and solenoids is presented in Figure 4.7.

The solenoids and the coils are constantly water cooled. A Labview interface (described in Section 4.3 controls the powers supplies, which are interlocked with the water cooling system. To power the coils and the solenoids 1500 W and 3000 W [74] DC power supplies are used.

4.2.4 Gas and vacuum

A major element of the Buffer Gas Trap system is pressure control. Indeed, as explained in Section 4.1, the gas pressure has an effect on the positron trapping efficiency, lifetime, and cooling. Moreover, the positron buffer gas accumulator uses relatively high pressures ($\sim 10^{-3}$ mbar), the rest of the GBAR equipment takes place under UHV (Ultra-high Vacuum) and even EHV (Extreme-High Vacuum) conditions (below 10^{-10} mbar). So the design and control of the BGT system should be such that it does not pollute either the LINAC nor the HFT.

Gauges

The vacuum in the positron line is monitored using a variety of pressure gauges. In our experiment, four kind of gauges are used:

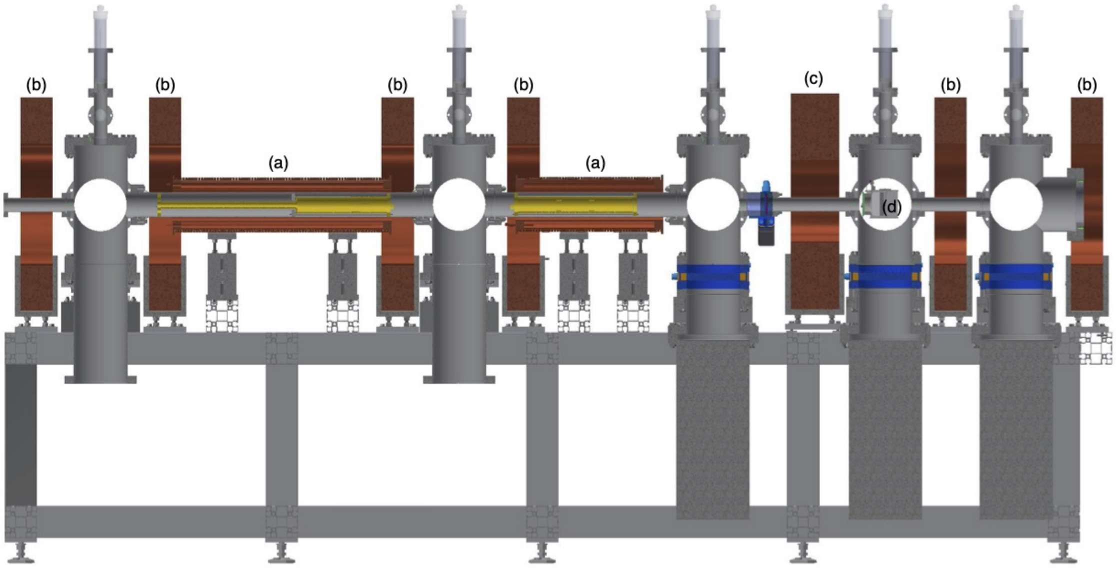

Figure 4.6 – Schematic of the Buffer Gas Trap. (a) Solenoids used to confined the positrons in the accumulator. (b) Transport coils. (c) Transport and compression coil. (d) MCP (see Section 4.4.1).

- The Capacitance gauges are used where there is no high vacuum (not below 10^{-3} mbar), in our case, they will allow us to monitor the N_2 and CO_2 injection (see P5 and P6 in Figure 4.8).
- The Pirani gauges, which are, similarly to the capacitance gauges, not appropriate for high vacuum but can read lower pressures than the capacitance gauges (not below 5×10^{-4} mbar). They are mainly used to be interlocked with gate valves, to isolate the trap from the rest of the positron line in case of issues related to the vacuum (see P8, P5 in Figure 4.8) or to let the appropriate pump acting on the system (see P1, ..., P4, P14 in Figure 4.8).
- The Cold Cathode gauges are used where there is a high vacuum (about 10^{-10} mbar), to read the pressures along the positrons line (see P9, ..., P13 in Figure 4.8).
- The Full Range gauges are used where a large range of pressure is expected. These gauges are a combination of Pirani and Cold Cathode gauges.

A Full Range gauge, combination of a Hot Cathode gauge and a Pirani gauge is used after the HFT (see Figure 4.8). The characteristics and the references of the gauges used in the experiment are presented in Table 4.5.

Pumps

In order to use the pumping restriction to prevent to much N_2 and CO_2 coming in the buffer gas accumulator and in order to maintain a low pressure (below 10^{-10} mbar) in the rest of the experiment, a combination of different technologies of pumps are used:

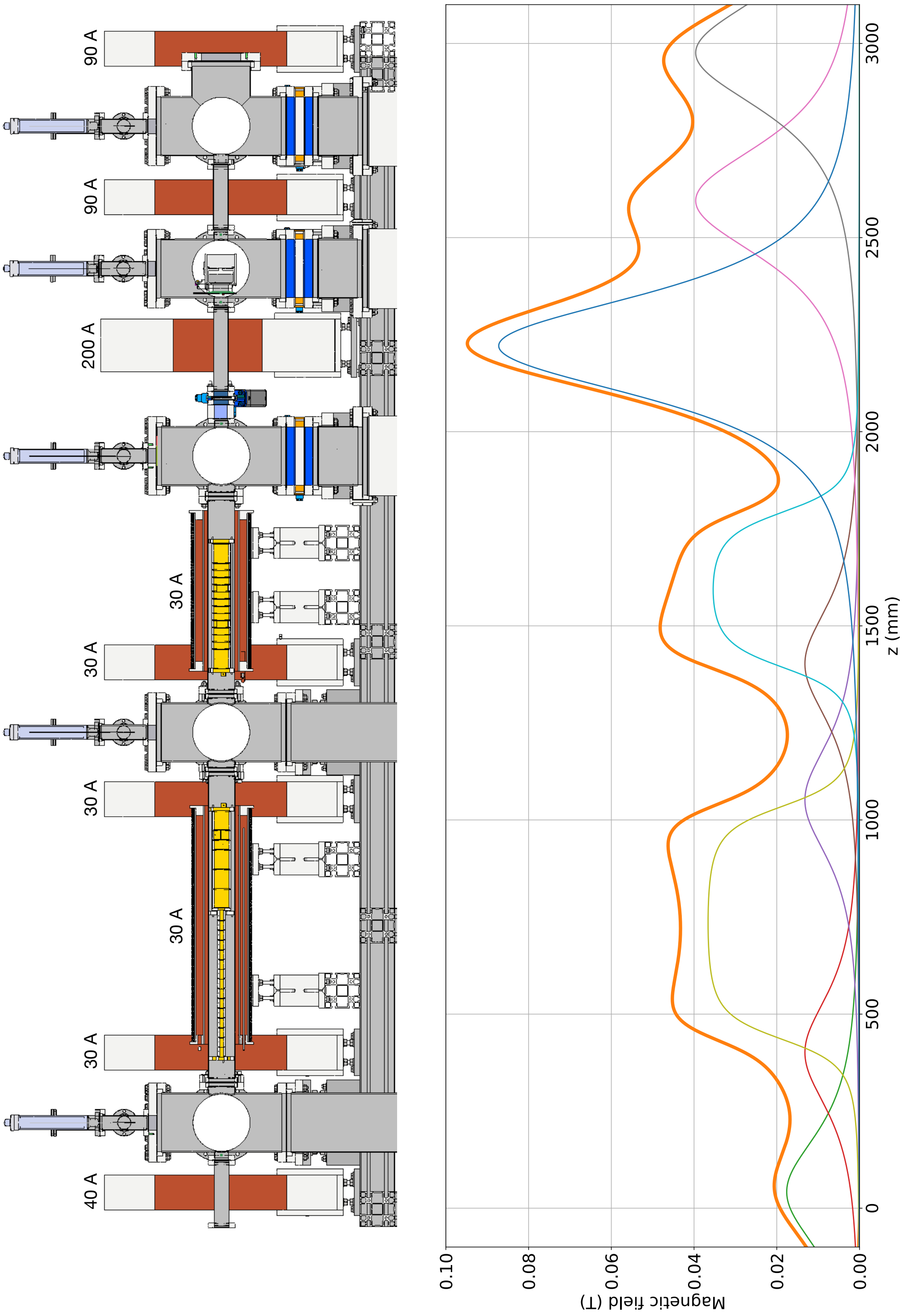

Figure 4.7 – Buffer Gas Trap's magnetic field map.

Gauge type	Model	Minimum	Maximum
Capacitance	PT R24 622	1×10^{-3} mbar	11 mbar
Pirani	PT R26 961A	5×10^{-4} mbar	1×10^{3} mbar
Cold cathode	PT R21 261	5×10^{-11} mbar	1×10^{-2} mbar
Full range	PT R26 252	5×10^{-9} mbar	1×10^{3} mbar
Full range	PT R27 002	5×10^{-10} mbar	1×10^{3} mbar

Table 4.5 – Table of the different kind of gauges used in the GBAR experiment. Manufacturer: Pfeiffer Vacuum. The positions of the different gauges along the positron line and the BGT system are shown in Figure 4.8.

- The dry scroll pumps whose main principle [75, 76] is to use two interleaving spinning scrolls in order to compress and eject the gas out of the system. These pumps are designed for large volumes to reach pressures of the order of 10^{-2} mbar. These pumps are used as a first stage of a vacuum system by pumping the system before the other pumps.

- The turbo-molecular pumps. Here the principle is to rotate quickly rotor blades in order to compress and eject the gases [77]. These pumps are used to pump directly the system after the action of the dry scroll pumps (see turbo 1 and 2 in Figure 4.8) or to pump before the cryogenic pumps (see turbo 3 in Figure 4.8). Two pumps of the model we used are able to provide a vacuum already convenient for the experiment with an ultimate pressure below 10^{-10} mbar.

- The cryogenic pumps are used to reach ultra-high vacuum in the positron line and to pump the gas outside of the Buffer Gas Trap. The principle of these pumps [78, 79] is to present a very cold surface (in our case, about 10 K) to the system, and then the gases freezes onto this surface. Thus, helium compressors are required to constantly cool the pumps. These pumps can be operated in vacuum range from 10^{-3} mbar to 10^{-12} mbar.

- The ion pump, whose principle is based on a small Penning trap [80, 81]. An electron cloud is created and stored in order to ionise the incoming molecules and then an electric field ejects the ions thereby created. It is of course a technique which can be used only when a good vacuum is already done (below 10^{-3} mbar), to finally reach an ultimate pressure of 10^{-11} mbar. On the positron line, only one pump is used to improve the vacuum in the High Field Trap.

All the references of the pumps used for the GBAR positron line are detailed in Table 4.6.

The pumps characteristics determine the procedure to start the vacuum system. Indeed, the pumps are working only when they are in their operating range as follows (the names refer to Figure 4.8). Then, the protocol is the following:

- After the isolation of Scroll 1 and Scroll 2 (V1, ..., V6, V12 closed), we start these pumps. When the pressure at the levels of the pumps (P1 and P7) is

Pump	Manufacturer	Model	S_p ($\mathrm{L\,s^{-1}}$)
Scroll 1	Edwards	nXDS10i	3.2
Scroll 2	Edwards	nXDS10i	3.2
Turbo 1	Oerlikon Leybold	MagW 600	550
Turbo 2	Oerlikon Leybold	MagW 600	550
Turbo 3	Edwards	nEXT300D	300
Cryo 1	SHI Cryogenics	Marathon CP-8	1500
Cryo 2	SHI Cryogenics	Marathon CP-8	1500
Cryo 3	SHI Cryogenics	APD 8	1200
Cryo 4	SHI Cryogenics	APD 8	1200
Ion pump	Agilent	VacIon Plus 300 Diode	300

Table 4.6 – Extracted from [48] and updated. Table of the pumps used in the trapping system. The connections and locations are shown in Figure 4.8. S_p: pumping speed.

low enough (10^{-2} mbar), the valves between the scroll pumps and the turbo pumps are opened (V1 and V2), and all the turbo pump are started (Turbo 1, 2 and 3). Then the pumping off the whole positron line starts from Cross I and Cross 2 in opening V11, V14 and V16. V3 is opened to pump Cross V.

- We wait until the pressure before the cryogenic pumps reach 10^{-4} mbar, we check that V8, V9 and V10 are close and then we open the valves before the cryogenic pumps (V1, ..., V6, V12). After switching on Compressor 1 and 2, all the cryogenic pumps can be turned on.
- If the pressure in the cross is low enough (below 10^{-4} mbar), the valves after the cryogenic pump are opened to pump the whole line. The conditions are now fulfilled to switch on the ion pump.

After half of a day, the pressure is low enough to at least use the Buffer Gas Trap accumulator.

Conductance and pressures

The pressures are measured in the crosses of the positron line (see Figure 4.8), but an estimation of the pressures in the stages of the buffer gas accumulator is required for the trapping optimisation. An easy way to determine the pressures is the analogy with an electric circuit. In this one, the electric sources correspond to the vacuum pumps, the electric current to the throughput, and the wire resistances to the impedances of the pipes. The throughput is conserved for a fixed temperature.

The total conductance (inverse of the impedance) for n vacuum components connected in series is given by [82]

$$\frac{1}{C_T} = \frac{1}{C_1} + \frac{1}{C_2} + \cdots + \frac{1}{C_n}, \tag{4.2.3}$$

the conductance C of a component being defined as the ratio of throughput Q to the pressure differential $(P_1 - P_2)$ between its two sections. Then we have for each

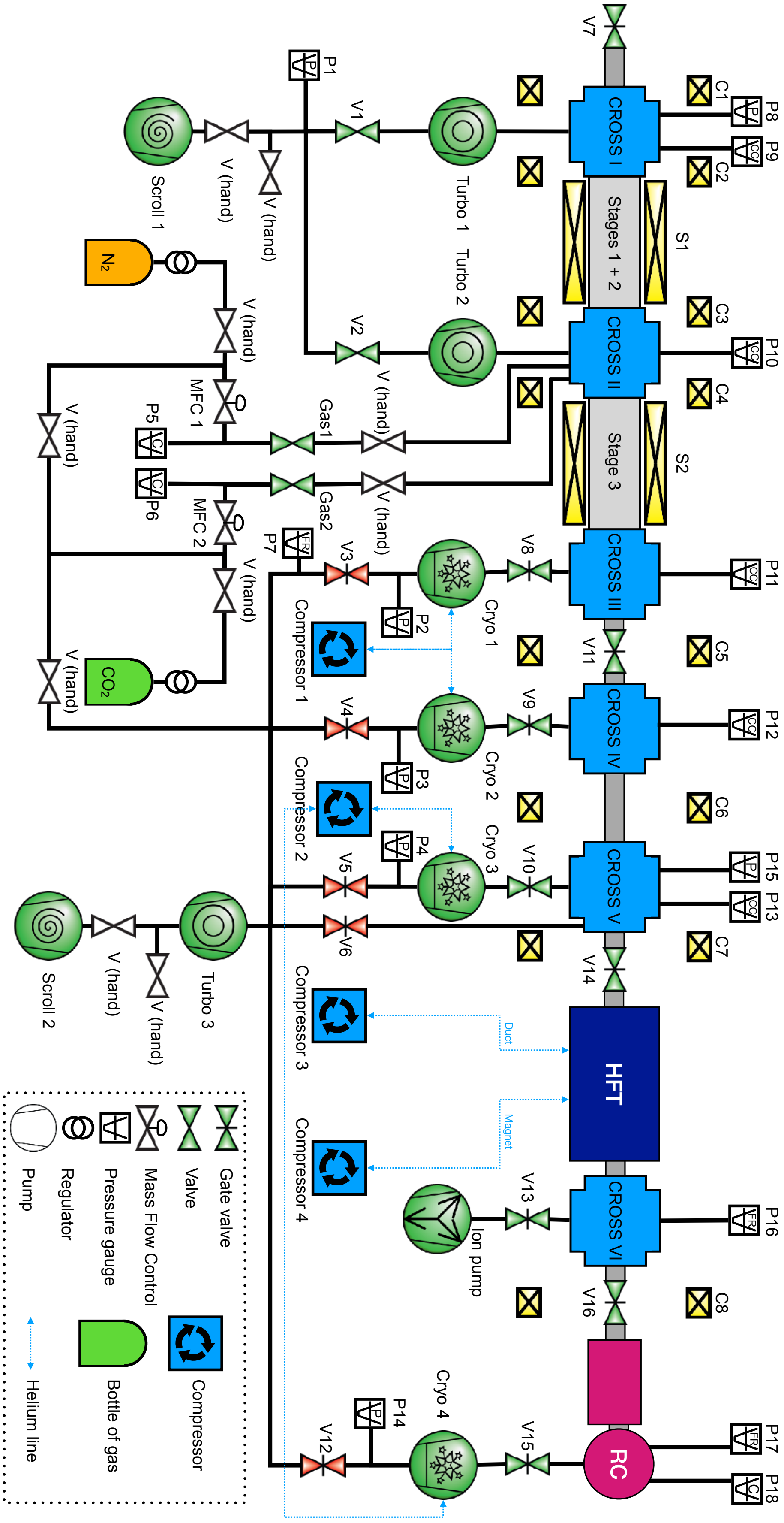

Figure 4.8 – Schematic of the vacuum system of both traps. Three kinds of pressure gauges **P**, CC: cold cathode gauge, C: capacitance gauge, P: Pirani gauge, FR: full range gauge.

element

$$Q = C(P_1 - P_2), \tag{4.2.4}$$

with the conductance expressed in $\mathrm{L\,s^{-1}}$ and the throughput in $\mathrm{mbar\,L\,s^{-1}}$.

The pumping speed being the volume of gas pumped per unit of time, it is defined by [82]

$$S = \frac{\mathrm{d}V}{\mathrm{d}t} = \frac{Q}{P}, \tag{4.2.5}$$

For a pump connected to the system with an aperture of conductance C, the net pumping speed S_n, also expressed in $\mathrm{L\,s^{-1}}$, is computed as a function of the pumping speed S_p and the conductance C is [82]

$$\frac{1}{S_\mathrm{n}} = \frac{1}{S_\mathrm{p}} + \frac{1}{C}. \tag{4.2.6}$$

with Q the throughput and P the pressure. More specifically, for two vessels connected with a pipe of conductance C, the first one with a pressure P_1 and the second with P_2, if the second one is connected to a pump of net pumping speed S_n (see schematic in Figure 4.9), the combination of 4.2.4 and 4.2.5 leads to

$$Q = C(P_1 - P2) = S_\mathrm{n} P_2. \tag{4.2.7}$$

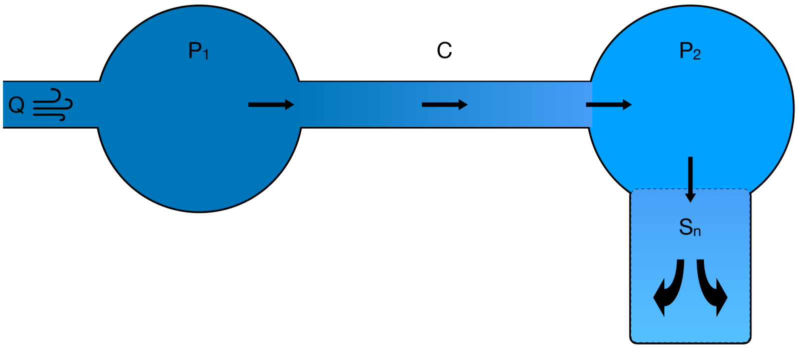

Figure 4.9 – Schematic of two vessels with one connected to a pump.

The gases are in the molecular flow regime, i.e., the mean free path of the molecules is larger than the diameter of the pipes, and the collisions between the molecules and the walls are more important than the collisions between molecules. One generally considers it is the case when the product of the mean pressure in mbar and the diameter of the pipe in cm is below 0.013 [83]. With a pressure in the system below 10^{-3} mbar and a minimal diameter of 0.1 cm, we can use the following formulas determined for the molecular flow regime.

In the case of an aperture with a surface A, the conductance is [82]

$$C = 3.64\sqrt{\frac{T}{M}}A \quad (\mathrm{L\,s^{-1}}), \tag{4.2.8}$$

with T in K, M in $\mathrm{g\,mol^{-1}}$ and A in $\mathrm{cm^2}$. For N_2 at $T = 23\,^\circ\mathrm{C}$, we have

$$C = 11.8A \quad (\mathrm{L\,s^{-1}}). \tag{4.2.9}$$

For a long pipe ($L \gg D$, L the length and D the diameter), the conductance is given by the expression [84]

$$C = 3.81\sqrt{\frac{T}{M}\frac{D^3}{L}} \quad (\mathrm{L\,s^{-1}}). \tag{4.2.10}$$

For N_2 at $T = 23\,^{\circ}\mathrm{C}$, we have

$$C = 12.4\frac{D^3}{L} \quad (\mathrm{L\,s^{-1}}). \tag{4.2.11}$$

Finally, in the case of a short pipe (if $L < 0.7D$ [83]), the conductance is

$$C = 11.8\frac{A}{1 + L/D}. \tag{4.2.12}$$

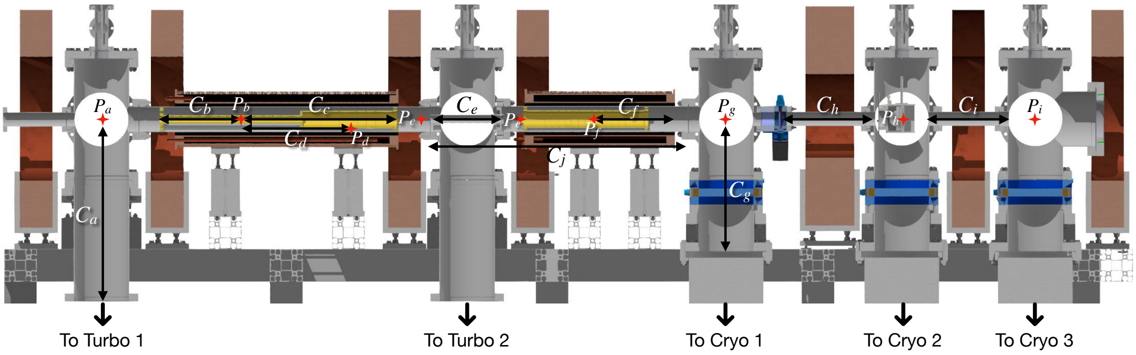

Figure 4.10 – Conductances of the pumping restriction elements. C_a: connection with the turbo-pumps. C_b: half first stage. C_c: half first stage and second stage. C_d: half first stage and half second stage. C_f: half third stage. C_g: connection with the cryo-pumps. C_e, C_h, C_i: small pipes. C_j: small pipe and third stage.

The calculated conductances of different parts of the system (see Figure 4.10) are shown in Table 4.7 and the net pumping speed of various pumps in Table 4.8. The net pumping speeds are computed taking into account the aperture of the pumps and the pipes that connect them to the crosses according to Equation 4.2.6.

It is now possible to compute the pressures. For this purpose, it is assumed that the gas is injected in the middle of the second stage and the pressure at the injection point P_b is a known parameter.

Considering throughput conservation in each cross, similarly to the expression 4.2.7, Equations 4.2.13 are obtained (the variables names are related to Figure 4.10, Ta-

Name	L(cm)	D(cm)	$C(\mathrm{L\,s^{-1}})$
C_a	68.0	15.0	615
C_b	19.0	1.6	2.67
C_c	(19.0, 26)	(1.6, 4.1)	2.37
C_d	(19.0, 13.0)	(1.6, 4.1)	2.49
C_e	30	2	3.31
C_f	17.5	4.1	29.6
C_g	43.0	15	973
C_h	21.5	3.7	29.2
C_i	17	3.7	36.9
C_j	(30, 35)	(2, 4.1)	2.91

Table 4.7 – Conductances of the elements of the pumping restriction. The conductance names are related to Figure 4.10.

Pump	D(cm)	$S_{\mathrm{p}}(\mathrm{L\,s^{-1}})$	$S_{\mathrm{n}}(\mathrm{L\,s^{-1}})$	S_{n}
Turbo 1	18	550	264	S_{n1}
Turbo 2	18	550	264	S_{n2}
Cryo 1	20	1500	509	S_{n3}
Cryo 2	20	1500	509	S_{n4}
Cryo 3	20	1200	469	S_{n5}

Table 4.8 – Pumping speeds and net pumping speeds. The names are related to Figure 4.8. The net pumping speeds come from the manufacturers' datasheet.

ble 4.7 and Table 4.8):

$$(P_b - P_a)C_b = P_a S_{\mathrm{n1}} \tag{4.2.13a}$$

$$\Leftrightarrow P_a = AP_b, A = \frac{C_b}{C_b + S_{\mathrm{n1}}}, \tag{4.2.13b}$$

$$(P_b - P_c)C_c = P_c S_{\mathrm{n1}} + (P_c - P_g)C_j \tag{4.2.13c}$$

$$\Leftrightarrow P_c = BP_b, B = \frac{C_c}{C_c + (1-D)S_{\mathrm{n1}} + C_j}, \tag{4.2.13d}$$

$$(P_c - P_g)C_j = P_g S_{\mathrm{n2}} + (P_g - P_h)C_h \tag{4.2.13e}$$

$$\Leftrightarrow P_g = DP_c = BDP_b, D = \frac{C_j}{C_j + (1-E)S_{\mathrm{n2}} + C_h}, \tag{4.2.13f}$$

$$(P_g - P_h)C_h = P_h S_{\mathrm{n3}} + (P_h - P_i)C_i \tag{4.2.13g}$$

$$\Leftrightarrow P_h = EP_g = BDEP_b, E = \frac{C_h}{C_h + (1-F)S_{\mathrm{n2}} + C_i}, \tag{4.2.13h}$$

$$(P_h - P_i)C_i = P_i S_{\mathrm{n3}} \tag{4.2.13i}$$

$$\Leftrightarrow P_i = FP_h = BDEFP_b, F = \frac{C_i}{C_i + S_{\mathrm{n3}}}. \tag{4.2.13j}$$

The conservation of the throughput between the points corresponding to the pressures P_b, P_d and P_d, P_c for the second stage (respectively between P_c, P_g and P_f, P_g

for the third stage), the following equations are obtained:

$$(P_b - P_d)C_d = (P_b - P_c)C_c \quad \Leftrightarrow \quad P_d = \left(1 - \frac{C_c}{C_d} + \frac{C_c}{C_d}B\right) P_b \tag{4.2.14a}$$

$$(P_f - P_g)C_f = (P_c - P_g)C_j \quad \Leftrightarrow \quad P_f = \left(1 - \frac{C_j}{C_f}BD + \frac{C_j}{C_f}B\right) P_b \tag{4.2.14b}$$

All pressures are proportional to P_b and therefore scale linearly according to the input parameter P_b to match the measurements. This model gives a good approximation of reality as shown in table 4.9.

Location	Name	Gauges	$P_b = 1 \times 10^{-3}$	$P_b = 6 \times 10^{-3}$	Measured
Cross I	P_a	P9	1×10^{-5}	6×10^{-5}	6×10^{-5}
1st stage	P_b	-	1×10^{-3}	6×10^{-3}	-
Cross II	P_c	P10	9×10^{-6}	6×10^{-5}	4×10^{-5}
2nd stage	P_d	-	6×10^{-5}	4×10^{-4}	-
3rd stage	P_f	-	9×10^{-7}	6×10^{-6}	-
Cross III	P_g	P11	5×10^{-8}	3×10^{-7}	6×10^{-7}
Cross IV	P_h	P12	2×10^{-9}	2×10^{-8}	1×10^{-8}
Cross V	P_i	P13	2×10^{-10}	1×10^{-9}	3×10^{-9}

Table 4.9 – N_2 pressures computed and measured at different positions of the traps. All the pressures are expressed in mbar. The fourth column corresponds to the computed pressures if we consider that $P_b = 1 \times 10^{-3}$ mbar and the fifth if $P_b = 6 \times 10^{-3}$ mbar. The last column corresponds to the measured pressures with the corresponding gauges for $P_b = 6 \times 10^{-3}$ mbar.

As explained later in Section 4.3, we know the N_2 and CO_2 pressures at the injection point, respectively the pressures P5 and P6 in Figure 4.8.

To determine what is the pressure of each gas, we first injected only N_2 and we recorded the corresponding pressures in Cross II and Cross III (respectively P10 and P11). Then, the same was done with only CO_2 and the results are presented in Figure 4.11. It is clear that there are quadratic relations between the pressures and they are fitted as followed:

$$\mathrm{P10} = \mathrm{P5}\left(4.81 \times 10^{-7}\mathrm{P5} + 3.80 \times 10^{-6}\right), \tag{4.2.15a}$$

$$\mathrm{P11} = \mathrm{P5}\left(9.89 \times 10^{-9}\mathrm{P5} + 3.41 \times 10^{-8}\right), \tag{4.2.15b}$$

$$\mathrm{P10} = \mathrm{P6}\left(1.06 \times 10^{-4}\mathrm{P6} + 5.66 \times 10^{-6}\right), \tag{4.2.15c}$$

$$\mathrm{P11} = \mathrm{P6}\left(7.01 \times 10^{-7}\mathrm{P6} + 4.23 \times 10^{-8}\right). \tag{4.2.15d}$$

As shown in Section 4.6, the pressures at the injection points are P5 = 5 mbar and P6 = 0.6 mbar. To determine the N_2 pressure in the second stage, one can consider according to Table 4.9 that there is a ratio of $\frac{20}{3}$ between the pressure in the second stage and the pressure in Cross II. P5 = 6 mbar giving P10 = 4×10^{-5} mbar, the N_2 pressure is estimated at $P_{N_2} = 2.6 \times 10^{-4}$ mbar in the second stage.

For the CO_2 pressure, P6 = 0.6 mbar gives P10 = 4.1×10^{-5} mbar. The CO_2 injection being done directly in Cross II, one can approximate the CO_2 in the second

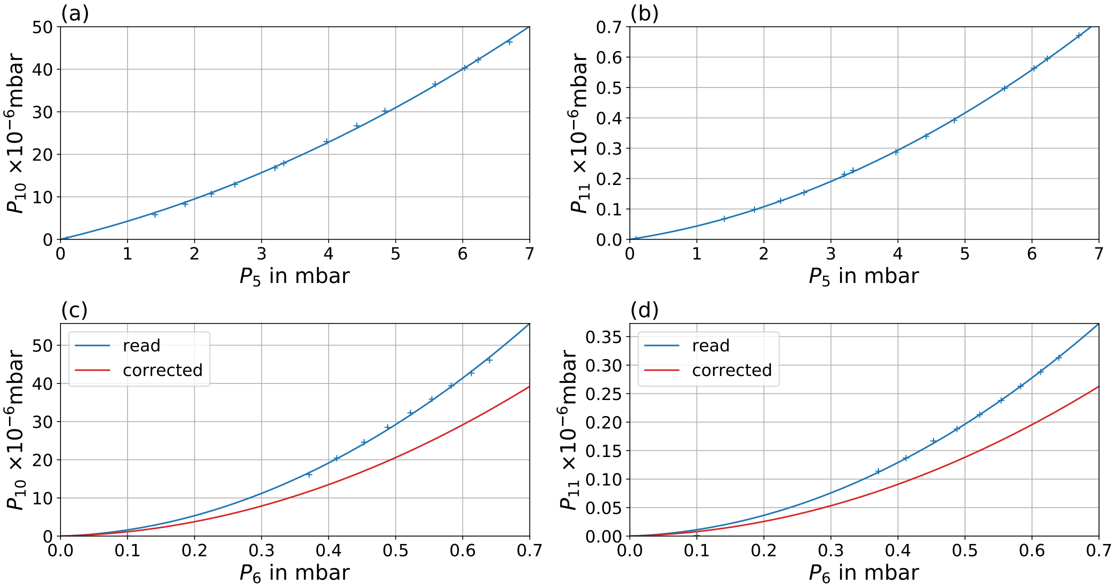

Figure 4.11 – (a) P10 as a function of P5 (only N_2). (b) P11 as a function of P5 (only N_2). (c) P10 as a function of P6 (only CO_2). (d) P11 as a function of P6 (only CO_2). The blue curves correspond to values read with the gauges. The red curves correspond to corrected values according to Ref. [85].

stage with P10. However, the gauges being calibrated for N_2 , a correction factor of 1.42 [85] is applied to obtain the CO_2 pressure. In conclusion, P6 $= 0.6\,$mbar leads to a CO_2 pressure of $P_{\mathrm{CO2}} = 2.9 \times 10^{-5}\,$mbar in the second stage.

To check the consistency of this model, we can compare with the positrons lifetime measured in Ref. [47] and presented in Table 4.3. For a pressure of $P_0 = 2.7 \times 10^{-8}\,$mbar of N_2 or respectively CO_2 , the positrons lifetime are $\tau_{\mathrm{N}_2} = 6300\,$s and $\tau_{\mathrm{CO}_2} = 2400\,$s. Considering that the inverse of the lifetime is proportional to the pressure, then in our situation, we can estimate the lifetime τ with

$$\frac{1}{\tau} = \frac{1}{\tau_{\mathrm{N}_2}} \frac{P_{\mathrm{N}_2}}{P_0} + \frac{1}{\tau_{\mathrm{CO}_2}} \frac{P_{\mathrm{CO}_2}}{P_0} \tag{4.2.16}$$

This gives a lifetime in the second stage $\tau = 0.5\,$s, which is consistent with the lifetime of 0.64 s presented in Section 4.6.

4.3 Trap control

The trap is controlled using Labview programs and National Instrument devices. In the past, all the system was operated from a PXI (combination of a controller and a computer) and CRIOs (controllers) were in charge of the vacuum and magnet control through the PXI. The PXI was also in charge of the electrode control and data acquisition (see Figure 4.14). This has been reorganised in April 2020 and now, a dedicated computer controls the CRIO for the BGT vacuum system and magnets (but also all the vacuum system of the antiproton line) and the PXI is only in charge of the electrode control and the signal acquisition.

4.3.1 Vacuum system and magnets control

To insert N_2 and CO_2 , a P-I-D algorithm was used to control piezo-electric valves (PEV) [48]. The input parameters were the desired pressures in P5 and P6 and the PEV were more or less opened to reach these pressures. Because the PEV were leaking, they have been replaced by Mass Flow Controller [86]. These MFC have an internal PID and the input parameters are the mass-flow and we read the pressures on the graphical interface (Figures 4.12). The graphical interface is presented in Figure 4.12.

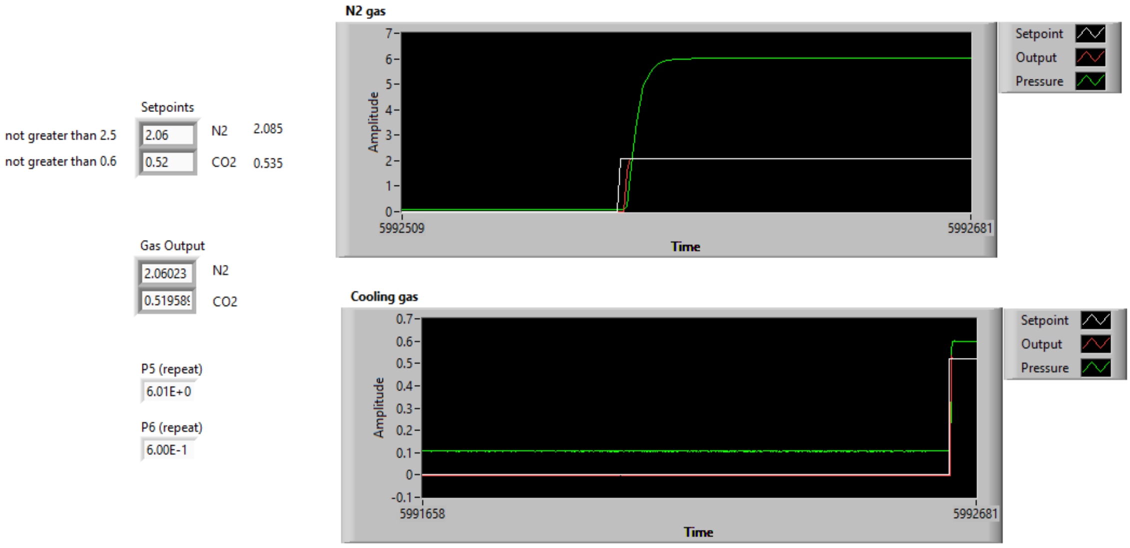

Setpoints
not greater than 2.5 2.06 N2 2.085
not greater than 0.6 0.52 CO2 0.535

Gas Output
2.06023 N2
0.51958(CO2

P5 (repeat)
6.01E+0

P6 (repeat)
6.00E-1

Figure 4.12 – Labview VI to control the Mass Flow Controller. The input parameters are the mass-flow (set-points), and the real mass flow are read (gas output). P5 (N_2 pressure) and P6 (CO_2 pressure) are also shown on the interface.

The pumps, valves, gauges and the magnets are controlled and monitored through the graphical interface presented in Figure 4.13. The CRIOs are in charge of the reading of the different parameters and send all the information to the overwatch computer to display them on the interface. The CRIOs, programmed through FPGA-based programs, are also used for the safety control of the vacuum and services.

4.3.2 Trapping control

The potentials and the data acquisition related to the BGT are controlled by a PXI. It is a National Instrument computer optimised for experiment control and data acquisition. The different elements on the PXI are:

- NI PXIe 8135, a Windows 10 computer to run the Labview programs;
- NI PXIe 6366, an analog input voltage card, to acquire some slow signals;
- NI PXIe 7820R, a digital input/output card, the FPGA program is run on it;
- NI PXIe 5160, an oscilloscope, to acquire some fast signals;

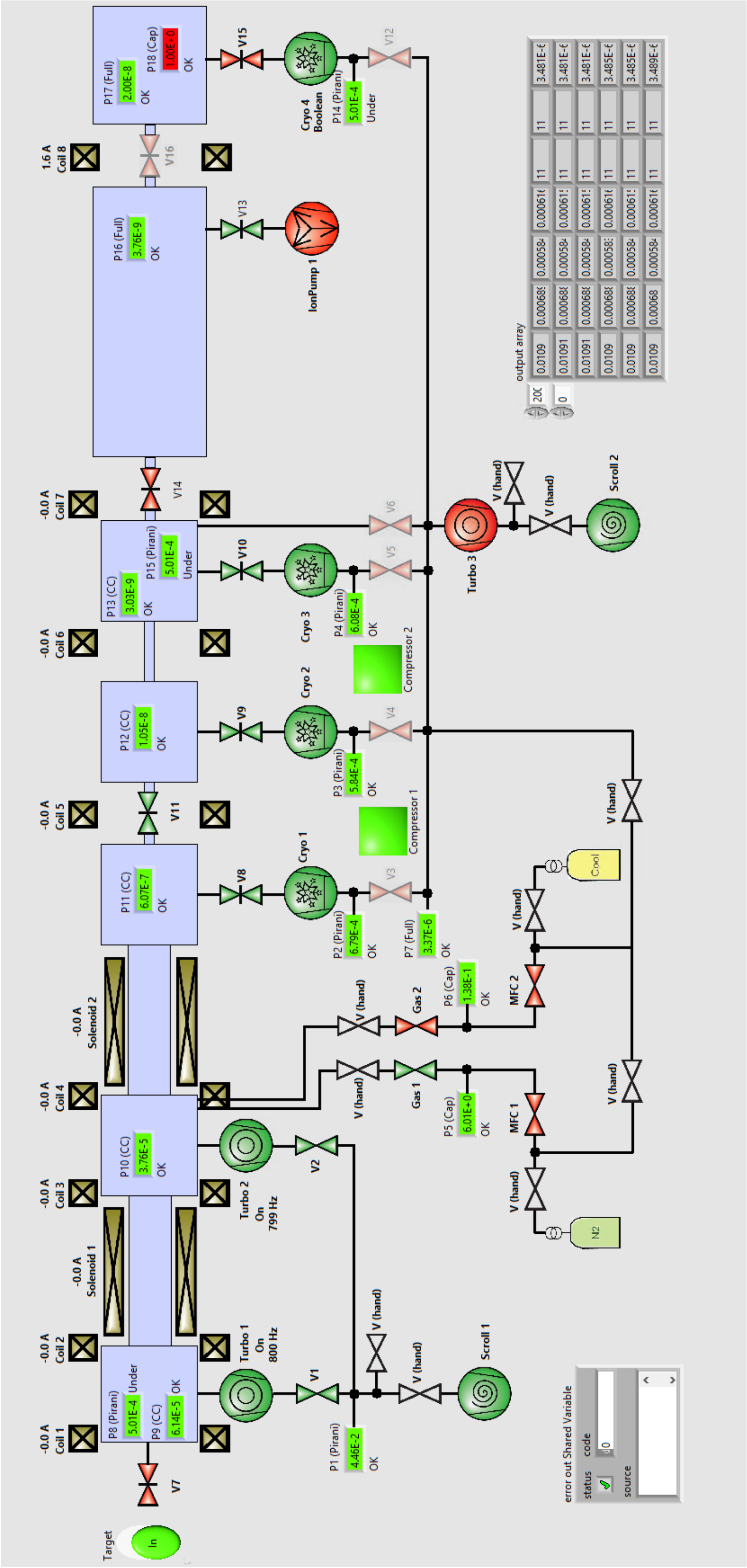

0.0109	0.00068	0.00058	0.00061	11		11		3.481E-
0.01091	0.00068	0.00058	0.00061	11		11		3.481E-
0.01091	0.00068	0.00058	0.00061	11		11		3.481E-
0.0109	0.00068	0.00058	0.00061	11		11		3.485E-
0.0109	0.00068	0.00058	0.00061	11		11		3.485E-
0.0109	0.00068	0.00058	0.00061	11		11		3.489E-

Figure 4.13 – Graphical user interface to control the Buffer Gas Trap magnets, monitor the pressures, and inject gas.

- NI PXI 6733, three analog input voltage cards, to control the High-Voltage Amplifiers;
- NI PXI 8252, a FireWire module to control a PCO camera.

A schematic of this system is presented in Figure 4.14.

To manipulate the positron cloud in the BGT, electric potential has to be set and changed at precise moments. For this purpose sequences are written to specify the potentials on the BGT electrodes. These sequences are written thanks to a Labview program presented in Figure 4.15. Each line of the Sequence Editor has 4 main inputs:

- Duration (**a** in Figure 4.15). This is the duration of the line. If there is no change of the potential and only the output trigger are changed, the minimal duration time is 12.5 ns, corresponding to the maximal speed of the 7820R card. If this duration is set at 0, then it is possible to wait for an input trigger (see last item). If we are changing the potential, the minimal time is 1.35 µs per ramp point, corresponding to the timing properties of the High-Voltage Amplifiers.
- Ramp points (**b** in Figure 4.15). This is the number of step to go from the previous potential profile to the new one, in order to change the potential more or less progressively, as an example, for a positron cloud compression.
- HVA voltages (**c** in Figure 4.15). If ramp point parameter is 1, then the potential profile is the one defined at this line for all the line's duration. If ramp point is greater than one, then the potential will be the one defined here at the end of the line's duration. If ramp point is 0, then the potential remains the previous one for this line and the program does not invite us to define a new potential profile.
- Output triggers (**d** in Figure 4.15). The 7820R card provides an output digital signal corresponding to what has been defined for the duration of the line.
- Input triggers (**e** in Figure 4.15). The system waits and remains with the previous parameters until the 7820R card receives the exact digital input configuration defined here.

The sequence editor provides a text file which can be interpreted by a Labview program (**b** in Figure 4.16). This program converts the text file into an array, defining for each time the configuration of the trap (potentials, triggers, waiting for triggers). The array is sent to a FPGA program running on the 7820R card (**a** in Figure 4.16). This card contacts the other cards to execute the sequence. It is also possible to prepare the execution of several sequences using the program shown in Figure 4.16-**d**. The program defines an array for each sequence and send it to the FPGA program. The rotating wall parameters are defined manually before starting an accumulation procedure (**c** in Figure 4.16).

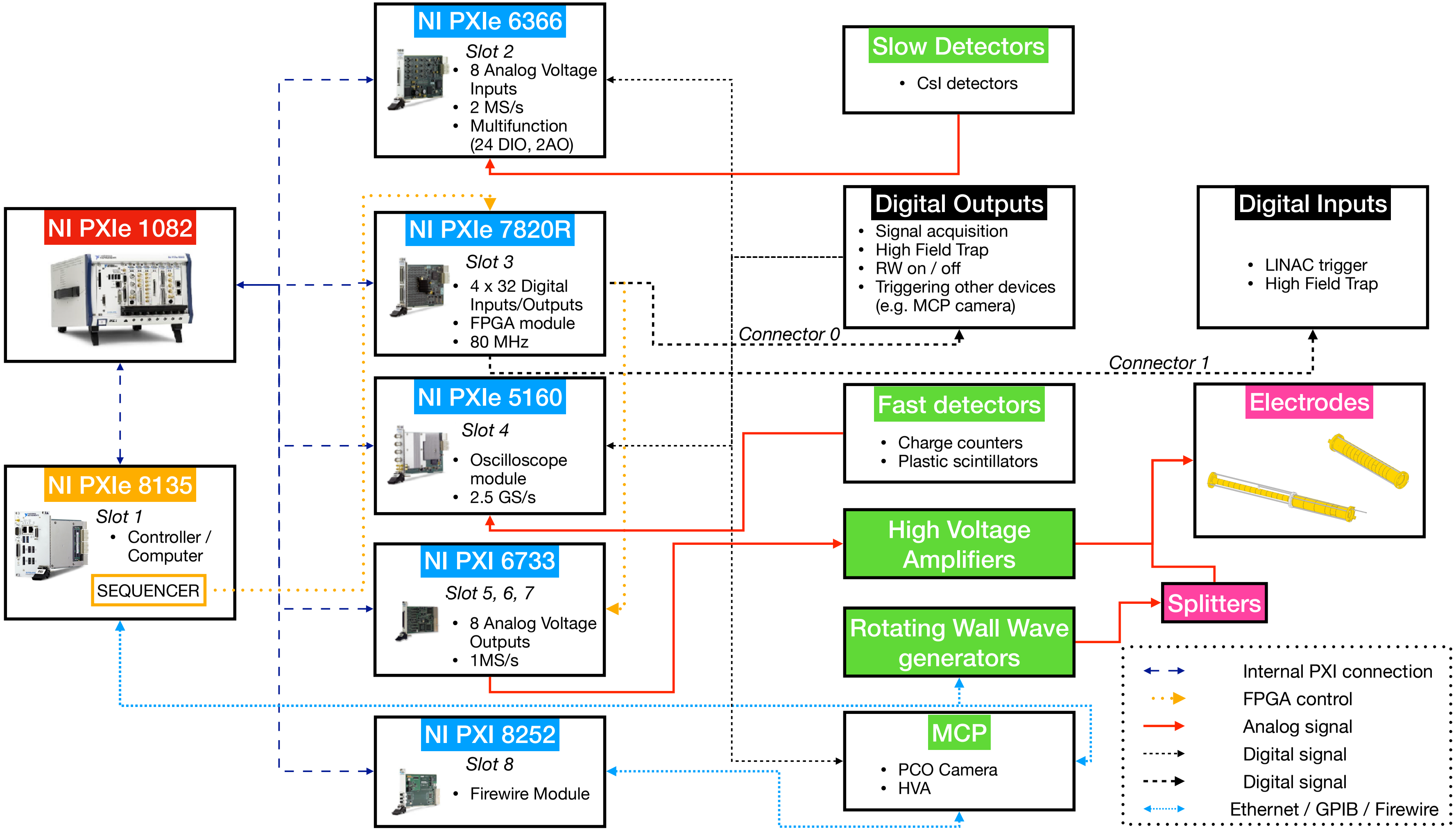

Figure 4.14 – Overview of the connections of the Buffer Gas Trap PXI computer. In order not to overload the schematic, Ethernet, GPIB, and Firewire connections have been merged. The wave generators are controlled through GPIB connections, the PCO camera through a Firewire connection, and the HV for the MCP are controlled using an Ethernet connection.

Total time (s): 1.10731705

selected path: C:\Users\gbar\Documents\Sequence CERN\Stacking_optimization\2019-07-31_SUBSEQ_2_10 stacks to RT - bgt triggered

error out: status ✓ code 0 source

Line	t	Total t	Ramp Points	1	2	3	4	5	6	7	8	9	10	11	12	13	14	15	16	17	18	19	20	21	22	23	24	Comments
0	100.0000	100.0000	1	37.5	26.5	26	25.5	22	21.5	140	60	15.5	15	14.5	10.5	10	140	140	0	0	0	0	0	-140	0	0	0	Accumulate for some time + RW2 + RWRIKEN
1	270.0000	100.2700	200	42.5	32.5	50	40	30	20	140	60	15.5	15	14.5	10.5	10	140	140	0	0	0	0	0	-140	0	0	0	Compress
2	625.0000	100.2706	0	0	0	0	0	0	0	0	0	0	0	0	0	0	0	0	0	0	0	0	0	0	0	0	0	Trigger exit gate second stage
3	1.0000u	100.2716	0	0	0	0	0	0	0	0	0	0	0	0	0	0	0	0	0	0	0	0	0	0	0	0	0	Trigger gate third stage first trap

Figure 4.15 – User interface for the sequence editor. (a) Duration of the line. (b) Number of steps to go from the previous voltage profile to the new one. (c) Voltages of each HVA (to 6366 card). (d) Output triggers (to 7820R card). (e) Input triggers (to 7820R card).

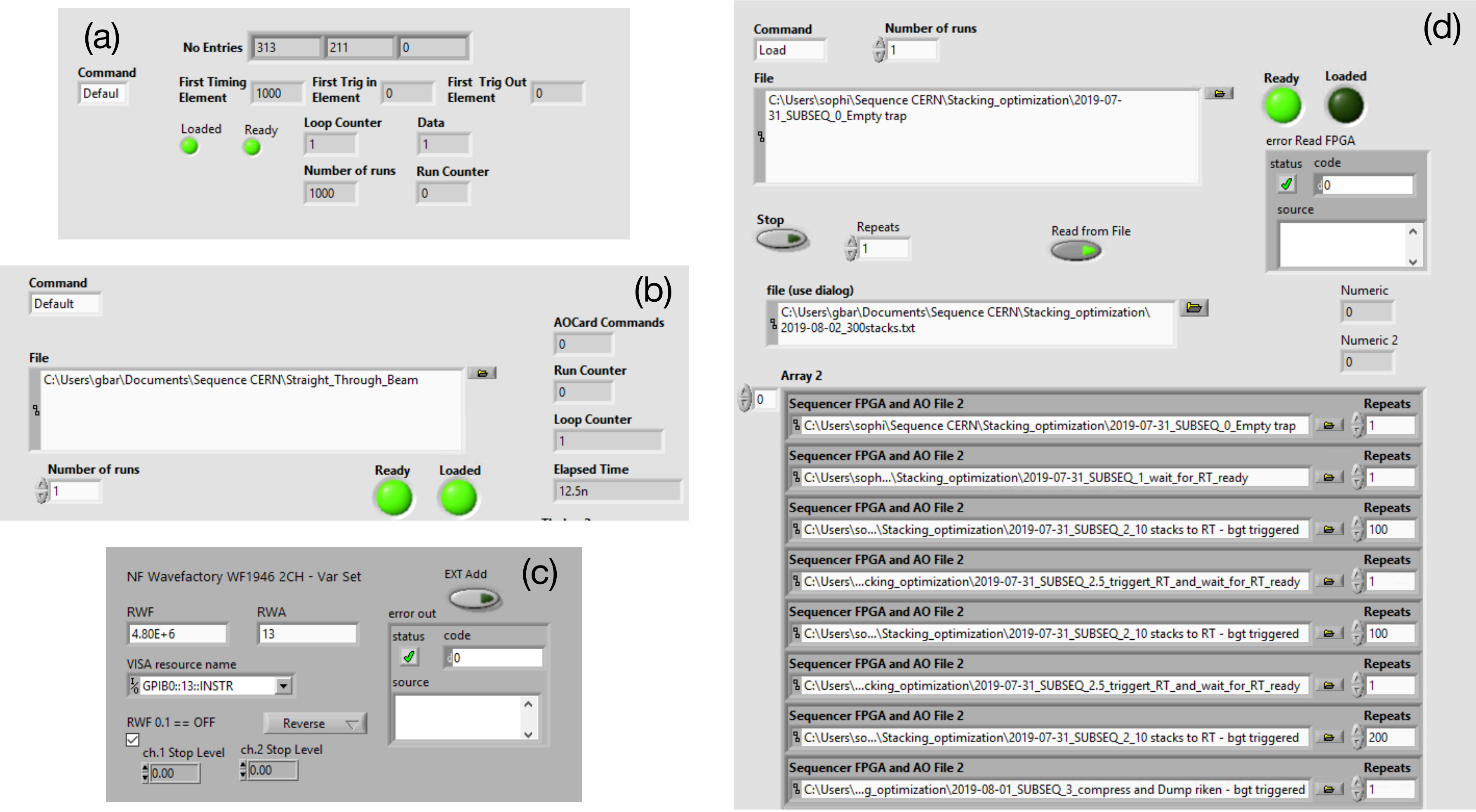

(a)

Command: Defaul
No Entries: 313 211 0
First Timing Element: 1000
First Trig in Element: 0
First Trig Out Element: 0
Loaded ●
Ready ●
Loop Counter: 1
Data: 1
Number of runs: 1000
Run Counter: 0

(b)

Command: Default
File: C:\Users\gbar\Documents\Sequence CERN\Straight_Through_Beam
Number of runs: 1
Ready ●
Loaded ●
AOCard Commands: 0
Run Counter: 0
Loop Counter: 1
Elapsed Time: 12.5n

(c)

NF Wavefactory WF1946 2CH - Var Set
RWF: 4.80E+6
RWA: 13
VISA resource name: GPIB0::13::INSTR
RWF 0.1 == OFF ☑
Reverse
ch.1 Stop Level: 0.00
ch.2 Stop Level: 0.00
EXT Add
error out
status ✓
code: 0
source

(d)

Command: Load
Number of runs: 1
File: C:\Users\sophi\Sequence CERN\Stacking_optimization\2019-07-31_SUBSEQ_0_Empty trap
Ready ●
Loaded ●
error Read FPGA
status ✓
code: 0
source
Stop
Repeats: 1
Read from File
file (use dialog): C:\Users\gbar\Documents\Sequence CERN\Stacking_optimization\2019-08-02_300stacks.txt
Numeric: 0
Numeric 2: 0
Array 2: 0

Sequencer FPGA and AO File 2	Repeats
C:\Users\sophi\Sequence CERN\Stacking_optimization\2019-07-31_SUBSEQ_0_Empty trap	1
C:\Users\soph...\Stacking_optimization\2019-07-31_SUBSEQ_1_wait_for_RT_ready	1
C:\Users\so...\Stacking_optimization\2019-07-31_SUBSEQ_2_10 stacks to RT - bgt triggered	100
C:\Users\...cking_optimization\2019-07-31_SUBSEQ_2.5_triggert_RT_and_wait_for_RT_ready	1
C:\Users\so...\Stacking_optimization\2019-07-31_SUBSEQ_2_10 stacks to RT - bgt triggered	100
C:\Users\...cking_optimization\2019-07-31_SUBSEQ_2.5_triggert_RT_and_wait_for_RT_ready	1
C:\Users\so...\Stacking_optimization\2019-07-31_SUBSEQ_2_10 stacks to RT - bgt triggered	200
C:\Users\...g_optimization\2019-08-01_SUBSEQ_3_compress and Dump riken - bgt triggered	1

Figure 4.16 – Graphic user interfaces running on the PXI computer. (a)The FPGA program. (b) Labview VI to load/run/abort a sequence. (c) . Labview VI to set the rotating wall wave generator (d). Labview VI to load/run/abort multiple sequences.

4.4 Positron detection

4.4.1 Micro-Channel Plate

A Micro-Channel Plate (MCP) is an electron multiplier. It allows to detect charged particles and is generally combined with a charge collector, or a phosphor screen to obtain the position of the particles.

A typical MCP [87] is a disk composed of 10^4-10^7 miniature electron multipliers channels, parallel one to another. The channels have a diameter around 10 µm-100 µm. The MCP is made of lead glass and the faces are covered by a metallic layer to create an electric field between the entrance and the exit of the MCP. This field determines the gain of the MCP, as well as α the ratio between the length and the diameter. Indeed, in the case of a single straight channel, the gain is

$$G = \left(\frac{AV}{2\alpha\sqrt{V_0}} \right)^{4V_0\alpha^2/V}, \tag{4.4.1}$$

with V, the potential between the faces, V_0 the initial energy of a secondary electron ($\sim 1\,\mathrm{eV}$), and A a proportionality constant. To increase the gain, it is also possible to use MCP in series. Thus, an incident charged particle at the front induces an electron shower in a channel, and the position of the incident particle can be determined if the MCP is followed by a phosphor screen (or the number of incoming particles if the gain is known). The electron shower can also create positive ions, depending on the residual gas pressure at the MCP location. This could reduce the measurement precision. To prevent this problem, the channels are generally inclined (typically 8°) as it is presented in Figure 4.17.

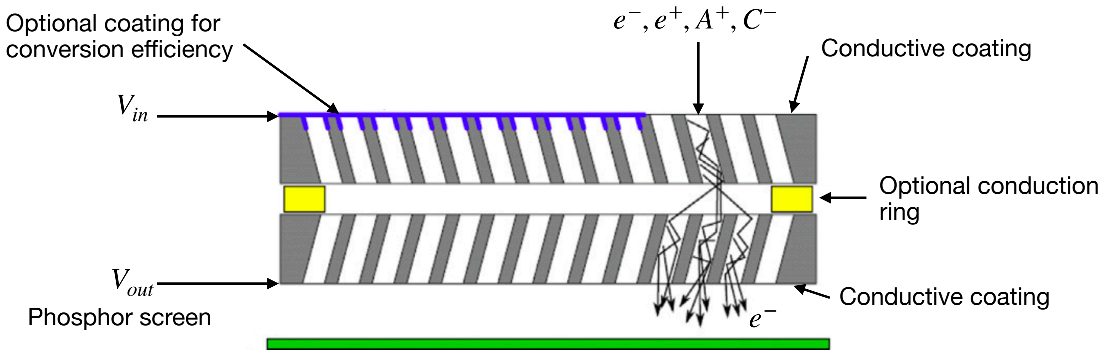

Figure 4.17 – Extracted from Ref. [88]. Schematic layout of an MCP Chevron stack, with two micro-channel plates and a phosphor screen.

In our case, we use a Chevron MCP manufactured by Photonis. These MCP have a diameter of 40 mm with channels of 10 µm to get a maximal gain of 10^7. A phosphor screen is place right after the MCP to obtain spots with a light proportional to the number of electrons coming out of each channel. The image of the spots on the phosphor screen can be collected to obtain physical information such as the radial density (the MCP conserving the radial density of the incoming particles, especially with a short response time below 100 ps). Thus, a mirror is placed at

40° as presented in Figure 4.18, and a PCO camera (16 bit CCD low noise cooled camera) can take a picture. It is possible to take a picture because the decay time of the phosphor screen is 80 µs [48].

The MCP support presented in Figure 4.18, only used at the exit of the BGT, has also a grid to repel negative particles with a potential. The fixation on the top allows us to vertically place the MCP with a retractable linear drive. Similar supports are used at different location of the GBAR experiment, except they do not have a grid and are placed by a push-pull system at the bottom of the MCP. Also, simpler CCD cameras are used (Baumer Camera).

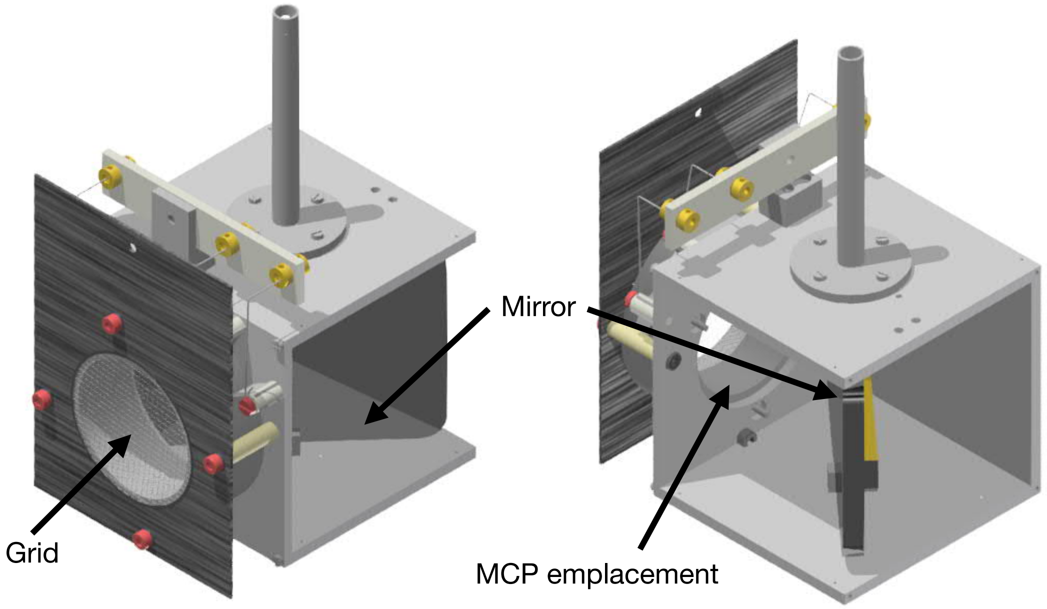

Figure 4.18 – Drawing of the MCP support at the exit of the BGT.

4.4.2 CsI detector

A CsI(Tl) detector (Caesium Iodide doped with Thallium) is a common scintillation based detector used for positron detection in a destructive way. Indeed, gamma rays resulting from positron annihilations can be seen by such detectors, allowing to determine the presence of positrons, and if calibrated, to deduce the number of annihilated positrons.

The principle of a scintillator is based on the property of luminescence. When a luminescent material is hit by an incoming particle (in our case a gamma ray), the energy is absorbed and light is emitted. This light can be converted into an electrical signal using a photomultiplier or a photodiode. It is about to use the appropriate material to detect the desired particle.

In our case, we use CsI(Tl) crystals with PIN diodes associated to a preamplifiers. This assembling is adapted to the gamma ray detection because the crystal produce a large light output (56γ/keV [89, 48]). Moreover, the use of PIN diodes is possible because CsI(Tl) has an emission spectrum (around 550 nm), which fits the absorption spectrum of silicon [90].

4.5 Electron repeller

To produce positrons for $\overline{\mathrm{H}}^+$ formation, 9 MeV electrons originating from the LINAC impinge on a tungsten target where the antiparticles are created by bremsstrahlung radiation ($e^- + Z \rightarrow e^- + Z + \gamma$), followed by γ conversion. A tungsten mesh moderator slows the positrons down to a fixed energy (3 eV for Tungsten) to a mono-energetic beam with an energy width of a few eV. The positrons are extracted at 50 eV.

Electrons, with an energy between 0 and few keV follow the same magnetic transport lines as the positrons and disturb positron trapping. Indeed, the electrons ionise the buffer gases, preventing the inelastic collisions required for the trapping to occur.

To remove the electrons, an initial electron repeller had been placed just before the Buffer Gas Trap (see Section 4.5.1). This repeller consists in a grid where a high voltage is applied. In June 2020, it has been replaced by a second repeller (see Section 4.5.2) composed of a set of 31 electrodes, connected together using resistors.

4.5.1 Electron repeller version 1

The electron repeller, as shown in Figure 4.19 consists of a tungsten grid (90% transparency) mounted in such a way that a negative potential can be applied. If the voltage is low enough, the electrons are repelled. However, when using large negative voltages, locally the positrons are accelerated in a non adiabatic way, which has an effect on their energy spread and consequently on the trapping rate.

Figure 4.19 – Picture of the electron repeller. A negative potential is applied on the grid to repel the electrons.

To estimate the electron number per LINAC pulse, a metallic plate at the entrance of the Buffer Gas Trap (BGT) has been connected to an oscilloscope with a total capacitance $C = 320\,\mathrm{pF}$. With a grounded potential on the repeller, a 107 mV peak height is detected on the oscilloscope, which corresponds to 2.14×10^8 electrons per LINAC pulse. The number of electrons per linac pulse decreases with decreasing voltages on the repeller down to $-5\,\mathrm{kV}$, as can be seen in Figure 4.20.

Electrons are no more detected above 2 kV. Then, a potential above 2 kV should improve positron trapping.

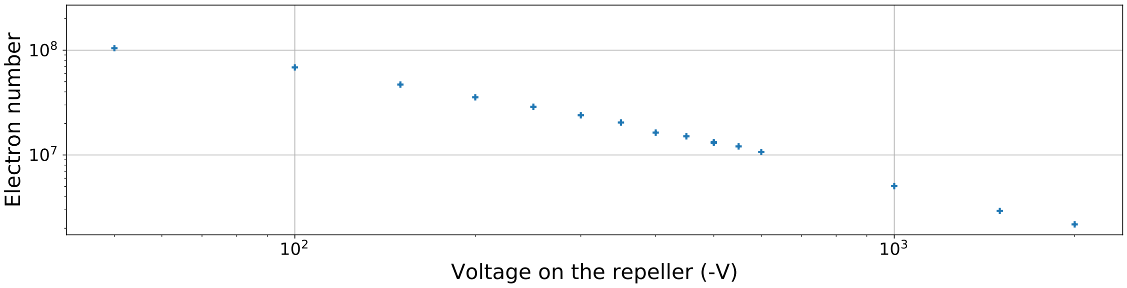

Figure 4.20 – Electron number as a function of the potential on the electron repeller at the entrance of the Buffer Gas Trap. LINAC frequency: 2 Hz.

To determine the positron energy distribution right after the repeller, a potential barrier is applied on the first BGT electrodes. CsI crystals detect the gamma rays resulting from the annihilation of the positrons when they intercept a metallic plate placed at the exit of the BGT. Their signals are collected for different potentials on the repeller. The results are presented in Figure 4.21-a. Assuming the energy distribution is gaussian, the signals are fitted with an error function. The corresponding energy distributions are shown in Figure 4.21-b, where we clearly observe that the mean value and the spread of energy is significantly influenced by the repeller voltage.

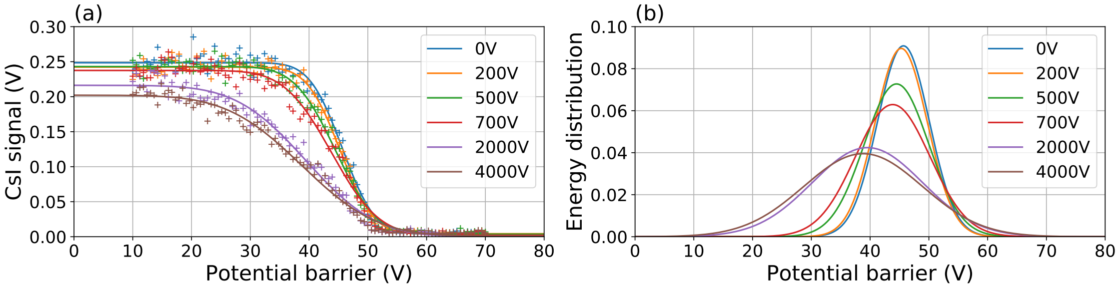

Figure 4.21 – (a) CsI signal for a straight through beam at the exit of the Buffer Gas Trap as a function of a potential barrier at the entrance of the trap for different potentials on the repeller. (b) Corresponding energy distribution. LINAC frequency: 200 Hz.

A smaller energy spread is required to gain better trapping rate in the BGT. Figure 4.22-a shows that the energy spread is increasing with the potential on the repeller (up to 3 kV, it is slightly decreasing after this point). Thus, an optimum has to be found between the electron number and the spread of energy. Furthermore, Figure 4.22-b shows that the mean energy decreases with the amplitude of the potential on repeller, which is also correlated with a loss of positrons as shown in Figure 4.22-c.

To determine the trapping rate, positrons are accumulated for 100 ms in the second stage and then dumped on a plate at the exit of the BGT (see more details

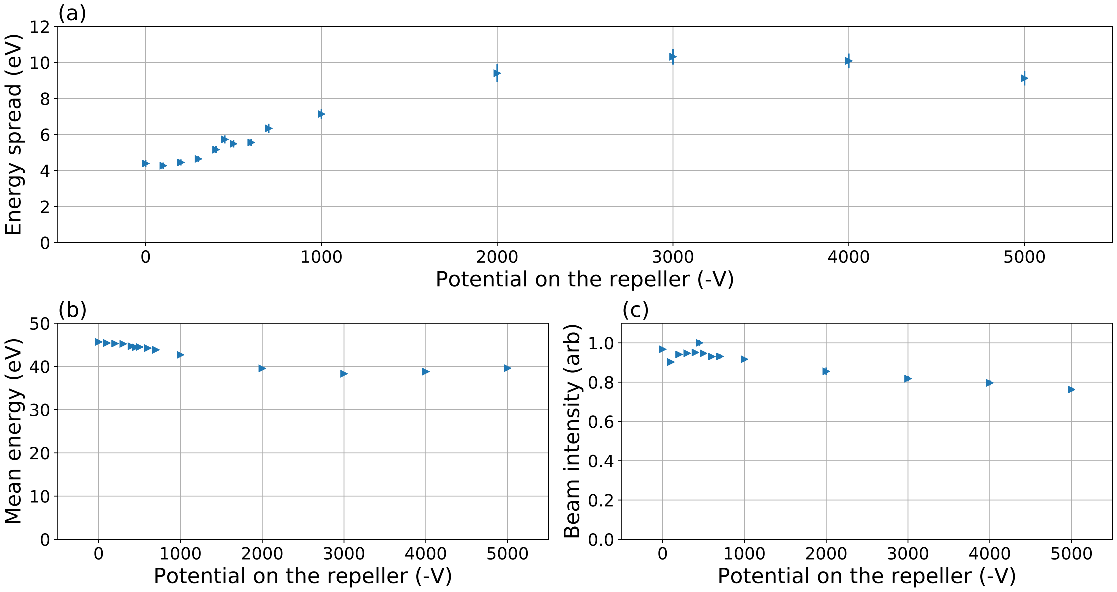

Figure 4.22 – Parameters of the gaussian fit $A\exp -\frac{1}{2}\left(\frac{V-V_0}{\sigma}\right)^2$ (corresponding to Figure 4.21). (a) Energy spread σ of a straight through beam at the exit of the Buffer Gas Trap as a function of the potential on the central electrode of the electron repeller. (b) Mean energy V_0. (c) Beam intensity A. LINAC frequency: 200 Hz.

on the positron accumulation in Section 4.6). The corresponding CsI signal thereby obtained is proportional to the trapping rate ($N = R\tau\left[1 - e^{-100\,\mathrm{ms}/\tau}\right]$, with N the positron number in the trap, R the trapping rate and τ the lifetime). The results for different potentials on the repeller are presented in Figure 4.23. This figure clearly shows an optimum for the trapping rate around 500 V on the repeller. As we could expect, it corresponds to a voltage providing a small energy spread with few remaining electrons (see Figure 4.24).

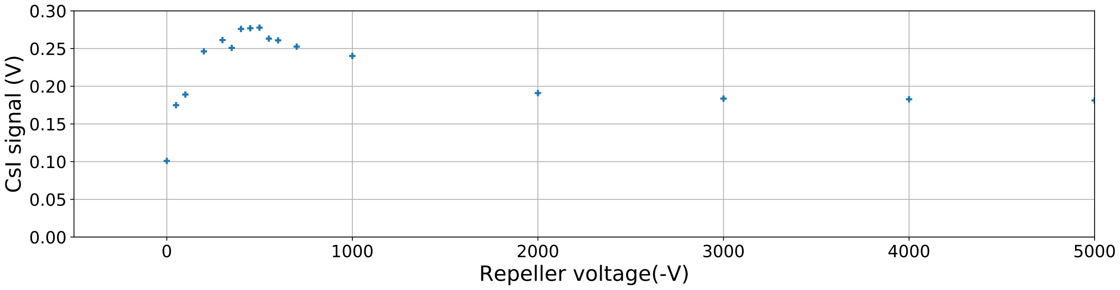

Figure 4.23 – CsI signal after accumulation in the Buffer Gas Trap's second stage for 100 ms as a function the potential on the repeller. LINAC frequency: 200 Hz.

The number of positrons in the second stage of the BGT is measured as a function of accumulation time for different voltages of the repeller. The lifetime of accumulated positrons is then measured as a function of the voltage on the repeller grid (Figure 4.25-b). It is clear that the remaining electrons have no effect for a potential above 500 V on the repeller.

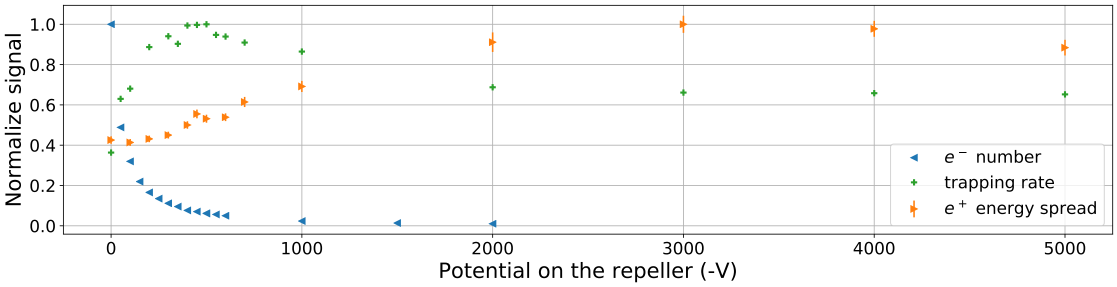

Figure 4.24 – Superposition of the curves from Figures 4.20, 4.22 and 4.23. LINAC frequency: 200 Hz.

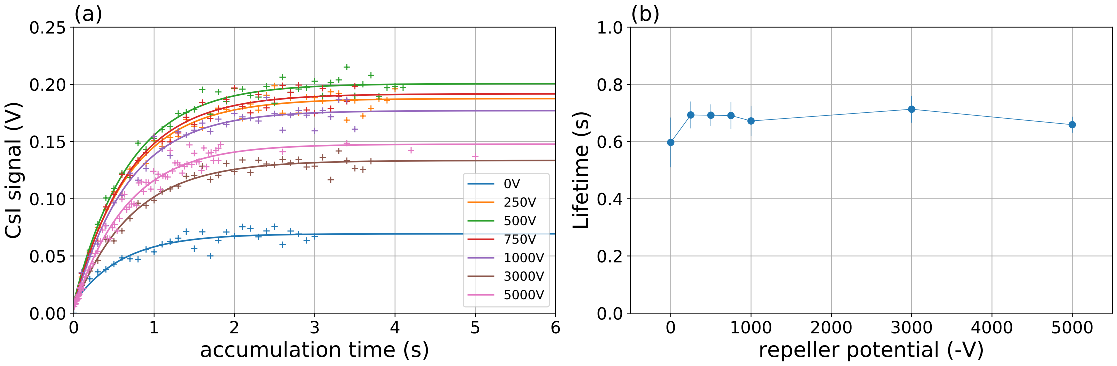

Figure 4.25 – (a) positron accumulation curves in the BGT's second stage for different potentials on the repeller. (b) Corresponding positron lifetimes. LINAC frequency: 200 Hz.

4.5.2 Electron repeller version 2

As illustrated in Figure 4.22, the electron repeller has an impact on the energy spread because of the non adiabatic transport of the positrons through the grid, influencing the trapping rate. Also, the presence a grid at the entrance of the trap is responsible for a loss of incoming positrons. Therefore, the electron repeller has been replaced (see Figure 4.26) with one which is composed of a set of 31 electrodes with 28.4 mm length and 61 mm inner diameter to create a more gradual field change.

Figure 4.26 – Pictures of the new electron repeller. The repeller is composed of a set of electrodes connected with resistors. The connection to the power supply is made at the center and the electrodes at the extremities are grounded.

Therefore, the electrodes are connected together with 4.7 MΩ resistors. The central electrode is connected to a high voltage power supply and the electrodes at the extremities are grounded. This is equivalent to the electrical circuit drawn in Figure 4.27.

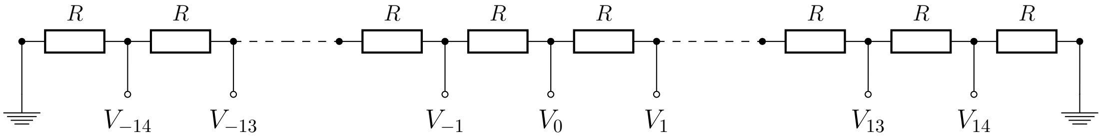

Figure 4.27 – Repeller circuit. V_0 corresponds to the potential on the center electrode defined with a high voltage power supply. $V_{\pm i}$ are the potentials on the electrodes with $V_{\pm 15} = 0\,\mathrm{V}$ because the electrodes at the extremities are grounded.

The potential V_i can then be determined as a function of the potential on the central electrode as:

$$V_i = \frac{15-i}{15} V_0, \quad i \in \{1, \cdots, 15\}. \tag{4.5.1}$$

The potential profile in the repeller is drawn in Figure 4.28.

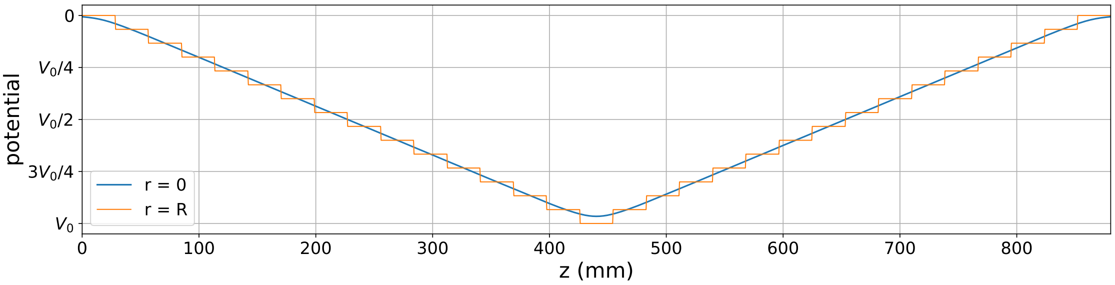

Figure 4.28 – Electric potential at the center of the repeller and on the electrodes. For each electrode, $R = 30.5\,\mathrm{mm}$ and $L = 28.4\,\mathrm{mm}$, with R the radius and L the length.

Using the new repeller, the same experiments as in Section 4.5.1 have been performed. Figure 4.29 shows that for electrons a similar effect is obtained and below $-1\,\mathrm{kV}$ a large part of the electrons are repelled.

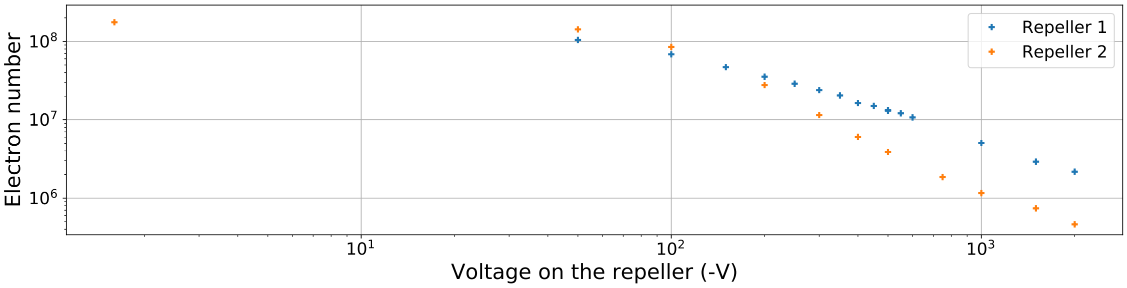

Figure 4.29 – Electron number at the entrance of the Buffer Gas Trap as a function of the potential on the central electrode of the electron repeller. LINAC frequency: 2 Hz.

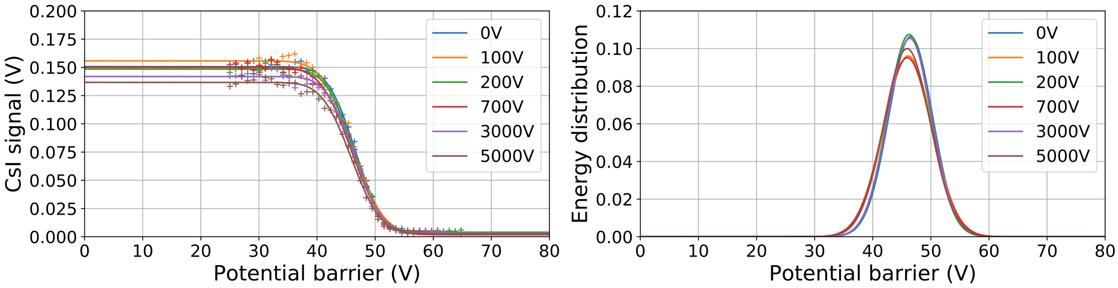

Figure 4.30 – Right: CsI signal for a straight through beam at the exit of the Buffer Gas Trap as a function of a potential barrier at the entrance of the trap for different potentials on the central electrode of the repeller. Left: Corresponding energy distribution. LINAC frequency: 200 Hz.

The positron energy distribution stays more or less the same no matter the potential applied on the electron repeller as presented in Figure 4.30.

In more detail, one can see that the width parameter of the gaussian fit remains constant around 4 eV as shown in Figure 4.31-a. So, the electron repeller can only improve the trapping efficiency, because it removes the electron, without disturbing the energy distribution of the positrons. Also, the mean value of the energy remains perfectly constant with the potential on the repeller (Figure 4.31-b). However, the intensity is still decreasing, but less than with the previous repeller (Figure 4.31-c).

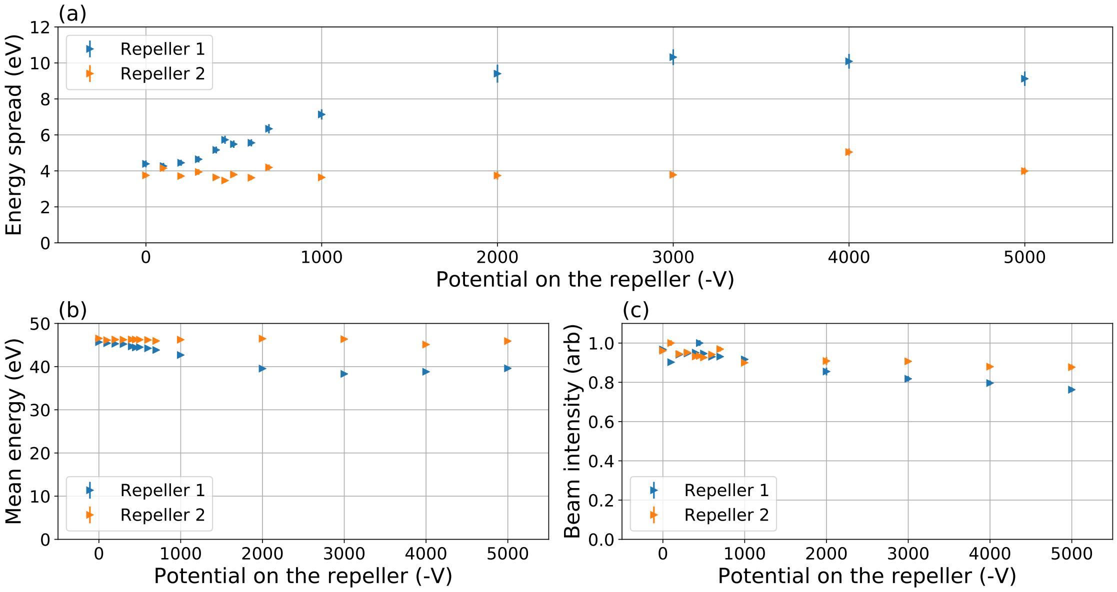

Figure 4.31 – Parameters of the gaussian fit $A\exp -\frac{1}{2}\left(\frac{V-V_0}{\sigma}\right)^2$ (corresponding to Figure 4.30). (a) Energy spread σ of a straight through beam at the exit of the Buffer Gas Trap as a function of the potential on the central electrode of the electron repeller. (b) Mean energy V_0. (c) Beam intensity A. LINAC frequency: 200 Hz.

Therefore, there is no more optimum of the trapping rate with this new repeller. As presented in Figure 4.32, this rate increases with the potential on the central electrode of the electron repeller and stabilised around −1 kV. It is clear in Figure 4.32 that the trapping rate is only influenced now by the electron flux.

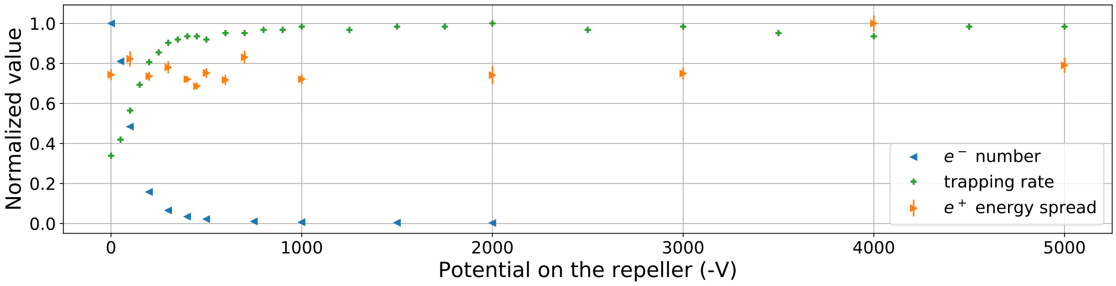

Figure 4.32 – Electron flux, positron trapping rate in the Buffer Gas Trap's second stage and positron energy spread as a function of the potential on the central electrode of the electron repeller. LINAC frequency: 200 Hz.

Similarly to what we had with the former repeller, except for 0 V, the lifetime is independent of the potential applied to repel electrons. This can be seen in the results presented in Figure 4.33.

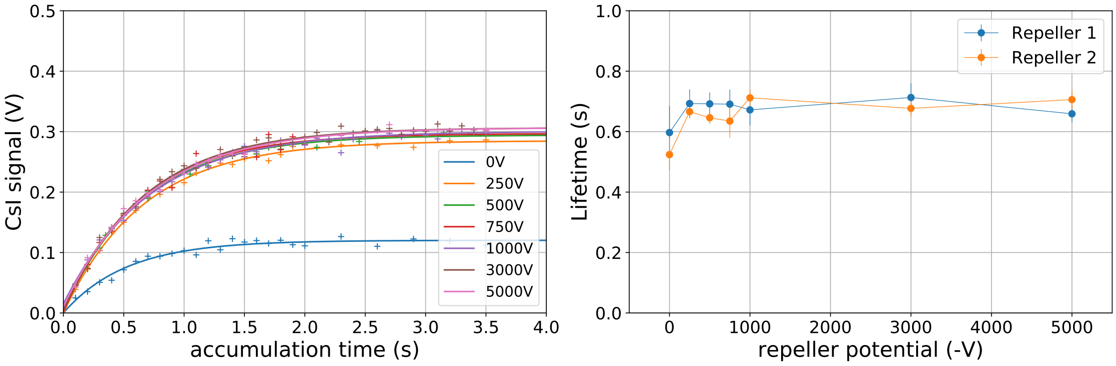

Figure 4.33 – Right: positron accumulation curves in the BGT's second stage for different potentials on the central electron of the repeller. Left: Corresponding positron lifetimes. LINAC frequency: 200 Hz.

This repeller should thus be used with a potential of at least −1 kV to prevent from non adiabatic acceleration, the electrons being removed without losing trapping efficiency. For the rest of the experiment, the potential is set at −5 kV.

4.6 Accumulation in the first and second stages

The first stage of the trap is where the pressure is the highest in the BGT ($\sim 10^{-3}$ mbar), the goal is to make the positrons lose energy by electronic excitation of the N_2 gas molecules (the positron kinetic energy at the entrance of the trap is ~ 50 eV). Then the coolest positrons can be trapped in the third stage, where they are further cooled by CO_2 gas (lower gas pressure of $\sim 10^{-4}$ mbar).

4.6.1 Gas parameters

The first step of the optimisation of the trapping process focusses on the trapping rate. As explained in the introduction of the BGT principle (Section 4.1), it is known that the best trapping gas is N_2 , but it is not a good cooling gas, the best being SF_6 [47, 72, 71]. However for safety reasons CO_2 is used as cooling gas instead in our experiment. To determine the effect of the gas on the trapping rate, the N_2 and CO_2 pressures were varied in the system, while the number of positrons accumulated in the second stage for different amount of time was measured.

The potential profile used for positron accumulation in the BGT's first and second stages are shown in Figures 4.34a-b. The first stage is a long section where the potential is slowly decreasing. It is followed by the second stage where a potential well traps the positrons. After an accumulation time t, the positron cloud is sent to the MCP at the exit of the trap (Figure 4.34c). The potentials applied on the electrodes are presented in Table 4.10.

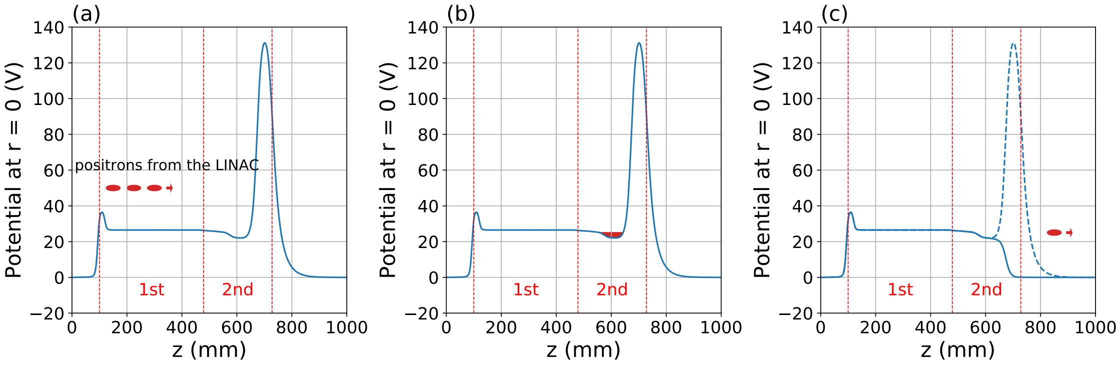

Figure 4.34 – Potential profiles used in the Buffer Gas Trap first and second stages. The coloured areas represent the positrons. (a) & (b) Accumulation of the incoming positrons from the LINAC. (c) Ejection of the positrons.

Electrode	E_0	E_F	E_1	E_2	E_3	E_4	E_5
Accumulation	37.5 V	26.5 V	26 V	25.5 V	22 V	21.15 V	140 V
Ejection	37.5 V	26.5 V	26 V	25.5 V	22 V	21.15 V	0 V

Table 4.10 – Voltage used for positron accumulation in the Buffer Gas Trap's first and second stages. The electrode names refer to Table 4.4.

The gamma rays resulting from positron annihilation on the MCP at the exit of the BGT are detected with CsI detectors. As the peak height of a CsI detector signal is proportional to the number of annihilated positrons, a linear calibration can be performed with a charge counter A230CF CoolFet [91]. This charge counter provides a 0.64 µV step output voltage per detected charge. It is biased at 20 V to prevent from secondary electron ejection leading to an overestimate of the charge.

The first CsI counter is placed a few cm from the valve located before the MCP, and the second one is placed about 1 meter above. The number of positrons is varied by changing the frequency of the LINAC, and the resultant change in CsI signal can be used to determine the correlation between CsI signal and number of positrons. The result is presented in Figure 4.35, and the following cross calibration is obtained:

$$V_1 = 1.69(2) \times 10^{-6}\,\mathrm{V/e^+} \tag{4.6.1}$$

$$V_2 = 1.48(2) \times 10^{-7}\,\mathrm{V/e^+} \tag{4.6.2}$$

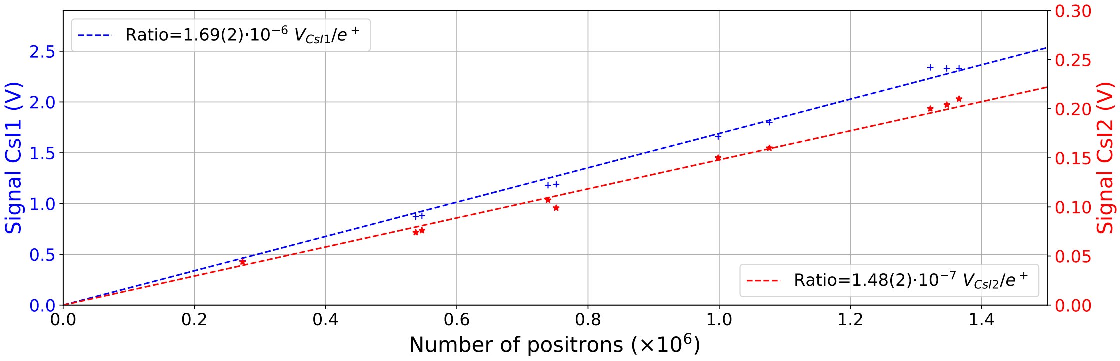

Figure 4.35 – CsI signal as a function of the number of positrons measured by the charge counter (0.64 µV/e^+).

The variation of the number of trapped positrons N per unit time decreases proportionally to the number of positrons in the trap, with a characteristic time τ, the lifetime. The incoming flux of positrons is characterised by R, the trapping rate. Then the differential equation for the number of positrons reads

$$\frac{\mathrm{d}N}{\mathrm{d}t} = -\frac{N}{\tau} + R, \tag{4.6.3}$$

which leads to

$$N(t) = R\tau\left(1 - e^{-\frac{t}{\tau}}\right). \tag{4.6.4}$$

If $t \ll \tau$, then $R(t) = Rt$, which means that we are in a linear regime and the accumulated positrons are not yet annihilated in the second stage. The goal is to maximise R, keeping τ large enough to remain in a linear regime, knowing that once the positrons are accumulated in the second stage, they can be transferred and stored in the third stage for a longer time.

N_2 effect

The role of N_2 pressure on positron trapping is tested by accumulating positrons for different durations and for different N_2 pressures. The results of these accumulations are presented in Figure 4.36a. One can clearly see in Figure 4.36b-c that the trapping rate R and the inverse of the positrons lifetime τ^{-1} are proportional to the N_2 pressure. Considering that we want to have R as large as possible, it would have been interesting to see how R evolves with higher pressures. However, it is not possible to inject more gas for protecting the LINAC. Therefore, the N_2 pressure in the second stage is set at $P_{N_2} = 2.67 \times 10^{-4}$ mbar for the rest of the experiment, corresponding to $P_5 = 6$ mbar according to Section 4.2.4, (P_5 pressure at the N_2 injection point, see Figure 4.8). This value of P_{N_2} corresponds to the best trapping efficiency within the acceptable range of gas pressure for safe LINAC operation. In these conditions, the trapping rate is $R = 0.82(3) \times 10^6\,\mathrm{e^+\,s^{-1}}$, and the lifetime is $\tau = 0.175(6)$ s.

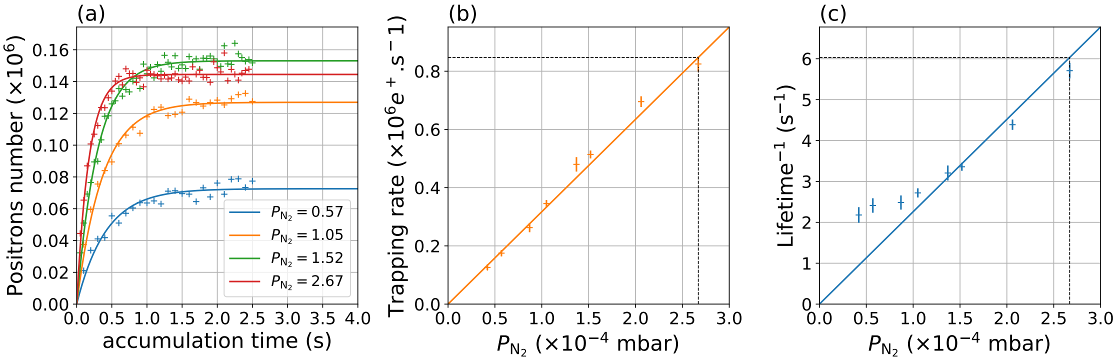

Figure 4.36 – (a) Accumulation curves for different N_2 pressures (in 10^{-4} mbar). (b) Trapping rate as a function of the N_2 pressures. (c) Inverse of the lifetime as a function of the N_2 pressures. LINAC frequency: 200 Hz.

CO_2 effect

Once the N_2 pressure is set, the impact of CO_2 pressure on positron trapping is tested following the same procedure as for N_2. Once again, the trapping rate and the inverse of the lifetime as a function of the CO_2 pressure are linear functions. The only limit is the LINAC safety, then the CO_2 pressure in the second stage is set at $P_{CO_2} = 0.29 \times 10^{-4}$ mbar for the rest of the experiment, corresponding to $P_6 = 0.6$ mbar according to Section 4.2.4. In these conditions, the trapping rate is $R = 1.60(5) \times 10^6\,\mathrm{e^+\,s^{-1}}$, and the lifetime is $\tau = 0.124(4)$ s.

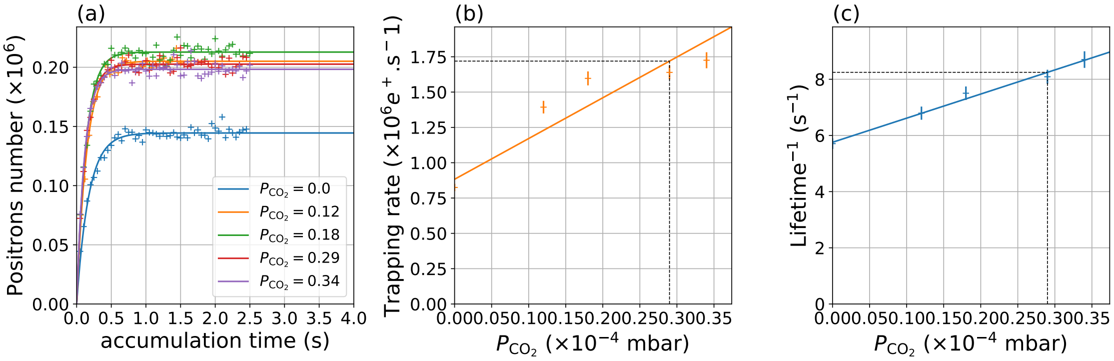

Figure 4.37 – (a) Accumulation curves for different CO_2 pressures (in 10^{-4} mbar). (b) Trapping rate as a function of the CO_2 pressures. (c) Inverse of the lifetime as a function of the CO_2 pressures. $P_{N_2} = 2.67 \times 10^{-4}$ mbar. LINAC frequency: 200 Hz.

In the next section, it will be shown that the best Rotating Wall parameters in the second stage are (1 V, 2.4 MHz). In that case, as determined from the accumulation curve presented in Figure 4.38, the trapping rate is increased up to $R = 2.30(4) \times 10^6\,\mathrm{e}^+\,\mathrm{s}^{-1}$, and the lifetime up to $\tau = 0.639(11)\,\mathrm{s}$. This is why in the rest of the experiment positrons are accumulated in the second stage for 100 ms, to stay in the linear regime.

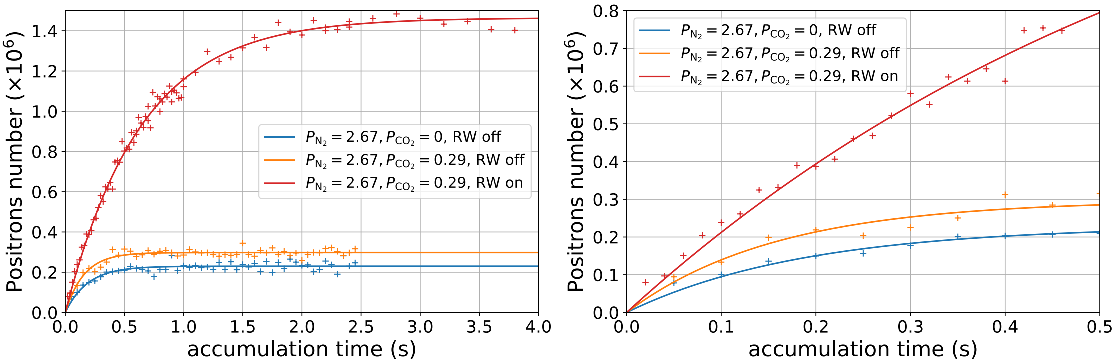

Figure 4.38 – Accumulation curves for different CO_2 and N_2 pressures (pressures in 10^{-4} mbar). Rotating Wall parameters: 1 V, 2.4 MHz. LINAC frequency: 200 Hz.

To be able to increase the trapping rate by increasing the gas pressure, an extra pumping station will be inserted between the LINAC and the BGT.

4.6.2 Rotating Wall optimisation

Once the positrons accumulated in the Buffer Gas Trap second stage, we would like to compress them radially and to store them in the BGT's third stage before sending them into the HFT and increase the lifetime. The Rotating Wall technique (RW), as presented in Section 3.3.2 is used for this purpose.

If the particles are considered in a single particle regime the best compression occurs when RW the frequency is $f_{\mathrm{RW}} = f_z + f_m$ (Section 3.3.2), with f_m the magnetron frequency (defined in Section 3.1.2) and f_z the inverse of the time it takes for a particle to make a round trip in the well.

For a particle in an electric field ϕ, its energy E and its velocity v are related according to

$$E = q\phi(z) + \frac{1}{2}mv^2, \tag{4.6.5}$$

with m and q the mass and the charge of the particle. If E is in eV and the particle is a positron, the relation becomes

$$qE = q\phi + \frac{1}{2}mv^2. \tag{4.6.6}$$

Then, if the particle is moving along the z-axis, $v = \frac{\mathrm{d}z}{\mathrm{d}t}$ and Equation 4.6.6 becomes

$$\mathrm{d}t = \sqrt{\frac{m}{2q}}\frac{\mathrm{d}z}{\sqrt{E - \phi(z)}}. \tag{4.6.7}$$

Defining z_1 and z_2, the positions where $E = \phi$, f_z can be determined by integration such as

$$\frac{1}{f_z(E)} = \sqrt{\frac{m}{2q}} \int_{z_1}^{z_2} \frac{\mathrm{d}z}{\sqrt{E - \phi(z)}}. \tag{4.6.8}$$

The computation of the RW frequency has been performed for different E and the result is presented in Figure 4.39b. For the computation of f_m, we use $B = 0.045\,\mathrm{T}$. According to this computation, we expect that the best compression occurs for $f_{\mathrm{RW}} \sim 3\,\mathrm{MHz}$.

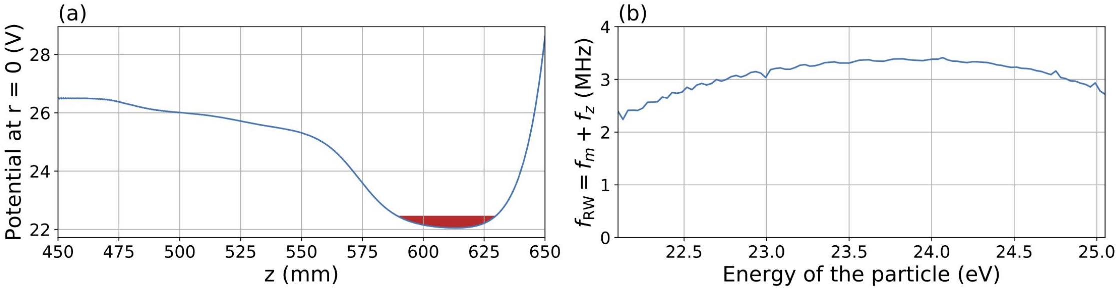

Figure 4.39 – (a) Potential well used to accumulate positrons. The coloured area represents the positrons. (b) Predicted RW frequencies as a function of the energy of the particle.

To determine the best RW parameters, after 100 ms accumulation, the positron cloud is dumped on an MCP at the exit of the BGT and a picture of the phosphor screen is taken. The x and y profiles are then fitted with gaussian distributions, as presented in Figure 4.40 (RW parameters: 2.4 MHz, 1 V, MCP parameters: $V_{\mathrm{grid}} = -2000\,\mathrm{V}$, $V_{\mathrm{in}} = -100\,\mathrm{V}$, $V_{\mathrm{out}} = 1300\,\mathrm{V}$, $V_{\mathrm{phos}} = 2400\,\mathrm{V}$). From these fits we obtain two radii and we consider that the radius of the cloud is the mean value of them.

The RW amplitude is set at 1 V and the frequency is varied. For each frequency, an MCP picture is taken and the CsI signal is recorded. We would like to find the frequency maximising the peak height of the CsI signal (proportional to the number of accumulated positrons), and minimising the radius of the cloud. According to the graph in Figure 4.41a, this corresponds to a frequency range between 1.6 MHz and 2.5 MHz. Up to 3 MHz the number of accumulated positrons remains constant, while it decreases after this threshold.

The same operation is performed but this time, the RW amplitude is varied. According to the graph in Figure 4.41b, an important compression without loss occurs between 0 and 1.5 V, with a significant decrease of the radius between 0 and 0.8 V. Above 1.5 V the radius is still decreasing along with the number of positrons.

Starting from now and for the following experiments, the RW frequency and amplitude in the BGT's second stage are set at 2.4 MHz and 1 V.

4.6.3 Energy distribution after second stage accumulation

A potential barrier of amplitude V is set on electrodes at the exit of the trap in order to determine the energy distribution. Only positrons of kinetic energy along

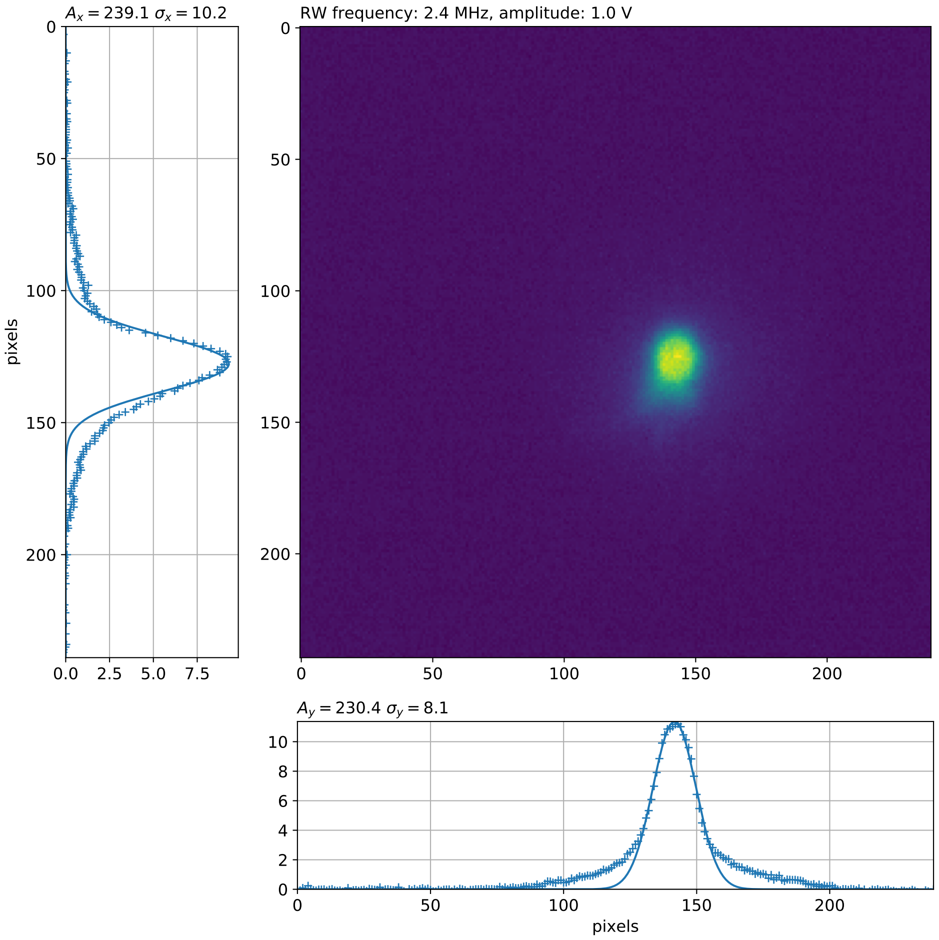

Figure 4.40 – Analysis of an MCP image, after an accumulation in the second stage.

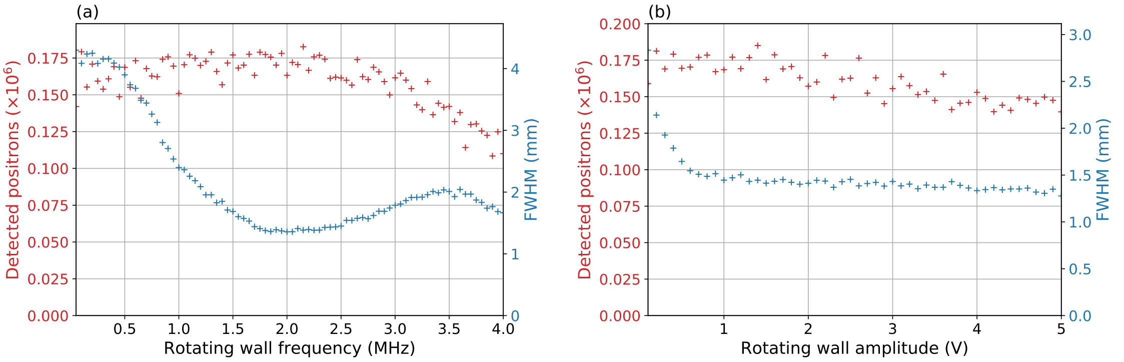

Figure 4.41 – (a) Positron number (red) and FWHM (blue) as a function of the rotating wall frequency. For 100 ms accumulation in the second stage. RW amplitude: 1 V. (b) Positron number (red) and FWHM (blue) as a function of the rotating wall amplitude. For 100 ms accumulation in the second stage. RW frequency: 2.4 MHz. LINAC frequency: 200 Hz.

the beam axis higher than $e \times V$ pass through the potential barrier to yield a detected annihilation signal (proportional to the number of accumulated positrons).

The potential profiles are presented in Figure 4.42. The measured signal as a function of V thus represents the cumulative energy distribution. Assuming the energy distribution is gaussian, a complementary error function is fit to the experimental cumulative distribution.

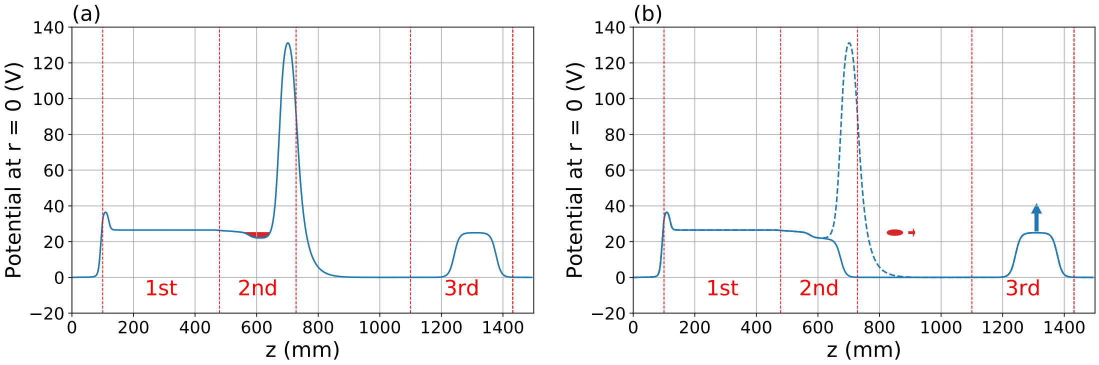

Figure 4.42 – Potential profiles used in the BGT to determine the energy distribution in the second stage. The coloured areas represent the positrons. The potential barrier at the exit is varied. (a) Accumulation of the incoming positrons from the LINAC. (b) Ejection of the positrons.

The energy distribution is determined after 100 ms accumulation in the second stage. The results of this experiment are presented in Figure 4.43. The gaussian fit indicates that the energy mean value is $E_0 = 19.30(2)$ eV with an energy spread of $\sigma = 0.68(3)$ eV (less than the 4 eV energy spread of the mean at the BGT's entrance).

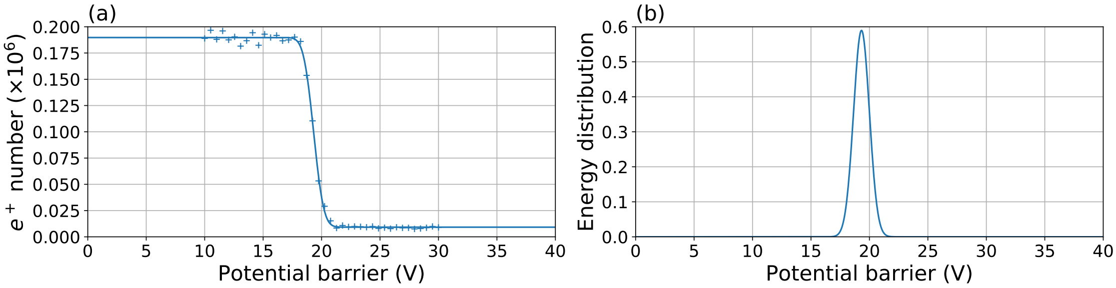

Figure 4.43 – (a) Positron number as a function of the potential barrier. (b) Energy distribution of the positrons after 100 ms accumulation in the BGT second stage. Rotating Wall parameters: 1 V, 2.4 MHz. LINAC frequency: 200 Hz.

4.7 Third stage

4.7.1 Re-trapping

After having been accumulated and compressed in the BGT second stage for 100 ms (Figure 4.44a-b), the positrons are ejected from the BGT second stage and re-trapped into the BGT's third stage (Figure 4.44c-d). After an adjustable time, they are first radially compressed using the RW technique (detailed in Section 4.7.2), then the well is lifted up and the positrons are ejected (Figure 4.44e-f). The potential applied on the electrodes for all these steps are presented in Table 4.11.

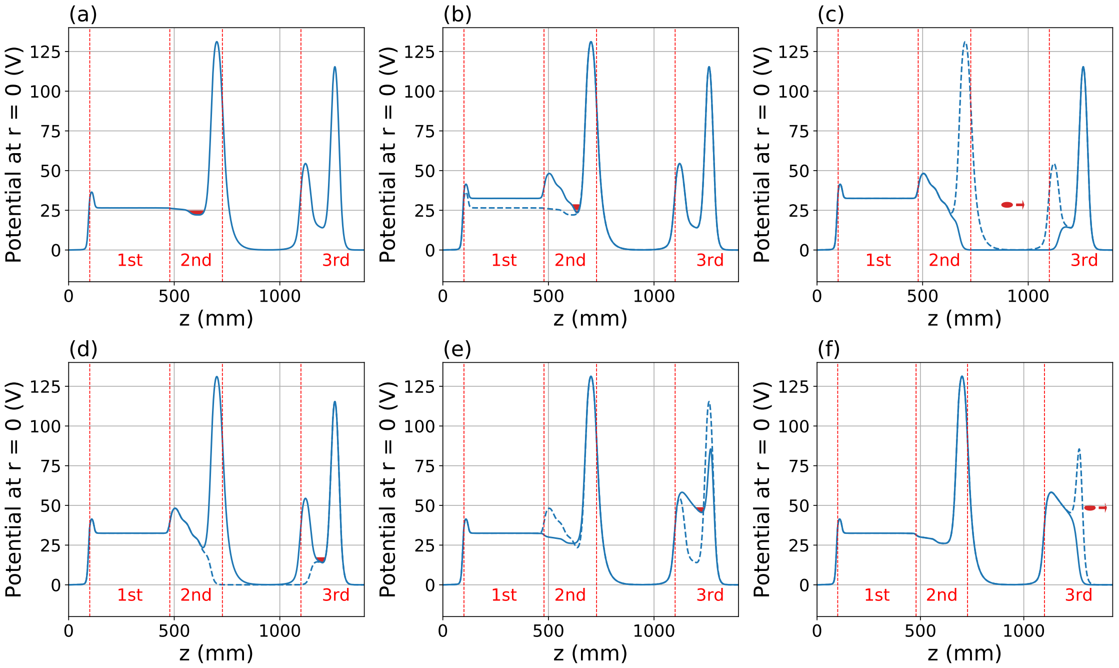

Figure 4.44 – Potential profiles used in the Buffer Gas Trap. The coloured areas represent the positrons. (a) Positron accumulation. (b) Axial compression of the positrons in the second stage. (c) Ejection from the second stage. (d) Re-trapping in the third stage. (e) Axial compression of the positrons in the third stage. (f) Ejection from the third stage.

	E_0	E_F	E_1	E_2	E_3	E_4	E_5	E_6	E_7	E_8	E_9	E_{10}	E_{11}	E_{12}	E_{13}
(a)	37.5	26.5	26	25.5	22	21.15	140	60	15.5	15	14.5	10.5	10	140	140
(b)	42.5	32.5	50	40	30	20	140	60	15.5	15	14.5	10.5	10	140	140
(c)	42.5	32.5	50	40	30	20	0	0	15.5	15	14.5	10.5	10	140	140
(d)	42.5	32.5	50	40	30	20	140	60	15.5	15	14.5	10.5	10	140	140
(e)	42.5	32.5	50	40	30	20	140	60	56	52	49	46	43	40	140
(f)	42.5	32.5	50	40	30	20	140	60	56	52	49	46	43	40	0

Table 4.11 – Voltage used for positron accumulation and axial compression in the Buffer Gas Trap's first and second stages. The electrode names refer to Table 4.4. The line letters are related to Figure 4.44.

To raise and lower the potential barriers between the second and the third stage (Figure 4.44c), fast switches having a rise time of the order of a ns are used (instead of µs for the other High Voltage Amplifiers). They allow to release the positrons almost simultaneously from the well in the second stage and to capture the positrons properly in the third stage. The positrons have typical speeds of a few $\mathrm{mm\,ns^{-1}}$ (at 25 eV, $v = 3\,\mathrm{mm\,ns^{-1}}$) and spatial dispersions of a few cm along the magnetic axis.

The transfer time δt has to be determined, i.e., the time during which the potential barriers between the second and third stages have to remain lowered to re-trap in third stage. For this purpose, the complete accumulation and re-trapping sequence is performed for different δt. The positrons are then ejected from the third stage and annihilated on the MCP at the exit of the BGT, and the CsI signal resulting from this annihilation is recorded to determine the number of positrons re-trapped in the third stage. If δt is too short, the positrons do not reach the third stage, so no positrons are detected at the end of the sequence. If δt is too long, the positrons bounce back and are not re-trapped in the third stage and again, no positrons are detected. The intermediate situation is when the positrons are re-trapped in the third stage. This situation corresponds to the first peak in Figure 4.45 presenting the number of re-trapped positrons as a function of δt.

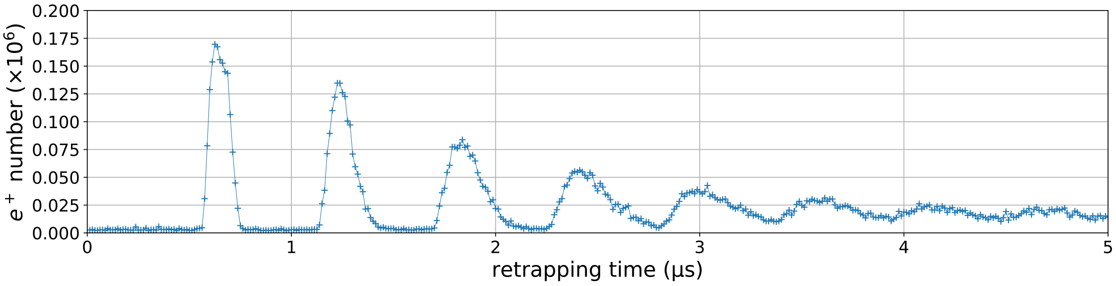

Figure 4.45 – Re-trapped positron number in the third stage as a function of opening time of the third stage. Best re-trapping time: $\delta t = 625\,\mathrm{ns}$. LINAC frequency: 200 Hz.

Indeed, several peaks are present in Figure 4.45. They result from positrons bouncing back and forth between the potential barrier at the entrance of the third stage and the potential at the exit of the second stage. The peaks are smaller and smaller because these travels back and forth are not without loss. They are also wider and wider, because the positron cloud is spreading during the travel. After a while, the bunch is too widened to be integrally trapped. Of course, we only retain the first peak to set $\delta t = 625\,\mathrm{ns}$, corresponding to a re-trapping efficiency close to 100%.

4.7.2 RW optimisation

Using the same method as the one used in Section 4.6.2, an estimation of the best RW frequency in the third stage is computed for different energies of the particles and presented in Figure 4.46. This indicates that the best RW value should be around 5 MHz.

The RW amplitude is set at 5 V and the frequency is varied. For each frequency, an MCP picture is taken to measure the radius of the positron cloud and the CsI signal is recorded to determine the positron number. An example of such a picture is shown in Figure 4.47 (Rotating Wall parameters: 5.5 MHz, 5 V, MCP parameters: $V_{\mathrm{grid}} = -2000\,\mathrm{V}$, $V_{\mathrm{in}} = -100\,\mathrm{V}$, $V_{\mathrm{out}} = 1300\,\mathrm{V}$, $V_{\mathrm{phos}} = 2400\,\mathrm{V}$).

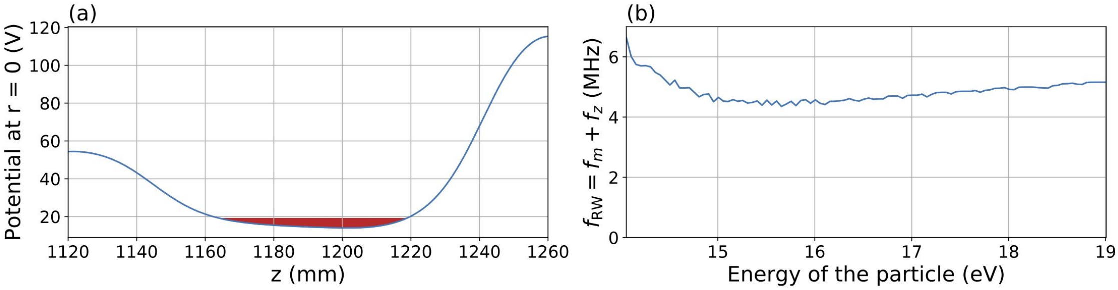

Figure 4.46 – (a) Potential well used to store positrons in the third stage. The coloured area represents the positrons. (b) Predicted RW frequencies as a function of the energy of the particle.

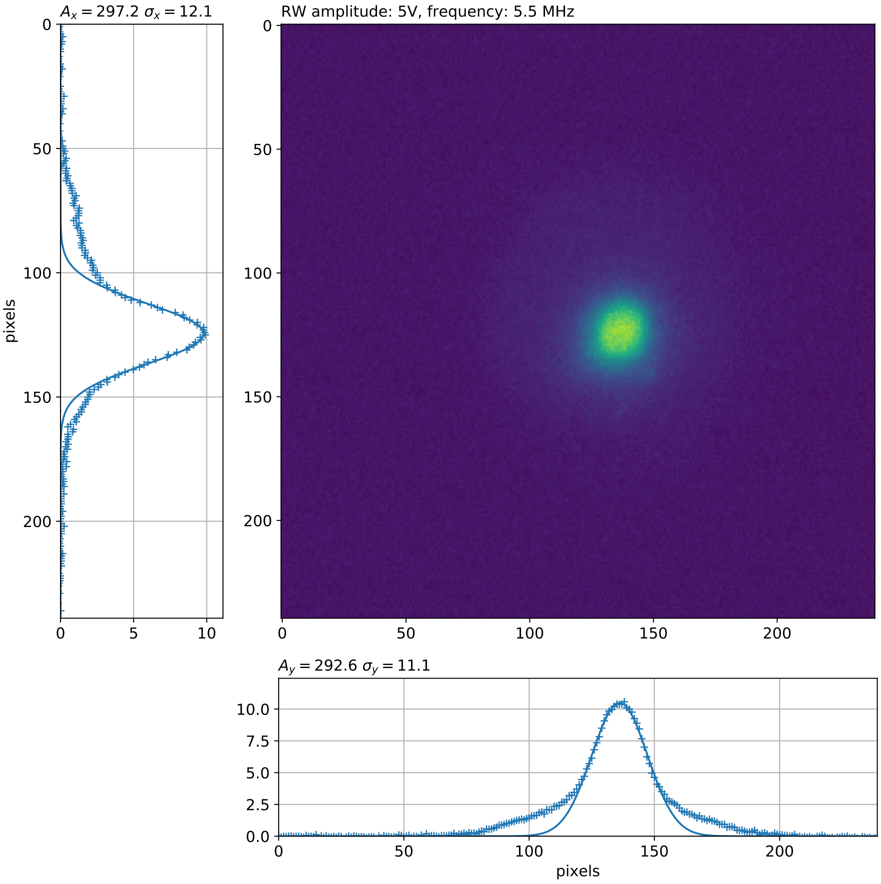

Figure 4.47 – Analysis of an MCP image, after the RW has been applied in the third stage.

As presented in Figure 4.48a, the best compression happens between 5 MHz and 7 MHz. After 7 MHz, the number of positrons is falling abruptly. Then, the frequency is set at 5.5 MHz and the amplitude is varied. The results presented in Figure 4.48b show that a significant compression occurs between 0 and 3.5 V. However, some positrons are lost in the process. After 3.5 V the radius remains constant, as the positron's number. For the following experiments, the RW frequency and amplitude in the BGT's third stage are set at 5.5 MHz and 5 V.

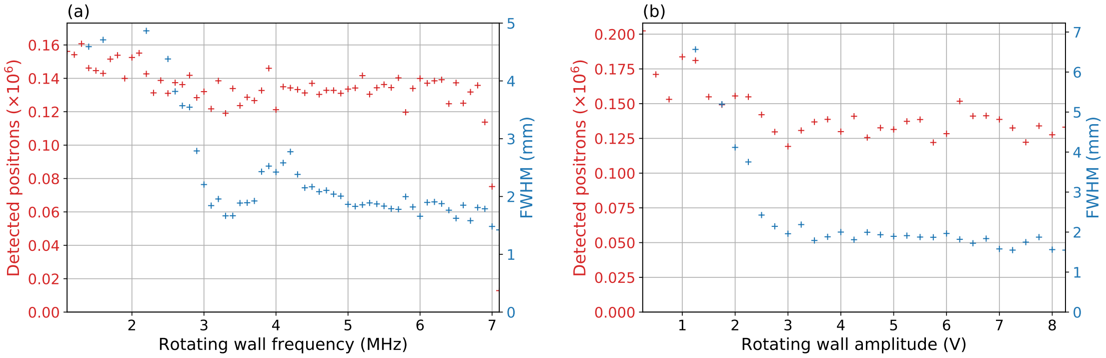

Figure 4.48 – (a) Positron number (red) and full width at half maximum (blue) as a function of the rotating wall frequency. For 100 ms accumulation in the second stage and 2 s waiting in the third stage. RW amplitude: 5 V. (b) Positron number (red) and full width at half maximum (blue) as a function of the rotating wall amplitude. For 100 ms accumulation in the second stage and 2 s waiting in the third stage. RW frequency: 5.5 MHz. LINAC frequency: 200 Hz.

Similarly to the second stage, we want to determine the lifetime of the positrons in the third stage. Here we start the stopwatch after the accumulation sequence is stopped so that $R = 0$. Thus the differential equation for the number of positrons becomes

$$\frac{\mathrm{d}N}{\mathrm{d}t} = -\frac{N}{\tau}, \tag{4.7.1}$$

which leads to

$$N(t) = N_0 e^{-\frac{t}{\tau}}. \tag{4.7.2}$$

To determine the positrons lifetime in the third stage, after the re-trapping of the positrons, we wait for different amounts of time, with the RW active, then the positrons are ejected and the number of positrons which were in the trap just before the ejection is determined using a CsI detector. The number of positrons as a function of the waiting time t (shown in Figure 4.49) is fit with $N(t) = N_0 e^{-\frac{t}{\tau}}$. This leads to a lifetime of $\tau = 9.44(17)$ s.

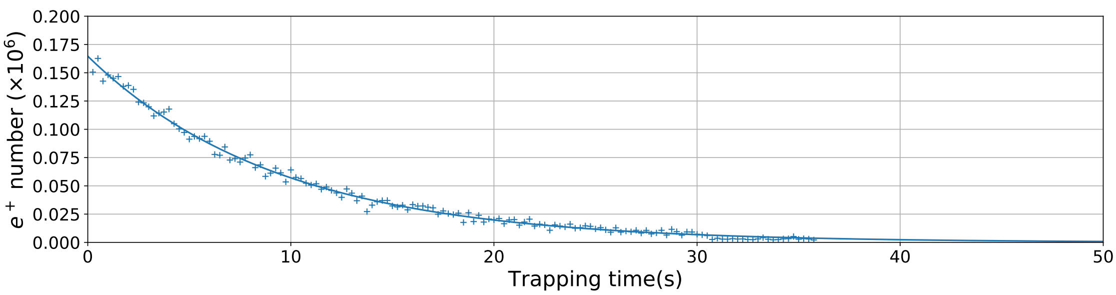

Figure 4.49 – Positron number as a function of the trapping time in the third stage. RW parameters: {1 V, 2.4 MHz}, {5 V, 5.5 MHz}. LINAC frequency: 200 Hz.

4.7.3 Energy distribution

To determine the energy distribution of the positrons in the third stage, the same procedure as the one presented in Section 4.6.3 is used. This time, after 100 ms waiting in the third stage, an adjustable potential barrier is set after the well. The positrons are ejected on the MCP to determine the number that have an energy greater than the barrier. The data of this experiment is presented in Figure 4.50a. The number of positrons is then fit with an erfc function to determine the energy distribution (Figure 4.50a). The mean value of the energy of the positrons is then $V_0 = 47.3(1)\,\mathrm{eV}$ and the energy spread is $\sigma = 1.52(12)\,\mathrm{eV}$.

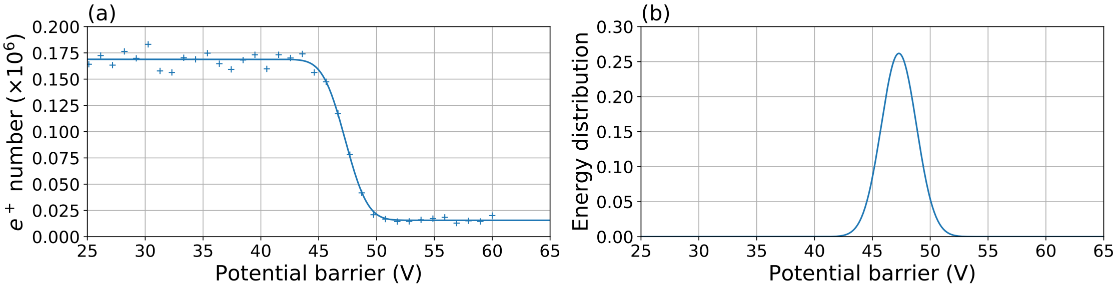

Figure 4.50 – For 100 ms accumulation in the second stage and 100 ms waiting in the third stage. (a) Number of positrons trapped in the third stage exiting the BGT as a function of the height of the potential barrier. (b) Energy distribution of the positrons in the third stage. RW parameters second stage: {1 V, 2.4 MHz}. RW parameters third stage: {5 V, 5.5 MHz}. LINAC frequency: 200 Hz.

4.7.4 Stacking

The lifetime of $\tau = 9.44(17)\,\mathrm{s}$ obtained in the third stage allows to stack in it the positrons from the second stage where the accumulation time is 100 ms in order to increase the number of positrons in the third stage. The sequence to re-trap positrons in the third stage is then reproduced. The number of positrons trapped in the third stage is expected to grow linearly with the number of stacks, providing all the positrons stored in the third stage remain while other positrons are accumulated in the second stage.

As shown in Figure 4.51b (crosses), if the potential profiles described in Figure 4.44 are used (i.e., the same as for one stack), then, a saturation is reached for 4 stacks. This is because the well is then full. The bottom of the well (electrodes $\mathrm{E}_9, \mathrm{E}_{10}$ in Table 4.11) is thus decreased of dV for each new stack (resulting potential profile in Figure 4.51a). As presented in Figure 4.51b, for $dV = 0.4\,\mathrm{V}$, it is possible to store at least 15 stacks in a linear way.

For the rest of the experiments, dV is set at 0.4 V and 10 stacks will be accumulated. With $0.15 \times 10^6 \mathrm{e}^+$ per stack, the BGT provides $1.5 \times 10^6 \mathrm{e}^+$ per second for a LINAC flux of $\sim 3 \times 10^7 \mathrm{e}^+$ per second, so with an overall efficiency of 5%.

Again, as presented in Figure 4.52, an energy distribution determination is performed for 10 stacks in the third stage. The mean value of the energy is $V_0 = 47.1(1)\,\mathrm{eV}$, with an energy spread of $\sigma = 3.11(10)\,\mathrm{eV}$.

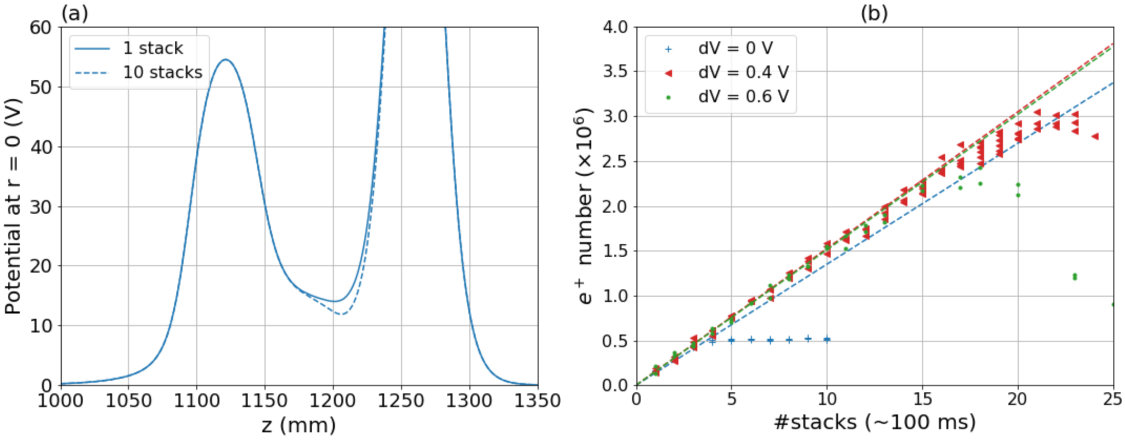

Figure 4.51 – (a) Potential profiles used for the stacking procedure. $dV = 0.4\,\mathrm{V}$. (b) Stacking in the third stage. Each stack corresponding to 100 ms accumulation in the second stage. RW parameters second stage: {1 V, 2.4 MHz}. RW parameters third stage: {5 V, 5.5 MHz}. LINAC frequency: 200 Hz.

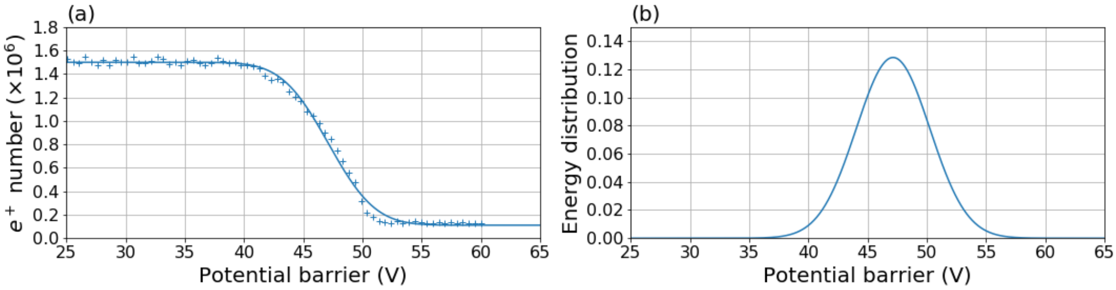

Figure 4.52 – For 10 stacks in the third stage. Each stack corresponding to 100 ms accumulation in the second stage. (a) Number of positrons trapped in the third stage exiting the BGT as a function of the potential well. (b) Energy distribution of the positrons in the third stage. RW parameters: {1 V, 2.4 MHz}, {5 V, 5.5 MHz}. LINAC frequency: 200 Hz.

.

4.8 Conclusion

In this chapter, the accumulation of positrons in the Buffer Gas Trap of the GBAR experiment has been presented. The positrons are first accumulated in the second stage for 100 ms. In this stage, with the parameters presented in this chapter, the positrons lifetime is about $\sim 0.6\,\mathrm{s}$ and the trapping rate is $\sim 1.7 \times 10^6\,\mathrm{e}^+\,\mathrm{s}^{-1}$. The role of the Rotating Wall is here essential for the trapping efficiency and for the radial compression.

Subsequently, the positrons are axially compressed by changing the shape of the well, in order to be re-trapped in the third stage of the BGT. The lifetime of the positrons in the third stage ($\sim 10\,\mathrm{s}$) is large enough to start a stacking procedure. Indeed, 10 bunches corresponding to $10 \times 100\,\mathrm{ms}$ accumulation in the second stage are sent into the third stage. Then positrons are again radially compressed using a

Rotating Wall.

In conclusion, currently, the BGT provides a bunch of $\sim 1.5 \times 10^6\,\mathrm{e}^+$ each second (some losses during the stacking procedure). This bunch has to be transferred in the High Field Trap where a stacking procedure can be applied to trap a larger number of positrons as is presented in the next chapter.

Chapter 5

The High Field Trap

> If there is no solution then there is no issue.
>
> A Shadock principle

Contents

In this chapter, the specifications of the High Field Trap, the second positron trap of the GBAR experiment, are described in Section 5.1. To perform some tests with the trap without using the LINAC, an electron gun has been placed at the entrance of the trap. A description of the gun and the associated control system is presented in Section 5.2 and the results of the experiments using electrons are shown in Section 5.3 (this work can be compared with the experiments made with the same trap at Riken and presented in Ref. [92]). Finally, we present in Section 5.4 the results of the experiments based on the re-trapping of the bunches of positrons produced in the BGT as explained in the previous chapter.

5.1 Description of the trap

The High Field Trap of the GBAR experiment has been built at Riken in Japan [49, 50] and has been given to the GBAR. This Penning-Malmberg trap has been installed at CERN in 2018.

The purpose of this trap in the context of the GBAR experiment is to store the largest possible quantity of positrons (goal 10^{10}) to produce enough positronium atoms for anti-hydrogen ion production. This trap is mainly constituted of a superconducting magnet able to reach 5 T and a set of 27 electrodes (able to accept a voltage of ± 4 kV with a maximal difference between two electrodes of 2 kV). Pictures of the trap are presented in Figure 5.1 and a schematic of the trap in Figure 5.2.

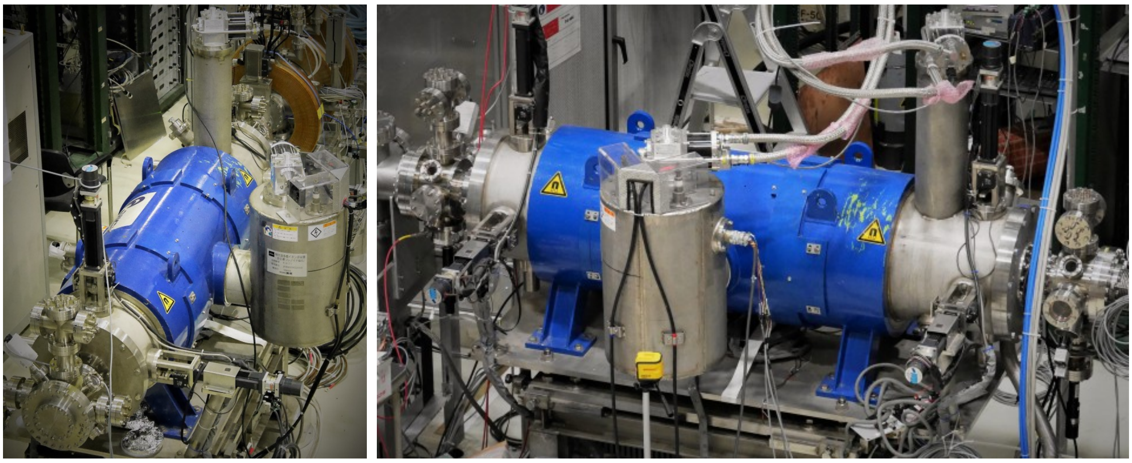

Figure 5.1 – High Field Trap pictures.

The duct being in contact with the electrodes, the entire trapping volume can be cooled to reach ~ 10 K. This is obtained with a cryo-head connected to the duct.

The duct and consequently the electrodes can be moved to align the electrodes main axis with the magnetic field. This alignment is performed thanks to 4 vertical arms, presented in Figure 5.3. The arms can be moved with a precision of 10 µm on a 4 mm range. Since a misalignment creates an $\mathbf{E} \times \mathbf{B}$ drift force which causes the expansion of the plasma, having the best alignment is essential.

5.1.1 The super conducting magnet

The niobium-titanium coils of the trap's electromagnet produce a 5 T uniform magnetic field over 500 mm along the field axis (the total length of the trap being 1940 mm) and for a circular section of 4 mm diameter. The uniformity in this region is estimated as better than 10^{-3}.

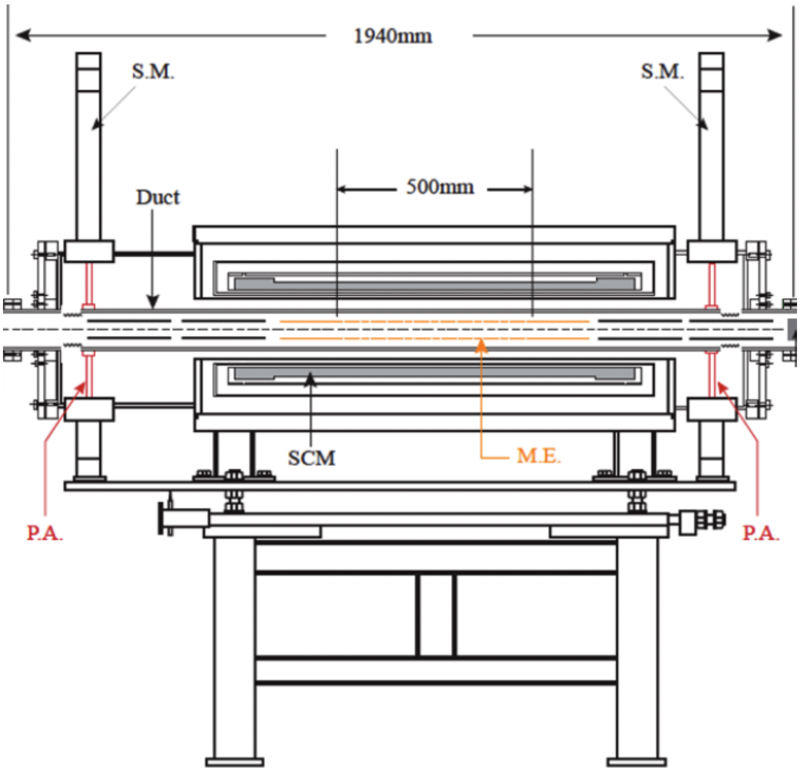

Figure 5.2 – High Field Trap schematic. Positrons and electrons arrive from the left and are dumped to the right. The grey part named SCM corresponds to the Superconducting Magnet. The steppers motors (SM in the figure) allow to move the duct in order to align the magnetic field with the electric field. The main electrodes (M.E.) are represented in orange, they provide a 500 mm length to trap the particles.

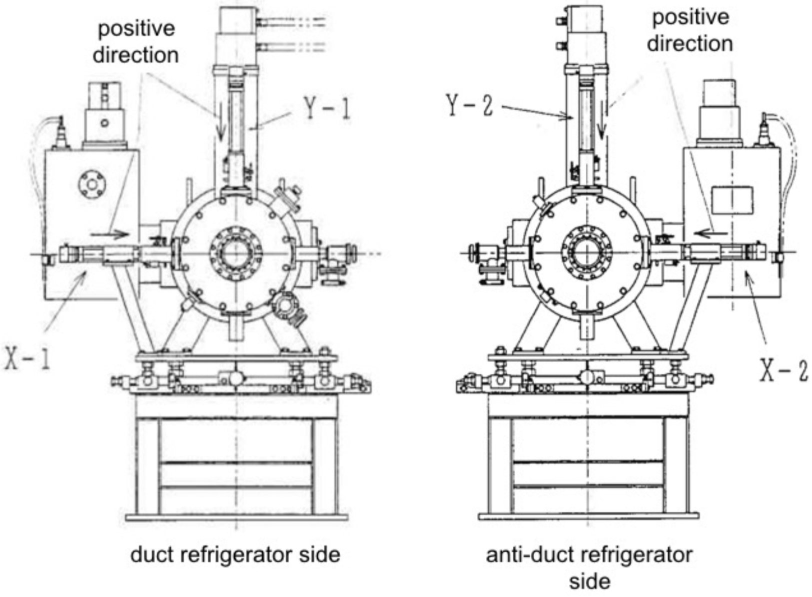

Figure 5.3 – Positive direction of drive axis.

To reach 5 T, the coils require to be cooled enough to reach the superconducting state thanks to a cryogenic head. When cold a 45 min ramp brings the current from 0 to 85 A. The electromagnet is surrounded by an insulation vacuum. A second insulation vacuum surrounds the duct (Figure 5.2), to keep the center of the duct around 10 K.

The control of the current is done by three elements: an analog convertor [93] (Figure 5.4a), a current generator (Figure 5.4b) and a protection system (Figure 5.4c). The analog convertor is controlled by a Labview program on (Figure 5.4d) a computer through a GPIB connection. The converter controls the current generator, which sends a feedback to the computer.

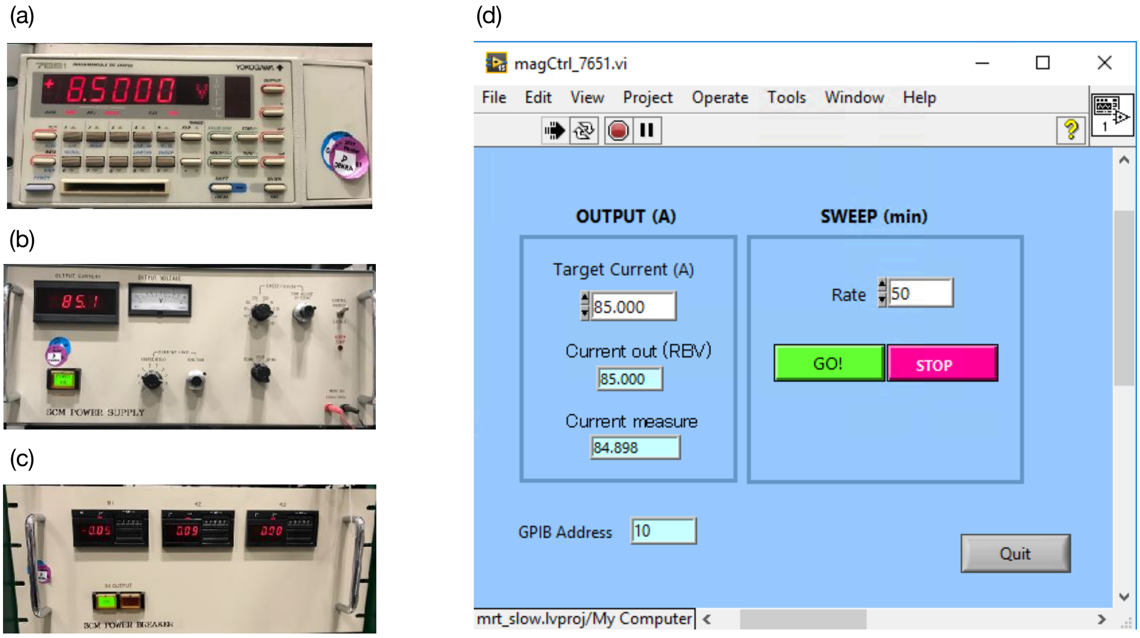

Target Current (A) 85.000

Current out (RBV) 85.000

Current measure 84.898

Rate 50

GPIB Address 10

Figure 5.4 – The different components to power the HFT's magnet. (a) Analog convertor. (b) Power supply. (c) Power breaker. (d) Labview VI to control the analog convertor.

5.1.2 The electrodes

The electric potential is created by a set of 27 cylindrical electrodes. The inner and outer diameters are respectively of 38 and 40 mm. They are made of oxygen-free copper, gold plated, and numbered from -13 to 13. The first three electrodes (-13, -12, -11) have respectively lengths of 270 mm, 270 mm, and 160 mm. The setup is symmetric for the last three ones (i.e., 11, 12, 13 have respectively lengths of 160, 270, and 270 mm). The remaining electrodes (from -10 to 10) all have a length of 20 mm and are separated by 3 mm gaps. Electrodes -2 and 2 (see Figure 5.5) are split in 4 azimuthally, for the rotating wall technique (see Section 3.3.2). As shown in Figure 5.6, electrodes -13 and -12, -11 to 11 and, 12, 13 are on three separated supports.

It is important to note that, because of the geometry, a difference of potential between two electrodes higher than 2 kV cannot be used. Otherwise, one would

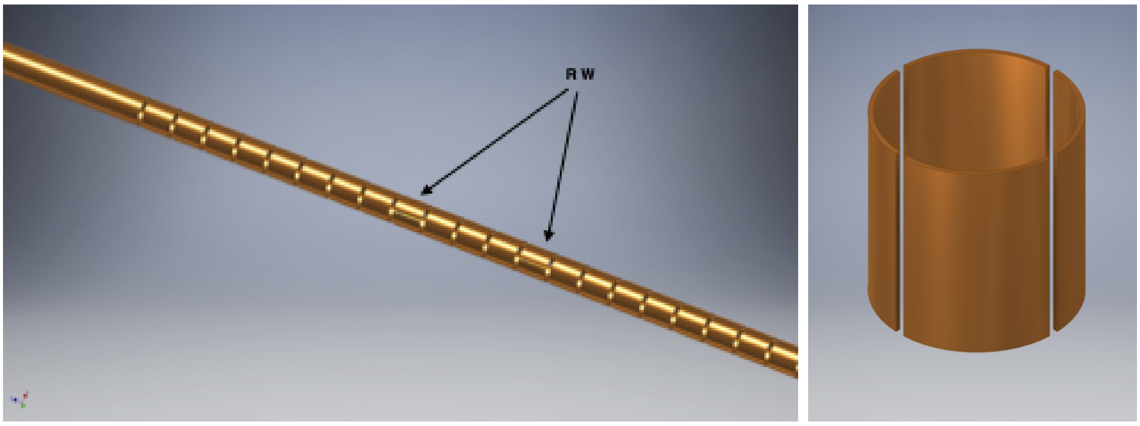

Figure 5.5 – Left: 3D view of the electrodes. Right: one of the rotating wall electrodes.

create sparks that could damage the system. The potential is applied using High Voltage Amplifiers [94].

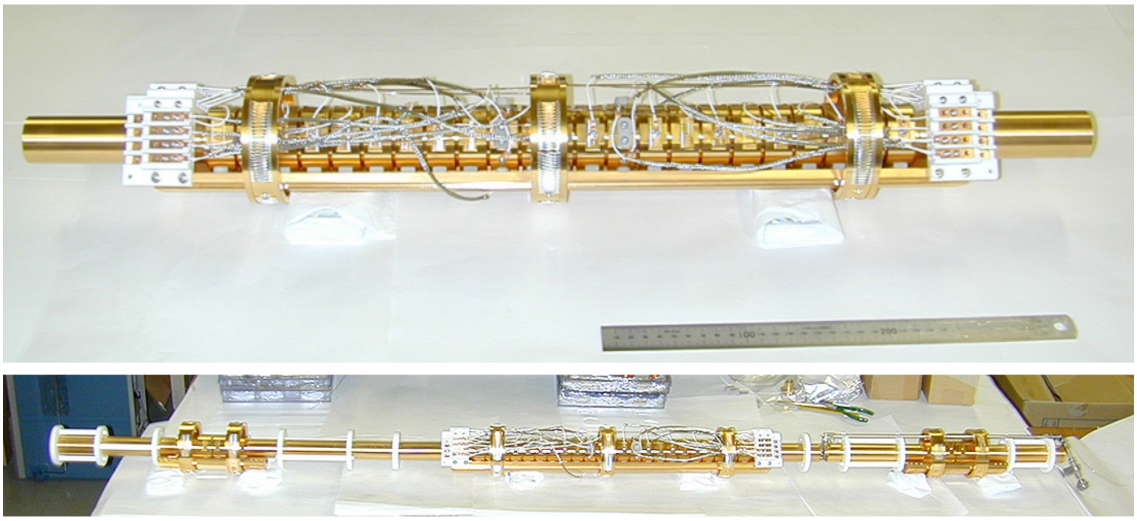

Figure 5.6 – Extracted from Ref. [51]. Top: Central support with the main electrodes. Bottom: The three supports assembled.

The electrodes are placed in a duct (see in Figure 5.2) in which the pressure is maintained below 1×10^{-9} mbar thanks to a cryo-pump upstream and an ion-pump downstream the HFT. The temperature of the electrodes in the trap influences directly the trapped plasma cooling, and is a limit for that. The temperature of the electrodes is related to the temperature of the duct which is cooled through a cryogenic cold head down to a temperature around 10 K.

5.1.3 Temperature probes

As shown in Figure 5.7, several types of temperatures probes are installed inside the trap to continuously monitor the temperatures of the duct and magnet.

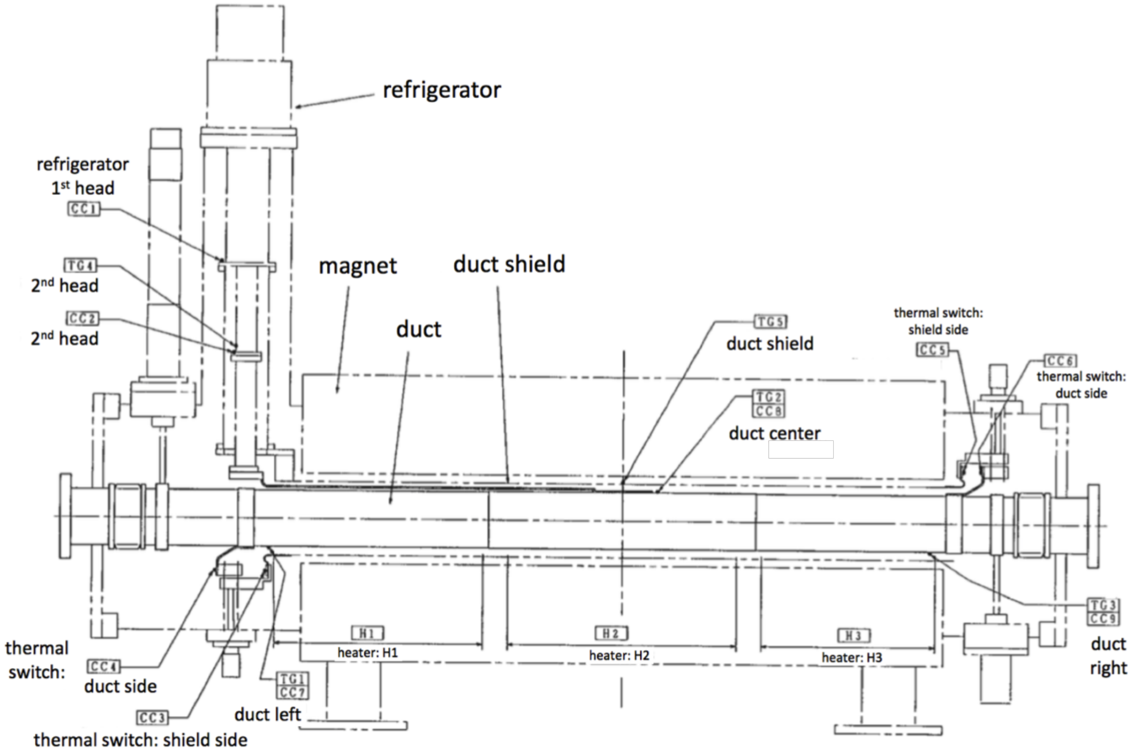

Figure 5.7 – Overview of the temperature probes inside the HFT. TGi corresponds to the Gallium-Aluminium-Arsenide diode based probes and CCi to the thermocouples probe. Hi corresponds to the heaters necessary for the baking of the system.

Three kinds of probes are used, the choice of which depends on the range of temperature we want to read. Some specifications of the probes are shown in Appendix D. To monitor the temperatures of the duct, we use Gallium-Aluminium-Arsenide diodes based probes, as detailed in Table 5.1, with expected values between 10 K and 60 K in the working mode. These temperatures are constantly read on an independent computer thanks to a Labview program.

Probe	Location	Automatically read in April 2020
TG1	Duct left side	yes, channel 3, currently broken
TG2	Duct center	yes, channel 2
TG3	Duct right side	yes, channel 1
TG4	Second stage of the cold head	no
TG5	Middle of duct shield	yes, channel 4

Table 5.1 – Temperatures read by the Gallium-Aluminium-Arsenide diodes based probes in the HFT.

It has to be noticed for a future user of the trap that we figured out that on the schematics, TG1 and TG3 has been reversed. The best way to know if the measurement is consistent is to check if we have TG4 $<$ TG1 $<$ TG2 $\sim$ TG5 $<$ TG3 (according to the position of the probes in Figure 5.7). The connector pins are presented in Figure D.1 and Table D.1.

Then, thermocouples are used to measure temperatures as defined in Table 5.2. They are used to measure temperatures between approximatively $-150\,°\mathrm{C}$ and $150\,°\mathrm{C}$. The most important probes are CC7, CC8 and CC9, corresponding respectively to the left, center and right of the duct because they are connected to the heaters necessary for the baking of the tube to improve the vacuum.

Probe	Details
CC1	First stage cold head magnet
CC2	Magnet radiation shielding or second stage of the cold head
CC3	Magnet radiation shielding left side
CC4	Thermal shield duct left side
CC5	Magnet radiation shielding right side
CC6	Shield duct right side
CC7	Duct left side, to compare with TG1
CC8	Duct center, to compare with TG2
CC9	Duct right side, to compare with TG3

Table 5.2 – Temperatures read by the thermocouple probes in the HFT.

The magnet is cooled using a helium circuit and compressor in order to reach a temperature of $\sim 4\,\mathrm{K}$. The magnet is insulated from the rest of the device thanks to a thermal shield (see “duct shield” in Figure 5.7): it is an empty cylindrical volume where the pressure is about $10^{-6} - 10^{-7}$mbar. The temperature of the magnet, being extremely low, we use Carbon Glass Resistors, with a range from 1.4 K to 100 K. As presented in Table 5.3, the probes are placed at 3 different positions: one on the cryostat, and the others on the super-conducting coils.

Probe	Details
CGR1	Cold point of the cold head
CGR2	Coils right side
CGR3	Coils left side

Table 5.3 – Temperatures read by the Carbon Glass Resistor based probes in the HFT.

Currently, the temperatures of the magnet are determined manually by measuring the values of the resistance and by extrapolating from the abaci presented in Tables D.3, D.4, D.5 and Figure D.2. In a next future, this measurement will be automated.

5.1.4 Trapping control

The trapping control is similar to the one of the BGT (described in Section 4.3.2), it is then performed by a PXI. The main difference is that the NI PXIe 8135 computer module has been replaced by a NI PXIe 8840 module. This module is a Real Time (RT) computer, allowing to run Real Time Labview programs, insuring a temporal precision and a reproducibility. However, it is not a standard computer, so another computer (a more common one, named HFT computer for the rest of this explanation) has to be connected (ethernet connection) to write and compile the RT programs then download them into the RT computer.

To be more specific, in our case, the sequencer program, a translating program to turn the sequence into a list of orders is on the HFT computer. A RT time program is running on the RT module, waiting for this array and this RT module will then control all the other modules of the PXI according to the sequence. This RT program is comparable to the FPGA program used for the BGT. The sequence is loaded, run or aborted with a Labview interface identical to the one of the BGT (Figure 4.16b). For the sequence editor, a copy of the one used for the BGT has been installed on the HFT computer. For more details, refer to Section 4.3.2 and Figure 4.15.

The Rotating Wall parameters are sent from the HFT computer to the RT computer with the graphical interface shown in Figure 5.8a. On a RT program is waiting to send this values to the generator (with a GPIB connection). A graphical interface, presented in Figure 5.8b is installed on the HFT computer to obtain feedbacks from the RT computer.

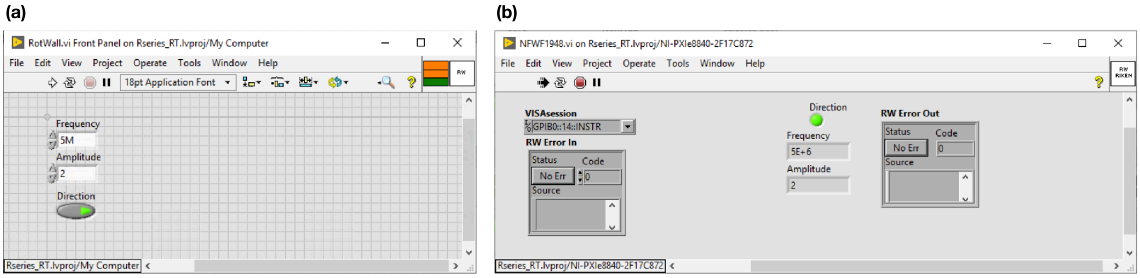

RotWall.vi Front Panel on Rseries_RT.lvproj/My Computer

Frequency: 5M

Amplitude: 2

Direction

Rseries_RT.lvproj/My Computer

NFWF1948.vi on Rseries_RT.lvproj/NI-PXIe8840-2F17C872

VISAsession: GPIB0::14::INSTR

RW Error In — Status: No Err, Code: 0, Source:

Direction

Frequency: 5E+6

Amplitude: 2

RW Error Out — Status: No Err, Code: 0, Source:

Rseries_RT.lvproj/NI-PXIe8840-2F17C872

Figure 5.8 – Labview interfaces on the HFT computer for the RW parameters (a) To send the parameters to the RT computer. (b) To check the parameters have been received and there is no problem with the GPIB connection.

Therefore, the element present on the NI PXIe 1078 are:

- NI PXIe 8840 the Real Time computer;
- NI PXIe 6366, an analog input voltage card, to acquire some slow signals;
- NI PXIe 7820R, a digital input/output card;
- NI PXI 6733, three analog input voltage cards, to control the High-Voltage Amplifiers;

A schematic of this system is presented in Figure 5.9.

Finally, a graphical interface has been installed on the HFT computer to show the potential profile in the HFT. The High Voltage Amplifiers connected to the electrodes give analog signals, proportional to the potential applied on the electrodes (with no good precision). These signals are acquired by the CRio module controlling the electron gun (see Section 5.2.3 for more details) and sent as and array every 10 ms to the HFT computer through an ethernet connection. The potential at the center of the electrode is then extrapolated and shown to the user with the interface presented in Figure 5.10.

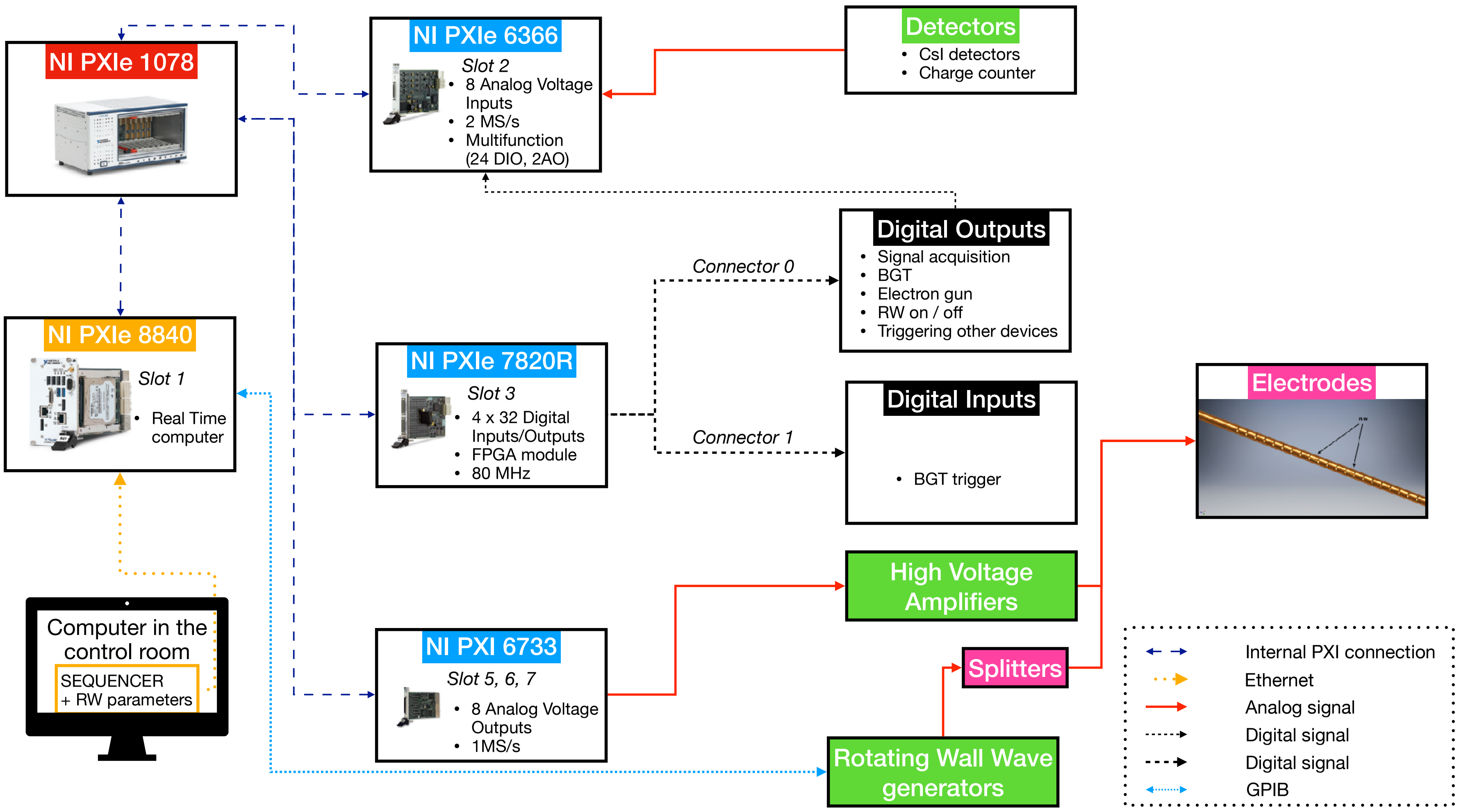

Figure 5.9 – Overview of the connections of the HFT's trapping control system.

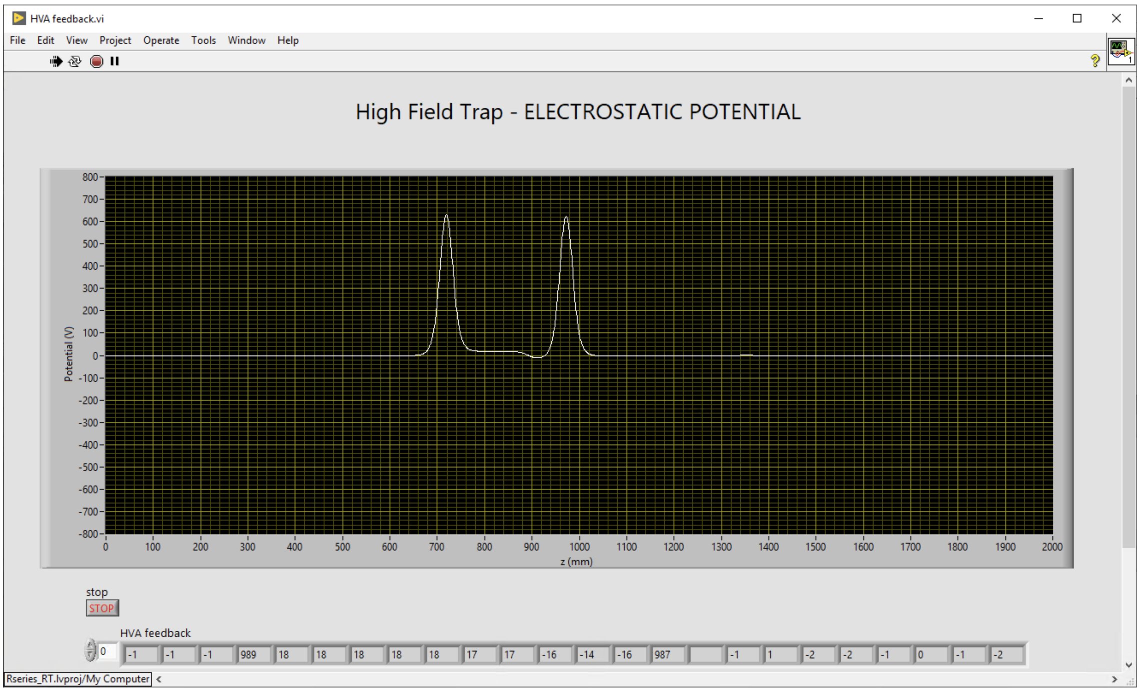

```
0 | -1 | -1 | -1 | 989 | 18 | 18 | 18 | 18 | 18 | 17 | 17 | -16 | -14 | -16 | 987 |  | -1 | 1 | -2 | -2 | -1 | 0 | -1 | -2
```

Figure 5.10 – Graphical interface showing in real time the potential at the center of the trap.

5.2 Electron gun

An electron gun has been placed between the Buffer Gas Trap and the High Field Trap. In this section, some important characteristics about the electron gun are presented, like how the system is connected, and how to control it.

5.2.1 Filament characteristics

The principle of the electron gun used in the experiment is the following: a filament heated by a current heats a disk made of Yttrium Oxide (Y_2O_3) (see in Figure 5.11) [95]. Then the Y_2O_3 disk emits electrons thanks to an electric field generated by the difference of potential between both sides of the filament (cathodes 1 and 2 in Figure 5.12) and the anode. In our system, the anode is a disk with a hole in the middle. In the presence of a magnetic field aligned with the disk axis, which is also the axis of the positron line, the electrons are channeled through the hole and ejected with a kinetic energy corresponding to the voltage applied at the anode. Without magnetic field, the electrons are absorbed by the anode.

Figure 5.12 shows how the electron gun is powered. Two floating ground generators are used [96]. One sets $V_2^+ = 0$ and $V_2^- = V_1^+$. The potentials fulfil $V_1^+ > V_1^-$ and $V_2^+ > V_2^-$. A 12 V Zener diode is used to apply a difference of potential of 12 V between cathode 2 and the anode to extract the electrons. Finally the micro-ammeter between point A and the ground will allow to determine the current of electrons that have gone through the hole of the anode.

To study the behaviour of the electron gun, the circuit presented in Figure 5.12 has been turned into the one presented in Figure 5.13. Here, one set $V_2^+ - V_2^- = 20\,\text{V}$,

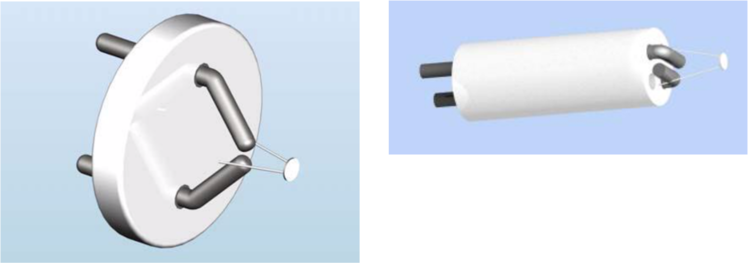

Figure 5.11 – Extracted from the “ES-535W Yttria coated Iridium disc on AEI base and CB-104 base” datasheet [95]. One can see the support of the filament, and the Yttrium Oxide disk which is heated to emit electrons.

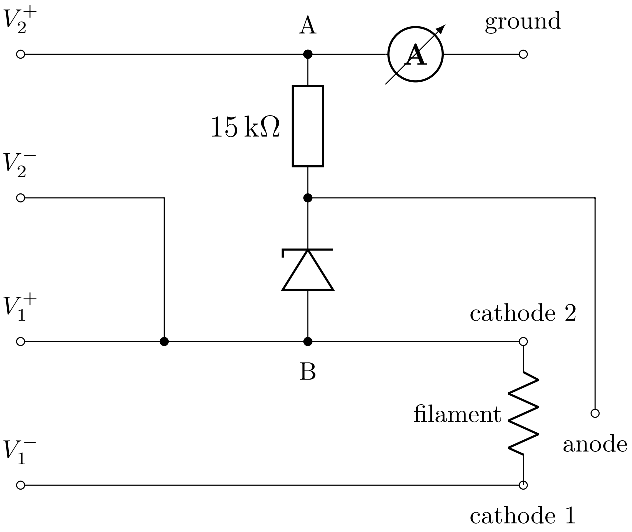

Figure 5.12 – Schematic circuit used to power the electron gun. The “cathode 1” and “cathode 2” outputs go to the filament and obviously, the “anode” output to the anode of the electron gun.

and connects the anode to the ground. A micro-ammeter is installed between points A and C which measures a current named I_{an}. The voltage V_{gen} and current I_{gen} are read on the generator’s monitor. Physically, I_{gen} corresponds to the number of electrons injected in the circuit per second. Then some of these electrons are emitted by the filament and go to the anode back to the generator resulting in a current I_{an} which is then the number of emitted electrons per second.

The measurement of I_{gen} and I_{an} as a function of V_{gen} is presented in Figure 5.14. The first observation is that as expected, the behaviour of the filament is not the behaviour of a simple linear resistance. However, the plot I_{gen} as a function of V_{gen} is different from what we would expect compared to the specifications [95]. This difference is due to the internal resistance of the wires connecting the output “cathode 1” and “cathode 2” to the filament (we measured $0.9\,\Omega$ of internal resistance of the wires). It is also shown in Figure 5.14 that electrons are emitted after a threshold of $V_{\mathrm{gen}} = 1.5\,\mathrm{V}$, $I_{\mathrm{gen}} = 1.5\,\mathrm{A}$ and the current I_{an} increases quickly after the threshold to reach about $0.6\,\mathrm{mA}$. The test is not performed for higher V_{gen} and I_{gen} to avoid

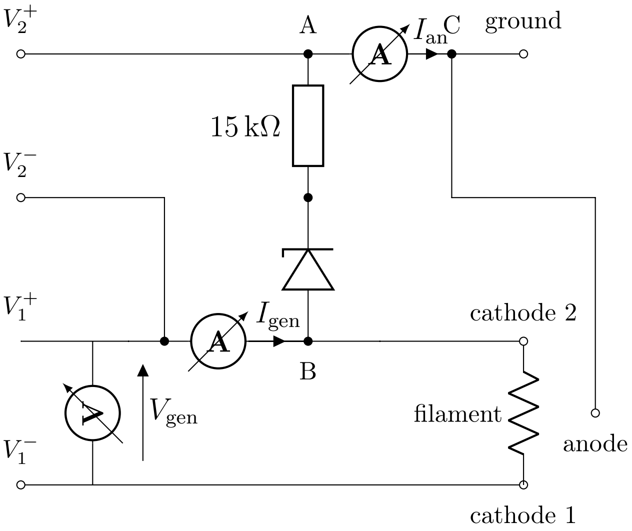

Figure 5.13 – Schematic circuit to determine the current of emitted electrons (I_{an}) by the filament of the electron gun.

burning the filament which cannot accept a current above $I_{gen} = 1.8\,\text{A}$.

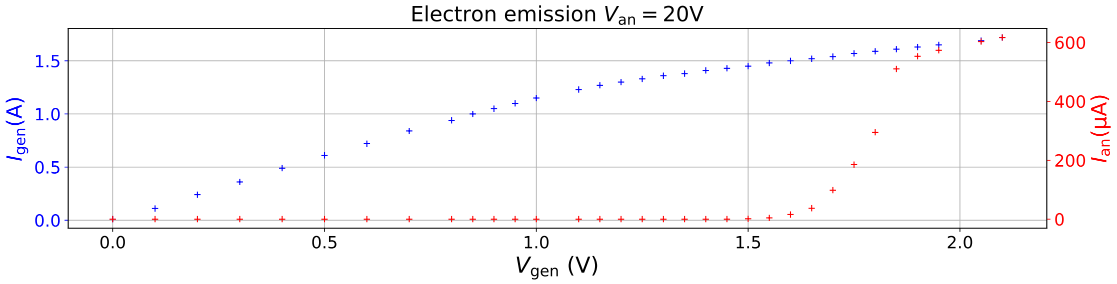

Figure 5.14 – I_{gen} and I_{an} as a function of V_{gen}. According to Figure 5.13, V_{gen} and I_{gen} are the voltage and current provided by the generator and I_{an} the current going through the anode i.e. the current of emitted electrons.

By this simple test, one can see that if we use a voltage of $V_{gen} \sim 2\,\text{V}$, we can emit electrons without burning the filament.

5.2.2 Power supply control

As explained in Section 5.2.1, a current higher than 1.8 A cannot be accepted in the electron gun filament. The generator providing this current has to be physically limited to prevent exceeding this threshold. Let's focus on the power supply connected on the filament, the one providing $V_1^\pm$ in Figure 5.12.

The power supply is controlled remotely, using a sub-D entrance as presented in Figure 5.15.

Pins 3 and 9, corresponding to V_3 and V_9, are used to limit the current. For a maximal current of 1.8 A, V_3 has to be connected in a way that $V_3/V_9 \leq 0.18$. This is why we use a voltage divider as presented in Figure 5.16. Indeed, using Millman's

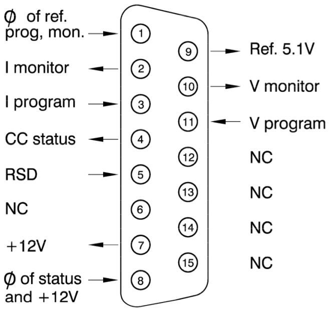

Figure 5.15 – Extracted from Ref. [96]. Remote control input of the generator.

theorem on V_3 we have:

$$V_3 = \frac{(V_1 = 0)/10\,\mathrm{k\Omega} + V_9/47\,\mathrm{k\Omega}}{1/10\,\mathrm{k\Omega} + 1/47\,\mathrm{k\Omega}} = V_9 \frac{10}{10+47} = 0.175V_9$$

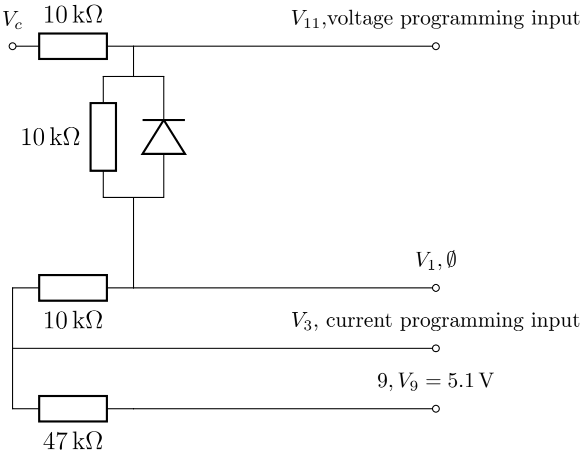

Figure 5.16 – Control of the generator

Thereby, it is now impossible to set a current greater than 1.8 A in the filament. Also, it is required to control remotely the voltage going out of this power supply. This is the purpose of voltage V_{11}. The controller provides a signal V_c between $-10\,\mathrm{V}$ and $10\,\mathrm{V}$, and we would like to have $5 > V_{11} > 0$ to fulfil the specifications of the power supply [96]. This is why we have the second voltage divider and the diode in Figure 5.16. Something similar has been done for the second power supply.

However, the system will not work like that. Indeed, according to the datasheet, V_1 in Figure 5.16 and V_1^- in Figure 5.12 are connected. So if the circuit presented in Figure 5.16 is directly used, we would have $V_1 = V_1^- =$ ground, and the electron gun would be short-circuited. This is why we have to use galvanic isolators for the wires going to the controller.

5.2.3 Control of the system

The power supplies [96] are controlled by a NI cRIO 9066 controller. On this cRIO, 5 modules are connected:

- NI 9205, an analog input module to display the feedback signals from the high voltage amplifiers which create the electric potential in the HFT (it is not relevant to have a dedicated cRIO only for that purpose);

- NI 9263, an analog input module to display the feedback signals from the electron gun power supplies;

- NI 9201, an analog output module to set the voltage of the electron gun power supplies;

- NI 9402, a digital IO module to get triggers when the electron gun has to be used according to a predefined sequence for the $e^{\pm}$ trapping;

- NI 9494, a 24 V digital output module to control the push/pull in order to put the electron gun in or out of the beam line.

As explained in Section 5.2.2, the signal wires connected to NI 9205 and NI 9201 have to go through galvanic isolators before being connected to the electron gun power supplies because of a grounding issue. A schematic of how the system is connected is presented in Figure 5.17.

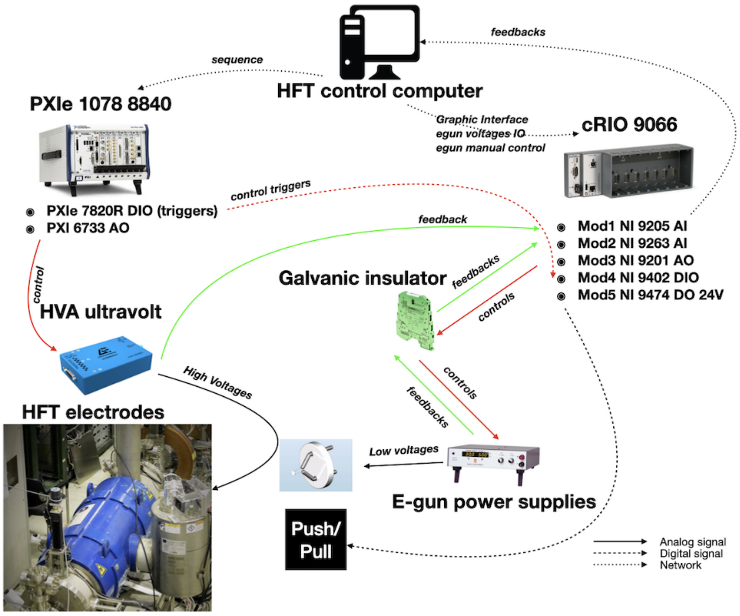

Figure 5.17 – Schematic of the connections. More information concerning the PXI are presented in Section 5.1.4.

To set the voltage on the power supplies, a graphic interface has been developed and is installed on the computer in charge of the HFT. It is shown in Figure 5.18. With this interface, it is also possible to manually control the electron gun, but it is only relevant to use it for tests. To control the electron gun during a trapping sequence, we use triggers coming from the PXIe, to control the push-pull, and to switch on/off the power supplies.

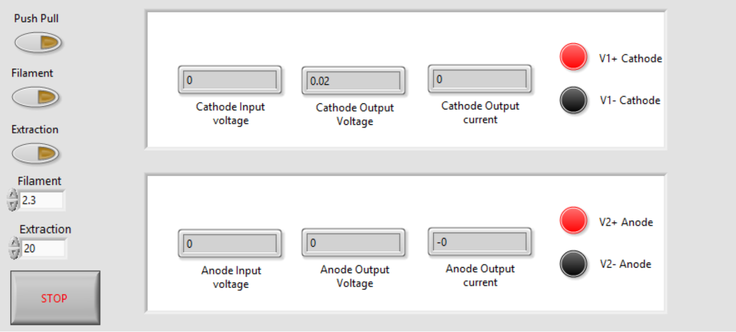

Filament 2.3
Extraction 20
Cathode Input voltage 0
Cathode Output Voltage 0.02
Cathode Output current 0
Anode Input voltage 0
Anode Output Voltage 0
Anode Output current -0

Figure 5.18 – Graphic interface

5.3 Electron trapping

5.3.1 Charge counter

In order to determine the number of trapped electrons, the front surface of the MCP is used as a Faraday cup. The charge counter used in Section 4.6 to determine the number of positrons cannot be used since the expected number of charges is above its saturation limit. The schematic of the homemade charge counter used here is shown in Figure 5.19.

Basically a charge counter consist of a RC circuit with an oscilloscope attached. When the charges arrive on the MCP front, creating a potential V_{MCP}, they are accumulated in a capacitor ($C_2 = 1\,\mathrm{nF}$) and there is a discharge in the resistor ($R \sim 0.5\,\mathrm{M\Omega}$). This lead to a step potential (or a large peak, $C_2 R \sim 0.5\,\mathrm{ms}$) V_{out}, with the relation $Q = V_{\mathrm{out}} C_2$, with Q the charge actually accumulated in the capacitor.

This charge does not correspond to the real charge touching the MCP front. The first reason is the presence of secondary electrons. Indeed, some electrons can leave the MCP to go backward, and this is a source of underestimation of the charge. A positive potential V_{bias} has to be applied on the MCP front to solve this problem. However, such a potential is not desired on the acquisition devices. This is why it has to be decoupled with a capacitance ($C_1 = 100\,\mathrm{nF}$).

Stray capacitances may add to C_2, and a calibration is needed. A pulse generator is used to generate a pulse of amplitude V_{cal}, allowing to quickly accumulate charges in a perfectly known capacitor ($C_{\mathrm{cal}} = 1.64(2)\,\mathrm{pF}$) and quickly discharge ($C_{\mathrm{cal}} \sim 900\,\mathrm{ns}/50\,\Omega$) to simulate charges coming from the MCP front. Knowing C_{cal} and V_{cal}, the charge is known ($Q = C_{\mathrm{cal}} V_{\mathrm{cal}}$), and a calibration can be done to determine the charge as a function of V_{out}.

Therefore, electric pulses of varying amplitude V_{cal} are used and we look at V_{out} to determine the charge Q as a function of V_{out} such as

$$Q = C_{\mathrm{cal}} V_{\mathrm{cal}} = \frac{1}{a} C_{\mathrm{cal}} V_{\mathrm{out}}, \tag{5.3.1}$$

if V_{out} is proportional to V_{cal} (i.e., $V_{\mathrm{out}} = a V_{\mathrm{cal}}$). As it is presented in Figure 5.20, a is obtained by varying V_{cal} with $a = 6.69(2) \times 10^{-3}$. The error on the charge

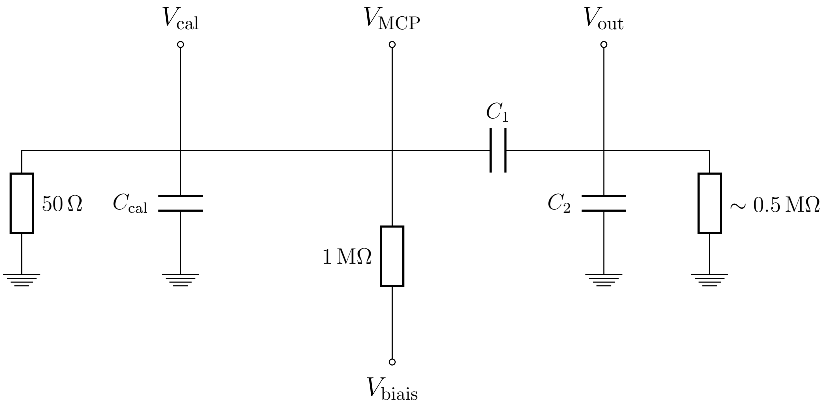

Figure 5.19 – Electric circuit of the charge counter. $C_{\mathrm{cal}} = 16.4\,\mathrm{pF}, C_1 = 100\,\mathrm{nF}, C_2 = 1\,\mathrm{nF}$.

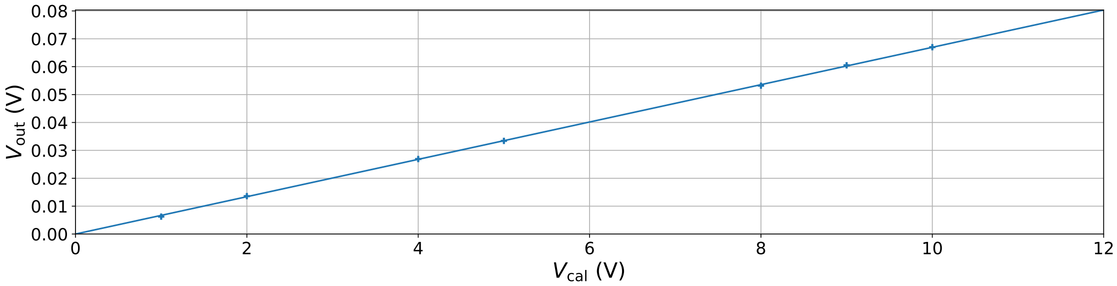

Figure 5.20 – Calibration of the charge counter. Output voltage as a function of the calibration signal amplitude.

measurement can be deduced from Equation 5.3.1 as following

$$\Delta Q = \frac{V_{\mathrm{out}}}{a}\Delta C_{\mathrm{cal}} \oplus \frac{C_{\mathrm{cal}}}{a}\Delta V_{\mathrm{out}} \oplus \frac{V_{\mathrm{out}}}{a^2}\Delta a. \tag{5.3.2}$$

Finally, the number of electrons N can be determined as a function of V_{out} using $N = Q/e$ (e $= 1.602\,176\,565(35) \times 10^{-19}\,\mathrm{C}$):

$$N = 1.532 \times 10^{10} V_{\mathrm{out}} \pm \left(0.006 \times 10^{10} V_{\mathrm{out}} \oplus 1.532 \times 10^{10} \Delta V_{\mathrm{out}}\right) \tag{5.3.3}$$

To determine the value of V_{bias} to avoid the secondary electron issue, a bunch of electrons is sent on the MCP's front for different values of V_{bias} while V_{out} is measured. The emission of secondary electrons leads to an underestimation of V_{out} as observed in Figure 5.21. By increasing V_{bias}, V_{out} is increased until there are no more secondary electrons if $V_{\mathrm{bias}} > 80\,\mathrm{V}$. For the following experiments, V_{bias} is set at 100 V.

5.3.2 Electron accumulation

Narrow wells

Electrons are accumulated in short wells (2 electrodes, i.e., 4.3 cm) or at the entrance either at the exit of the HFT. The potential profiles and the potential applied on the electrodes are presented respectively in Figure 5.22 and Table 5.4.

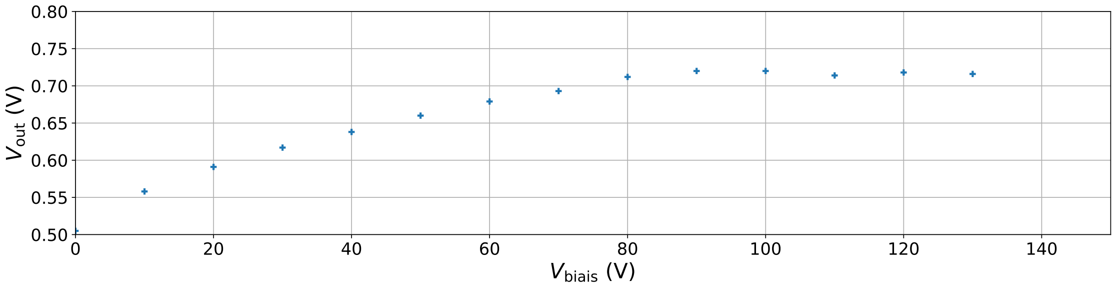

Figure 5.21 – Output signals for different biases. One can clearly see that the effect of the secondary electrons disappears above $V_{\text{bias}} = 100\,\text{V}$.

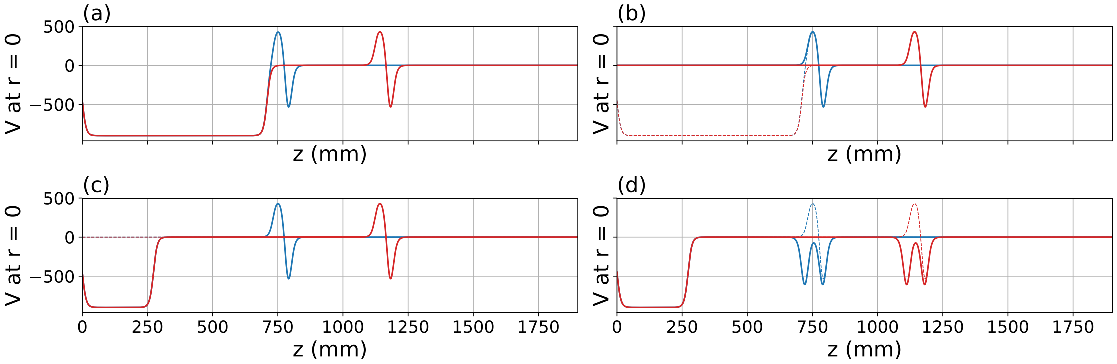

Figure 5.22 – Potential profiles in the HFT. Blue: HFT's entrance. Red: HFT's exit.

Electrode	-13	-12	-11	-10	-9	-8	-7
Electrode	-13	-12	-11	7	8	9	10
(a)	-900	-900	-900	0	500	500	-920
(b)	0	0	0	0	500	500	-920
(c)	-900	0	0	0	500	500	-920
(d)	-900	0	0	-920	0	0	-920

Table 5.4 – Potentials on the electrodes corresponding to the potential profiles in Figure 5.22.

The procedure used is the following:

- (a) the electron gun is turned on (warming up time 2.5 s, $V_{\text{gen}} = 2.6\,\text{V}, V_{\text{an}} = 15\,\text{V}$), a long barrier is applied to repel the incoming electrons, and the accumulation potential is set;
- (b) with the electron gun on, the entrance barrier is lowered to accumulate electrons for an adjustable time;
- (c) the electron gun is turned off, the entrance barrier is raised;
- 100 ms waiting;
- the electrons stay trapped for another adjustable time;

- (d) the electron plasma is prepared to be ejected by changing the potential in 2.7 ms and in 2000 steps;
- the exit potential is set to 0 V using a fast switch and consequently, the electrons are ejected from the trap to the MCP's front.

Figure 5.23 shows the number of trapped electrons as a function of the accumulation time. We could expect a number increasing with time and remaining constant when the well is full. However, this is not what we see here. Indeed, after and accumulation time of ~ 0.3 s, there is an instability in the number of detected electrons, inducing large error bars. These error bars are determined with Equation 5.3.3, with an error on the electric signal determined with 10 measurements. After a transitional period of few hundred of ms, the instability disappears and the number of detected electrons decrease slowly. Our hypothesis is that the hottest electrons are agitated and ejected by the incoming beam explaining the instability. It is also clear in Figure 5.23 that concerning the accumulation, the behaviour is the same if the trapping occurs at the entrance or the exit of the trap.

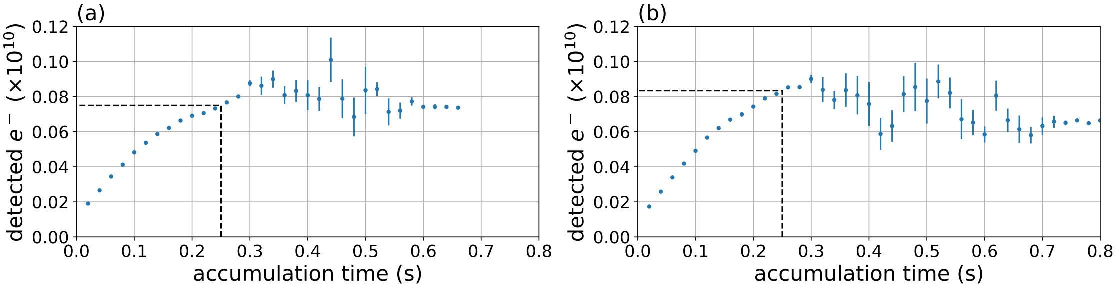

Figure 5.23 – Trapped electron number as a function of the accumulation time for a well at the entrance (a) or at the exit (b) of the HFT Electron gun: $V_{\text{gen}} = 2.6\,\text{V}, V_{\text{an}} = 15\,\text{V}$.

Therefore the accumulation time is set at 0.25 s, in order to produce a stable plasma of $\sim 8 \times 10^8$ electrons and to study the behaviour of electrons while they are trapped as presented in Figure 5.24. The number electrons N as a function of the trapping time t can be fit with $N(t) = N_1 e^{-t/\tau_1} + N_2 e^{-t/\tau_2}$. As a first interpretation,

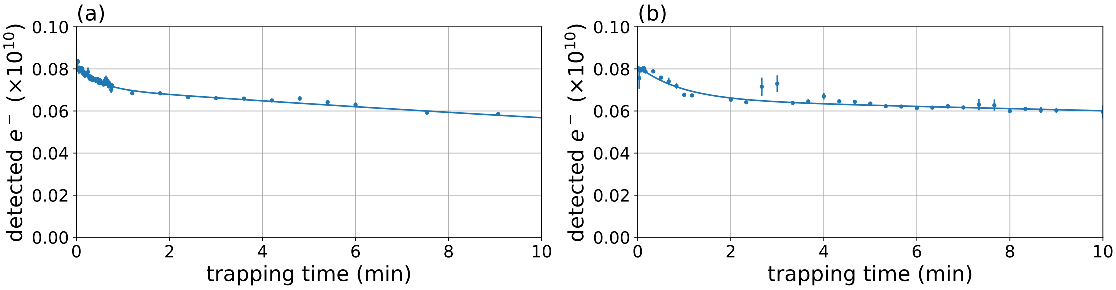

Figure 5.24 – Trapped electron number as a function of the waiting time after 0.25 s accumulation for a well at the entrance (a) or at the exit (b) of the HFT. Electron gun: $V_{\text{gen}} = 2.6\,\text{V}, V_{\text{an}} = 15\,\text{V}$.

there could be two populations N_1 and N_2 with different lifetimes τ_1 and τ_2 with $N_2 > N_1$ and $\tau_2 \gg \tau_1$. However it is more likely that it is the result of a misalignment of the electrodes with the magnetic field and after a certain time, there is a better stability of the trapped electrons, explaining the apparent two populations. The results of the fit are presented in Table 5.5. Even if in that case, we see that there is a difference between the well at the entrance and the well at the exit, we have the same order of magnitudes. This difference can be explained with a small misalignment, and with the difference of temperature between the entrance and the exit of the trap.

	N_1	N_2	τ_1	τ_2
(a) entrance	$1.1(1) \times 10^8$	$7.1(10) \times 10^8$	0.45(10) min	45(8) min
(b) exit	$1.6(2) \times 10^8$	$6.5(2) \times 10^8$	0.94(24) min	120(70) min

Table 5.5 – Parameters of the fit function $N(t) = N_1 e^{-t/\tau_1} + N_2 e^{-t/\tau_2}$ according to the data presented in Figure 5.24.

Wide wells

The same experiments as the ones presented in Section 5.3.2 are performed but with wider wells. Instead of using a well made of 2 electrodes, 6 electrodes are used (i.e., 13.5 cm long). The potential profiles are presented in Figure 5.25 and the potential applied on the electrodes in Table 5.6.

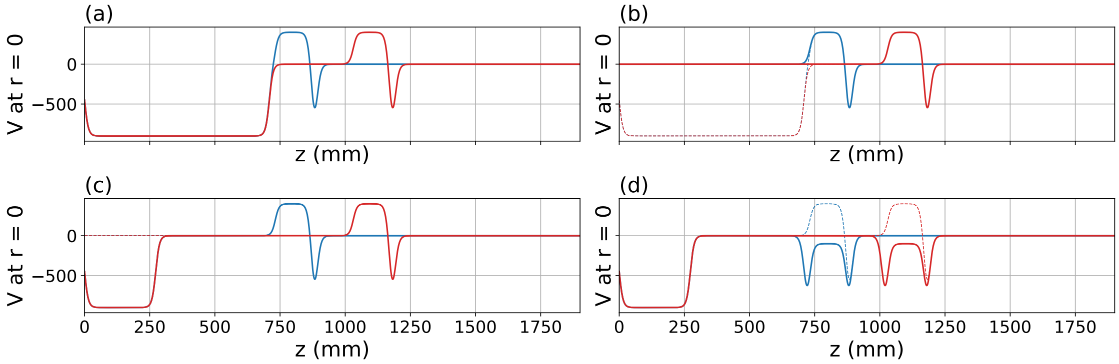

Figure 5.25 – Potential profiles in the HFT. Blue: HFT's entrance. Red: HFT's exit.

The accumulation curves presented in Figure 5.26 are similar to those for the short wells (Section 5.3.2). Indeed, there are instabilities when the electron number reaches the saturation limit after which the instabilities disappear and the number of accumulated electrons decreases slowly. The duration of the accumulation is set at 0.6 s in order to provide a stable plasma of 2.4×10^9 electrons.

The accumulation procedure being defined we estimate the lifetime in the well thanks to the data presented in Figure 5.27. Here again, it looks like there are two populations, one with a short lifetime (~ 1 min) and one with a longer lifetime (~ 10 min). The results of the fits are in Table 5.7. It is expected to have a smaller

Electrode	-13	-12	-11	-10	-9	-8	-7	-6	-5	-4	-3
Electrode	-13	-12	-11	3	4	5	6	7	8	9	10
(a)	-900	-900	-900	0	400	400	400	400	400	400	-920
(b)	0	0	0	0	400	400	400	400	400	400	-920
(c)	-900	0	0	0	400	400	400	400	400	400	-920
(d)	-900	0	0	-920	-100	-100	-100	-100	-100	-100	-920

Table 5.6 – Potentials on the electrodes corresponding to the potential profiles in Figure 5.25.

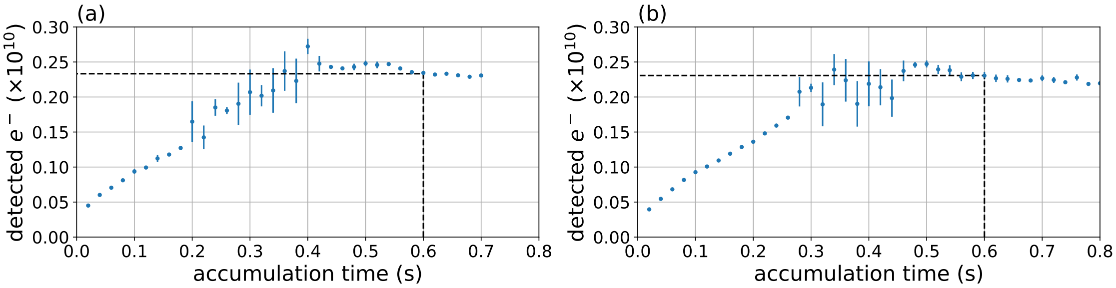

Figure 5.26 – Trapped electron number as a function of the accumulation time for a well at the entrance (a) or at the exit (b) of the HFT. Electron gun: $V_{\text{gen}} = 2.6\,\text{V}, V_{\text{an}} = 15\,\text{V}$.

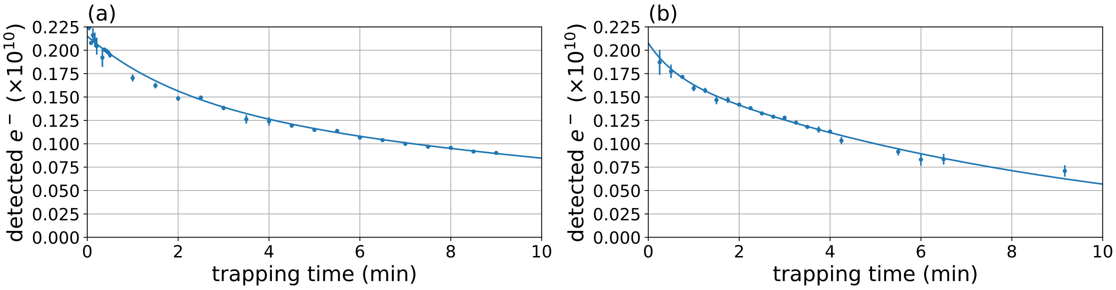

Figure 5.27 – Trapped electron number as a function of the waiting time after 0.6 s accumulation for a well at the entrance (a) or at the exit (b) of the HFT. Electron gun: $V_{\text{gen}} = 2.6\,\text{V}, V_{\text{an}} = 15\,\text{V}$.

	N_1	N_2	τ_1	τ_2
(a) entrance	$0.07(2) \times 10^{10}$	$0.14(2) \times 10^{10}$	2.1(6) min	19(5) min
(b) exit	$0.03(2) \times 10^{10}$	$0.17(1) \times 10^{10}$	0.6(4) min	9(1) min

Table 5.7 – Parameters of the fit function $N(t) = N_1 e^{-t/\tau_1} + N_2 e^{-t/\tau_2}$ according to the data presented in Figure 5.27.

lifetime ([97, 92]) than with the shorter wells and again, a difference is observed between the results obtained with wells at the entrance and the exit.

Wider well

Let's see what is happening with a single wider well (10 electrodes, i.e., 22.7 cm). The potential profiles and the potential applied on the electrodes are respectively presented in Figure 5.28 and Table 5.8.

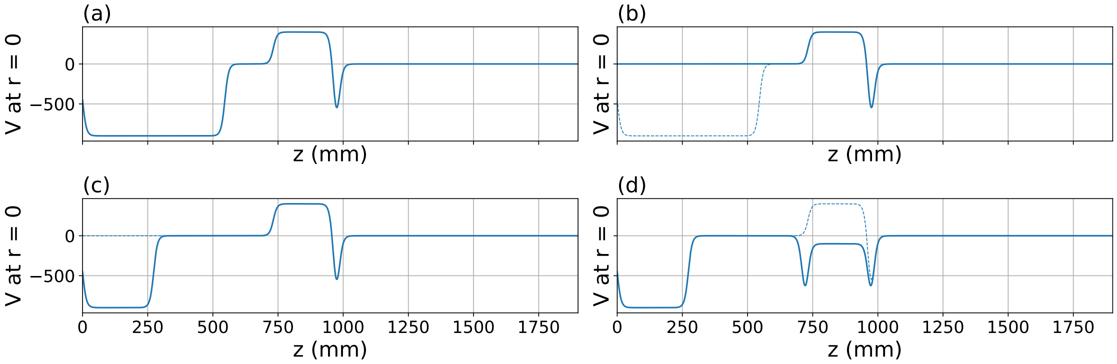

Figure 5.28 – Potential profiles in the HFT. See Table 5.8.

El.	-13	-12	-1	-10	-9	···	0	1
(a)	-900	-900	0	0	400	···	400	-920
(b)	0	0	0	0	400	···	400	-920
(c)	-900	0	0	0	400	···	400	-920
(d)	-900	0	0	-920	-100	···	-100	-920

Table 5.8 – Potentials on the electrodes corresponding to the potential profiles in Figure 5.28.

The same behaviour as the one presented in the previous experiment is observed for the accumulation (Figure 5.29a). This time, accumulating for 0.6 second a stable plasma of 3.5×10^9 electrons is obtained. A study of the lifetime in this configuration is reported in Figure 5.29a and Table 5.9. Compared to Table 5.7, It is observed that

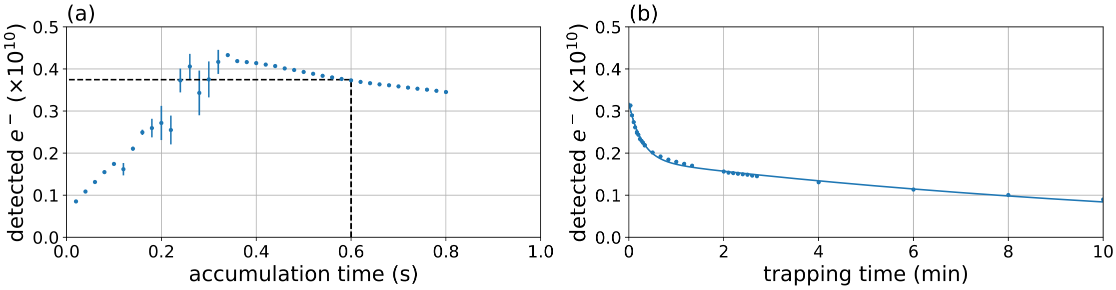

Figure 5.29 – (a) Trapped electron number as a function of the accumulation time. (b) Trapped electron number as a function of the waiting time after 0.6 s accumulation corresponding to the potentials presented in Table 5.8. Electron gun: $V_{\text{gen}} = 2.6\,\text{V}$, $V_{\text{an}} = 15\,\text{V}$.

N_1	N_2	τ_1	τ_2
$0.134(2) \times 10^{10}$	$0.183(1) \times 10^{10}$	0.28(1) min	12.8(2) min

Table 5.9 – Parameters of the fit function $N(t) = N_1 e^{-t/\tau_1} + N_2 e^{-t/\tau_2}$ according to the data presented in Figure 5.29.

the lifetime has decreased with the length of the trap. But this time, the fractions of short-lifetime and long-lifetime population are similar.

From all of these measurements a few remarks can be made. If we want to optimise the lifetime, it is more interesting to focus on a narrower well. Then, if we want to increase the number of trapped particles, it is better to increase the depth of the well. If it has not been done earlier, it is because we placed an electrical safety on the control system to prevent to apply a potential higher than 930 V on the electrode, to not reach the limit of 2 kV between two electrodes. This safety system has been removed now, and we are free to use higher potentials. Also, it might be interesting to focus on parabolic wells, because it has been shown that the lifetime is higher in that case [92].

Parabolic well

The potential applied on the n^{th} electrode is set such as $V_n = -an^2 + V_0$, with V_0 the potential applied on the electrode at the center of the well and for this electrode $n = 0$, to ensure a parabolic well, with $n \leq 5$. V_0 is set at 1000 V and $a = 4$ V to ensure $V_5 = 0$ V.

The energy of the incoming electrons and the heating of the filament are decreased to avoid the instability issue during the injection. The accumulation procedure has been changed compared to the previous sections, to obtain a sequence closer to what is described in Ref. [92]:

- (a) the electron gun is turned on (warming up time 2.5 s, $V_{\text{gen}} = 2.3$ V, $V_{\text{an}} = 13$ V), a long barrier is applied to repel the incoming electrons, and the accumulation potential is set;
- (b) with the electron gun on, the entrance barrier is lowered to accumulate electrons for an adjustable time;
- (c) the electron gun is turned off, the entrance barrier is raised;
- 100 ms waiting;
- the electrons stay trapped for another adjustable time;
- (d) the potential at the exit of the well is set at -2 kV, but the fast switch is not triggered, consequently, the voltage on the electrode is still 0 V and the barrier is raised in few nano seconds at the beginning of the next step;
- (e) the electron plasma is prepared to be ejected by changing the potential in 30 ms and in 2000 steps;

- (f) the exit potential is set to 0 V using a fast switch and consequently, the electrons are ejected from the trap to the MCP's front.

The potential profiles are presented in Figure 5.30 and the potentials applied on the electrodes in Table 5.10. The reason for step (d) is that it is not possible to directly go from step (c) to step (e). Indeed the fast switch is designed to go to a desired voltage quickly, but the rise of the potential after the fast switch is not the same as the HVA connected directly to the electrodes. Then, without this step, we would take the risk to make the plasma more unstable during the lifting of the well.

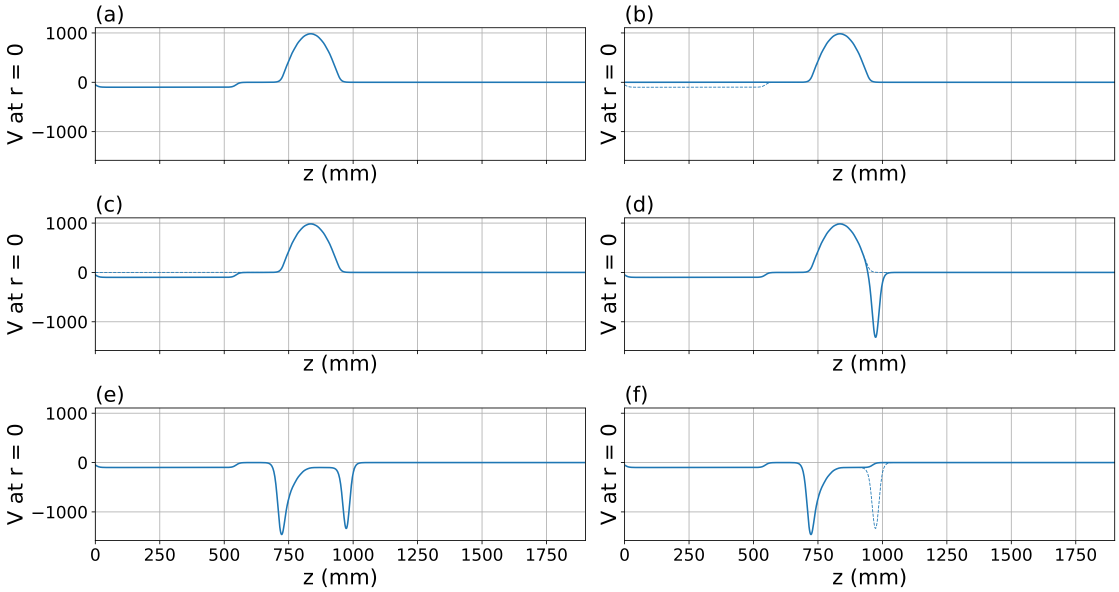

Figure 5.30 – Potential profiles in the HFT. See Table 5.10.

El.	-13	-12	-10	-9	-8	-7	-6	-5	-4	-3	-2	-1	0	1
(a)	-100	-100	0	360	640	840	960	1000	960	840	640	360	0	0
(b)	0	0	0	360	640	840	960	1000	960	840	640	360	0	0
(c)	-100	-100	0	360	640	840	960	1000	960	840	640	360	0	0
(d)	-100	-100	0	360	640	840	960	1000	960	840	640	360	0	-2000
(e)	-100	-100	-2000	-740	-460	-260	-140	-100	-100	-100	-100	-100	-100	-2000
(f)	-100	-100	-2000	-740	-460	-260	-140	-100	-100	-100	-100	-100	-100	0

Table 5.10 – Potentials on the electrodes corresponding to the potential profiles in Figure 5.30.

As desired and expected, a softer injection of the electrons prevents from the instabilities during the accumulation. This can be seen in Figure 5.31a. However, this leads to a longer accumulation time, and this is why this one is set at 2.5 s, providing a stable plasma of 6.6×10^9 electrons. Unfortunately, this parabolic well did not prevent from the loss of a large part of the electrons at the beginning of the trapping as shown in Figure 5.31b and the results of the fit in Table 5.11. Also, even if the lifetime is larger for the second population of electrons ($\sim$ 15 min instead of $\sim$ 12 min in the previous section), the difference is not significant enough compared to our expectation of a few hours.

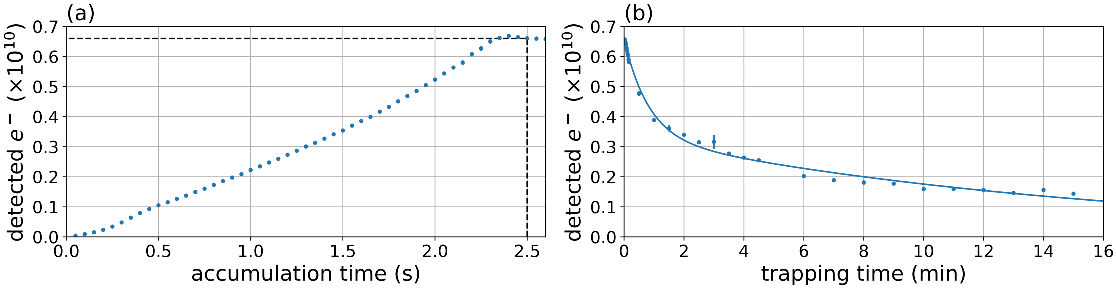

Figure 5.31 – (a) Trapped electron number as a function of the accumulation time. (b) Trapped electron number as a function of the waiting time after 2.5 s accumulation in the HFT. Electron gun: $V_{\text{gen}} = 2.3\,\text{V}, V_{\text{an}} = 13\,\text{V}$.

N_1	N_2	τ_1	τ_2
$0.322(4) \times 10^{10}$	$0.335(4) \times 10^{10}$	0.805(33) min	15.4(3) min

Table 5.11 – Parameters of the fit function $N(t) = N_1 e^{-t/\tau_1} + N_2 e^{-t/\tau_2}$ according to the data presented in Figure 5.31b.

From these experiments, we can conclude that it is possible to trap charged particles in the HFT for a long time. However, there is an issue during the confinement leading to a significant loss of the particles. This may be the resultant of an alignment issue between the electrodes and the magnetic field.

Parabolic well after partial realignement

An attempt to find a better alignment has been performed. Basically, we looked at the electron number for different positions of the duct at different trapping times. However, an optimal position of the electrodes has not been found, even if the situation has been improved, as presented in Figure 5.32 and Table 5.12 with an electron lifetime multiplied by a factor of of 2 compared to Table 5.11.

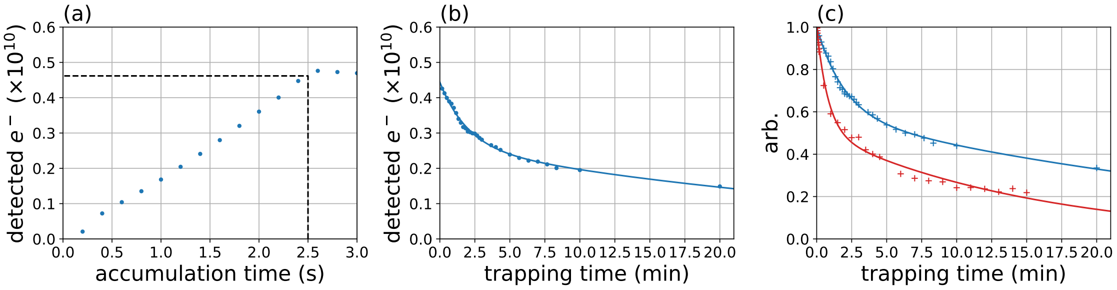

Figure 5.32 – After the electrodes have been displaced. (a) Trapped electron number as a function of the accumulation time. (b) Trapped electron number as a function of the waiting time after 2.5 s accumulation in the HFT. (c) Comparison with Figure 5.31b. Electron gun: $V_{\text{gen}} = 2.3\,\text{V}, V_{\text{an}} = 13\,\text{V}$.

Even if improvements are possible, we showed in this section that it is possible to reach around 10^{10} e^- in the HFT. In the next section we use the positron bunch

N_1	N_2	τ_1	τ_2
$0.183(5) \times 10^{10}$	$0.261(6) \times 10^{10}$	1.97(11) min	34.60(253) min

Table 5.12 – Parameters of the fit function $N(t) = N_1 e^{-t/\tau_1} + N_2 e^{-t/\tau_2}$ according to the data presented in Figure 5.32.

presented in the previous chapter, and stack as many positrons as possible.

5.4 Positron trapping

5.4.1 One stack in the HFT

The Buffer Gas Trap provides a bunch of $\sim 1.5 \times 10^6$ positrons each second, with the parameters presented in Chapter 4. The goal is to stack in the High Field trap to reach the maximal number of positrons. We first start with one stack re-trapped into the HFT. The entrance gate of the HFT is opened thanks to a fast switch, lowering the potential to 0 V for a duration δt which has to be determined (Figure 5.33a). Then the barrier is raised using the fast switch again (Figure 5.33b). Once this positron bunch is captured in the HFT, we wait for a duration t. Then, the potential well is lifted up to prepare the ejection (Figure 5.33c). This change of potential is made in 4.05 ms with 3000 steps. Finally, the positrons are ejected out of the trap by lowering the last potential barrier to 0 V with a fast switch (Figure 5.33d). The potentials applied on the electrodes during the sequence are presented in Table 5.13.

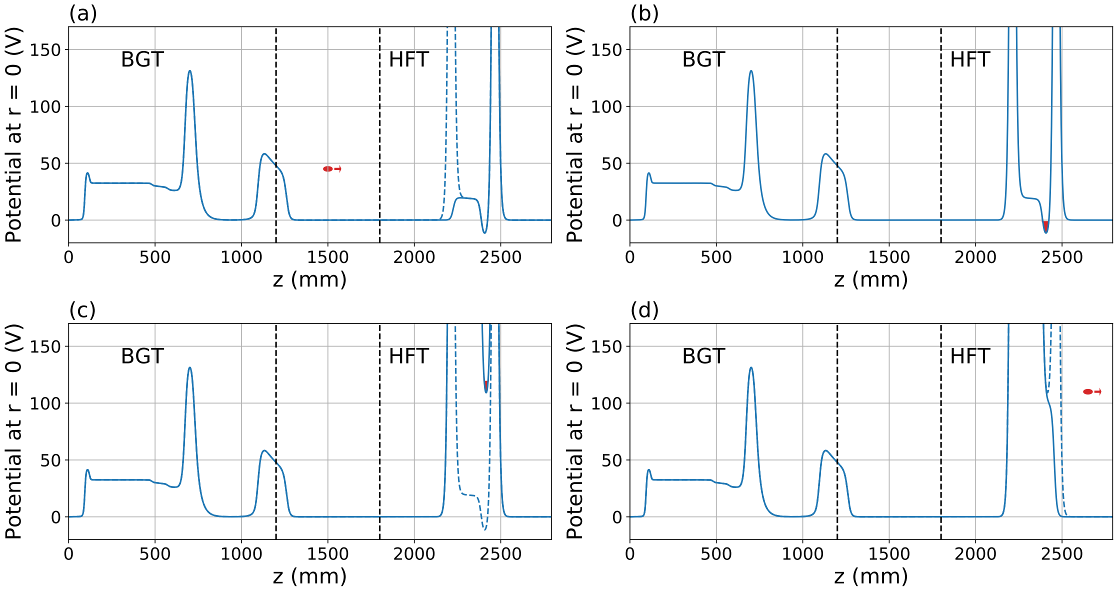

Figure 5.33 – Potential profiles used in the Buffer Gas Trap and High Field Trap. (a) Transfer into the HFT. (b) Positrons re-trapped. (c) Preparation for ejection. (d) Ejection. The coloured areas represent the positrons.

El.	-13	-12	-10	-9	-8	-7	-6	-5	-4	-3	-2	-1	0	1
(a)	0	0	0	20	19.75	19.5	19.25	19	18.75	18.5	-15	-15	-15	1000
(b)	0	0	1000	20	19.75	19.5	19.25	19	18.75	18.5	-15	-15	-15	1000
(c)	0	0	1000	400	390	380	370	360	350	340	-100	-100	-100	1000
(d)	0	0	1000	400	390	380	370	360	350	340	-100	-100	-100	0

Table 5.13 – Potentials on the electrodes. Potential profiles represented in Figure 5.33.

The amount of time δt, corresponding to opening time of the HFT's entrance, has to be adjusted. The idea is to vary δ, wait for 10 ms with the gate closed and look at a signal from a CsI probe close to the MCP at the exit of the HFT. If δt is too short, the positrons do not have the time to reach the potential well in the HFT, and consequently, no signal is detected. If it is too long, the positrons leave the trap and no signal is detected. As presented in Figure 5.34a, the CsI signal as function of δt displays a peak and the maximum of captured positrons is for $\delta t = 787.5$ ns.

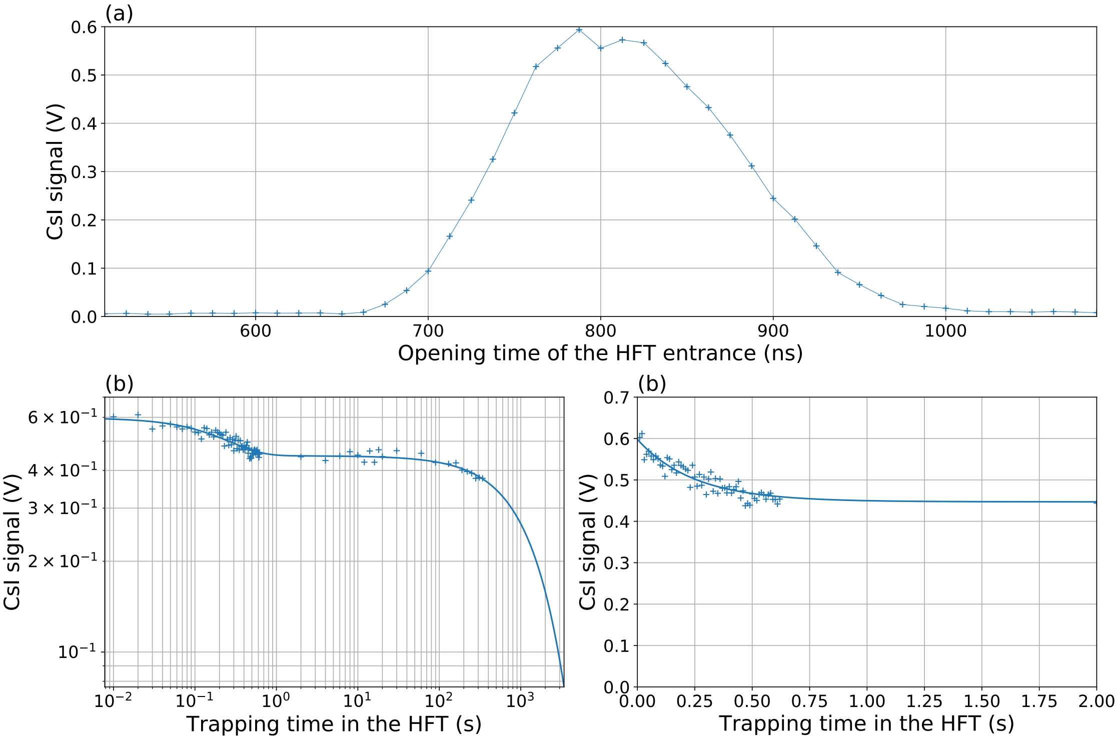

Figure 5.34 – (a) CsI signal as a function of the opening time of the HFT. (b) CsI signal as a function of the trapping time of the positrons in the HFT; the right picture is a zoom of the left one.

Once the positron bunch is trapped, we are interested in the lifetime. Figure 5.34b shows the CsI signal resulting from the annihilation of the positrons as a function of the trapping time. A similar effect to the one observed with the electron trapping occurs now: there is a loss of a third of the positrons in less than one second while the remaining positrons remain in the trap with a lifetime around 2000 s. The results of the fit are presented in Table 5.14.

N_1	N_2	τ_1	τ_2
$1.50(4) \times 10^{-1}$ V	$4.47(7) \times 10^{-1}$ V	$2.47(25) \times 10^{-1}$ s	$1.94(27) \times 10^{3}$ s

Table 5.14 – Parameters of the fit function $N(t) = N_1 e^{-t/\tau_1} + N_2 e^{-t/\tau_2}$ according to the data presented in Figure 5.34b.

This affects for the overall trapping efficiency (10^6 positrons are trapped while 1.5×10^6 were sent), and this problem must be solved if we want to reach 10×10^{10} positrons in the trap. For now, even if the situation is not optimal, we have to deal with this situation.

5.4.2 Stacking

Despite the efficiency issue, the lifetime of the remaining positrons in the trap is long enough to allow a stacking procedure. Thus, every 1.1 second, a bunch of 1.5×10^6 positrons from the third stage of the BGT is trapped in the HFT. The potentials used to trap one bunch in the previous section and presented in Figure 5.33 are also used for this sequence.

Figure 5.35 shows the CsI signal when n stacks are trapped and annihilated. After approximatively 40 stacks the CsI signal remains constant, which means that the well is full.

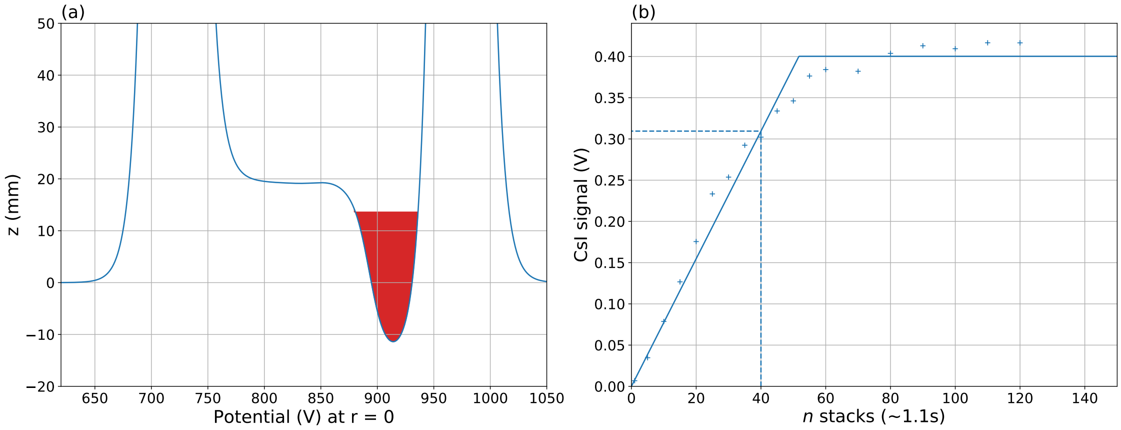

Figure 5.35 – (a) Potential profiles used for the stacking procedure. The coloured area represents the positrons(b) CsI signal as a function of the number of stack for the successive potential wells.

We would like to increase the number of stacks in the HFT by making the well deeper. However, we noticed that if the depth is too important, almost all the positrons are lost. It might be a consequence of the misalignment issue, knowing that the speed of the first positrons increases with the depth of the well. This is why the depth has been firstly set at −15 V. As we will see, when a stable plasma is already present in the trap, the problem disappears. Our procedure is to stack until the saturation limit, then the well is deepened in a way insuring to keep stacking with the same rate, i.e., to maintain the same slope on the linear part of the graph.

This operation is repeated until a new saturation limit is reached. The bottom of the well is decreased by applying the same voltage on the electrodes -2, -1 and 0 (see Table 5.13).

Therefore, after 40 stacks, the bottom of the well is decreased to −50 V and 70 stacks are added. With a potential of −80 V 50 stacks are added, with −120 V, 40 more stacks and finally the bottom of the well is lowered to −180 V and then a further 100 stacks are added to reach a total number of 300 stacks in the trap. The potential profiles used for these operations are presented in Figure 5.36a and the experimental results in Figure 5.36b.

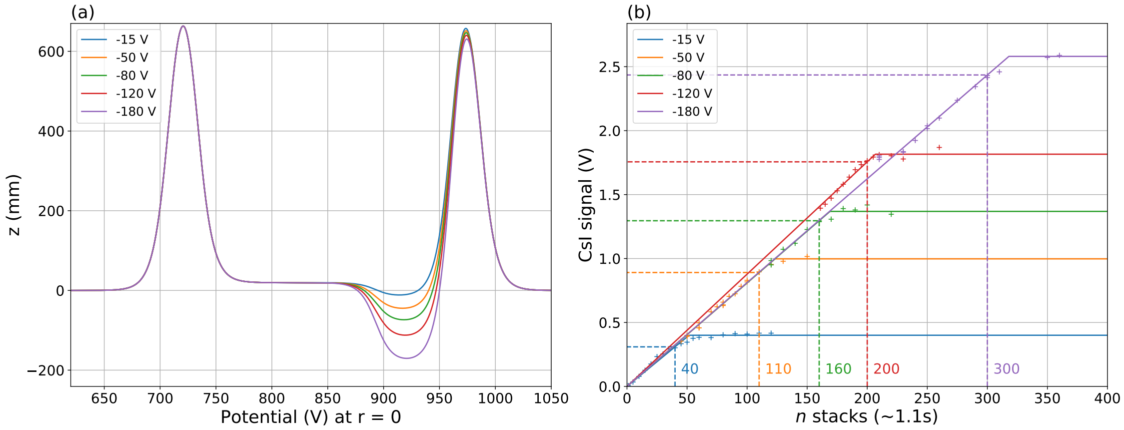

Figure 5.36 – (a) Potential profiles used for the stacking procedure. (b) CsI signal as a function of the number of stack for the successive potential wells.

From Figure 5.36b, two comments can be made. Firstly, the slopes seem similar, except for the fourth step of the stacking procedure. Data have been taken several times for this configuration, ensuring reproducibility of the measurement. However, when we go to the fifth step, the slope decreases to go back to a value similar to the previous one. Secondly, the saturation reached with the bottom of the well at −180 V is not due to the saturation of the well but to a saturation of the CsI detector. Once this has been understood, a second detector has been placed further away to provide a signal about 10 times smaller than the first detector (11.87 smaller). Then the data with this well have been taken again with both detectors to be able to compare the data from the second detector to the one for the first one. This is presented in Figure 5.37 where we clearly see that the saturation with the second detector appears later allowing to accumulate 350 stacks. The potential is then lowered consequently to −250 V and 400 V to add 250 and 400 stacks for a total of 1000 stacks as presented in Figure 5.37b. The slope and the limits are summarised in Table 5.15. The slopes decreases (except the fourth one as explained earlier) and this is not surprising because it reflects that positrons have a lifetime in the trap. The well just before the ejection has been changed during the measurements to ensure that the depth of the trapping well is deeper than the ejection well. These potential are presented in Table 5.16.

A calibration of the CsI detectors has been performed with a charge counter A230CF CoolFet [91], to determine the number of positrons hitting the MCP front

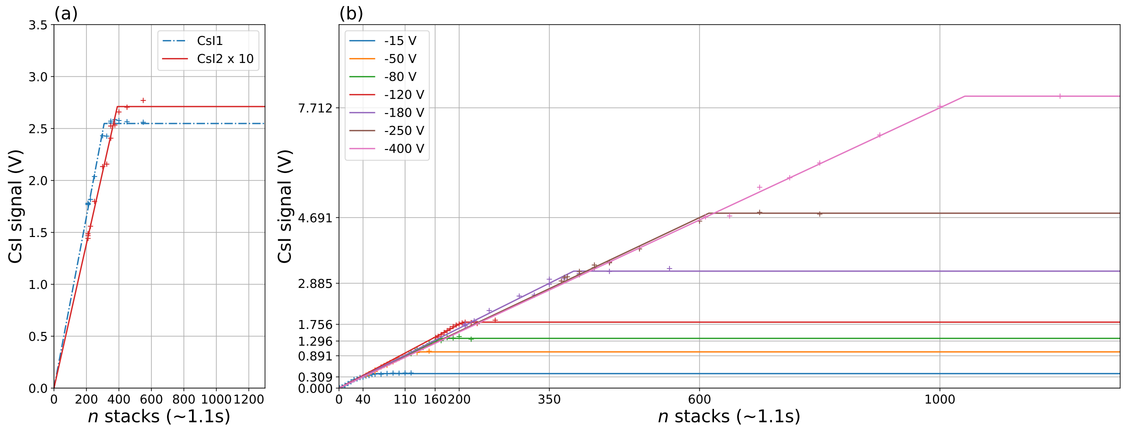

Figure 5.37 – Positron number as a function of the number of stack for the successive potential wells. (a) For the fifth well, with two CsI probes. (b) Starting from the fifth well, the second CsI is used and the data are extrapolated form the left plot.

bottom of the well	slope	stacking limit
$-15\,\mathrm{V}$	$7.73(21)\,\mathrm{mV}$ per stack	40
$-50\,\mathrm{V}$	$8.10(5)\,\mathrm{mV}$ per stack	$40 + 70 = 110$
$-80\,\mathrm{V}$	$8.10(8)\,\mathrm{mV}$ per stack	$110 + 50 = 160$
$-120\,\mathrm{V}$	$8.78(4)\,\mathrm{mV}$ per stack	$160 + 40 = 200$
$-180\,\mathrm{V}$	$8.24(8)\,\mathrm{mV}$ per stack	$200 + 150 = 350$
$-250\,\mathrm{V}$	$7.82(5)\,\mathrm{mV}$ per stack	$350 + 250 = 600$
$-400\,\mathrm{V}$	$7.71(6)\,\mathrm{mV}$ per stack	$600 + 400 = 1000$

Table 5.15 – Results of the fits in Figures 5.37b. The slopes are measured in the unit of the first CsI detector.

Bottom of well / El.	-10	-9	-8	-7	-6	-5	-4	-3	-2	-1	0	1
$-15\,\mathrm{V}$ to $-180\,\mathrm{V}$	1000	400	390	380	370	360	350	340	-100	-100	-100	1000
$-250\,\mathrm{V}$	1000	500	495	490	485	480	475	470	-100	-100	-100	1000
$-400\,\mathrm{V}$	1000	600	600	600	600	600	600	600	-100	-100	-100	1000

Table 5.16 – Potentials on the electrodes just before the ejection for the different stacking wells. The stacking wells corresponds to the situation in Figure 5.33b and the potentials just before the ejection to the one in Figure 5.33c

biased at 80 V. By measuring at the same time the CsI signal V_{CsI} (first probe) and the output voltage of the charge counter V_{out}, we obtained the following relationship:

$$V_{\mathrm{out}} = aV_{\mathrm{CsI}}, \quad a = 81.9(4). \tag{5.4.1}$$

The counter giving a signal of $v = 0.64\,\mu\mathrm{V}$ per positron, the CsI signal can be then calibrated such as

$$N = \frac{V_{\mathrm{out}}}{v} = a\frac{V_{\mathrm{CsI}}}{v} \pm \left(\Delta a\frac{V_{\mathrm{CsI}}}{v} \oplus a\frac{\Delta V_{\mathrm{CsI}}}{v}\right), \tag{5.4.2}$$

which gives numerically,

$$N = 1.28\times10^{8}V_{\mathrm{CsI}} \pm \left(6.25\times10^{5}V_{\mathrm{CsI}} \oplus 1.28\times10^{8}\Delta V_{\mathrm{CsI}}\right). \tag{5.4.3}$$

Then, the CsI signals are converted into positrons number and selecting only the points when the well are not full and considering that there is a bunch exactly every 1.1 s, the Figure 5.38 is obtained. According to this Figure 5.38, it has been possible following our procedure to store up to 1×10^9 positrons in the HFT in 1100 s (an extra-point corresponding to the saturation of the last well has been also displayed to show the maximum amount trapped). Finally, the data are fit with

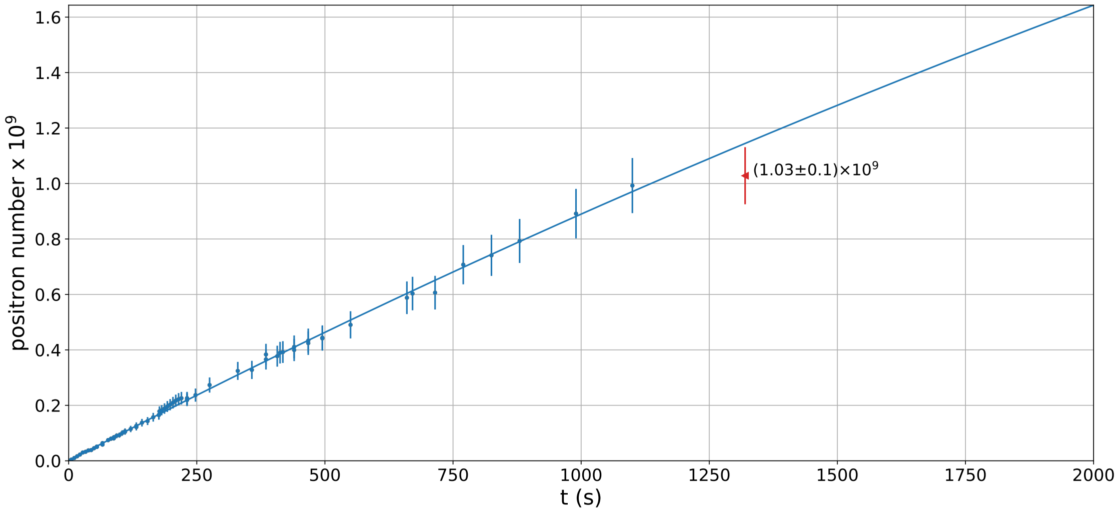

Figure 5.38 – Positron number as a function of the number of stacks and fit with $N(t) = R\tau\,(1 - \exp{(-t/\tau)})$. The data corresponds to the values from Figure 5.37 excluding the points corresponding to a saturation situation.

$N(t) = R\tau\,(1 - \exp{(-t/\tau)})$, with R the number of positrons trapped per second and τ the lifetime. We obtain $R = 0.97(10) \times 10^6\,\mathrm{s}^{-1}$ and $\tau = 6.0(9) \times 10^3\,\mathrm{s}$. The value of R is consistent with the loss observed with one stack while the value of τ is really promising because it implies one could reach ($\sim 5.8 \times 10^9$) positrons if the procedure is continued for a long time of several hours. However the trapping rate has yet to be increased by about two to reach 1×10^{10} positrons. More over a gain by two order of magnitudes is still needed to get such amount of positrons in 100 s.

5.5 Conclusion

In this chapter the High Field Trap of the GBAR experiment has been presented. This is a 5 T Penning-Malmberg trap allowing a confinement of a large amount of particles. Indeed, it was proven in Section 5.3 that it was possible to store much more than 10^9 electrons coming from the electron gun presented in Section 5.2. However, this also showed that there is probably an issue with the alignment of the electrodes with respect to the magnetic field. The same problem seems to occur during re-trapping of the positrons coming from the Buffer Gas Trap leading to a loss of about a third of the incoming positrons as presented in Section 5.4.

Nevertheless, a stacking of the positrons has been performed leading to a new record concerning the positrons trapping at the GBAR experiment with 10^9 positrons accumulated in 1100 s. The world record being of 4×10^9 in 14 400 s for the ATRAP collaboration, our result is really encouraging (see Table 5.17).

Device	$B(\mathrm{T})$	$N_{\mathrm{max}} \times 10^7$	$\tau_{\mathrm{c}}(\mathrm{s})$
UCSD	0.01	30	300
FPSI	0.04	10	∼ 1000
ALPHA	1	3	
ATHENA	3	120	∼ 9000
ATRAP	1	400	∼ 14400
GBAR (this work)	5	100	∼ 1100

Table 5.17 – Comparison to the maximum number of positrons trapped between different experiments. Data extracted from Ref. [98].

The work presented in this chapter was performed without the use of the Rotating Wall technique in the HFT, which is the next step in the positron trapping at the GBAR experiment. With this current settings, the overall efficiency is 3%.

Chapter 6

Future of the e^+ trapping at the GBAR experiment

> - It's time for plan B.
> - We have a plan B?
> - No ... but it's time for one.
>
> J. O'Neill, S. Carter, Stargate SG-1

Contents

As explained in the presentation of the GBAR experiment, it would be optimal to deliver 10^{10} positrons every 100 s in the reaction chamber. With the result in Section 5.4.2, we demonstrated the possibility of 10^8 positrons trapped in 100 s. A factor of 100 remains to be gained.

6.1 LINAC optimisation

The first idea is to increase the LINAC frequency to increase the number of incoming positrons per second. With the latest improvements of the LINAC [44] (end of 2020), it has been shown that the LINAC can operate for a long time at 200 Hz providing between 3×10^7 and 4×10^7 positrons per second. It is reasonable to affirm that in the next months, the LINAC will be able to run at 300 Hz and it has been shown that in that case, it could provide 5×10^7 positrons per second. Then a factor between 1.25 and 1.6 will be gained easily.

The LINAC could even provide more positrons. As shown in Figure 6.1, the number of positrons per pulse decreases with the LINAC frequency leading to a non-linearity between the frequency and the number of positrons per second. For example there are $2.6 \times 10^7\,\mathrm{e^+\,s^{-1}}$ at 100 Hz and $5 \times 10^7\,\mathrm{e^+\,s^{-1}}$ at 300 Hz. If it were linear, the LINAC would provide $7.8 \times 10^7\,\mathrm{e^+\,s^{-1}}$ at 300 Hz representing a gain of a factor of 2.6 relative to the operating point at 200 Hz.

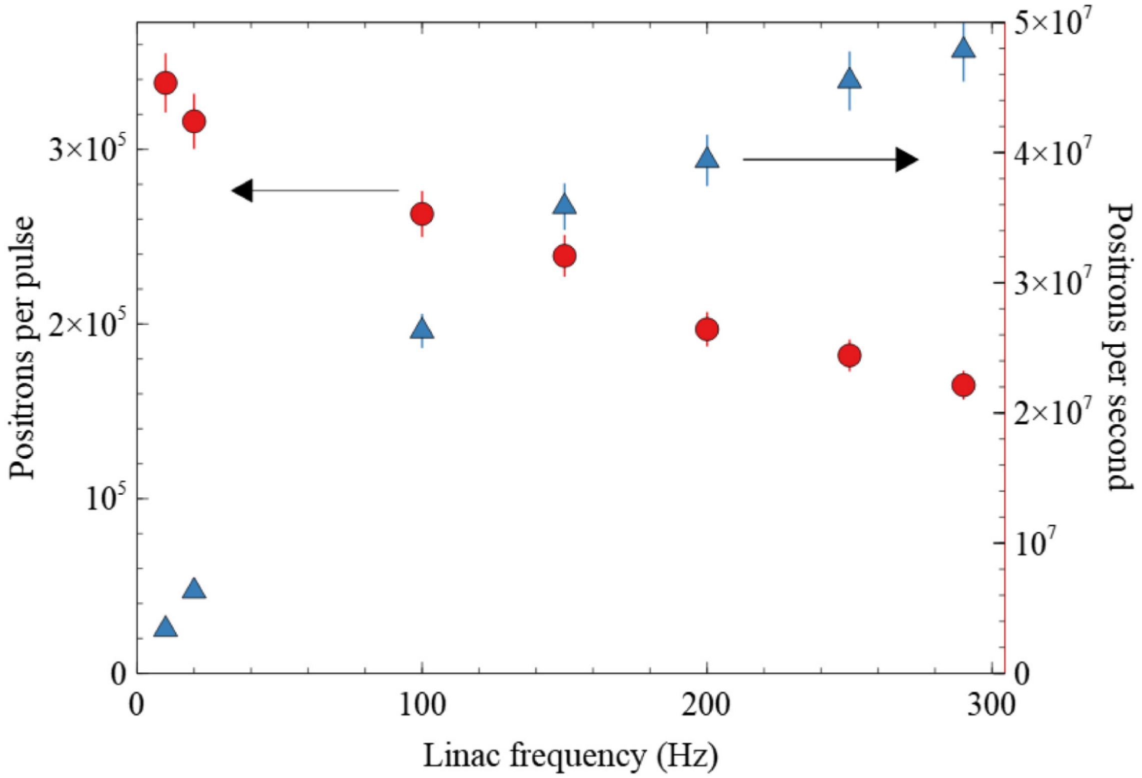

Figure 6.1 – Slow positron yield of the GBAR positron source as a function of the LINAC frequency. Both the number of positrons per pulse (circles) and the number of positrons per second (positron flux) (triangles) are shown. The yield was measured after more than 30 min operation at a given frequency. Extracted from Ref. [44].

The non-linearity is due to the heating of the target. To work around this problem, the idea is to move slightly and periodically the electron beam using a magnetic field to heat different areas of the target. This procedure will be implemented in the following months.

6.2 BGT optimisation

Another way to increase the positron trapping rate, is to keep optimising the BGT. It has been shown that this trap should provide an efficiency of 12% [48]. With a current efficiency of 5% (similar to the results obtained at the AIST [99]), a factor of 2.4 at least is expected to be gained. Together with the previous optimisation, we should gain a factor of 6.4, still far from 100.

However, it might be possible to increase the efficiency to 25%, as was obtained in a similar setup when the positron source was a 150-mCi ^{22}Na source [71].

6.3 Electron cooling

The improvement of the source and the BGT being not enough, a more efficient setup has to be tested: the electron cooling [51, 52]. This technique is also using the fact that we use a LINAC instead of a radioactive source.

As shown in Figure 6.2 the idea is to open and close quickly the HFT's entrance gate when a bunch of positrons is coming from the LINAC to trap the bunch (the BGT being then used as a simple magnetic guide line). Then the positrons are cooled thanks to coulombic interactions with an electron cloud previously trapped.

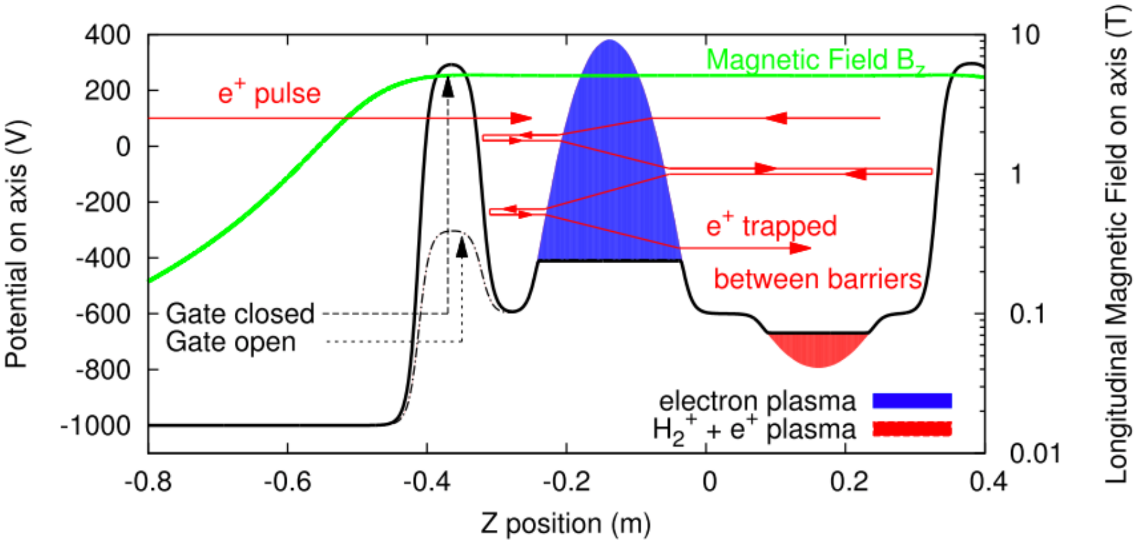

Figure 6.2 – Principle of the trapping and electron cooling of bunches of positrons from the LINAC into the HFT. Extracted from Ref. [51].

This technique should lead to an overall efficiency of 70% [52], compared to 3% ($3 \times 10^7 e^+$s coming from the LINAC and $1 \times 10^6 e^+$s accumulated in the HFT), providing then a factor of 20 and together with the LINAC optimisation, a factor of 50. Taking into account that we are installing an antiproton trap, it should be then possible to accumulate the antiprotons and to send 10^{10} positrons every 200 s (instead of every 100 s). The electron cooling might be a very good solution, considering that all the main elements (LINAC, electron gun and HFT) are already in place and functioning.

6.4 Si-C moderator

Another idea, currently tested at CEA Saclay and soon implemented at the GBAR experiment is to replace the N_2 by a SiC re-moderator [100] in the BGT. The rest of the cooling would be performed by the inelastic collisions with the CO_2 (scheme in Figure 6.3).

With this method still in development (Figure 6.4) the re-moderated positrons have a longitudinal energy of 2.4 eV with an energy spread $\sigma \sim 1$ eV.

If this new setup works then the efficiency of the BGT goes from 5% to 60%, giving a factor of 12. Together with the improvement of the LINAC it gives a factor

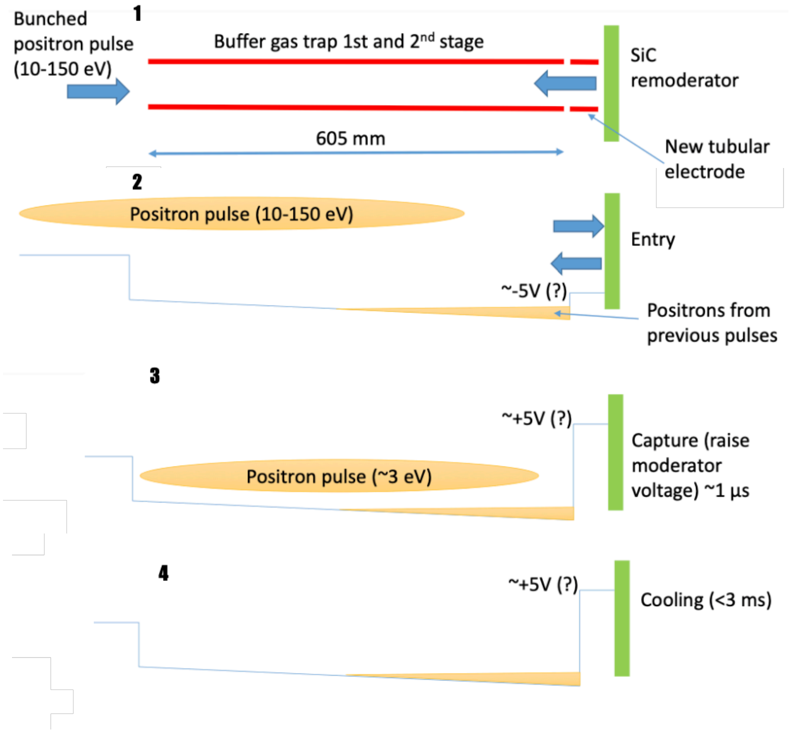

Figure 6.3 – Scheme of the trapping in the BGT using the SiC re-moderator. 1– the position of the elements. 2 – the exit barrier is lowered to let the incoming positrons interact with the SiC. 3 – the barrier is closed and the re-moderated positrons are trapped. 4 – cooling of the positrons with CO_2. The SiC re-moderator is movable to send the positrons into the HFT. Source L. Liszkay.

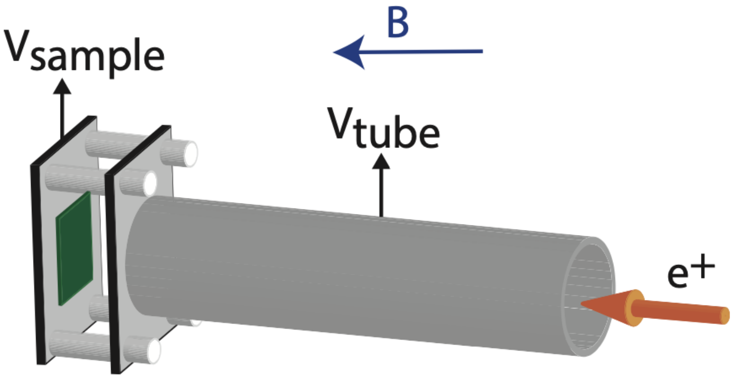

Figure 6.4 – Schematic diagram of the experimental setup. Positrons are accelerated onto the 4H-SiC target by applying the bias V_{sample} to a 30 cm long tube. Extracted from Ref. [48] (Chapter 7).

of 31, which could be a part of the solution and a complete solution if the transfer between the BGT and the HFT is improved.

6.5 Conclusion

In this chapter, a brief overlook of the future optimisations of the positron trapping at the GBAR experiment has been presented. The problem being that the final rate of the positron trapping is 100 times slower than what we would like for the $\overline{\mathrm{H}}^+$ production. Short term improvements have been presented such as the LINAC optimisation. However, deeper modifications have to be developed, such as the use of a Si-C re-moderator in the BGT or the electron cooling in the HFT. All together, these optimisations should provide a factor around 50. Then, instead of creating $\overline{\mathrm{H}}^+$ every 100 s, it would be every 200 s.

Chapter 7

Rocket equations

> The most unbelievable part of the film is that anyone with a PhD in physics would go anywhere near 1/4 gram of antimatter contained by a device built by someone with a PhD in physics
>
> Jeffrey Hangst

Contents

In this chapter, we will establish the equations of motion for a rocket. However, if we use antimatter to propel a rocket, we would like to see if it is possible to reach speeds close to the speed of light. In that case we also have to determine the equations of motion of a rocket within the framework of the special relativity.

An idea to reach such speeds would be to annihilate anti-hydrogen atoms and hydrogen atoms at rest (or almost at rest), to generate in majority π^+, π^-, π^0 and photons with a high momentum to use them as propellant. However, these particle should be ejected with a momentum in the opposite direction of the motion of the rocket and for that, we can use magnetic mirrors to realign the charged particles, but not the neutrals ones which leave the annihilation point in a quasi-isotropic way (it is done in chapter 8). Thus we also have to take into account in our equations a loss of propellant and this is what we will do in this chapter.

In our computations and schemes, we will consider the flux of neutral particles as two opposite jets, perpendicular to the rocket. But it is obvious that all the directions of the jets are equivalent as long as the jets are opposite (i.e. the sum of the momentum is zero).

The equations in the frame of the newtonian mechanics are presented in Section 7.1 and Section 7.2. As explained above, it is required to adapt the equations to the frame of the special relativity. It is done in Section 7.4 and Section 7.3. We finally present in Section 7.5 some numerical applications.

All this chapter can be compared with the articles of R.H. Frisbee [101, 102, 103] which are reference articles about the antimatter rocket study (but containing some miscalculations).

7.1 Classical equations

For the computation, we define a closed system Σ^* with a momentum $\overrightarrow{p}^*$ composed of the rocket and its propellant. Then the momentum $\overrightarrow{p}^*$ has to be conserved during the ejection of the propellant.

We apply momentum conservation for $\overrightarrow{p}^*$ relative to an inertial frame $\mathcal{R}_0$ between the moments t and $t + \mathrm{d}t$, of the closed system Σ^*. We note $m(t)$ the rocket's mass, $\overrightarrow{v}(t) = v(t)\overrightarrow{e_x}$ its velocity relative to $\mathcal{R}_0$ (assuming the rocket is moving along the x axis), $\mathrm{d}m_p$ the mass of propellant ejected between t and $t + \mathrm{d}t$, $\overrightarrow{w} = -w\overrightarrow{e_x}$, the velocity of ejection of the propellant relative to the rocket frame $\mathcal{R}_r$ (with $w > 0$ for an acceleration of the rocket and $w < 0$ for a deceleration).

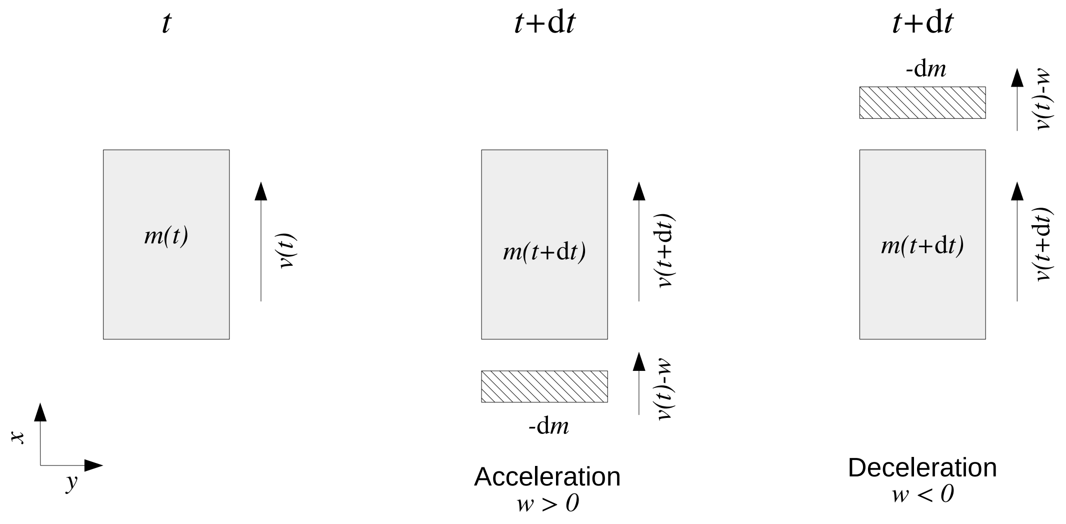

Figure 7.1 – Scheme representing the momentum conservation. The velocities are defined with respect to an inertial frame $\mathcal{R}_0$.

At moment $t + \mathrm{d}t$, we consider the momentum of the rocket which contains propellant but also the mass of propellant $-\mathrm{d}m$ ejected at the relative velocity w. The variation of the mass of the rocket containing propellant corresponds in absolute value to the mass of propellant ejected during the interval $[t, t + \mathrm{d}t]$.

$$p^*(t) = m(t)v(t), \tag{7.1.1a}$$
$$p^*(t + \mathrm{d}t) = m(t + \mathrm{d}t)v(t + \mathrm{d}t) - \mathrm{d}m(v(t) - w). \tag{7.1.1b}$$

Let's expand the Equation 7.1.1b with Taylor's expansion of first order:

$$\begin{aligned} p^*(t + \mathrm{d}t) &= (m(t) + \mathrm{d}m)(v(t) + \mathrm{d}v) - v(t)\mathrm{d}m + w\mathrm{d}m, \\ p^*(t + \mathrm{d}t) &= m(t)v(t) + m(t)\mathrm{d}v + w\mathrm{d}m, \end{aligned}$$

then we apply the momentum conservation:

$$p^*(t + \mathrm{d}t) - p^*(t) = 0 \Rightarrow m(t)\mathrm{d}v + w\mathrm{d}m = 0.$$

This gives us the following differential equation:

$$\mathrm{d}v = -w\frac{\mathrm{d}m}{m}. \tag{7.1.2}$$

This equation, once integrated, leads to:

$$v(t) - v(t_0) = -w \ln\left(\frac{m(t)}{m(t_0)}\right). \tag{7.1.3}$$

The mass of the rocket $m(t)$ is expressed simply by integrating the mass flow ($D_m(t) \leq 0$) which is a characteristic data of the rocket.

$$D_m(t) = \frac{\mathrm{d}m(t)}{\mathrm{d}t} \Leftrightarrow m(t) = m(t_0) + \int_{t_0}^{t} D_m(t')\mathrm{d}t'. \tag{7.1.4}$$

At this level of the computation, it is interesting to define the specific impulse I_{sp} [104], a characteristic number used to compare the propellants. If Equation 7.1.2 is rewritten as

$$m\frac{\mathrm{d}v}{\mathrm{d}t} = -w\frac{\mathrm{d}m}{\mathrm{d}t}, \tag{7.1.5}$$

it appears clearly that the thrust force is $F = -w\frac{\mathrm{d}m}{\mathrm{d}t}$. Then the total impulse is

$$I_{\mathrm{tot}} = \int_0^t F(t')\mathrm{d}t'. \tag{7.1.6}$$

To obtain a characteristic number independent of the rocket (then only related to the propellant), the specific impulse I_{sp} is defined as the ratio between the total impulse and the weight of propellant i.e.

$$I_{\mathrm{sp}} = \frac{\int_0^t F(t')\mathrm{d}t}{-g\int_0^t \frac{\mathrm{d}m}{\mathrm{d}t'}\mathrm{d}t'}, \tag{7.1.7}$$

expressed in seconds, where g is the gravitational acceleration on Earth. In the case of w being constant, the specific impulse is

$$I_{\mathrm{sp}} = \frac{w}{g}. \tag{7.1.8}$$

Another way to understand the I_{sp} is to consider it as the time in seconds during which a propellant can propel its own mass with an acceleration g. Indeed, if $\frac{\mathrm{d}v}{\mathrm{d}t} \to g$, Equation 7.1.2 leads to

$$\frac{\mathrm{d}m}{\mathrm{d}t} + \frac{m}{I_{\mathrm{sp}}} = 0 \to m(t) = m_0 \exp\left(-\frac{t}{I_{\mathrm{sp}}}\right). \tag{7.1.9}$$

7.2 Classical equations with loss of propellant

This time, we consider that the mass $-\mathrm{d}m$ of propellant ejected by the rocket between t and $t+\mathrm{d}t$ is ejected for a fraction ξ along the main axis and for a fraction $(1-\xi)$, along the perpendicular axis on both sides of the rocket such that the momentum along this axis is zero with a speed w' relative to $\mathcal{R}_r$ (Figure 7.2).

In the closed system {rocket + ejected propellant} at the moment t, the momentum along the x axis is written:

$$p^*(t) = m(t)v(t). \tag{7.2.1}$$

At the moment $t+\mathrm{d}t$, we have to consider three terms:

- the momentum of the rocket with propellant inside
- the momentum of the mass $-(1-\xi)\mathrm{d}m$ of propellant ejected perpendicularly (but it has a non-zero contribution to the overall momentum along the x axis due to the velocity v relative to the inertial frame $\mathcal{R}_0$)
- the momentum of the mass $-\xi\mathrm{d}m$ of propellant ejected along the x axis

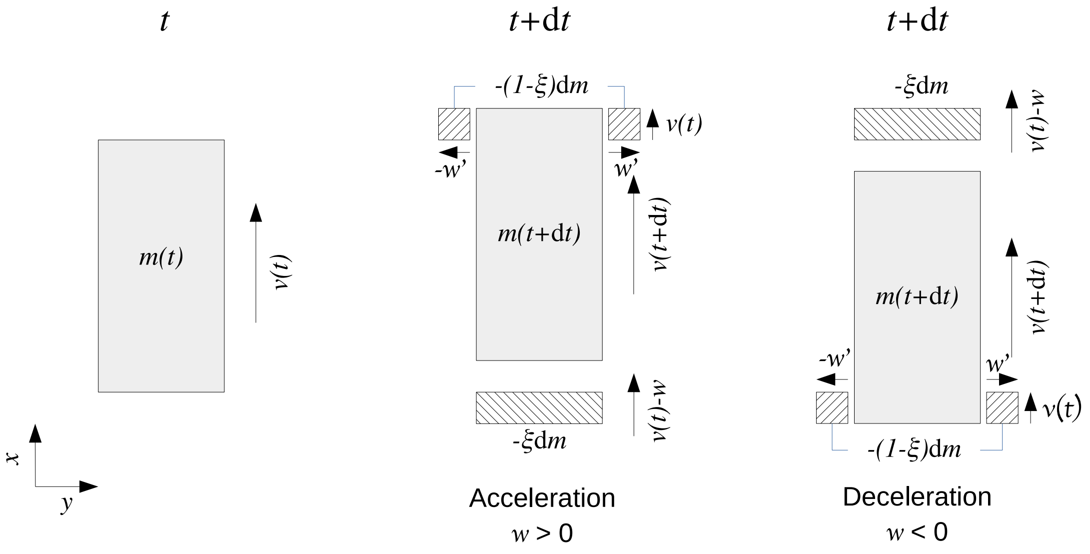

Acceleration $w > 0$

Deceleration $w < 0$

Figure 7.2 – Scheme representing the momentum conservation. In that case, we consider a loss of propellant. The velocities are defined with respect to an inertial frame $\mathcal{R}_0$.

Also, the momentum conservation can be written:

$$\begin{aligned} p^*(t+\mathrm{d}t) &= (m+\mathrm{d}m)(v+\mathrm{d}v) - (1-\xi)v\mathrm{d}m - \xi(v-w)\mathrm{d}m, \\ &= p^*(t) + m\mathrm{d}v + \xi w\mathrm{d}m. \end{aligned}$$

This leads to the following differential equation:

$$\mathrm{d}p^* = m\mathrm{d}v + \xi w\mathrm{d}m. \tag{7.2.2}$$

Thanks to the momentum conservation (i.e. $\frac{\mathrm{d}p^*(t)}{\mathrm{d}t} = 0$) we establish this differential equation for the velocity

$$\mathrm{d}v = -\tilde{w}\frac{\mathrm{d}m}{m}, \tag{7.2.3}$$

where $\tilde{w} = \xi w$. This equation can be easily integrated as

$$v(t) - v(t_0) = -\tilde{w}\ln\left(\frac{m(t)}{m(t_0)}\right). \tag{7.2.4}$$

If we compare the equations 7.1.3 and 7.2.4, we see that finally, the loss of propellant described in this model is equivalent to a decrease of the propellant ejection velocity, and therefore, to a diminution of the specific impulse defined as

$$I_{sp} = \xi\frac{w}{g} < \frac{w}{g}, \tag{7.2.5}$$

where g is the acceleration of earth gravity.

The result presented in this section differs from what is presented in the first Frisbee's article. For example, Eq. 7.2.3 can be compared with Eq. A-20 in Ref. [101] (but corrected in Ref. [103]). Indeed, in Eq. A-18, it has been forgotten that the lost propellant has a momentum along the x-axis. With our notations, this equation should be transformed as

$$\mathrm{d}\,(mv) = (v - w)\xi\mathrm{d}m \rightarrow \mathrm{d}\,(mv) = -(v - w)\xi\mathrm{d}m + (1 - \xi)\,v\mathrm{d}m, \tag{7.2.6}$$

to add the missing component and then the same result as ours would be obtained.

7.3 Relativistic equations

To obtain the relativistic equations, we need to define 3 frames:

- $\mathcal{R}_0$ a reference intertial frame,
- $\mathcal{R}_r$ the moving frame of the rocket,
- $\mathcal{R}_c(t)$ the comoving frame, an inertial frame coinciding with $\mathcal{R}_r$ at a given moment t and moving at a constant velocity $V = v(t)$ with respect to $\mathcal{R}_0$.

This apparent complication allows us in particular to use the Lorentz transformation (see Appendix A about special relativity) and the laws deriving from it since it only applies for reference frames in uniform rectilinear motion.

We can now apply the energy-momentum conservation in the comoving frame (Figure 7.3).

- proper instant τ (the time in $\mathcal{R}_r$, see definition in Appendix A):
  - the rocket is at rest in the comoving frame, the energy-momentum 4-vector is written as

$$\mathbf{P}(\tau) = \begin{pmatrix} mc \\ 0 \\ 0 \\ 0 \end{pmatrix},$$

- proper instant $\tau + \mathrm{d}\tau$:
    - the rocket acquires an infinitesimal velocity $\mathrm{d}v'$ in this frame and its mass becomes $m(\tau + \mathrm{d}\tau) = m + \mathrm{d}m$,
    - A mass $\mathrm{d}m_p$ of propellant is ejected at relative velocity $-w$,
    - $\mathbf{P}(\tau + \mathrm{d}\tau) = \mathbf{P}_{\text{rocket}} + \mathbf{P}_{\text{p}}$

$$\mathbf{P}_{\text{rocket}} = \begin{pmatrix} \gamma(\mathrm{d}v')(m + \mathrm{d}m)c \\ \gamma(\mathrm{d}v')(m + \mathrm{d}m)\mathrm{d}v' \\ 0 \\ 0 \end{pmatrix}, \mathbf{P}_{\text{p}} = \begin{pmatrix} \gamma(w)\mathrm{d}m_p c \\ -w\gamma(w)\mathrm{d}m_p \\ 0 \\ 0 \end{pmatrix},$$

with the function $\gamma(v) = \frac{1}{\sqrt{1-\left(\frac{v}{c}\right)^2}}$, and at the first order in $\mathrm{d}v'$, $\gamma(\mathrm{d}v') = 1 + o(\mathrm{d}v')$.

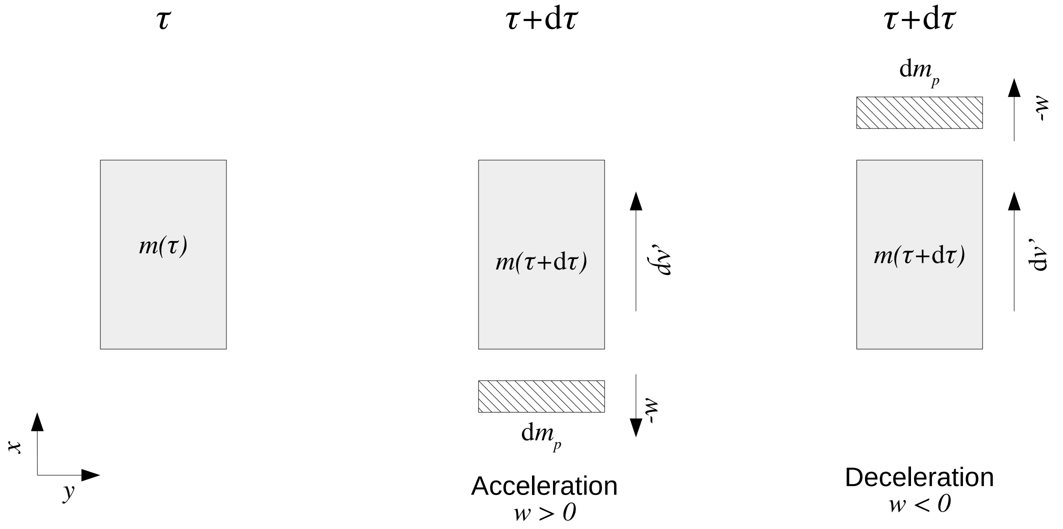

Figure 7.3 – Scheme representing the energy-momentum conservation. The velocities are here defined with respect to the comoving frame.

The energy-momentum conservation ($\mathbf{P}(\tau+\mathrm{d}\tau) = \mathbf{P}(\tau)$) with Taylor's expansion of first order in $\mathrm{d}v', \mathrm{d}m$ and $\mathrm{d}m_p$ gives us

$$\gamma(w)\mathrm{d}m_p = -\mathrm{d}m,$$
$$\gamma(w)\mathrm{d}m_p = \frac{m\mathrm{d}v'}{w}.$$

So we get a differential equation comparable to the classical case (Equation 7.1.2):

$$\mathrm{d}v' = -w\frac{\mathrm{d}m}{m}. \tag{7.3.1}$$

Now, we need to know the $\mathrm{d}v$ variation corresponding to the difference of velocity but in the inertial frame $\mathcal{R}_0$. For that, we use the velocity composition law between the inertial frame $\mathcal{R}_0$ and the comoving frame $\mathcal{R}_c$ (Equation A.2.2):

$$v'_x = \frac{v_x - V}{1 - v_x V/c^2} \Rightarrow \mathrm{d}v'_x = \frac{\mathrm{d}v_x}{1 - v_x V/c^2} - \frac{(v_x - V) \times (v/c^2) \times \mathrm{d}v_x}{(1 - v_x V/c^2)^2},$$

however $V = v(t)$, $v_x = v(t)$, $\mathrm{d}v_x = \mathrm{d}v$ and $\mathrm{d}v'_x = \mathrm{d}v'$:

$$\mathrm{d}v' = \frac{\mathrm{d}v}{1 - \left(\frac{v}{c}\right)^2}.$$

This leads to the differential equation (similar to Ref. [101], Eq. A-13):

$$\frac{\mathrm{d}m}{m} = \frac{-1}{w} \frac{\mathrm{d}v}{1 - \left(\frac{v}{c}\right)^2}. \tag{7.3.2}$$

This equation with separate variables can be easily integrated:

$$\int_{m(t_0)}^{m(t)} \frac{\mathrm{d}m}{m} = \frac{-c^2}{w} \int_{v(t_0)}^{v(t)} \frac{\mathrm{d}v}{1 - \left(\frac{v}{c}\right)^2} = \frac{-c}{w} \int_{v(t_0)/c}^{v(t)/c} \frac{\mathrm{d}x}{1 - x^2},$$

$$\ln\left(\frac{m(t)}{m(t_0)}\right) = \frac{-c}{2w} \ln\left(\frac{(1 + \frac{v(t)}{c})(1 - \frac{v(t_0)}{c})}{(1 - \frac{v(t)}{c})(1 + \frac{v(t_0)}{c})}\right),$$

$$\left(\frac{m(t)}{m(t_0)}\right)^{\frac{-2w}{c}} = \frac{(c + v(t))(c - v(t_0))}{(c - v(t))(c + v(t_0))}. \tag{7.3.3}$$

And we finally obtain the expression of $v(t)$:

$$v(t) = c \frac{\left(\frac{m(t)}{m(t_0)}\right)^{\frac{-2w}{c}} \left(\frac{c+v(t_0)}{c-v(t_0)}\right) - 1}{\left(\frac{m(t)}{m(t_0)}\right)^{\frac{-2w}{c}} \left(\frac{c+v(t_0)}{c-v(t_0)}\right) + 1}, \tag{7.3.4}$$

with as a reminder $w > 0$ for an acceleration and $w < 0$ for a deceleration.

Note: with Taylor's expansion of first order in $\frac{w}{c}$ and $\frac{v(t_0)}{c}$

$$\left(\frac{m(t)}{m(t_0)}\right)^{\frac{-2w}{c}} = 1 - \frac{2w}{c} \ln\left(\frac{m(t)}{m(t_0)}\right), \qquad \frac{2w}{c} \ll 1,$$

$$\frac{c + v(t_0)}{c - v(t_0)} = \frac{1 + \frac{v(t_0)}{c}}{1 - \frac{v(t_0)}{c}} = 1 + 2\frac{v(t_0)}{c}, \qquad \frac{v(t_0)}{c} \ll 1,$$

we can find the expression of v in the classical limit (Equation7.1.3).

Looking at the Equation 7.3.4, we need to know what is the expression of $m(t)$. But it is more difficult than in the previous case because the mass flow rate is defined in the frame associated to the rocket, so we can no longer use $D_m(t) = \frac{\mathrm{d}m(t)}{\mathrm{d}t}$. The article W. L. Bade [105] help us to overcome this problem. Let's reformulate the differential Equation 7.3.2 to correspond to the article:

$$w\left[1 - \frac{v^2}{c^2}\right] \mathrm{d}m + m\mathrm{d}v = 0, \tag{7.3.5}$$

and we define the mass flow on board the rocket by:

$$\rho(\tau) = \frac{\mathrm{d}m}{\mathrm{d}\tau}, \tag{7.3.6}$$

with τ the proper time of the rocket, this gives us the evolution of the mass as a function of τ:

$$m(\tau) = m(\tau_0) + \int_{\tau_0}^{\tau} \rho(\tau')\mathrm{d}\tau'. \tag{7.3.7}$$

The rapidity θ is defined as a function of the proper time θ by

$$\cosh\theta = \frac{\mathrm{d}t}{\mathrm{d}\tau}, \tag{7.3.8a}$$

$$c\sinh\theta = \frac{\mathrm{d}x}{\mathrm{d}\tau}, \tag{7.3.8b}$$

$\cosh\theta$ being by definition the Lorenz factor γ. Then, the velocity can be expressed as a function of the rapidity

$$v = \frac{\mathrm{d}x}{\mathrm{d}t} = c\tanh\theta, \tag{7.3.9a}$$

$$\theta(\tau) = \mathrm{argth}\frac{v}{c}. \tag{7.3.9b}$$

Injecting 7.3.9a in 7.3.5 and assuming $v_0 = 0$, we obtain

$$\frac{\mathrm{d}\theta}{\mathrm{d}\tau} = -\frac{w}{m(\tau)c}\rho(\tau), \tag{7.3.10}$$

giving us a expression of $\theta(\tau)$ thanks to $\rho(\tau)$ and $m(\tau)$:

$$\theta(\tau) = \theta(\tau_0) - \frac{w}{c}\int_{\tau_0}^{\tau} \frac{\rho(\tau)}{m(\tau)}\mathrm{d}\tau'. \tag{7.3.11}$$

Then now we have the travelled distance and the corresponding time in the reference frame as a function of the proper time of the rocket (because the mass flow rate as a function of the proper time is a characteristic of the rocket):

$$x(\tau) = x(\tau_0) + c\int_{\tau_0}^{\tau} \sinh\left(\theta(\tau')\right)\mathrm{d}\tau', \tag{7.3.12a}$$

$$t(\tau) = t(\tau_0) + \int_{\tau_0}^{\tau} \cosh\left(\theta(\tau')\right)\mathrm{d}\tau'. \tag{7.3.12b}$$

In summary, we now have the velocity, the travelled distance and the time in the reference frame as a function of the proper time of the rocket, the whole being connected to the mass flow measured on board the rocket.

7.4 Relativistic equations with propellant loss

We now apply the energy-momentum conservation law, considering that a fraction of propellant is ejected perpendicularly to the rocket in its proper frame $\mathcal{R}_c$ (Figure 7.4). We place us in the co-moving frame at the proper time τ.

This time we have to pay more attention to the handled terms. During the amount of time $\mathrm{d}\tau$, the rocket lost a mass $-\mathrm{d}m$, so an energy $-(\mathrm{d}m)c^2$. This energy is distributed according a fraction ξ for the useful propellant (ejected with a velocity $-w$ along the x axis) and $(1-\xi)$ for the lost propellant (ejected with a velocity $\pm w_\perp$):

$$-(\mathrm{d}m)c^2 = \underbrace{-(\mathrm{d}m)\xi c^2}_{\gamma(w)\mathrm{d}m_{p_1}c^2}\underbrace{-(1-\xi)(\mathrm{d}m)c^2}_{\gamma(w_\perp)\mathrm{d}m_{p_2}c^2}. \tag{7.4.1}$$

So we have $\mathrm{d}m_{p_1}$ the mass of propellant ejected along x with a velocity w and $\mathrm{d}m_{p_2}$ ejected along the y axis with a relative velocity $\pm w_\perp$:

$$\gamma(w)\mathrm{d}m_{p_1} = -(\mathrm{d}m)\xi, \tag{7.4.2a}$$

$$\gamma(w_\perp)\mathrm{d}m_{p_2} = -(1-\xi)(\mathrm{d}m). \tag{7.4.2b}$$

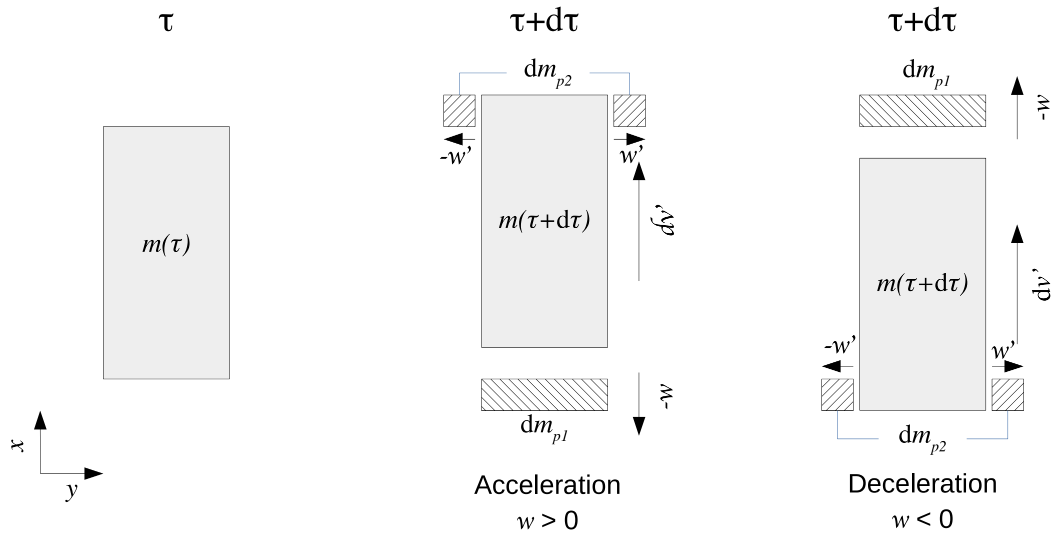

Figure 7.4 – Scheme of the energy-momentum conservation. The velocities are here defined with respect to the comoving frame to the rocket at the proper time τ.

Now we can apply the energy-momentum conservation law:

- proper time τ:
    - the rocket is at rest in its comoving frame

$$\mathbf{P}(\tau) = \begin{pmatrix} mc \\ 0 \\ 0 \\ 0 \end{pmatrix}$$

- proper time $\tau + \mathrm{d}\tau$:
    - the rocket acquires a velocity $\mathrm{d}v'$ in that frame
    - $\mathrm{d}m_{p_1}$ is ejected with the velocity $-w$ along the main axis
    - $\frac{1}{2}\mathrm{d}m_{p_2}$ is ejected with the velocities $+w_\perp$ et $-w_\perp$ along the perpendicular axis
    - $\mathbf{P}(\tau + \mathrm{d}\tau) = \mathbf{P}_{\mathrm{rocket}} + \mathbf{P}_{\mathrm{p}} + \mathbf{P}_{\mathrm{p}\perp 1} + \mathbf{P}_{\mathrm{p}\perp 2}$

$$\mathbf{P}_{\mathrm{rocket}} = \begin{pmatrix} \gamma(\mathrm{d}v')(m+\mathrm{d}m)c \\ \gamma(\mathrm{d}v')(m+\mathrm{d}m)\mathrm{d}v' \\ 0 \\ 0 \end{pmatrix} \qquad \mathbf{P}_{\mathrm{p}} = \begin{pmatrix} \gamma(w)\mathrm{d}m_{p_1}c \\ -\gamma(w)\mathrm{d}m_{p_1}w \\ 0 \\ 0 \end{pmatrix} = \begin{pmatrix} \xi\mathrm{d}mc \\ \xi\mathrm{d}mw \\ 0 \\ 0 \end{pmatrix}$$

$$\mathbf{P}_{\mathrm{p}\perp 1} = \begin{pmatrix} \gamma(w_\perp)\frac{1}{2}\mathrm{d}m_{p_2}c \\ 0 \\ \gamma(w_\perp)\frac{1}{2}\mathrm{d}m_{p_2}w_\perp \\ 0 \end{pmatrix} = \begin{pmatrix} -\frac{1}{2}(1-\xi)\mathrm{d}mc \\ 0 \\ -\frac{1}{2}(1-\xi)\mathrm{d}mw_\perp \\ 0 \end{pmatrix}$$

$$\mathbf{P}_{\mathrm{p}\perp 2} = \begin{pmatrix} \gamma(w_\perp)\frac{1}{2}\mathrm{d}m_{p_2}c \\ 0 \\ -\gamma(w_\perp)\frac{1}{2}\mathrm{d}m_{p_2}w_\perp \\ 0 \end{pmatrix} = \begin{pmatrix} -\frac{1}{2}(1-\xi)\mathrm{d}mc \\ 0 \\ \frac{1}{2}(1-\xi)\mathrm{d}mw_\perp \\ 0 \end{pmatrix}$$

with the function $\gamma(v) = \frac{1}{\sqrt{1-\left(\frac{v}{c}\right)^2}}$, and at the first order in $\mathrm{d}v'$, $\gamma(\mathrm{d}v') = 1 + o(\mathrm{d}v')$.

The conservation of the energy-momentum ($\mathbf{P}(\tau + \mathrm{d}\tau) = \mathbf{P}(\tau)$) using Taylor's expansion of first order in $\mathrm{d}v'$ and $\mathrm{d}m$ gives

$$\mathrm{d}v' = -\tilde{w}\frac{\mathrm{d}m}{m} \tag{7.4.3}$$

with $\tilde{w} = \xi w$. Using the velocity composition law as for the Equation 7.3.1, we obtain a similar differential equation:

$$\frac{\mathrm{d}v}{1-\left(\frac{v}{c}\right)^2} = -\tilde{w}\frac{\mathrm{d}m}{m} \tag{7.4.4}$$

which can be integrated as the Equation 7.3.2:

$$\left(\frac{m(t)}{m(t_0)}\right)^{\frac{-2\tilde{w}}{c}} = \frac{(c+v(t))\,(c-v(t_0))}{(c-v(t))\,(c+v(t_0))} \tag{7.4.5}$$

We can also do the same reasoning as in the classical case with respect to the specific impulse: the loss of fuel can be interpreted as a reduction of the specific impulse.

$$I_{sp} = \xi\frac{w}{g}$$

This result differs strongly from the H.R. Frisbee articles. For example, Eq. 7.4.4 can be compared with Eq. A-26 in Ref. [101], or with Eq. 4 in Ref. [102], or with Ref. [103]. Here again, the difference comes from that the lost propellant considered emitted at rest which is not the case (because each element of lost propellant is emitted with a certain velocity relative to the rocket, carrying also a non-zero kinetic energy). A similar work is presented in Ref. [106], giving a result similar to the one presented in this section.

Once again we can give an expression of the velocity, position, and time thanks to the mass flow, replacing w by $\tilde{w}$ in the expressions of the previous section:

$$\theta(\tau) = \theta(\tau_0) - \frac{\tilde{w}}{c}\int_{\tau_0}^{\tau} \frac{\rho(\tau)}{m(\tau)} \mathrm{d}\tau' \tag{7.4.6a}$$

$$v(\tau) = c \tanh\theta \tag{7.4.6b}$$

$$x(\tau) = x(\tau_0) + c\int_{\tau_0}^{\tau} \sinh\left(\theta(\tau')\right)\mathrm{d}\tau' \tag{7.4.6c}$$

$$t(\tau) = t(\tau_0) + \int_{\tau_0}^{\tau} \cosh\left(\theta(\tau')\right)\mathrm{d}\tau' \tag{7.4.6d}$$

7.5 Numerical applications

For the numerical application we use $\xi = 0.4$ and $w = 0.99c$, so with $I_{\mathrm{sp}} = 1.2 \times 10^7\,\mathrm{s}$. These values will be justified in Chapter 8 (we will see that we have $\xi w \sim 0.4c$ mainly due to the neutral particles considered as the lost propellant).

In Figure 7.5 the curve are represented $\frac{m(t_0)}{m(t)}$ as a function of $v(t)/c$ for $v(t_0) = 0$ in the cases

- classical equation without loss of propellant (Equation 7.1.2)
- relativistic equation without loss of propellant (Equation 7.3.2)
- classical equation with loss of propellant (Equation 7.2.3)
- relativistic equation with loss of propellant (Equation 7.4.4)

We then find that, as the equations show, the propellant loss decreases the specific impulse, more propellant is needed if there is loss to reach the same velocity. As for the relativistic effects, we can see that they are quite weak for velocities $< 0.2c$, but when they are visible, we can see that they predict a greater propellant expenditure compared to the predictions of classical mechanics.

7.6 Conclusion

We developed in this chapter the equations of motion of the rocket and we saw that the classical and relativistic equations give the same results for a velocity small compared to the speed of light. However, the classical equations are more simple but underestimate the mass of propellant and are completely wrong because they allow a rocket velocity higher than the speed of light.

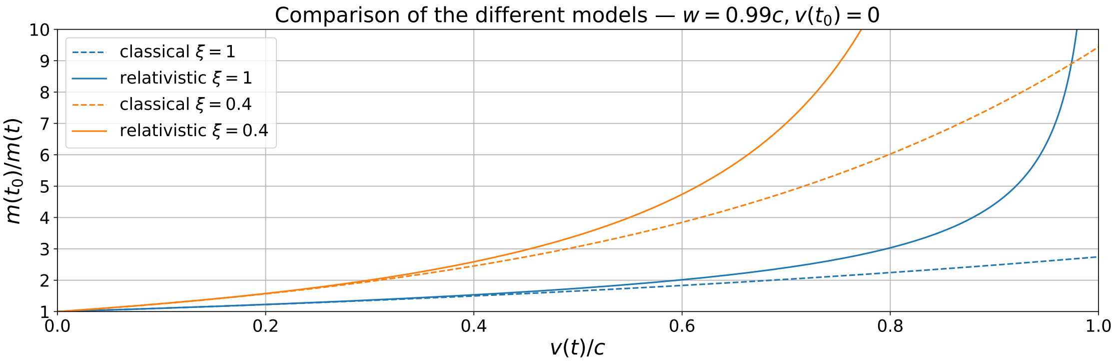

Figure 7.5 – Ratio between the initial mass of the rocket and the mass at t as a function of the velocity of the rocket. The propellant is ejected with a relative speed of $w = 0.99c$. This plot differs and can be compared with Fig. 1 in Ref. [103].

If we consider a fraction $1 - \xi$ of propellant isotropically lost, we simply have to replace the ejection speed w by $\tilde{w} = \xi w$ in the equation without loss.

We will propose in the next chapter, a way to use antimatter to reach such velocities and determine w and ξ.

Chapter 8

The beamed core

> Une maquette ? Vous n'aviez pas dit que c'était une catapulte ?
>
> Perceval, Kaamelott, livre III

Contents

In this chapter, we detail a simulation of a beamed core engine based on an antiproton beam. The concept of the beamed core [107, 108, 109, 110] is to focus a beam in a precise direction to move our rocket. Here we annihilate p and $\bar{p}$, two massive particles to obtain light particles with a high kinetic energy (it means with speed close to the speed of light) to have a propellant with I_{sp} of the same order of magnitude as discussed in the previous chapter.

The idea is to force the produced particles to go opposite to the direction of motion to participate to the momentum ejected along the z axis (see illustration in

Figure 8.1). To do that we place a coil to create a magnetic mirror to realign as much as possible the charged particles. However, it means we loose for the total momentum the neutral particles, giving an explanation to the loss rate discussed in Section 7.2 and Section 7.4.

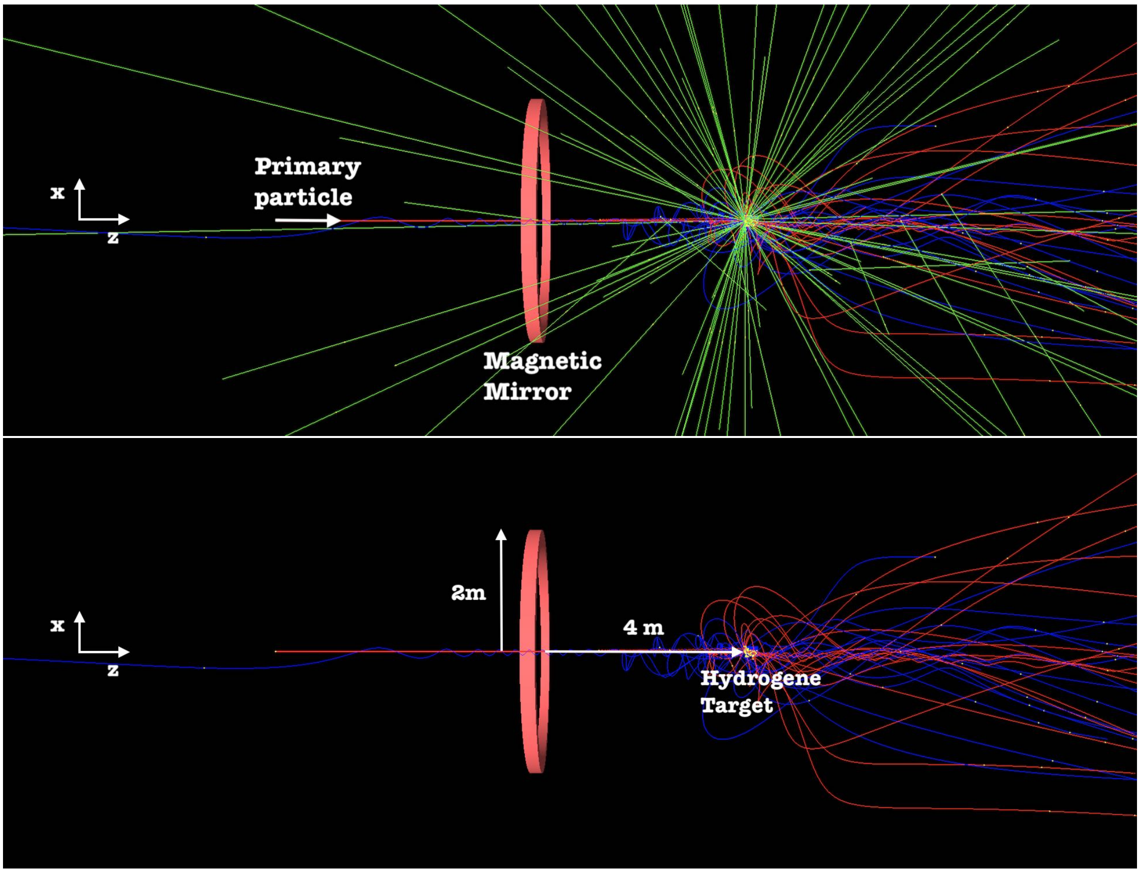

Figure 8.1 – Concept of the beamed core engine. On the top all the particles produced by the annihilation reaction of $p\bar{p}$ are drawn. On the bottom, only the charged one. This illustration comes from our GEANT4 simulation.

This also explain the choice to focus only on the $p\bar{p}$ annihilation. Indeed, it is easier to produce and store positrons, but the electrons and positrons are light compared to the nucleons. They annihilate into gamma rays of small energies and their energy cannot be exploited. Therefore, the most simple antimatter element corresponding to our requirements is antiproton.

The results of our simulations, based on the annihilations of antiprotons on an hydrogen target in a presence of a high magnetic field are presented in Section 8.2. Our simulation is based on the GEANT4 library [111].

Channel	Branching fraction in %
$n\pi^0 (n \geq 1)$	$4.1^{+0.2}_{-0.6}$
$\pi^+ + \pi^- + \pi^0$	5.8 ± 0.4
$\pi^+ + \pi^- + 2\pi^0$	9.3 ± 3.0
$\pi^+ + \pi^- + 3\pi^0$	23.3 ± 3.0
$\pi^+ + \pi^- + 4\pi^0$	2.8 ± 0.7
$2\pi^+ + 2\pi^-$	6.9 ± 0.6
$2\pi^+ + 2\pi^- + \pi^0$	19.6 ± 0.7
$2\pi^+ + 2\pi^- + 2\pi^0$	16.6 ± 1
$3\pi^+ + 3\pi^-$	2.1 ± 0.25

Table 8.1 – Some branching fractions for main (rate $\geq 2\%$) $p\bar{p}$ annihilation channels. Extracted from Ref. [114].

.

8.1 Concept

8.1.1 Proton-antiproton annihilation

As explained in introduction, the model described in this chapter is based on antiproton-proton annihilation. The interactions of antiproton with matter has been studied theoretically for a long time since a first paper in 1956 [112] and are still studied (many examples given in Section 1.2.2).

When an antiproton enters into a target of matter, it is first slowed by electromagnetic interactions with electrons of the target, as would happened for any kind of charged particle. This process also creates electrons-ions pairs in the target. Also, if its kinetic energy is lower than a few eV, it ejects one electron from a given atom and binds with the resulting ions. Then it cascades down to lower energy levels releasing X-ray and Auger electrons in the process. Finally, when the lowest energy level is reached, the antiproton is sufficiently close to the nucleus and annihilates with a nucleon, which happens to be a proton in the case of the target made of hydrogen in our simulation.

Many output decay channels exist, possibly involving intermediate resonances (for example: $\rho \rightarrow \pi^+\pi^-$) [113], and these channels lead in majority to pions as detailed in Table 8.1 which presents the branching fractions from the main channels. If the most representative channel are only taken into account the results of the annihilation can be written such as

$$p\bar{p} \rightarrow 1.5\pi^+ + 1.5\pi^- + 2\pi^0, \tag{8.1.1}$$

and $n_\pi = 4.98 \pm 0.13$, $n_{\pi^\pm} = 3.05 \pm 0.04$, and $n_{\pi^0} = 1.93 \pm 0.12$ [113]. Charged pions decay following $\pi^+ \rightarrow \mu^+\nu$ with a lifetime corresponding to $c\tau = 7.804\,\mathrm{m}$ decay length. Muons also decay following $\mu^\pm \rightarrow e^\pm\nu\bar{\nu}$ with $c\tau = 659\,\mathrm{m}$. In the beam core model, these charged particles are useful to the propulsion. This is not the case of neutral pions, which decay instantaneously to $\gamma\gamma$ (98.8%) or $e^+e^-\gamma$ (1.17%).

Among the other products and still representative, there are the kaons particles. These unstable particles [115] are produced at a typical rate of $\sim 5\%$. Charged kaons decay mostly following $K^+ \to \mu^+\nu$ or $K^+ \to \pi^+\pi^0$ with $c\tau = 3.71\,\mathrm{m}$, therefore, they can participate, in our model to propel a rocket.

8.1.2 Estimates about kinematics in $p\bar{p}$ annihilation and I_{sp}

In this section, we use the knowledge of the decay channels presented in the previous section, considering that all the charged particles can be oriented in a way to increase the thrust, to estimate the specific impulse (I_{sp}) of the beamed core engine.

We focus on the pions because they are the most representative. Their masses are roughly equal ($m_{\pi^0} = 135\,\mathrm{MeV}, m_{\pi^\pm} = 140\,\mathrm{MeV}$), then for this computation we write the mass of a pion $m_\pi = 140\,\mathrm{MeV}$. As explained in the previous section, in the most simple picture, 3 charged pions and 2 neutral pions are obtained. This means that the charged particles carry $\sim 60\%$ of the initial energy while the neutral ones $\sim 40\%$.

If we consider the initial particles at rest, the initial energy is twice the mass energy of a proton $E = 2m_pc^2 = 2 \times 940\,\mathrm{MeV}$. Therefore the kinetic energy of each pion is $K_\pi = \frac{1}{5}(2m_p - 5m_\pi)c^2 = \gamma m_\pi c^2 - m_\pi c^2$, leading to $\gamma = \frac{2m_p}{5m_\pi}$. Then, each resulting pion has a velocity (compared to the speed of light c) of

$$\frac{v}{c} = \sqrt{1 - \frac{1}{\gamma^2}} = 0.93. \tag{8.1.2}$$

As the neutral pions decay to two photons $\pi^0 \to \gamma\gamma$ more than 98.8% of the time, neutral pions yields a high intense radiation of photons. So about 40% of the available energy is lost in quasi-isotropic γ radiation. Thankfully, this is not the case for the charged pions. Therefore, they can theoretically be re-directed using a magnetic field and ejected oppositely to the rocket movement. Considering that the charged pions carry about 60% of the available energy and travels at $\sim 0.93c$, a first rough estimate of the possible specific impulse is

$$I_{\mathrm{sp}} = 0.6 \times 0.93\frac{c}{g} = 0.56\frac{c}{g} = 1.7 \times 10^7\,\mathrm{s}. \tag{8.1.3}$$

8.1.3 Magnetic mirroring

The magnetic mirror is made of a huge current loop to generate an important magnetic field. Assuming the main axis is the z axis, the expression of this field is [116]

$$B_x = \frac{Cxz}{2\alpha^2\beta\rho^2}\left(\left(a^2+r^2\right)E\left(k^2\right) - \alpha^2K\left(k^2\right)\right) \tag{8.1.4a}$$

$$B_y = \frac{Cyz}{2\alpha^2\beta\rho^2}\left(\left(a^2+r^2\right)E\left(k^2\right) - \alpha^2K\left(k^2\right)\right) \tag{8.1.4b}$$

$$B_z = \frac{C}{2\alpha^2\beta}\left(\left(a^2-r^2\right)E\left(k^2\right) + \alpha^2K\left(k^2\right)\right) \tag{8.1.4c}$$

where $\rho^2 = x^2+y^2$, $r^2 = x^2+y^2+z^2$, $\alpha^2 = a^2+r^2-2a\rho$, $\beta^2 = a^2+r^2+2a\rho$, $k^2 = 1-\frac{\alpha^2}{\beta^2}$, $C = \frac{\mu_0 I}{\pi}$, K and E are the complete elliptic integrals of the first and second kind, respectively, and μ_0 the magnetic permeability of vacuum. We have implemented these formula in the GEANT4 simulation. The corresponding magnetic field lines in the (ρ, z) plane of cylindric coordinates are shown in Figure 8.2.

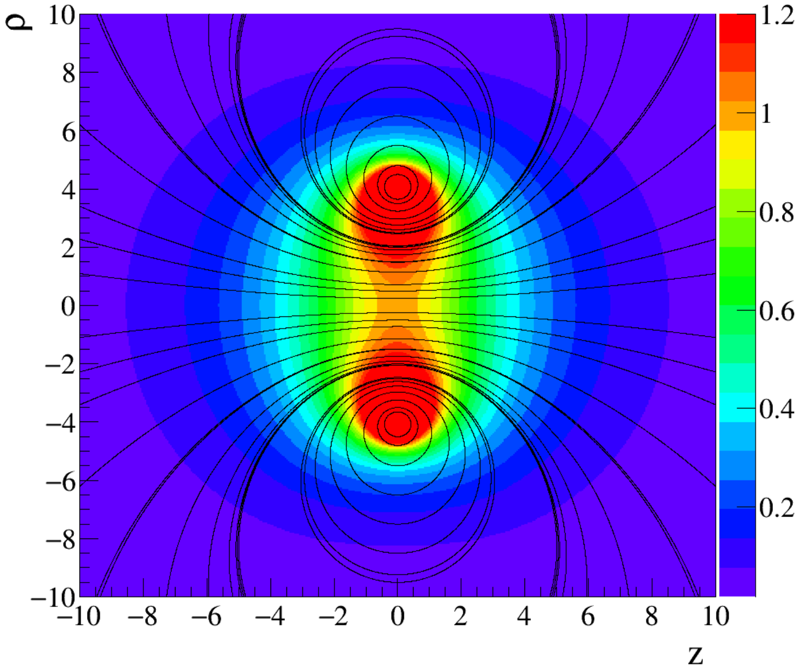

Figure 8.2 – Magnetic field line and strength in the (ρ, z) plane of cylindric coordinate, as produced by a current loop of radius 4. Length and magnetic units are arbitrary.

The effect of the magnetic mirror can be seen in Figure 8.3 where we display the trajectories of particle varying the magnetic strength. We clearly see on these pictures that the charged particles are more aligned with the main axis (which increases the I_{sp}) for a strong magnetic field.

8.1.4 Scale invariance

For the case of a current loop of radius R centred around the z-axis at $z = 0$, the Maxwell's equation defining the magnetic field is

$$\overrightarrow{\nabla} \times \overrightarrow{B} = \mu_0 \overrightarrow{j} = \mu_0 \overrightarrow{I} \delta(z) \delta(\sqrt{x^2 + y^2} - R), \tag{8.1.5}$$

where $\overrightarrow{j}$ is the current density, which is then translated into the current loop intensity $\overrightarrow{I}$ using the δ functions defining the location of the loop. Such equation could be generalised for different shape of current loop, using the appropriate δ parameterisation. The trajectory for the particles is obtained considering the Lorentz

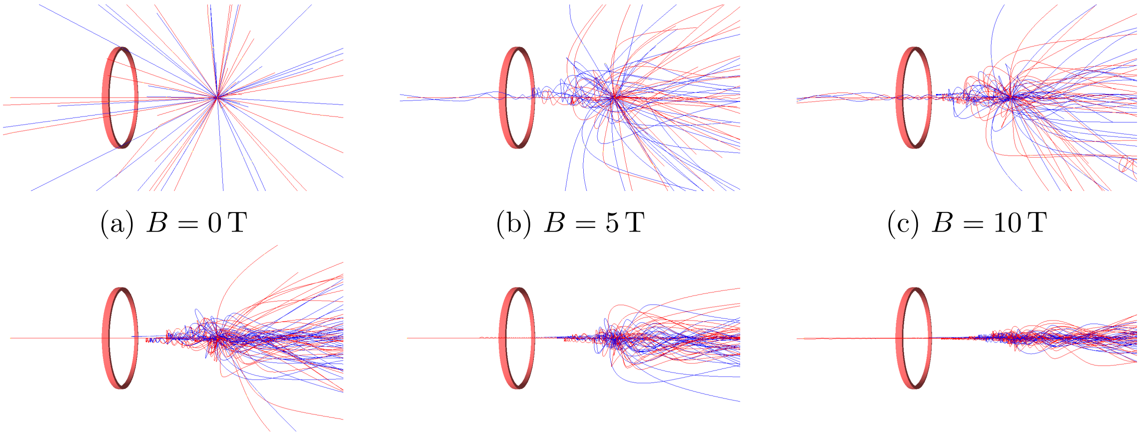

(a) $B = 0\,\mathrm{T}$ (b) $B = 5\,\mathrm{T}$ (c) $B = 10\,\mathrm{T}$

(d) $B = 20\,\mathrm{T}$ (e) $B = 40\,\mathrm{T}$ (f) $B = 80\,\mathrm{T}$

Figure 8.3 – Event displays from the GEANT4 simulation showing only the charged particles. The loop is located at 4 m from the target and has a radius of 2 m. We simulate 20 antiprotons hitting the target, while the magnetic field in the center of the loop is varied from 0 to 80 T.

force:

$$\frac{d}{dt}\left(\frac{m\overrightarrow{v}}{\sqrt{1-\frac{v^2}{c^2}}}\right) = q\overrightarrow{v} \times \overrightarrow{B}. \tag{8.1.6}$$

Equation 8.1.5 and Equation 8.1.6 are invariant under the transform of parameter α:

$$\overrightarrow{x} \to \alpha\overrightarrow{x}, \qquad t \to \alpha t, \tag{8.1.7a}$$

$$\overrightarrow{v} \to \overrightarrow{v}, \tag{8.1.7b}$$

$$\overrightarrow{B} \to \overrightarrow{B}/\alpha, \qquad I \to I. \tag{8.1.7c}$$

Here we naturally imply the transform of the radius $R \to \alpha R$ is identical to the transform of $\overrightarrow{x}$. Such invariance implies that if charged and stable particles are produced somewhere at $t = 0$, then the outgoing momentum, $\gamma m\overrightarrow{v}$, of the particles for $t \to \infty$ is unchanged if one applies or not the transform.

Therefore, the resulting I_{sp} is invariant under such a transform. For example, the I_{sp} obtained with a loop of $a = 2$ m and $B = 20$ T at the center should be the same as obtained with a loop of $a = 4$ m and $B = 10$ T. Also both, the transformation law of I from Equation 8.1.7 and the well known formula giving the magnetic field in the center of the loop $B = \mu_0 I/2R$ state that the current intensity is the same in both configurations.

This scale invariance simplifies a possible optimisation process, as the magnetic field and the dimension of the device are not independent parameters. However, there are two limitations in this. First, the current loop is an ideal object of vanishing thickness. In practice, a real system would be a solenoid. The length and width of the solenoid break the scale invariance. Second, the actual particles resulting from the $p\bar{p}$ annihilation are unstable with a given decay length. The bigger the magnetic system is, the longer are the trajectories close to the magnet and the larger is the amount of particle decaying in flight while being channeled. The typical decay length being given by $\beta\gamma c\tau \sim 20$ m (see 8.1.1), it is expected to see an effect when the magnetic system has a size not small compared to 20 m.

8.2 Results

8.2.1 Presentation of the simulation

Our simulation is based on the GEANT4 library which is widely used in particle and nuclear physics as a toolkit to simulate particles, their decays, their trajectory in a magnetic field and their interaction with matter. Our implementation consists of a cubic hydrogen target of $8\,\mathrm{cm}^3$ located on the axis of a current loop. We shot a beam of antiprotons, along the z-axis to produce annihilation onto the target. The interactions of particles with matter are described by the "QGSP_BERT_EMX" model [117] included in Geant4.

We first study the outcome of antiproton annihilations. Our simulation provides results in fair agreement with the expectations presented in Section 8.1.1. Indeed, the final state of each collision provides on average $n_\pi = 5.19 \pm 0.15$, $n_{\pi^\pm} = 3.12 \pm 0.12$, $n_{\pi^0} = 2.07 \pm 0.08$ (uncertainties here are statistical), the π^0 decaying quickly to two γ, such as illustrated in Figure 8.4

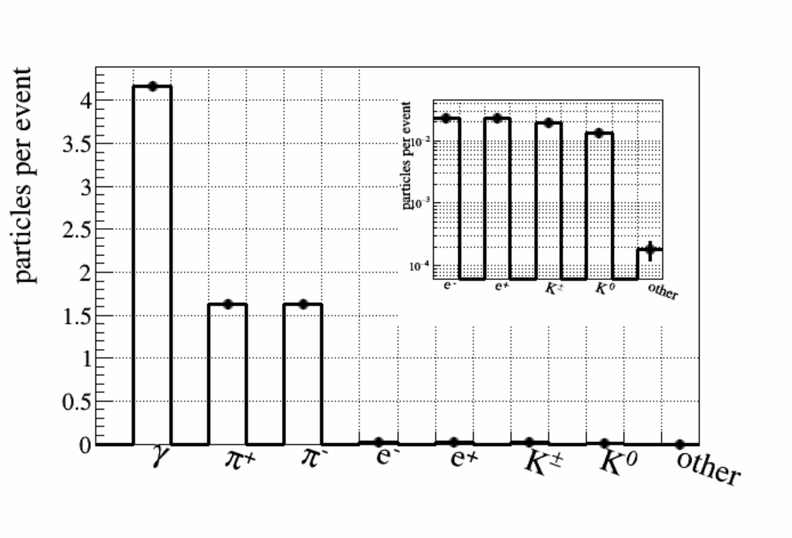

Figure 8.4 – Final states for 1000 $p\bar{p}$ collisions.

8.2.2 First results

We simulate the annihilation of antiprotons on a target of hydrogen (see illustration in Figure 8.1) including the magnetic field of a current loop. The target is at 4 m of a 2 m radius loop.

Let's take the example of a loop generating a 10 T magnetic field. $N = 10000$ antiprotons are annihilated onto a target of hydrogen. The momentum distribution of the $n = 127631$ produced particles is reported in Figure 8.5. As expected, the mean momentum along the x axis (and y axis) with $\bar{p_x} = 0.1032\,\text{MeV}$ ($\bar{p_y} = -0.1421\,\text{MeV}$) is negligible compared to the mean momentum along the z axis with a mean value of $\bar{p_z} = 64.52\,\text{MeV}$. It means this engine yields a force pushing the rocket in the right direction.

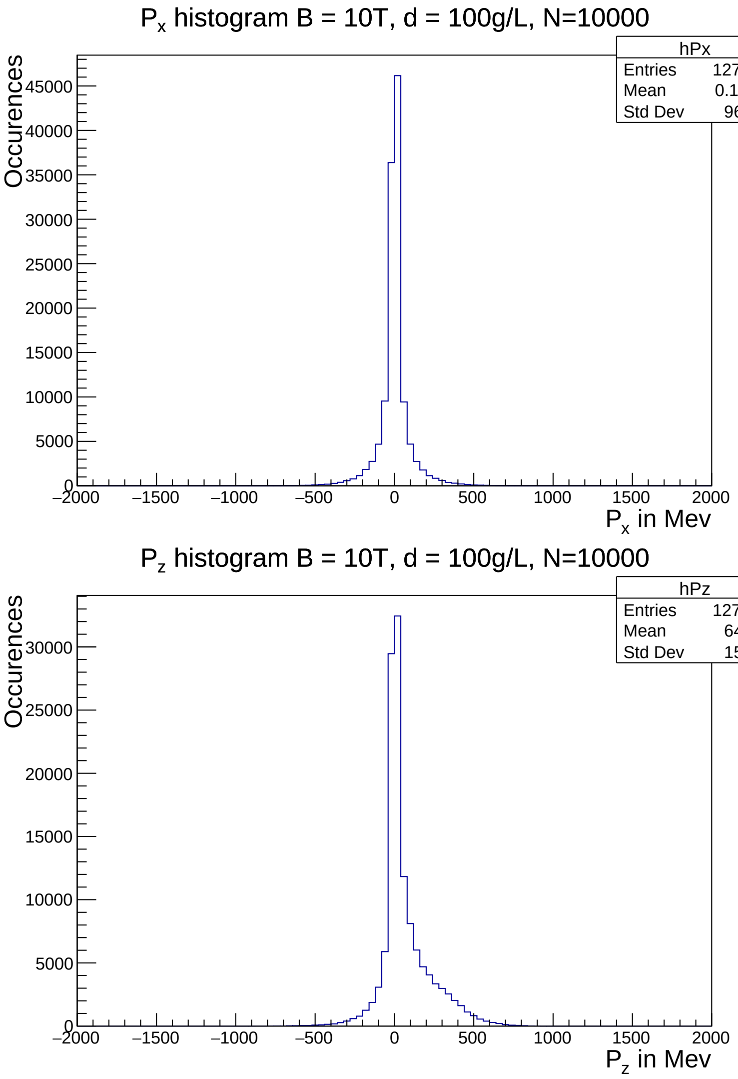

Figure 8.5 – Momentum distribution of the particles after the annihilation (10000 primary antiprotons).

To estimate ξw and then the $I_{sp} = \frac{\xi w}{g}$, we start from the definition of the energy (E) and momentum (p) of a particle

$$E = \gamma m c^2, \tag{8.2.1a}$$

$$p = \gamma m v, \tag{8.2.1b}$$

which leads to

$$\frac{v}{c} = \frac{pc}{E}. \tag{8.2.2}$$

Considering v as the mean value of the speed of the particles, we have $v = \xi w$ and $\bar{p_z} = p$. To estimate E, the initial total energy of the protons and antiprotons at rest $E_0 = 2Nm_pc^2$ (m_p the proton's mass) is divided by the number of produced particles n. This lead to

$$\frac{\xi w}{c} = \frac{\bar{p_z}c}{m_pc^2} \times \frac{n}{2N} = \frac{64.52\,\mathrm{MeV}}{938\,\mathrm{MeV}} \times \frac{127631}{2 \times 10000} = 0.43. \tag{8.2.3}$$

Therefore, the specific impulse is $I_{\mathrm{sp}} = 0.43c/g = 1.3 \times 10^7$ s.

8.2.3 Optimisation of the target's position

In the previous section, the distance between the 2 m radius loop and the target was arbitrary fixed at 4 m. To determined what is the effect of this distances, similar simulations has been performed for different distances and 4 values of the field. The results of these simulations are presented in Figure 8.6. The first observation is that there is an optimal distance for each value of the field. However, this optimal value remains around 4 m, corresponding to a distance of $\sim 2 \times R$.

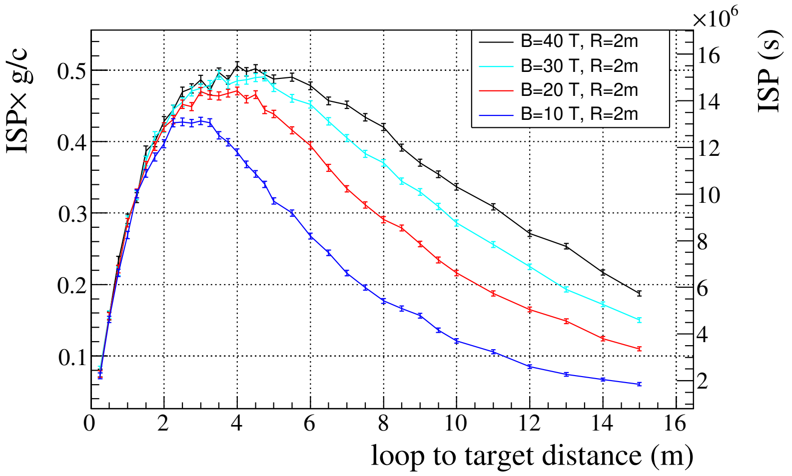

Figure 8.6 – I_{sp} as a function of the distance of the center of the loop to the target, for different magnetic field intensities (sampled at the center of loop) and a fixed loop radius of 2 m

8.2.4 Optimisation of the field

The magnetic field strength is varied for different geometry, keeping the aspect ratio $R : d = 1 : 2$. The resulting I_{sp} as a function of the magnetic field is shown in Figure 8.7. For $R = 2$ m and $d = 4$ m, it can be seen that an asymptotic value close to $I_{\mathrm{sp}} = 0.5c/g = 1.5 \times 10^7$ s is reached for $B \geq 30$ T. Namely we find $I_{\mathrm{sp}} \times g/c = 0.467 \pm 0.002$, 0.485 ± 0.002, and 0.497 ± 0.002, for respectively $B = 20$, 30, and 50 T. The I_{sp} at $B = 20$ T is just 6% below the asymptotic value which sounds as a reasonable compromise to work at value of the field not too unrealistic. This corresponds to a current of 6.36×10^7 A. Note that in a real system made of a solenoid, this current is shared among the different loops.

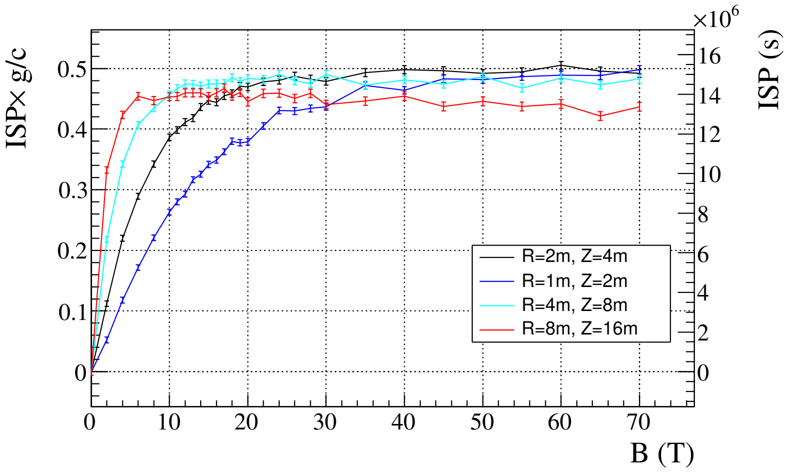

Figure 8.7 – I_{sp} as a function of the magnetic field B for different geometries that have the same aspect ratios.

Figure 8.8, shows the different curves are overlaid when I_{sp} is plotted as a function of $B \times R$, as expected from the scaling law discussed in Section 8.1.4. This shows that the relevant parameter is rather the current intensity circulating in the loop rather than the magnetic intensity. A notable departure is however observed for $R = 8\,\text{m}$, $d = 16\,\text{m}$. This is understood to be due to inflight decays of pions, resulting in a significant momentum carried by neutrinos before being deflected by the magnetic nozzle, as anticipated in Section 8.1.1 and Section 8.1.4.

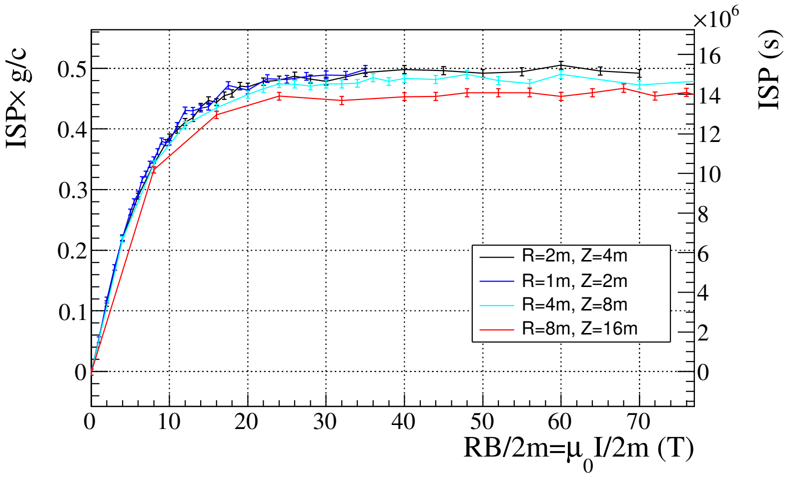

Figure 8.8 – I_{sp} as a function of the magnetic field B scaled by the loop radius R (in units of $2\,\text{m}$). BR is proportional to the current I circulating in the loop.

8.3 Energy evacuation

Each collision produces on average four 190 MeV photons in a quasi-isotropic way i.e. about 760 MeV per collision. Thus the elements of the rocket receive a power of

$$P_r = \frac{\mathrm{d}m_{\text{fuel}}}{\mathrm{d}t} c^2 \epsilon \frac{\Omega}{4\pi} \tag{8.3.1}$$

where m_{fuel} is the mass of propellant consumed during an acceleration phase (and so $\frac{\mathrm{d}m_{\text{fuel}}}{\mathrm{d}t}$ is the consumed mass of propellant per time unit), ϵ the fraction of energy dissipated (~ 0.4, see Section 8.1.2), and Ω, the solid angle under which one can see from the target the considered element of the rocket.

Such amount of radiation would yield damages to the rocket as would do any ionising radiations, and also deposit heat. Thus, the rocket must be shielded against the flux of gamma rays. In the following we assume the energy deposited in the shield is only transformed into heat and do not study the impact of radiation damages which are expected to have ageing effects on any kind of shield. However, the heat deposit in the shield which has to be dissipated by a radiating system represents by itself a major challenge for an antimatter rocket, as we discuss in the following.

8.3.1 Radiator

Let's consider a metallic radiator. Assuming it behaves like a black body at temperature T, its surface S would radiate a power such as described by the Stefan-Boltzmann law:

$$P_e = S\sigma T^4, \tag{8.3.2}$$

where σ is the Stefan-Boltzmann constant ($\sigma = 5.670\,373 \times 10^{-8}\,\mathrm{W\,m^{-2}\,K^{-4}}$). Combining Equation 8.3.1 and Equation 8.3.2, the required surface to evacuate this power is obtained:

$$S = \frac{\mathrm{d}m_{\text{fuel}}}{\mathrm{d}t} c^2 \epsilon \frac{\Omega}{4\pi\sigma T^4}. \tag{8.3.3}$$

During the rocket's acceleration, a mass m_{fuel} of propellant is consumed to give a speed Δv to the rocket (with a total mass m). Assuming that the propellant is delivered constantly and the acceleration duration is τ, the consumed mass per time unit is then m_{fuel}/τ. Also, it is assumed that the radiator is composed of panels, with a thickness e and a mass per unit volume ρ, the mass of the radiator is related to the surface S as

$$m_{\text{rad}} = \rho e \frac{S}{2}, \tag{8.3.4}$$

with a factor 2 because there are 2 faces. Derived from Equation 8.3.3 the following equation is obtained

$$m_{\text{rad}} = \frac{1}{r} m_{\text{fuel}}, \qquad r = 8\pi\sigma \frac{\tau T^4}{e\rho c^2 \epsilon \Omega}. \tag{8.3.5}$$

The total mass of the rocket before the acceleration m_{tot}, being the sum of the mass of the ejected propellant m_{fuel}, the mass of the radiator m_{rad} and the remaining mass of the rocket m_{rem}, Equation 8.3.5 leads to

$$m_{\text{tot}} = (1 + r) m_{\text{rad}} + m_{\text{rem}}. \tag{8.3.6}$$

Let's estimate the value of r. We consider a one year acceleration phase and a radiator made of tungsten, for its high temperature of fusion (3000 K), with a density of $\rho = 19.3\,\mathrm{g\,cm^{-3}} = 19.3 \times 10^3\,\mathrm{kg\,m^{-3}}$. Taking $\epsilon \sim 0.4$, $e = 1\,\mathrm{cm}$, with a solid angle $\Omega = 0.4\pi$, we obtain $r \sim 3 \times 10^{-4}$.

r is found to be a small number. This implies that the mass of the radiator is dominant over the rest in the rocket for sizeable amount of antimatter. The rocket equation 7.2.4 becomes

$$\Delta v = -I_{\mathrm{sp}} g \log\left(\frac{m_{\mathrm{rem}} + m_{\mathrm{fuel}}/r}{m_{\mathrm{rem}} + m_{\mathrm{fuel}} + m_{\mathrm{fuel}}/r}\right), \tag{8.3.7}$$

which is independent of the amount of fuel when m_{fuel}/r is large. The reason is that any supplement of fuel requires an additional mass of radiator. The supplemental fuels serves only to accelerate the supplemental radiators. Thus it is not possible to reach speed close the I_{sp}, and for $m_{\mathrm{fuel}} \to \infty$, $\Delta v = I_{\mathrm{sp}} g \log(1 + r)$. If $I_{\mathrm{sp}} = 1.5 \times 10^7\,\mathrm{s}$ then maximal speed is $\Delta v/c = 1.4 \times 10^{-4}$.

Thereby the mass of the radiator drastically impact the velocity of the rocket. If the tungsten is replaced by PICA (a composite material for thermic shield used by NASA), with a density $\rho = 250\,\mathrm{kg\,m^{-3}}$ and a temperature of fusion $T = 1500\,\mathrm{K}$, the r parameter becomes, $r = 1.3 \times 10^{-3}$, leading to a maximal speed $\Delta v/c = 6.4 \times 10^{-4}$. Some optimisation of the geometry can be done to increase the r parameter and consequently the final speed, however it is hard to see how one could gain more than one order of magnitude on the r parameter. If we consider ten years of accelerating phase, we gain one more order of magnitude. So at the end, it is hard to see how one could go beyond a $\Delta v = 0.06c$.

8.3.2 Shield

The radiation energy resulting from the annihilation process first need to be absorbed before being evacuated by the radiators. The photons have to interact with the matter of a shield placed between the target and the rest of the rocket.

The shield has to be designed to be able to stop the γ, and this is can be done with the basics information coming from the Particle Data Group [115]. For a material with a high atomic number Z (heavier than lead), the probability P_0 that an interaction between a 100 MeV photon and an atomic nucleus results in a (e^+, e^-) pair is close to 100%. The probability P_i that this photon causes the creation of such a pair after going through a thickness l of material is then

$$P_i = \left(1 - e^{-l/l_0}\right), \tag{8.3.8}$$

where l_0 is a characteristic length of the material. In the case of lead, this length is $l_{\mathrm{Pb}} = 0.9\,\mathrm{cm}$, which means that a 2.5 cm thickness is enough to turn 99% of the incoming γ to a (e^+, e^-) pair, leading to an electromagnetic shower. This first process initiates and electromagnetic cascade of pair productions and Brehmstrahlung emission generating more and more photons and electrons of lower energies. The cascade ends when the electrons energies are below a critical energy $E_c \simeq \frac{610\,\mathrm{MeV}}{Z+1.2}$, then the remaining energy is deposited by ionization and excitation of the material. The characteristic longitudinal length of the cascade is given by the radiation length X_0, which amounts to $X_0 = 0.56\,\mathrm{cm}$ for lead. In practice more than 99% of the energy is deposited within $10X_0$ for a γ of 100 MeV.

Also, in the transverse plane, 99% of the shower energy is contained in a radius of $3.5R_M$. R_M, the Molière radius, is another characteristic of the material such as

$$R_M = X_0 \frac{E_s}{E_c}, \quad E_s \simeq 21\,\mathrm{MeV}. \tag{8.3.9}$$

$R_M = 1.6\,\mathrm{cm}$ in the case of a 100 MeV radiation in lead. The energy of the shower is therefore essentially contained in a cylinder of $5.5 \times 10^{-4}\,\mathrm{m}^3$ weighing 6.2 kg and mainly heats the material. So it appears that a shield of a few l_{Pb} is enough to contain almost all of the energy.

In the end, the power received by the shield is colossal: $10 \times 10^{10}\,\mathrm{W\,m^{-2}}$, if a ton of antiprotons is annihilated over a year. This power being delivered on a thin layer (a few l_{Pb}), one can consider it will be vaporised extremely quickly. A way to solve this problem would be to move the target further away from the magnetic mirror, but this would decrease the I_{sp}, except if the magnetic field is increased. Then, a new optimal condition taking into account the shield remains to be found.

8.4 Antimatter production and storage

The final limitation of the concept of the beamed core engine is that it requires tones of antimatter. This is really the main limitation, because there is no way to produce such amount of antimatter, and our current way of storing antimatter do not allow such quantities.

Let's start with the storage. As presented in detail in Chapter 3, a well known way to store antimatter is to trap it in Penning traps as non neutral plasma. And here comes the first limitation: there is a maximum density of particles which can be stored in such a trap. This is what is named the Brillouin limit

$$n_B = \frac{B^2/(2\mu_0)}{mc^2}, \tag{8.4.1}$$

where B is the magnetic field, m the mass of one particle, c the speed of light, and μ_0 the vacuum permeability.

This lead to a maximal energy per unit volume of $\epsilon_B = \frac{B^2}{2\mu_0} = 0.4\,\mathrm{kJ\,L^{-1}} \times \left(\frac{B}{1\,\mathrm{T}}\right)^2$, which means that to store one gram of antiprotons, a volume of $10^8\,\mathrm{m}^3$ is required (for a 1 T field). Or if we desire the same compactness of the diesel ($40\,\mathrm{MJ\,L^{-1}}$), a 320 T magnet is required (Neurospin magnet at CEA: 11.7 T).

The key would be to store neutral antimatter. Even if it has been possible to store antihydrogen atoms for 1000 s [28], it was about dozens of atoms, which is far from the quantity required for a space travel.

About production, one cannot be very optimistic. Currently, a 26 GeV production beam of 10^{13} protons is necessary in order to inject the required 5×10^7 antiprotons into the AD to deliver at the end 10^7 antiprotons per minute [17]. So the energy efficiency is of about 4×10^{-8}. Furthermore, with this production rate, assuming that all the antiprotons are captured and turned into antihydrogen atoms, it will take about 10^{11} years to obtain a single gram of antihydrogen. It has to be understood that these limitations are more due to the Standard Model of Physics than to the technology, so except if a source of antimatter is discovered, using antimatter as a propellant remains highly hypothetical.

8.5 Conclusion

In this chapter, the principle of the beamed core engine has been presented. It has been found with a rough estimate that such engine could provide a specific impulse of 1.7×10^7 s (to compare with current existing space rocket with $I_{\rm sp} \sim 400\,{\rm s}$).

A GEANT4 simulation has been developed to study this model, and we found that it is possible to reach 1.5×10^7 s, with a 20 T magnetic field and the appropriate geometry.

However, our simulation is based on the presence of a hypothetic antiproton gun which is for now not something realistic. A rocket propelled with antimatter should be shielded against the radiations resulting from the annihilation reactions. It is not clear yet if the shielding and the high mass of the radiator represents a physical limit or simply a technological challenge. In spite of the promising $I_{\rm sp}$ of 1.5×10^7 s, our studies suggests that reaching speeds above $0.05c$ may be impossible for an antimatter rocket.

In the end, even if this model has some interesting points in theory, the quantity of antimatter required to make it work is infinitely bigger than what it is possible to produce.

Chapter 9

Conclusion

> Un savant dans son laboratoire n'est pas seulement un technicien, c'est aussi un enfant placé en face des phénomènes naturels qui l'impressionnent comme un conte de fées.
>
> Marie Sklodovska-Curie

Positron trapping

The goal of the GBAR experiment is to determine the effect of gravity on an antihydrogen atom. To create antihydrogen atoms by neutralising antihydrogen ions $\overline{\mathrm{H}}^{+}$ at the GBAR experiment, 10×10^{10} positrons are required. They are then turned into positronium atoms which will react twice with antiprotons to give the desired $\overline{\mathrm{H}}^{+}$. Therefore positrons are produced using a 9 MeV LINAC accelerating electrons into a tungsten target equipped with a mesh moderator biased at 50 V.

The LINAC based source provides 3×10^{7} positrons per second which then need to be accumulated. They are accumulated into a Buffer Gas Trap, a Penning trap with N_2 and CO_2 in it, leading to inelastic collisions which insure the trapping and the cooling of the positrons. Positrons are accumulated in the second stage for 100 ms with a trapping rate of $\sim 1.7 \times 10^{6}\,\mathrm{e}^{+}\,\mathrm{s}^{-1}$, then they are transferred into the BGT's third stage. This accumulation and transfer procedure is reproduced 10 times to finally provide a bunch of 1.5×10^{6} positrons every 1.1 s (a loss happens during this stacking operation and 100 ms are added for a final radial compression using the Rotating Wall technique, the trapping efficiency is then 5%). This new bunch is then ready to be sent and re-trapped into the High Field Trap.

The High Field Trap is a 5 T Penning-Malmberg trap allowing to trap large amounts of charged particle for hours. We first tested this trap with electrons by trapping about 5×10^{9} of them. The experiments on the electrons lead to the conclusion that a better alignment of the electrodes with respect to the magnetic field must be done. However, an acceptable situation has been found allowing to re-trap the positrons with 66% efficiency. Then, accumulating the positrons bunches coming from the BGT, it has been possible to accumulate 1×10^9 positrons in 1100 s. This is a really promising result for the GBAR experiment. For the future, it is about to do 10 times more, 10 times faster to collect the desired amount of positrons each time the ELENA decelerator provides a bunch of antiprotons.

The trapping efficiency has to be increase, the goal being to trap 1×10^{10} positrons in 100 s. The idea will be then to replace the Buffer Gas Trap by an electron cloud at the entrance of the High Field Trap. We hope to be able to create our first anti-hydrogen ion in 2021, when ELENA will be back online.

Antimatter rocket

Using antimatter to propel a rocket is a very exciting idea. Indeed, the energy resulting from the antimatter-matter annihilation reaction has a higher intrinsic efficiency than any other propellant. In our study, we focused on the fact that the annihilation reaction proton-antiproton produces particles going close to the speed of light which could be used to accelerate a rocket up to speeds also close to the speed of light.

The system we studied is named the beamed core engine. The principle is to annihilate protons and antiprotons in a high magnetic field in order to have the annihilation products aligned with the direction of the thrust. Of course, with this model, the neutral particles are lost, explaining why we developed the equations in case of a loss of propellant. A simulator has been developed using GEANT4 to evaluate some parameters such as the intensity of the field and more studies will be performed to optimise this theoretical engine model. According to our simulation, it is then possible to get a rocket with a specific impulse of $I_{\mathrm{sp}} \sim \frac{0.5c}{g} \sim 1.5 \times 10^7\,\mathrm{s}$, which is outsized if it is compared to the best French rocket (434 s for Vulcain, propelling Ariane 5). However, this model assumes the capability to produce and store a macroscopic number of antiprotons, which might be an insurmountable showstopper. Also, with this model, a large amount of gamma rays are produced and must be evacuated. This evacuation could be performed using a lead shield and a tungsten radiator, but the presence of these elements decreases drastically the speed of the rocket: our studies suggests that reaching speeds above $0.05c$ may be impossible for an antimatter rocket.

Appendix A

Useful notions of special relativity

A.1 Definitions and notations

Let's consider the spacetime position 4-vector $\mathbf{x}$ of a body in movement relative to an inertial reference frame

$$\mathbf{x} = \begin{pmatrix} ct \\ x \\ y \\ z \end{pmatrix}. \tag{A.1.1}$$

For this chapter, we represent a 4-vector $\mathbf{a}$, by one of its components a^μ ($\mu \in \{0, 1, 2, 3\}$) and the spatial part $\overrightarrow{a}$.

This space is a Minkowski space if we define the scalar product between two 4-vectors 2 4-vectors a^μ, b^μ by

$$(\mathbf{a}.\mathbf{b}) = g(\mathbf{a}, \mathbf{b}) = a^\mu b_\mu = \eta_{\mu\nu} a^\mu b^\nu, \tag{A.1.2a}$$

$$\eta = \begin{pmatrix} 1 & 0 & 0 & 0 \\ 0 & -1 & 0 & 0 \\ 0 & 0 & -1 & 0 \\ 0 & 0 & 0 & -1 \end{pmatrix}. \tag{A.1.2b}$$

The following equation defines the infinitesimal interval of proper time using $\mathrm{d}s = \sqrt{\mathrm{d}x^\mu \mathrm{d}x_\mu}$ which is the infinitesimal interval between two events

$$\mathrm{d}\tau = \frac{1}{c}\mathrm{d}s = \frac{1}{c}\sqrt{v^\mu v_\mu}\mathrm{d}t = \sqrt{1 - \frac{v^2}{c^2}}\mathrm{d}t = \frac{1}{\gamma}\mathrm{d}t, \tag{A.1.3}$$

with $v^\mu = \frac{\mathrm{d}x^\mu}{\mathrm{d}t}$ et $v^2 = \left(\frac{\mathrm{d}x}{\mathrm{d}t}\right)^2 + \left(\frac{\mathrm{d}y}{\mathrm{d}t}\right)^2 + \left(\frac{\mathrm{d}z}{\mathrm{d}t}\right)^2$.

We define the 4-velocity and the 4-acceleration by

$$\mathbf{u} = \frac{\mathrm{d}\mathbf{x}}{\mathrm{d}\tau}, \tag{A.1.4a}$$

$$\mathbf{a} = \frac{\mathrm{d}\mathbf{u}}{\mathrm{d}\tau} = \frac{\mathrm{d}^2\mathbf{x}}{\mathrm{d}\tau^2}. \tag{A.1.4b}$$

From these definitions follow

$$(\mathbf{u}.\mathbf{u}) = c^2 > 0, \qquad \text{(constant norm and } \mathbf{u} \text{ is time like)} \tag{A.1.5a}$$

$$(\mathbf{a}.\mathbf{u}) = 0, \qquad \text{(}\mathbf{a} \text{ and } \mathbf{u} \text{ orthogonal)} \tag{A.1.5b}$$

$$(\mathbf{a}.\mathbf{a}) < 0. \qquad \text{(}\mathbf{a} \text{ is space like)} \tag{A.1.5c}$$

A.2 Composition of velocities

Let's consider an inertial frame $\mathcal{R}$ and an inertial frame $\mathcal{R}'$ moving at a constant speed V along the x-axis relative to $\mathcal{R}$ (Figure A.1).

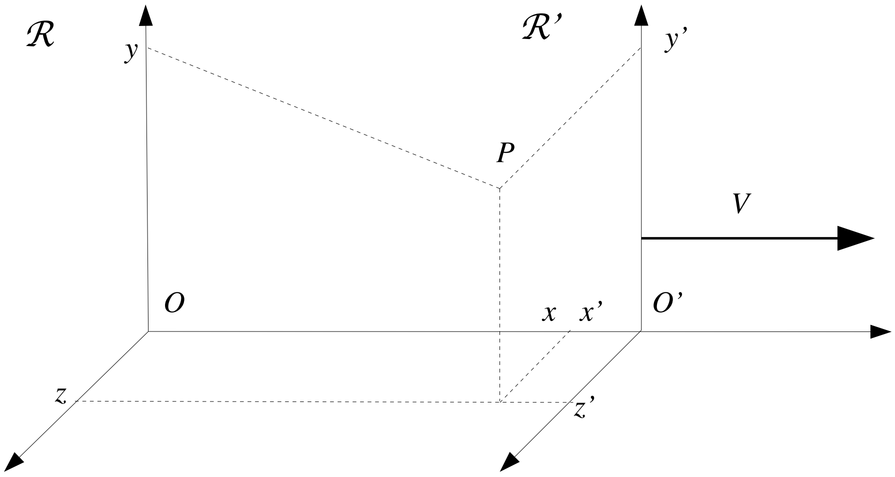

Figure A.1 – Two inertial frames linked by a Lorentz special transformation.

We note x^μ the coordinates in $\mathcal{R}$ and x'^μ in $\mathcal{R}'$. We can go from one set of coordinates to another by a Lorentz transformation

$$x'^\mu = \Lambda^\mu_\nu x^\nu \qquad , \Lambda = \begin{pmatrix} \gamma & -\beta\gamma & 0 & 0 \\ -\beta\gamma & \gamma & 0 & 0 \\ 0 & 0 & 1 & 0 \\ 0 & 0 & 0 & 1 \end{pmatrix}, \tag{A.2.1}$$

with $\gamma = \frac{1}{\sqrt{1-\left(\frac{V}{c}\right)^2}}$ and $\beta = \frac{V}{c}$. We apply this relation to an infinitesimal difference between two events, which gives us the following relations:

$$\begin{aligned} c\mathrm{d}t' &= c\gamma\mathrm{d}t - \beta\gamma\mathrm{d}x, \\ \mathrm{d}x' &= -c\beta\gamma\mathrm{d}t + \gamma\mathrm{d}x, \\ \mathrm{d}y' &= \mathrm{d}y, \\ \mathrm{d}z' &= \mathrm{d}z. \end{aligned}$$

To know the velocity composition law, we use the definition of velocity in both frames. For example on the x axis, $v_x = \frac{\mathrm{d}x}{\mathrm{d}t}$ and $v'_x = \frac{\mathrm{d}x'}{\mathrm{d}t'}$:

$$\frac{\mathrm{d}x'}{\mathrm{d}t'} = \frac{\mathrm{d}x - V\mathrm{d}t}{\mathrm{d}t - \frac{V}{c^2}\mathrm{d}x} = \frac{v_x - V}{1 - \frac{v_x V}{c^2}}.$$

And so we obtain the velocity relative to an inertial frame moving along x axis:

$$v'_x = \frac{v_x - V}{1 - \frac{v_x V}{c^2}}, \tag{A.2.2}$$

$$v'_y = \frac{1}{\gamma}\frac{v_y}{1 - \frac{v_x V}{c^2}}, \tag{A.2.3}$$

$$v'_z = \frac{1}{\gamma}\frac{v_z}{1 - \frac{v_x V}{c^2}}. \tag{A.2.4}$$

A.3 Body under a proper constant acceleration

Let's consider a first inertial frame $\mathcal{R}$ with $\mathcal{B} = (\mathbf{e_0}, \mathbf{e_1}, \mathbf{e_2}, \mathbf{e_3})$ its associated orthonormal basis and a system of coordinates (ct, x, y, z) and second frame $\mathcal{R}'$ which is accelerated, with his own associated orthonormal basis $\mathcal{B}' = (\mathbf{e_0}', \mathbf{e_1}', \mathbf{e_2}', \mathbf{e_3}')$ and system of coordinates (ct', x', y', z'). We assume these following restrictions:

- the motion is contained in a plane $\Pi = \mathrm{vect}\,(\mathbf{e_0}, \mathbf{e_1})$, otherwise written

$$\mathbf{u}(t') = u^0(t')\mathbf{e_0} + \mathbf{u^1}(\mathbf{t'})\mathbf{e_1} \tag{A.3.1a}$$

$$\mathbf{a}(t') = a^0(t')\mathbf{e_0} + \mathbf{a^1}(\mathbf{t'})\mathbf{e_1} \tag{A.3.1b}$$

- $\mathcal{R}'$ is moving along $v(t)\mathbf{e_1}$ in the frame $\mathcal{R}$, this leads to

$$\mathrm{d}t = \frac{1}{\sqrt{1 - \left(\frac{v(t)}{c}\right)^2}}\mathrm{d}t' \tag{A.3.2}$$

- $a = \sqrt{-(\mathbf{a}.\mathbf{a})}$ the proper acceleration is constant, so

$$a^2 = (a^1)^2 - (a^0)^2 \tag{A.3.3a}$$

$$c^2 = (u^0)^2 - (u^1)^2 \tag{A.3.3b}$$

$$a^0 u^0 = a^1 u^1 \tag{A.3.3c}$$

As noticed in the book of E. Gourgoulhon [118], $\mathbf{a}$ cannot be a constant because the only way to respect the relations A.1.5 would be to have $\mathbf{a} = \mathbf{0}$.

Taking the definition of the four-acceleration A.1.4b (with the notation $\mathrm{d}\tau \to \mathrm{d}t'$), we get the differential equations of u^0 and u^1:

$$\frac{1}{\sqrt{\left(\frac{u^0}{c}\right)^2 - 1}}\frac{\mathrm{d}u^0}{\mathrm{d}t'} = a, \tag{A.3.4a}$$

$$\frac{1}{\sqrt{\left(\frac{u^1}{c}\right)^2 + 1}}\frac{\mathrm{d}u^1}{\mathrm{d}t'} = \pm a. \tag{A.3.4b}$$

with + for an acceleration and − for a deceleration. Using the definition of the four-velocity A.1.4a, we have

$$u^\mu = \frac{\mathrm{d}x^\mu}{\mathrm{d}\tau} = \gamma\frac{\mathrm{d}x^\mu}{\mathrm{d}t} = \frac{1}{\sqrt{1-\left(\frac{v(t)}{c}\right)^2}}v^\mu(t),$$

and with the second component, we can write a relation as a function of v:

$$\begin{aligned}\frac{\mathrm{d}u^1}{\mathrm{d}t'} &= \pm a\sqrt{\left(\frac{u^1}{c}\right)^2+1},\\ \gamma\frac{\mathrm{d}\gamma v}{\mathrm{d}t} &= \pm a\sqrt{\left(\frac{\gamma v}{c}\right)^2+1},\\ \gamma\frac{\mathrm{d}\gamma v}{\mathrm{d}t} &= \pm a\gamma,\end{aligned}$$

$$\frac{\mathrm{d}\gamma v(t)}{\mathrm{d}t} = \pm a. \tag{A.3.5}$$

Note: Doing a limited expansion at the first order in $\frac{v}{c}$, we get the equations of classical mechanics:

$$\begin{aligned}\gamma &= 1+\frac{1}{2}\left(\frac{v}{c}\right)^2+o\left(\frac{v}{c}\right)^2,\\ \gamma\frac{v}{c} &= \frac{v}{c}+o\left(\frac{v}{c}\right),\\ \Rightarrow \frac{\mathrm{d}\gamma v(t)}{\mathrm{d}t} &= \frac{\mathrm{d}v(t)}{\mathrm{d}t} = \pm a + o\left(\frac{v}{c}\right).\end{aligned}$$

If we integrate, considering $v(0)=0$ and a positive acceleration we get

$$v(t) = c\frac{at}{\sqrt{c^2+(at)^2}}. \tag{A.3.6}$$

Integrating [1] a second time, we get the position (considering $x(0)=0$)

$$x(t) = \frac{c^2}{a}\left[\sqrt{1+\left(\frac{at}{c}\right)^2}-1\right]. \tag{A.3.7}$$

Using the A.1.3 relation, we get the proper time (see Figure A.2)

$$\tau = \int_0^t \sqrt{1-\left(\frac{v(\lambda)}{c}\right)^2}\,\mathrm{d}\lambda = \int_0^t \frac{\mathrm{d}\lambda}{1+\left(\frac{a\lambda}{c}\right)^2} = \frac{c}{a}\mathrm{argsh}\left(\frac{at}{c}\right). \tag{A.3.8}$$

To compare numerically with Newton's classical mechanics we use a proper constant acceleration ($a = 1\,\mathrm{ly}\,\mathrm{y}^{-2} = 9.5\,\mathrm{m}\,\mathrm{s}^{-2}$) in the classical case (v_c) and relativistic

---

[1] $\int \frac{x}{\sqrt{1+x^2}} = \sqrt{1+x^2}$

case (v). Newton's classical mechanics give us

$$\frac{\mathrm{d}v_c(t)}{\mathrm{d}t} = a, \tag{A.3.9a}$$

$$v_c(t) = at, \tag{A.3.9b}$$

$$x_c(t) = \frac{1}{2}at^2. \tag{A.3.9c}$$

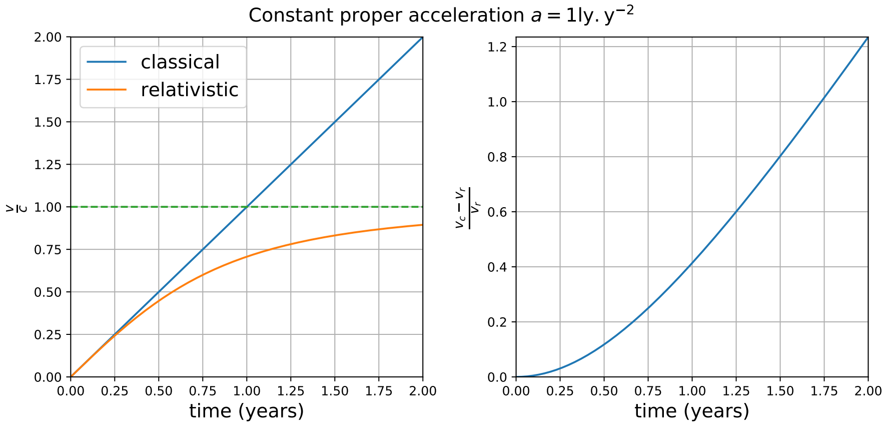

Figure A.2 – Velocities in the classical and relativistic frames for a proper constant acceleration of 1 ly y^{-2}. Left: velocities computed in the both frames; right: relative differences of the velocities.

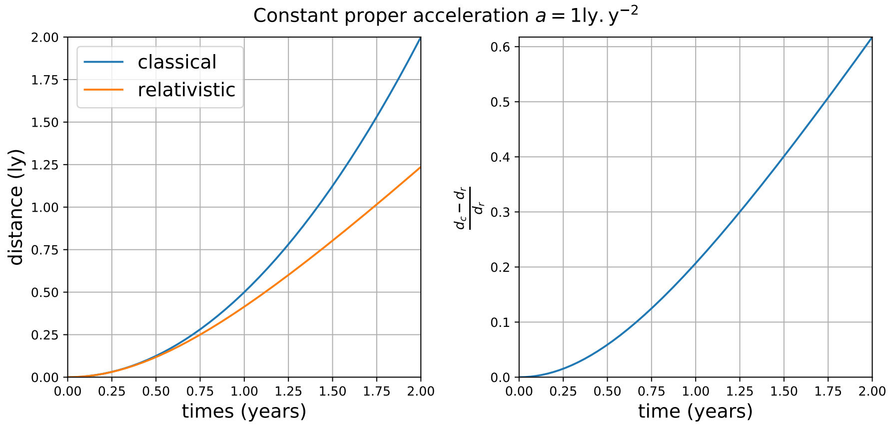

Figure A.3 – Travelled distances in the classical and relativistic frames for a proper constant acceleration of 1 ly y^{-2}. Left: distance computed in the both frames; right: relatives differences of the distances.

Figure A.2 shows us that in the relativistic frame, we cannot overpass the speed of light, and this is not predicted by the classical mechanics. Moreover, at small velocity both models are equivalent. Figure A.4 highlights the time dilatation in the

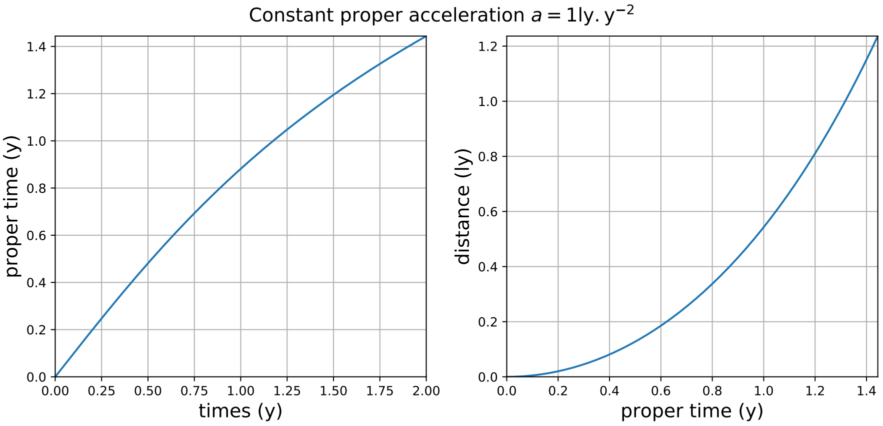

Figure A.4 – For a proper constant acceleration of $1\,\text{ly}\,\text{y}^{-2}$. Left: proper time as a function of the time in the reference frame; right: travelled distance as a function of the proper time.

moving frame. For example, when 2 years have passed in the reference frame, 1.4 years have passed in the moving frame.

Appendix B

Dirac Equation

B.1 Notations

As defined in A.1, we note in this section of 4-vector $\mathbf{x}$ as:

$$\mathbf{x} = \begin{pmatrix} ct \\ x \\ y \\ z \end{pmatrix} \tag{B.1.1}$$

we note x^μ (or any greek letter) a space-time component of $\mathbf{x}$, $\overrightarrow{x}$ the spatial part and x^k (or any latin letter) a spatial component. To make the writing easier, the component of a vector and the vector can be used with the same meaning.

The energy-momentum 4-vector is noted and defined as,

$$\mathbf{p} = p^\mu = \begin{pmatrix} E/c \\ \overrightarrow{p} \end{pmatrix}, \tag{B.1.2}$$

with E the energy of a particle, c the speed of light, and $\overrightarrow{p}$ the momentum.

To make the equation more readable, the partial derivative along a coordinate x^μ, $\frac{\partial}{\partial x^\mu}$ might be written ∂_μ. We use Einstein convention of implicitly summing over repeated indices.

B.2 Motivation

The main idea behind the work from Dirac was to determine an equation ruling the wave function of an electron. Before Dirac established in 1928 his equation [1], the Schrödinger equation was used to describe the behaviour of an electron. Indeed the correspondence principle of quantum mechanics $E \leftrightarrow= i\hbar\frac{\partial}{\partial t}$, $\overrightarrow{p} = -i\hbar\overrightarrow{\nabla}$, leads to

$$E\psi = H\psi, \tag{B.2.1a}$$

$$i\hbar\frac{\partial \psi}{\partial t} = -\frac{\hbar^2}{2m}\overrightarrow{\nabla}^2\psi + V\psi, \tag{B.2.1b}$$

with H the Hamiltonian of the system, and ψ the wave function, the first term of H corresponding to the kinetic energy ($\frac{\overrightarrow{p}^2}{2m}$) and V the interaction potential. Thereby the possible values of the energy E are the eigenvalues of the operator H.

However, the Schrödinger equation has two shortcomings. Firstly, it is not relativistic, and considering the mass of an electron, it appears obvious that a relativistic equation to govern its behaviour has to be found. Secondly, the spin does not appear naturally and it is an ad-hoc element of the quantum theory.

To obtain a relativistic equation, once again, the correspondence principle can be applied on the relation $E^2 = (\overrightarrow{p}c)^2 + (mc^2)^2$. This leads to the Klein-Gordon equation ($\hbar = c = 1$)

$$(\partial_\mu \partial^\mu + m^2)\psi = 0. \tag{B.2.2}$$

If the wave function really describes the motion of a particle, the Klein Gordon equation has to be compatible with a continuity law:

$$\frac{\partial \rho}{\partial t} + \overrightarrow{\nabla} \cdot \overrightarrow{j} = 0. \tag{B.2.3}$$

And this is the case. Indeed Equation B.2.2 leads to

$$\begin{aligned}
\psi^*(\partial_\mu \partial^\mu + m^2)\psi &= 0 \\
\psi(\partial_\mu \partial^\mu + m^2)\psi^* &= 0 \\
\Rightarrow \psi^* \partial_\mu \partial^\mu \psi - \psi \partial_\mu \partial^\mu \psi^* &= 0 \\
\Leftrightarrow \partial_t i \left(\psi^* \partial_t \psi - \psi \partial_t \psi^*\right) + \overrightarrow{\nabla} i \left(\psi^* \overrightarrow{\nabla} \psi - \psi \overrightarrow{\nabla} \psi^*\right) &= 0
\end{aligned}$$

which is a continuity law with $\rho = i\left(\psi^* \partial_t \psi - \psi \partial_t \psi^*\right)$ and $\overrightarrow{j} = i\left(\psi^* \overrightarrow{\nabla} \psi - \psi \overrightarrow{\nabla} \psi^*\right)$. The solution for the Klein-Gordon equation has the form $\psi = Ne^{-ip_\mu x^\mu}$. Indeed, the equation applied to this wave function leads to $p_\mu p^\mu = (mc^2)^2$, i.e. $E^2 = (\overrightarrow{p}c)^2 + (mc^2)^2$. In that case, $\rho = 2E|N|^2$, but there are two solutions for E, $\pm\sqrt{\overrightarrow{p}c)^2 + (mc^2)^2}$, and this means that ρ might be negative, which is impossible if we want to understand it as a probability density.

The idea is now to try to find a linear expression of the hamiltonian, of the form

$$H = \alpha^k p^k c + \beta mc^2 \tag{B.2.4}$$

in order to have $H^2\psi = E^2\psi$ with $E^2 = (\overrightarrow{p}c)^2 + (mc^2)^2$. In that case, α^k and β cannot be numbers if we want to preserve rotational invariance. So it will be assumed that α^k and β are $N \times N$ matrices and ψ a vector of dimension $N > 1$.

B.3 Building of the equation

We would like to find an linear hamiltonian for the electron as

$$H = \alpha^k p^k c + \beta mc^2. \tag{B.3.1}$$

Let's first see if it is compatible with a continuity law. Starting from $E\psi = H\psi \Leftrightarrow E\psi^\dagger = \psi^\dagger H^\dagger$, the following equations are found:

$$\begin{cases}
E\psi = i\hbar\partial_t\psi = \alpha^k p^k \psi c + \beta\psi mc^2 & = -i\hbar c\alpha^k \partial_k \psi + \beta\psi mc^2, \\
E\psi^\dagger = -i\hbar\partial_t\psi^\dagger & = i\hbar c\partial_k \psi^\dagger (\alpha^k)^\dagger + \psi^\dagger \beta^\dagger mc^2.
\end{cases}$$

α^k, β are hermitian (i.e. ${\alpha^k}^\dagger = \alpha^k, \beta^\dagger = \beta^\dagger$) because H is hermitian. We multiply the first line by $\psi^\dagger$ and the second by ψ to finally obtain

$$i\hbar\left(\psi^\dagger\partial_t\psi + \psi\partial_t\psi^\dagger\right) = -i\hbar c(\psi^\dagger\alpha^k\partial_k\psi + \partial_k\psi^\dagger\alpha^k\psi),$$

which can be written as a continuity law:

$$\partial_t\left(\psi^\dagger\psi\right) + \partial_k\left(c\psi^\dagger\alpha^k\psi\right) = 0, \tag{B.3.2}$$

with $\rho = \psi^\dagger\psi, \mathbf{j} = c\psi^\dagger\alpha\psi$ and we have $\rho \geq 0$, which means that ρ can be understood as a probability density.

To find a relation between α^k and β, we start again from $H^2\psi = E^2\psi$, because is it known that $E^2 = c^2\left(\overrightarrow{p}^2 + m^2c^2\right)$. If we note I_N, the neutral element of $\mathcal{M}_N(\mathbb{C})$, we have

$$\begin{aligned}(\overrightarrow{\alpha}\cdot\overrightarrow{p} + \beta mc)^2 &= \left(\overrightarrow{p}^2 + m^2c^2\right)I_N\\ \frac{1}{2}[\alpha^j,\alpha^k]p^jp^k + \frac{1}{2}\{\alpha^j,\alpha^k\}p^jp^k + \{\alpha^k,\beta\}p^k + \beta^2m^2c^2 &= \left(\overrightarrow{p}^2 + m^2c^2\right)I_N\end{aligned}$$

So if α^k and β fulfil

$$\{\alpha^j,\alpha^k\} = 2\delta^{jk}I_N, \tag{B.3.3a}$$

$$\{\alpha^k,\beta\} = 0, \tag{B.3.3b}$$

$$\beta^2 = I_N, \tag{B.3.3c}$$

then $H^2\psi = E^2\psi$ is true. Equations B.3.3 describe a Clifford algebra associated to the metric δ^{jk} ($\delta^{jk} = 1$ if $j = k$, $\delta^{jk} = 0$ otherwise).

The second equation of B.3.3 lets us know that N is even. Indeed:

$$\begin{aligned}\{\alpha^k,\beta\} &= 0,\\ \alpha^k\beta &= -\beta\alpha^k,\\ det(\alpha^k\beta) &= det(-\beta\alpha^k),\\ det(\alpha^k\beta) &= (-1)^N det(\alpha^k\beta),\\ 1 &= (-1)^N.\end{aligned}$$

Let's try with $N = 2$. We take $\alpha^k = \sigma^k$, with σ^k the Pauli's matrices

$$\sigma^x = \begin{pmatrix}0 & 1\\ 1 & 0\end{pmatrix}, \sigma^y = \begin{pmatrix}0 & -i\\ i & 0\end{pmatrix}, \sigma^z = \begin{pmatrix}1 & 0\\ 0 & -1\end{pmatrix}, \tag{B.3.4}$$

which fulfil

$$[\sigma^i,\sigma^j] = 2i\epsilon^{ijk}\sigma^k \tag{B.3.5a}$$

$$\{\sigma^i,\sigma^j\} = 2\delta^{ij} \tag{B.3.5b}$$

$$\Rightarrow \sigma^i\sigma^j = \delta^{ij} + i\epsilon^{ijk}\sigma^k \tag{B.3.5c}$$

Also, $\mathcal{B} = (I_2, \sigma^x, \sigma^y, \sigma^z)$ can be taken as a basis of hermitian matrices subspace. Thereby, β can be written as $\beta = x^k\sigma^k + y$.

However, in that case, $\{\beta, \alpha^k\} = 0$ leads to $\{\beta, \sigma^k\} = 0 = 2x^k + 2y\sigma^k$ so $x^k = y = 0$. This means that β has to be null, which not acceptable. We therefore try $N = 4$.

For $N = 4$, let's have a look at the standard representation of the Clifford algebra (associated to the euclidian metric of $\mathbb{R}$)

$$\alpha^k = \begin{pmatrix} 0 & \sigma^k \\ \sigma^k & 0 \end{pmatrix}, \beta = \begin{pmatrix} I_2 & 0 \\ 0 & -I_2 \end{pmatrix}. \tag{B.3.6}$$

In that case

$$\begin{aligned} E\psi &= H\psi, \\ i\hbar\partial_t\psi &= c\alpha^k p^k\psi + \beta mc^2\psi, \\ i\hbar\partial_t\psi &= -i\hbar c\alpha^k\partial_k\psi + \beta mc^2\psi, \\ i\hbar\partial_0\psi + i\hbar\alpha^k\partial_k\psi &= \beta mc\psi, \\ i\hbar(\beta\partial_0 + \beta\alpha^k\partial_k)\psi &= mc\psi, \end{aligned}$$

and defining $\gamma^0 = \beta$ and $\gamma^k = \beta\alpha^k$ we get

$$\left(i\hbar\gamma^\mu\partial_\mu - mc\right)\psi = 0, \tag{B.3.7}$$

which is the Dirac equation, with

$$\gamma^0 = \begin{pmatrix} I_2 & 0 \\ 0 & -I_2 \end{pmatrix}, \gamma^k = \begin{pmatrix} 0 & \sigma^k \\ -\sigma^k & 0 \end{pmatrix}, \tag{B.3.8}$$

the Dirac matrices. Writing $\overline{\psi} = \psi^\dagger\gamma^0$, the current $j^\mu = (\rho/c, \overrightarrow{j})$ is conserved $(\partial_\mu j^\mu = 0)$ with $j^\mu = c\overline{\psi}\gamma^\mu\psi$.

B.4 Solutions

Now the goal is to solve the Dirac equation

$$(i\hbar\gamma^\mu\partial_\mu - mc)\psi = 0, \tag{B.4.1}$$

and as a reminder, ψ is a 4 dimensions wave function vector.

If we assume a wave function of the form $\psi = u(p^\mu)\exp\left(-\frac{i}{\hbar}p_\mu x^\mu\right)$ with

$$u(p^\mu) = \begin{pmatrix} f(p^\mu) \\ g(p^\mu) \end{pmatrix},$$

f, g two 2-dimension vectors, then the Dirac equation leads to

$$(p_\mu\gamma^\mu - mc)u(p^\mu) = 0 \tag{B.4.2}$$

$$\begin{cases} (E - mc^2)f - p^k\sigma^k cg &= 0, \\ pk\sigma^k cf - (E + mc^2)g &= 0. \end{cases} \tag{B.4.3}$$

$f=0, g=0$ being solution of B.4.3, the only way to have a non trivial solution is to fulfil $(E-mc^2)(E+mc^2)-p_k\sigma^k p_l\sigma^l c^2$, which leads to $E^2=\left(\overrightarrow{p}c\right)^2+\left(mc^2\right)^2$, as anticipated.

In other words, the system has two eigenvalues $\pm E=\pm\sqrt{\left(\overrightarrow{p}c\right)^2+\left(mc^2\right)^2}$, one corresponding to particles with a positive energy, the second to particles with a negative energy.

Let's start with $E>0$:

$$\begin{cases}(E-mc^2)\,f-\overrightarrow{p}\cdot\overrightarrow{\sigma}cg & =0\\ \overrightarrow{p}\cdot\overrightarrow{\sigma}cf-(E+mc^2)g & =0\end{cases} \tag{B.4.4}$$

$$\Rightarrow g=\frac{\overrightarrow{p}\cdot\overrightarrow{\sigma}}{E+mc^2}cf \tag{B.4.5}$$

So, we have two eigenvectors associated to $+E$, corresponding to $f=\begin{pmatrix}1\\0\end{pmatrix}$ or $\begin{pmatrix}0\\1\end{pmatrix}$:

$$u_\uparrow=N_\uparrow\begin{pmatrix}1\\0\\\frac{\overrightarrow{p}\cdot\overrightarrow{\sigma}}{E+mc^2}c\begin{pmatrix}1\\0\end{pmatrix}\end{pmatrix},u_\downarrow=N_\downarrow\begin{pmatrix}0\\1\\\frac{\overrightarrow{p}\cdot\overrightarrow{\sigma}}{E+mc^2}c\begin{pmatrix}0\\1\end{pmatrix}\end{pmatrix} \tag{B.4.6}$$

Because ψ has to be a wave function, we can determine $N_\uparrow$ and $N_\downarrow$:

$$\int \mathrm{d}^3x\psi^\dagger\left(\overrightarrow{x},\overrightarrow{p}\right)\psi\left(\overrightarrow{x},\overrightarrow{q}\right)=\delta\left(\overrightarrow{p}-\overrightarrow{q}\right)\Rightarrow|N_\uparrow|^2=|N_\downarrow|^2=\frac{E+mc^2}{2E}. \tag{B.4.7}$$

To determine the other wave functions, we perform the following substitution in Equation B.4.3 $E\to -E, \overrightarrow{p}\to-\overrightarrow{p}$ which leads to the relation $f=\frac{\overrightarrow{p}\cdot\overrightarrow{\sigma}}{E+mc^2}cg$. Thereby, two new wave function are obtained:

$$v_\uparrow=N_\uparrow\begin{pmatrix}\frac{\overrightarrow{p}\cdot\overrightarrow{\sigma}}{E+mc^2}c\begin{pmatrix}1\\0\end{pmatrix}\\1\\0\end{pmatrix},v_\downarrow=N_\downarrow\begin{pmatrix}\frac{\overrightarrow{p}\cdot\overrightarrow{\sigma}}{E+mc^2}c\begin{pmatrix}0\\1\end{pmatrix}\\0\\1\end{pmatrix} \tag{B.4.8}$$

A basis of solution of the Dirac equation can be summarised as

$$\psi_s^{(+)}(p^\mu,x^\mu)=u_s(\overrightarrow{p})e^{-ip^\mu x_\mu},\psi_s^{(-)}(p^\mu,x^\mu)=v_s(\overrightarrow{p})e^{ip^\mu x_\mu}, \tag{B.4.9}$$

with

$$u_s(\overrightarrow{p})=\sqrt{\frac{E+mc^2}{2E}}\begin{pmatrix}\phi_s\\\frac{\overrightarrow{p}\cdot\overrightarrow{\sigma}}{E+mc^2}c\phi_s\end{pmatrix},v_s(\overrightarrow{p})=\sqrt{\frac{E+mc^2}{2E}}\begin{pmatrix}\frac{\overrightarrow{p}\cdot\overrightarrow{\sigma}}{E+mc^2}c\phi_s\\\phi_s\end{pmatrix} \tag{B.4.10}$$

and

$$\phi_s=\begin{pmatrix}1\\0\end{pmatrix}\text{ or }\begin{pmatrix}0\\1\end{pmatrix}. \tag{B.4.11}$$

u_s described electrons with 2 possible states for each particle, up and down, corresponding to the two spin states. This beautifully fulfils the original goal: a quantum and relativistic equation of the electron naturally encompasses the description of the spin. But there is more, and even more spectacular: the solution v_s was first seen as spurious, but Dirac finally proposed that it describes a real particle of charge opposed to that of the electron. This was the invention of the positron.

B.5 Spin

In classical quantum physics, the spin was an ad-hoc parameter introduce to match the experiments. A first great result of the Dirac equation is that the electrons or the positrons have two states. We will show in this section that these states are actually the spin states.

Defining the angular momentum operator as $\overrightarrow{L} = \overrightarrow{x} \times \overrightarrow{p}$, and the spin operator (which is also an angular momentum) $\overrightarrow{S} = \frac{\hbar}{2}\overrightarrow{\Sigma}$

$$\Sigma^k = \begin{pmatrix} \sigma^k & 0 \\ 0 & \sigma^k \end{pmatrix}, \tag{B.5.1}$$

the total angular momentum is $\overrightarrow{J} = \overrightarrow{L} + \overrightarrow{S}$. One can first observe that $[\overrightarrow{J}, H] = [\overrightarrow{L}, H] + [\overrightarrow{S}, H] = i\hbar c(\overrightarrow{\alpha} \times \overrightarrow{p} - \overrightarrow{\alpha} \times \overrightarrow{p}) = \overrightarrow{0}$, so the total angular momentum is conserved.

In the case of a motionless particle, it is pretty obvious that basis vectors of solutions of the Dirac equations are eigenvectors of Σ^z. Indeed if $\overrightarrow{p} = 0$,

$$u_\uparrow = \begin{pmatrix} 1 \\ 0 \\ 0 \\ 0 \end{pmatrix}, u_\downarrow = \begin{pmatrix} 0 \\ 1 \\ 0 \\ 0 \end{pmatrix}, v_\uparrow = \begin{pmatrix} 0 \\ 0 \\ 1 \\ 0 \end{pmatrix}, v_\downarrow = \begin{pmatrix} 0 \\ 0 \\ 0 \\ 1 \end{pmatrix}, \tag{B.5.2}$$

then

$$S^z u_\uparrow = \frac{\hbar}{2} u_\uparrow, S^z u_\downarrow = -\frac{\hbar}{u_\downarrow} 2, S^z v_\uparrow = \frac{\hbar}{2} v_\uparrow, S^z v_\downarrow = -\frac{\hbar}{2} v_\downarrow. \tag{B.5.3}$$

This remains true for a particle moving along the z-axis:

$$u_\uparrow = \sqrt{\frac{E+mc^2}{2E}} \begin{pmatrix} 1 \\ 0 \\ \frac{pc}{E+mc^2} \\ 0 \end{pmatrix}, S^z u_\uparrow = \frac{\hbar}{2} \begin{pmatrix} 1 & 0 & 0 & 0 \\ 0 & -1 & 0 & 0 \\ 0 & 0 & 1 & 0 \\ 0 & 0 & 0 & -1 \end{pmatrix} \begin{pmatrix} 1 \\ 0 \\ \frac{pc}{E+mc^2} \\ 0 \end{pmatrix} = \frac{\hbar}{2} u_\uparrow,$$

$$u_\downarrow = \sqrt{\frac{E+mc^2}{2E}} \begin{pmatrix} 0 \\ 1 \\ 0 \\ \frac{pc}{E+mc^2} \end{pmatrix}, S^z u_\downarrow = \frac{\hbar}{2} \begin{pmatrix} 1 & 0 & 0 & 0 \\ 0 & -1 & 0 & 0 \\ 0 & 0 & 1 & 0 \\ 0 & 0 & 0 & -1 \end{pmatrix} \begin{pmatrix} 0 \\ 1 \\ 0 \\ \frac{pc}{E+mc^2} \end{pmatrix} = -\frac{\hbar}{2} u_\downarrow.$$

The same can be done for a v_s function which gives $S^z v_\uparrow = \frac{\hbar}{2} v_\uparrow, S^z v_\downarrow = -\frac{\hbar}{2} v_\downarrow$.

In conclusion, the two different states for each particle correspond to the spin with the spin operator written as $\overrightarrow{S} = \hbar/2\mathrm{diag}(\overrightarrow{\sigma}, \overrightarrow{\sigma})$, where σ^k are Pauli matrices.

Appendix C

Buffer Gas Trap electrodes schematics

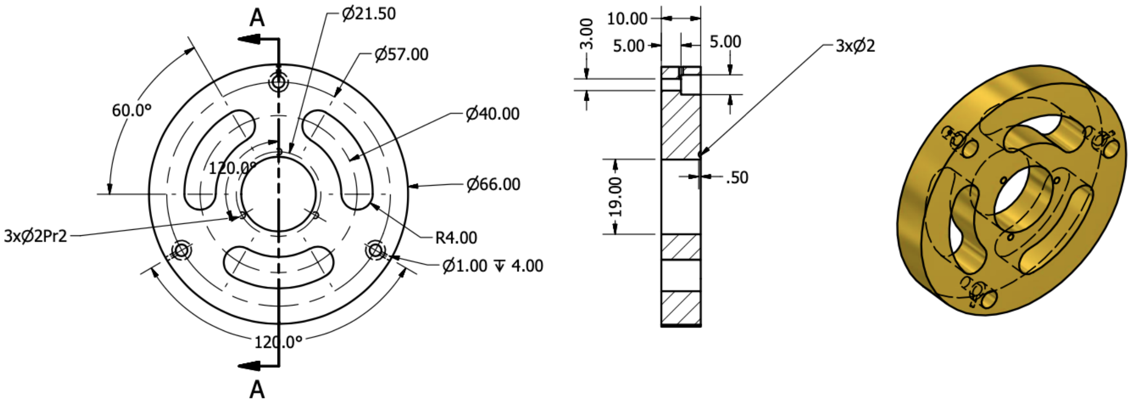

Figure C.1 – Schematic of the grounded ring at the entrance of the Buffer Gas Trap first stage.

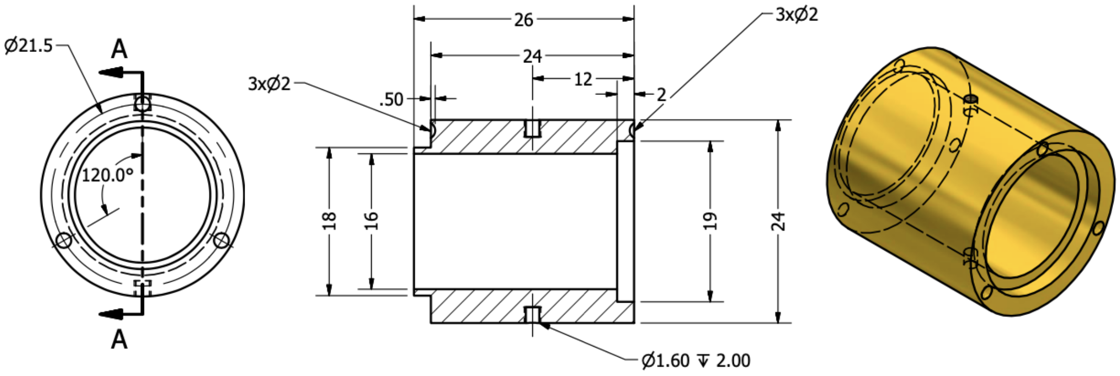

Figure C.2 – Schematic of the electrodes composing the Buffer Gas Trap first stage.

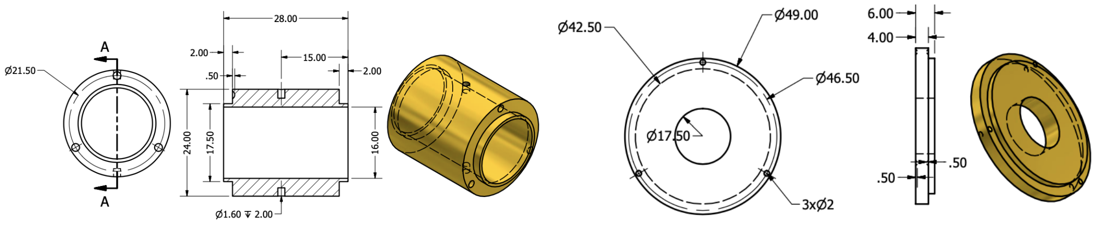

Figure C.3 – Left: Schematic of the last electrode of the Buffer Gas Trap first stage. Right: Schematic of the transition ring between the BGT first stage and second stage.

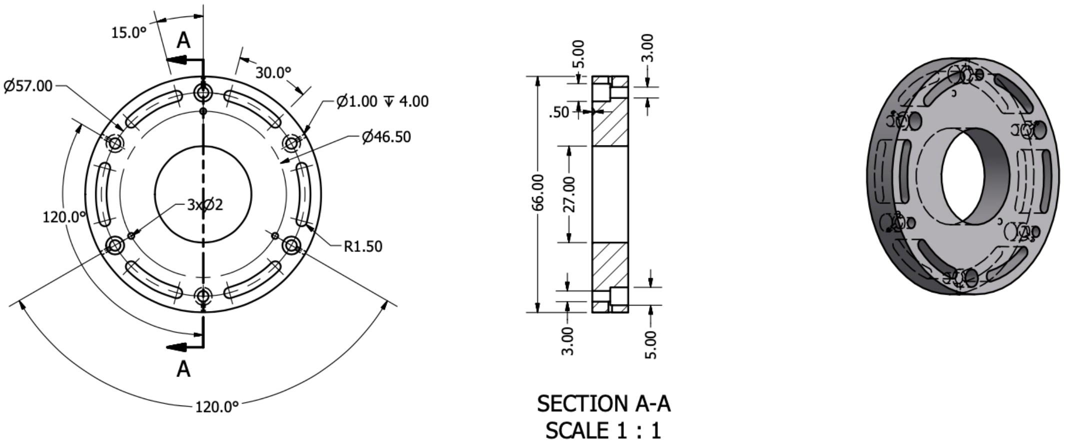

Figure C.4 – Schematic of the grounded ring at the end of the first stage to support the electrodes.

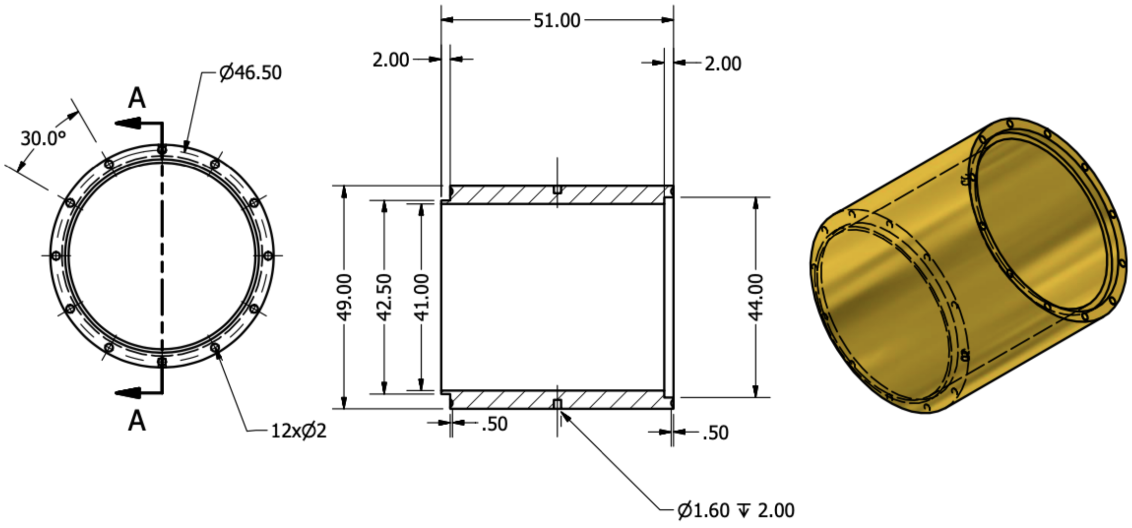

Figure C.5 – Schematic of the long electrodes composing the Buffer Gas Trap second stage. This is also the last electrode of the third stage.

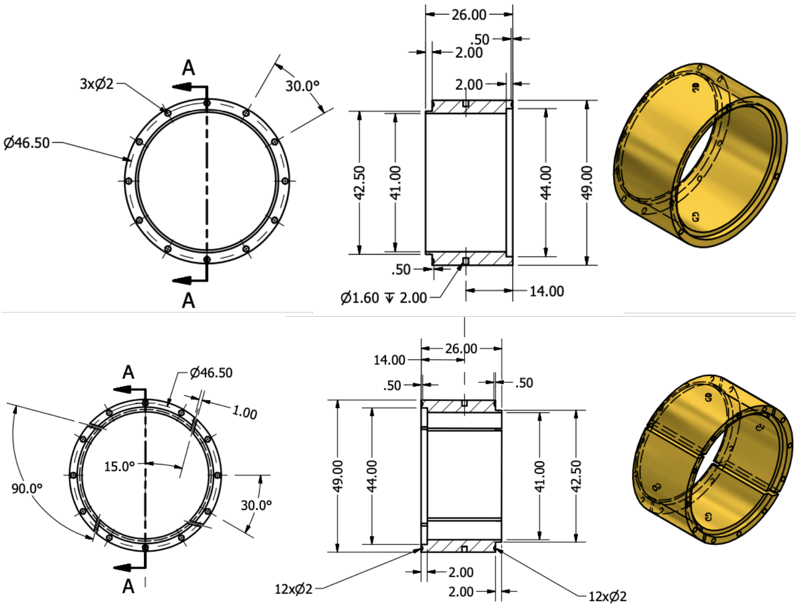

Figure C.6 – Schematic of the half-length electrodes used for the Rotating Wall technique in the Buffer Gas Trap second stage. On both electrodes, the same static potential is applied. The electrode described on the bottom picture is split in four, to apply the oscillating potential for the Rotating Wall technique (see Section 3.3.2).

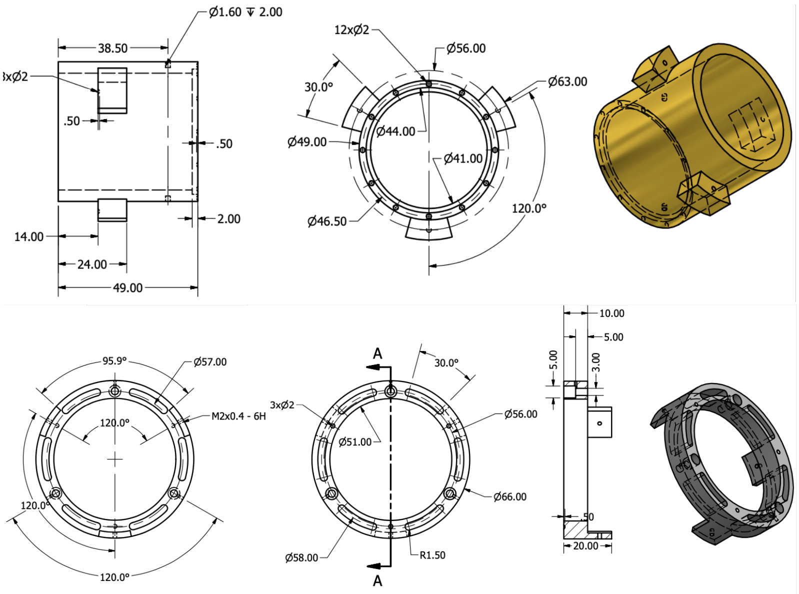

Figure C.7 – Top: Schematic of the last electrode of the Buffer Gas Trap second stage and first electrode of the BGT third stage. Bottom: Schematic of the grounded support ring surrounding the electrodes presented on the left (see the assembly view in Figure 4.4).

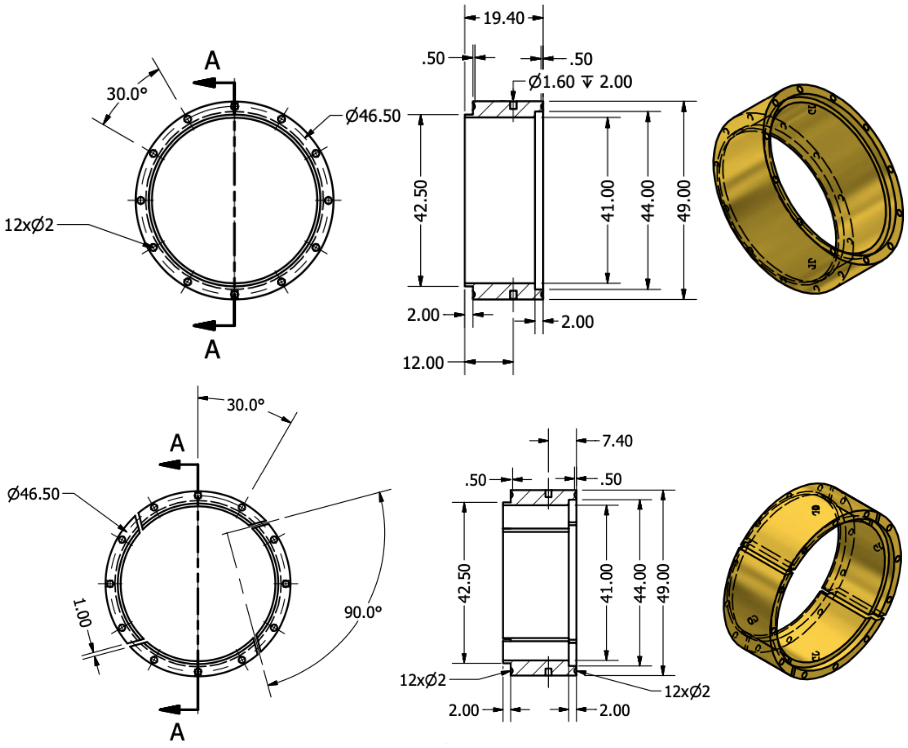

Figure C.8 – Schematic of the electrodes composing the main part of the Buffer Gas trap third stage. The schematic on the left present the electrodes on which a static potential is applied. On the right, the split electrodes for the Rotating Wall technique (see Section 3.3.2).

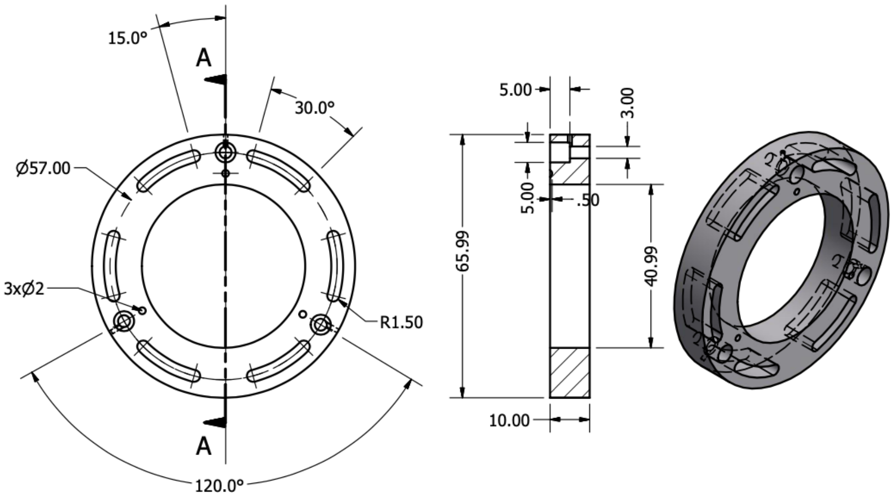

Figure C.9 – Schematic of the grounded ring at the exit of the Buffer Gas Trap third stage.

Appendix D

HFT probes

D.1 Temperature probes connections

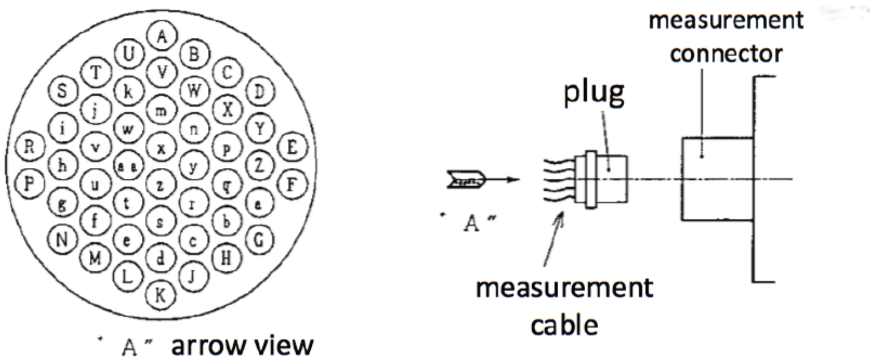

Figure D.1 – Measurement connector pins.

pin	name	pin	name	pin	name	pin	name
A	TG1 V+	P	TG2 V-	a	CC5 -	p	CC9 +
B	TG5 V-	R	TG2 V+	b	CC5 +	q	H3 -
C	TG5 V+	S	TG1 I-	c	CC4 -	r	H3 +
D	TG4 I-	T	TG1 I+	d	CC4 +	s	H2 -
E	TG4 I+	U	TG1 V-	e	CC3 -	t	H2 +
F	TG4 V-	V	TG5 I+	f	CC3 +	u	H1 -
G	TG4 V+	W	CC7 -	g	CC2 -	v	H1 +
H	TG3 I-	X	CC7 +	h	CC2 +	w	CC8 -
J	TG3 I+	Y	CC6 -	i	CC1 -		
K	TG3 V-	Z	CC6 +	j	CC1 +		
L	TG3 V+			k	TG5 I-		
M	TG2 I-			m	CC8 +		
N	TG2 I+			n	CC9 -		

Table D.1 – Layout of duct measurement connector pins

pin	name	pin	name	pin	name	pin	name
A	CGR1 V+	P	CGR2 V-	a	CC7 -	j	CC3 +
B	CC1 -	R	CGR2 V+	b	CC7 +	k	CC2 -
C	CC1 +	S	CGR1 I-	c	CC6 -	q	V4 coil out -
H	CGR3 I-	T	CGR1 I+	d	CC6 +	r	V3 coil out +
J	CGR3 I+	U	CGR1 V-	e	CC5 -	s	V2- P/L2+
K	CGR3 V-	V	CC2 +	f	CC5 +	t	V1- P/L2-
L	CGR3 V+	Y	CC8 -	g	CC4 -	u	V2+ P/L1-
M	CGR2 I-	Z	CC8 +	h	CC4 +	v	V1+ P/L1+
N	CGR2 I+			i	CC3 -		

Table D.2 – Layout of coils measurement connector pins

D.2 Carbon Glass Resistor based probes abaci

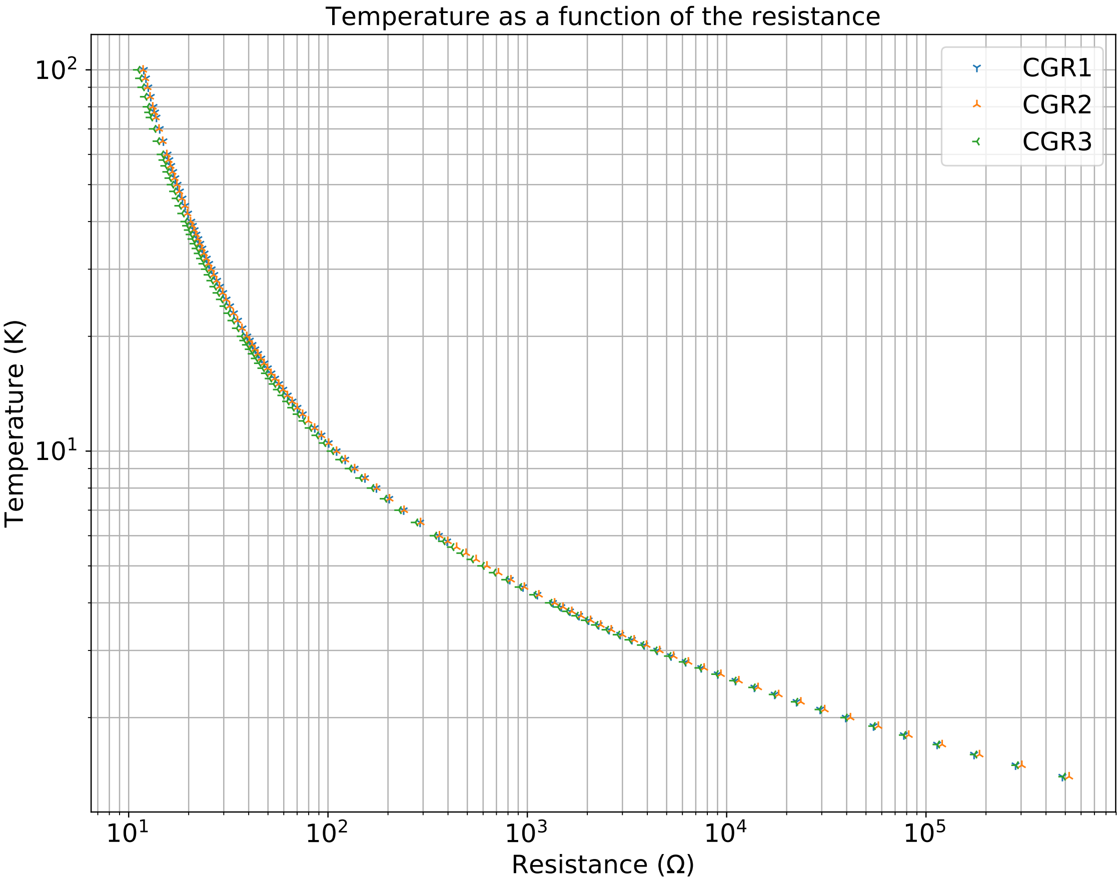

Figure D.2 – Abacus for CGR1, CGR2, CGR3.

T	ρ	$\mathrm{d}\rho/\mathrm{d}T$	$\mathrm{dlog}(\rho)/\mathrm{dlog}(T)$	T	ρ	$\mathrm{d}\rho/\mathrm{d}T$	$\mathrm{dlog}(\rho)/\mathrm{dlog}(T)$
1.4	483554.0	-2780900.0	-8.0514	15.5	54.2987	-4.8252	-1.3774
1.5	281464.0	-1431900.0	-7.6311	16.0	52.0005	-4.378	-1.347
1.6	174277.0	-786870.0	-7.2241	16.5	49.9111	-3.9884	-1.3185
1.7	113724.0	-459320.0	-6.8662	17.0	48.0042	-3.6467	-1.2914
1.8	77443.1	-283620.0	-6.5921	17.5	46.2575	-3.346	-1.2658
1.9	54549.1	-182870.0	-6.3694	18.0	44.6525	-3.0797	-1.2415
2.0	39564.0	-121740.0	-6.1542	18.5	43.1728	-2.8433	-1.2184
2.1	29447.3	-83455.0	-5.9515	19.0	41.805	-2.6322	-1.1963
2.2	22424.2	-58753.0	-5.7642	19.5	40.5369	-2.4434	-1.1754
2.3	17421.9	-42361.0	-5.5924	20.0	39.3584	-2.2736	-1.1553
2.4	13779.4	-31182.0	-5.4311	21.0	37.2353	-1.9823	-1.118
2.5	11073.6	-23386.0	-5.2796	22.0	35.3765	-1.7428	-1.0838
2.6	9027.72	-17838.0	-5.1374	23.0	33.7362	-1.5439	-1.0526
2.7	7455.32	-13818.0	-5.0042	24.0	32.2782	-1.3768	-1.0237
2.8	6229.24	-10851.0	-4.8773	25.0	30.974	-1.2355	-0.99721
2.9	5260.42	-8629.4	-4.7573	26.0	29.8	-1.1158	-0.9735
3.0	4485.61	-6942.5	-4.6432	27.0	28.7371	-1.0123	-0.95112
3.1	3859.02	-5644.4	-4.5342	28.0	27.7711	-0.92173	-0.92932
3.2	3347.16	-4634.1	-4.4304	29.0	26.8896	-0.84333	-0.90952
3.3	2925.01	-3839.6	-4.3319	30.0	26.081	-0.77511	-0.89158
3.4	2573.82	-3207.9	-4.2377	31.0	25.3368	-0.71668	-0.87443
3.5	2279.27	-2701.3	-4.148	32.0	24.6494	-0.66099	-0.8581
3.6	2030.35	-2291.3	-4.0627	33.0	24.0128	-0.61319	-0.84269
3.7	1818.5	-1956.7	-3.9811	34.0	23.4214	-0.57045	-0.82811
3.8	1637.03	-1681.6	-3.9035	35.0	22.8705	-0.53195	-0.81407
3.9	1480.61	-1453.8	-3.8294	36.0	22.3562	-0.49731	-0.80082
4.0	1345.01	-1263.8	-3.7585	37.0	21.8747	-0.46603	-0.78826
4.2	1123.3	-969.96	-3.6267	38.0	21.4232	-0.43756	-0.77614
4.4	951.6	-750.03	-3.505	39.0	20.9988	-0.41171	-0.76464
4.6	816.369	-602.08	-3.3925	40.0	20.599	-0.38814	-0.75372
5.8	396.06	-195.21	-2.8587	42.0	19.8653	-0.34675	-0.7331
6.0	359.918	-167.18	-2.787	44.0	19.2077	-0.3118	-0.71424
6.5	289.762	-117.32	-2.6318	46.0	18.6147	-0.28202	-0.69691
7.0	239.721	-85.073	-2.4842	48.0	18.0769	-0.25638	-0.68077
7.5	202.916	-63.55	-2.3489	50.0	17.5868	-0.23424	-0.66594
8.0	175.032	-48.911	-2.2355	52.0	17.1381	-0.2149	-0.65206
8.5	153.288	-38.598	-2.1403	54.0	16.7256	-0.19791	-0.63896
9.0	135.983	-31.001	-2.0518	56.0	16.3451	-0.18299	-0.62695
9.5	121.97	-25.307	-1.9711	58.0	15.9926	-0.16972	-0.61552
10.0	110.454	-20.95	-1.8967	60.0	15.6652	-0.15791	-0.60482
10.5	100.857	-17.57	-1.8292	65.0	14.9395	-0.13345	-0.58064
11.0	92.7664	-14.897	-1.7664	70.0	14.3215	-0.1145	-0.55963
11.5	85.8708	-12.761	-1.6557	75.0	13.7879	-0.099493	-0.54119
12.5	74.7883	-9.6145	-1.607	77.35	13.5613	-0.093501	-0.53331
13.0	70.2833	-8.4419	-1.5615	80.0	13.3217	-0.087411	-0.52492
13.5	66.3138	-7.4642	-1.5195	85.0	12.9102	-0.077533	-0.51048
14.0	62.7937	-6.6394	-1.4803	90.0	12.5436	-0.069351	-0.49759
14.5	59.6534	-5.9399	-1.4438	95.0	12.2145	-0.062489	-0.48602
15.0	56.8371	-5.3408	-1.4095	100.0	11.9169	-0.056689	-0.4757

Table D.3 – Abacus for CGR1 (Refrigerator 2nd head). Temperature range: 1.40 K to 100 K. Sensor Serial Number: C19051. Sensor Model: CGR1-1-1000-1.4D. Sensor Excitation: 2 mV±50%.

T	ρ	dρ/dT	dlog(ρ)/dlog(T)	T	ρ	dρ/dT	dlog(ρ)/dlog(T)
1.4	522593.0	-2996100.0	-8.0264	14.0	62.5701	-6.6493	-1.4878
1.5	302687.0	-1568900.0	-7.7751	14.5	59.4256	-5.9471	-1.4511
1.6	185598.0	-852350.0	-7.3479	15.0	56.6063	-5.3457	-1.4166
1.7	120532.0	-489770.0	-6.9078	15.5	54.0658	-4.9284	-1.3842
1.8	81974.8	-300770.0	-6.6042	16.0	51.7665	-4.3796	-1.3537
1.9	57699.0	-193940.0	-6.3863	16.5	49.6765	-3.9889	-1.3249
2.0	41796.3	-129330.0	-6.1885	17.0	47.7696	-3.5452	-1.2976
2.1	31039.1	-88810.0	-6.0086	17.5	46.0235	-3.3447	-1.2718
2.2	23563.7	-62535.0	-5.8385	18.0	44.4192	-3.0778	-1.2472
2.3	18242.0	-45029.0	-5.6773	18.5	42.9407	-2.8408	-1.2239
2.4	14375.1	-33047.0	-5.5174	19.0	41.5742	-2.6294	-1.2017
2.5	11512.7	-24687.0	-5.3608	19.5	40.3076	-2.4402	-1.1805
2.6	9357.34	-18751.0	-5.21	20.0	39.1308	-2.2701	-1.1603
2.7	7707.88	-14463.0	-5.0664	21.0	37.0114	-1.9785	-1.1226
2.8	6426.86	-11316.0	-4.9297	22.0	35.1565	-1.7388	-1.0881
2.9	5419.19	-8970.0	-4.801	23.0	33.5202	-1.5399	-1.0566
3.0	4613.83	-7198.1	-4.6803	24.0	32.0662	-1.3728	-1.0275
3.1	3964.82	-5840.7	-4.5667	25.0	30.7659	-1.2316	-1.0008
3.2	3435.55	-4788.4	-4.3601	26.0	29.5959	-1.1118	-0.97668
3.3	2999.57	-3963.5	-4.3605	27.0	28.537	-1.0083	-0.95399
3.4	2637.18	-3309.1	-4.2663	28.0	27.5749	-0.91802	-0.93218
3.5	2333.41	-2785.2	-4.1777	29.0	26.6969	-0.83982	-0.91227
3.6	2076.8	-2361.7	-4.0938	30.0	25.8919	-0.77171	-0.89416
3.7	1858.48	-2016.2	-4.014	31.0	25.1509	-0.71147	-0.87693
3.8	1671.51	-1732.3	-3.9381	32.0	24.4667	-0.65798	-0.86057
3.9	1510.41	-1497.1	-3.8656	33.0	23.833	-0.61035	-0.84511
4.0	1370.8	-1300.9	-3.796	34.0	23.2443	-0.56776	-0.83047
4.2	1142.69	-997.3	-3.6656	35.0	22.696	-0.52937	-0.81635
4.4	966.28	-778.21	-3.5436	36.0	22.1842	-0.49483	-0.803
4.6	827.567	-616.97	-3.4294	37.0	21.7053	-0.46363	-0.79033
4.8	716.8	-496.26	-3.3232	38.0	21.256	-0.43524	-0.7781
5.0	627.153	-404.3	-3.2233	39.0	20.8339	-0.40945	-0.76647
5.2	553.694	-333.29	-3.1292	40.0	20.4364	-0.38594	-0.75541
5.4	492.861	-277.35	-3.0388	42.0	19.707	-0.34465	-0.73453
5.6	441.978	-233.16	-2.9542	44.0	19.1535	-0.30981	-0.71544
5.8	399.014	-197.77	-2.8748	46.0	18.4643	-0.28014	-0.69791
6.0	362.413	-169.24	-2.8019	48.0	17.9302	-0.25462	-0.68163
6.5	291.4	-118.76	-2.6491	50.0	17.4435	-0.23259	-0.66669
7.0	240.758	-86.05	-2.5019	52.0	16.9979	-0.21327	-0.65274
7.5	203.555	-64.191	-2.3651	54.0	16.5885	-0.19648	-0.6396
8.0	175.407	-49.341	-2.2504	56.0	16.2106	-0.18167	-0.62757
8.5	153.485	-38.891	-2.1538	58.0	15.8607	-0.16849	-0.61615
9.0	136.058	-31.203	-2.0641	60.0	15.5357	-0.15677	-0.60545
9.5	121.96	-25.449	-1.9823	65.0	14.8152	-0.1325	-0.58132
10.0	110.384	-21.05	-1.907	70.0	14.2016	-0.11368	-0.56032
10.5	100.744	-17.644	-1.8389	75.0	13.6719	-0.098773	-0.54184
11.0	92.6215	-14.951	-1.7756	77.35	13.4469	-0.092817	-0.53391
11.5	85.7023	-12.802	-1.7178	80.0	13.2091	-0.086761	-0.52546
12.0	79.7518	-11.06	-1.6642	85.0	12.8006	-0.076932	-0.51085
12.5	74.5885	-9.6379	-1.6152	90.0	12.437	-0.068783	-0.49775
13.0	70.0733	-8.4597	-1.5694	95.0	12.1106	-0.061944	-0.48591
13.5	66.096	-7.4776	-1.5273	100.0	11.8158	-0.056161	-0.4753

Table D.4 – Abacus for CGR2 (Right side coil). Temperature range: 1.40 K to 100 K. Sensor Serial Number: C19065. Sensor Model: CGR1-1-1000-1.4D. Sensor Excitation: 2 mV±50%.

T	ρ	dρ/dT	dlog(ρ)/dlog(T)	T	ρ	dρ/dT	dlog(ρ)/dlog(T)
1.4	487265.0	-2834800.0	-8.145	14.0	58.8825	-6.2687	-1.4905
1.5	282956.0	-1438200.0	-7.6239	14.5	55.9184	-5.6049	-1.4534
1.6	175237.0	-793940.0	-7.249	15.0	53.2617	-5.0365	-1.4184
1.7	113940.0	-465830.0	-6.9502	15.5	50.8685	-4.5478	-1.3857
1.8	77211.6	-285960.0	-6.6665	16.0	48.7031	-4.124	-1.3548
1.9	54224.8	-182910.0	-6.4089	16.5	46.7353	-3.7552	-1.3258
2.0	39260.9	-121460.0	-6.1872	17.0	44.9403	-3.4321	-1.2983
2.1	29167.9	-83252.0	-5.9939	17.5	43.2968	-3.1479	-1.2723
2.2	22163.7	-58570.0	-5.8137	18.0	41.787	-2.8965	-1.2477
2.3	17179.6	-42182.0	-5.6473	18.5	40.3956	-2.6734	-1.2243
2.4	13554.8	-31007.0	-5.4901	19.0	39.1096	-2.4744	-1.2021
2.5	10866.4	-23212.0	-5.3403	19.5	37.9177	-2.2964	-1.181
2.6	8837.88	-17664.0	-5.1967	20.0	36.8101	-2.1366	-1.1608
2.7	7282.67	-13648.0	-5.06	21.0	34.8153	-1.8624	-1.1234
2.8	6073.09	-10691.0	-4.9289	22.0	33.0691	-1.637	-1.0891
2.9	5119.95	-6808.7	-4.8044	23.0	31.5284	-1.4501	-1.0578
3.0	4358.95	-6808.7	-4.686	24.0	30.1592	-1.2927	-1.0287
3.1	3745.01	-5525.1	-4.5735	25.0	28.9348	-1.1598	-1.0021
3.2	3244.38	-4528.8	-4.4668	26.0	27.8326	-1.0478	-0.97883
3.3	2832.11	-3747.3	-4.3664	27.0	26.8344	-0.95045	-0.95632
3.4	2489.56	-3127.2	-4.2709	28.0	25.9281	-0.86414	-0.93319
3.5	2202.55	-2630.9	-4.1807	29.0	25.102	-0.79007	-0.91275
3.6	1960.21	-2229.9	-4.0952	30.0	24.3445	-0.72621	-0.89492
3.7	1754.11	-1902.9	-4.0139	31.0	23.6471	-0.66975	-0.878
3.8	1577.68	-1634.4	-3.9367	32.0	23.0029	-0.61954	-0.86186
3.9	1425.69	-1412.2	-3.8632	33.0	22.4062	-0.57469	-0.84641
4.0	1294.01	-1227.0	-3.7928	34.0	21.852	-0.5345	-0.83163
4.2	1078.87	-940.61	-3.6618	35.0	21.3359	-0.49825	-0.81734
4.4	912.466	-734.17	-3.5403	36.0	20.8543	-0.46561	-0.80376
4.6	781.575	-582.34	-3.4274	37.0	20.4017	-0.43612	-0.79087
4.8	676.994	-468.68	-3.323	38.0	19.9812	-0.40934	-0.77849
5.0	592.312	-381.98	-3.2245	39.0	19.5842	-0.38506	-0.7668
5.2	522.894	-314.95	-3.1321	40.0	19.2103	-0.36296	-0.75576
5.4	465.367	-262.41	-3.0449	42.0	18.5243	-0.32421	-0.73508
5.6	417.197	-220.86	-2.9646	44.0	17.9094	-0.29155	-0.71629
5.8	376.489	-187.4	-2.8869	46.0	17.3548	-0.26374	-0.69905
6.0	341.821	-160.21	-2.8122	48.0	16.8519	-0.23977	-0.68295
6.5	274.784	-111.78	-2.6442	50.0	16.3936	-0.21903	-0.66804
7.0	227.119	-81.135	-2.5006	52.0	15.9741	-0.2009	-0.65398
7.5	191.945	-60.818	-2.3764	54.0	15.5886	-0.18493	-0.64062
8.0	165.274	-46.708	-2.2609	56.0	15.233	-0.17091	-0.6283
8.5	144.561	-36.682	-2.1569	58.0	14.9039	-0.15843	-0.61656
9.0	128.139	-29.387	-2.064	60.0	14.5984	-0.14734	-0.60556
9.5	114.862	-23.966	-1.9822	65.0	13.9215	-0.12442	-0.5809
10.0	103.959	-19.828	-1.9072	70.0	13.3455	-0.10674	-0.55989
10.5	94.8784	-16.624	-1.8398	75.0	12.8479	-0.092825	-0.54187
11.0	87.2237	-14.093	-1.7773	77.35	12.6364	-0.087282	-0.53428
11.5	80.7	-12.073	-1.7204	80.0	12.4127	-0.081652	-0.52625
12.0	75.0877	-10.433	-1.6673	85.0	12.028	-0.072513	-0.51244
12.5	70.2172	-9.0915	-1.6185	90.0	11.685	-0.064909	-0.49994
13.0	65.9581	-7.9794	-1.5727	95.0	11.3769	-0.05848	-0.48833
13.5	62.207	-7.0515	-1.5303	100.0	11.0986	-0.052982	-0.47737

Table D.5 – Abacus for CGR3 (Left side coil). Temperature range: 1.40 K to 100 K. Sensor Serial Number: C19066. Sensor Model: CGR1-1-1000-1.4D. Sensor Excitation: 2 mV±50%.

Bibliography

[1] Dirac, P. A. M. "The quantum theory of the electron," *Proceedings of the Royal Society of London. Series A, Containing Papers of a Mathematical and Physical Character*, *117*(778):610–624 (February 1928).

[2] Dirac, P. A. M. "Quantised singularities in the electromagnetic field," *Proceedings of the Royal Society of London. Series A, Containing Papers of a Mathematical and Physical Character*, *133*(821):60–72 (September 1931).

[3] Rajasekaran, G. "The discovery of Dirac equation and its impact on present-day physics," *Resonance*, *8*(8):59–74 (August 2003).

[4] Anderson, C. D. "The apparent existence of easily deflectable positives," *Science*, *76*(1967):238–239 (September 1932).

[5] Anderson, Carl D. "The Positive Electron," *Physical Review*, *43*(6):491–494 (March 1933).

[6] Glashow, Sheldon L. "Partial-symmetries of weak interactions," *Nuclear Physics*, *22*(4):579–588 (February 1961).

[7] Englert, F. and R. Brout. "Broken Symmetry and the Mass of Gauge Vector Mesons," *Physical Review Letters*, *13*(9):321–323 (August 1964).

[8] Higgs, Peter W. "Broken Symmetries and the Masses of Gauge Bosons," *Physical Review Letters*, *13*(16):508–509 (October 1964).

[9] Guralnik, G. S., et al. "Global Conservation Laws and Massless Particles," *Physical Review Letters*, *13*(20):585–587 (November 1964).

[10] Weinberg, Steven. "A Model of Leptons," *Physical Review Letters*, *19*(21):1264–1266 (November 1967).

[11] Salam, Abdus. "Weak and Electromagnetic Interactions," *Conf. Proc.*, *C680519*:367–377 (1968).

[12] Canetti, Laurent, et al. "Matter and antimatter in the universe," *New Journal of Physics*, *14*(9):095012 (September 2012).

[13] Kostelecký, V. Alan and Arnaldo J. Vargas. "Lorentz and CPT tests with hydrogen, antihydrogen, and related systems," *Physical Review D*, *92*(5) (September 2015).

[14] Chamberlain, Owen, et al. “Observation of Antiprotons,” *Physical Review*, *100*(3):947–950 (November 1955).

[15] Baur, G., et al. “Production of antihydrogen,” *Physics Letters B*, *368*(3):251–258 (February 1996).

[16] Blanford, G., et al. “Observation of Atomic Antihydrogen,” *Phys. Rev. Lett.*, *80*:3037–3040 (Apr 1998).

[17] Maury, S. “The Antiproton Decelerator: AD,” *Hyperfine Interactions*, *109*(1/4):43–52 (1997).

[18] Oelert, W. “The ELENA Project at CERN,” *Acta Physica Polonica B*, *46*(1):181 (2015).

[19] Hangst, Jeffrey S and Paul Bowe. *The ALPHA Collaboration Antihydrogen Laser PHysics Apparatus*. Technical Report CERN-SPSC-2004-026. SPSC-I-228, Geneva: CERN, September 2004.

[20] Gabrielse, G, et al. *Proposal presented to the SPSLC: The production and study of cold antihydrogen*. Technical Report CERN-SPSC-97-8. SPSC-P-306, Geneva: CERN, 1997.

[21] Azuma, T, et al. *Atomic spectroscopy and collisions using slow antiprotons*. Technical Report CERN-SPSC-97-19. SPSC-P-307, Geneva: CERN, 1997.

[22] Ulmer, S, et al. *Direct High-Precision Measurement of the g-Factor of a Single Antiproton Stored in a Cryogenic Penning Trap*. Technical Report CERN-SPSC-2012-019. SPSC-I-241, Geneva: CERN, June 2012.

[23] Drobychev, G Yu, et al. *Proposal for the AEGIS experiment at the CERN antiproton decelerator (Antimatter Experiment: Gravity, Interferometry, Spectroscopy)*. Technical Report CERN-SPSC-2007-017. SPSC-P-334, Geneva: CERN, June 2007.

[24] Hangst, Jeffrey S. *Addendum to the ALPHA Proposal; The ALPHA-g Apparatus*. Technical Report CERN-SPSC-2016-031. SPSC-P-325-ADD-1, Geneva: CERN, July 2016.

[25] Chardin, G, et al. *Proposal to measure the Gravitational Behaviour of Antihydrogen at Rest*. Technical Report CERN-SPSC-2011-029. SPSC-P-342, Geneva: CERN, September 2011.

[26] Amoretti, M., et al. “Production and detection of cold antihydrogen atoms,” *Nature*, *419*(6906):456–459 (September 2002).

[27] Gabrielse, G., et al. “Background-Free Observation of Cold Antihydrogen with Field-Ionization Analysis of Its States,” *Physical Review Letters*, *89*(21) (October 2002).

[28] Andresen, G. B., et al. “Confinement of antihydrogen for 1, 000 seconds,” *Nature Physics*, *7*(7):558–564 (June 2011).

[29] Ulmer, S., et al. “High-precision comparison of the antiproton-to-proton charge-to-mass ratio,” *Nature*, *524*(7564):196–199 (August 2015).

[30] Ahmadi, M., et al. “Observation of the 1S-2S transition in trapped antihydrogen,” *Nature*, *541*(7638):506–510 (December 2016).

[31] Maggi, Filippo, et al. “Efficient solid rocket propulsion for access to space,” *Acta Astronautica*, *66*(11-12):1563–1573 (June 2010).

[32] Wagner, T A, et al. “Torsion-balance tests of the weak equivalence principle,” *Classical and Quantum Gravity*, *29*(18):184002 (August 2012).

[33] Chardin, Gabriel and Giovanni Manfredi. “Gravity, antimatter and the Dirac-Milne universe,” *Hyperfine Interactions*, *239*(1) (October 2018).

[34] Walz, J. and T. W. Hänsch. “A Proposal to Measure Antimatter Gravity Using Ultracold Antihydrogen Atoms,” *General Relativity and Gravitation*, *36*(3):561–570 (March 2004).

[35] Nieto, Michael Martin and T. Goldman. “The arguments against “antigravity” and the gravitational acceleration of antimatter,” *Physics Reports*, *205*(5):221–281 (July 1991).

[36] Comini, Pauline, et al. “Antihydrogen ion production from collisions between positronium and keV antiprotons for GBAR,” *Hyperfine Interactions*, *228*(1-3):159–165 (February 2014).

[37] Crivelli, P., et al. “Measurement of the orthopositronium confinement energy in mesoporous thin films,” *Physical Review A*, *81*(5) (May 2010).

[38] Latacz, Barbara Maria. *Study of the antihydrogen atom and ion production via charge exchange reaction on positronium*. PhD dissertation, Université Paris Saclay, September 2019.

[39] Husson, Audric. *Deceleration of antiprotons from CERN’s ELENA synchrotron and transport of antimatter beams through the GBAR experiment*. PhD dissertation, Université Paris Saclay, December 2018.

[40] Herfurth, F, et al. “A linear radiofrequency ion trap for accumulation, bunching, and emittance improvement of radioactive ion beams,” *Nuclear Instruments and Methods in Physics Research Section A: Accelerators, Spectrometers, Detectors and Associated Equipment*, *469*(2):254–275 (August 2001).

[41] Brown, Lowell S. and Gerald Gabrielse. “Geonium theory: Physics of a single electron or ion in a Penning trap,” *Reviews of Modern Physics*, *58*(1):233–311 (January 1986).

[42] Gabrielse, G., et al. “First Capture of Antiprotons in a Penning Trap: A Kiloelectronvolt Source,” *Physical Review Letters*, *57*(20):2504–2507 (November 1986).

[43] Howell, R. H., et al. “Production of slow positrons with a 100-MeV electron linac,” *Applied Physics Letters*, *40*(8):751–752 (April 1982).

[44] Charlton, M., et al. “Positron production using a 9 MeV electron linac for the GBAR experiment,” *Nuclear Instruments and Methods in Physics Research Section A: Accelerators, Spectrometers, Detectors and Associated Equipment*, *985*:164657 (January 2021).

[45] Coleman, P. G. “The generation and transportation of positron beams.” *Positron Beams and Their Applications* 11–40, World Scientific, January 2000.

[46] Surko, C. M., et al. “Positron Plasma in the Laboratory,” *Phys. Rev. Lett.*, *62*:901–904 (February 1989).

[47] Greaves, R.G. and C.M. Surko. “Positron trapping and the creation of high-quality trap-based positron beams,” *Nuclear Instruments and Methods in Physics Research Section B: Beam Interactions with Materials and Atoms*, *192*(1-2):90–96 (May 2002).

[48] Leite, A.M.M. *Development of a buffer gas trap for the confinement of positrons and study of positronium production in the GBAR experiment*. PhD dissertation, Université Paris Saclay, December 2017.

[49] Oshima, N., et al. “Development of a cold HCI source for ultra-slow collisions,” *Nuclear Instruments and Methods in Physics Research Section B: Beam Interactions with Materials and Atoms*, *205*:178–182 (May 2003).

[50] Oshima, N., et al. “New Scheme for Positron Accumulation in Ultrahigh Vacuum,” *Physical Review Letters*, *93*(19) (November 2004).

[51] Dupré, Pierre. *Piégeage de positons dans un piège de Penning Malmberg, en vue de leur accumulation avec un faisceau pulsé*. PhD dissertation, Université Paris 6, 2011.

[52] Grandemange, Pierre. *Trapping and accumulation of positrons from a pulsed beam produced by a linear accelerator for gravitational interaction of antimatter study*. PhD dissertation, Université Paris Sud - Paris XI, December 2013.

[53] Liszkay, L., et al. “Positronium reemission yield from mesostructured silica films,” *Applied Physics Letters*, *92*(6):063114 (February 2008).

[54] Liszkay, L., et al. “Mesoporous silica films with varying porous volume fraction: Direct correlation between ortho-positronium annihilation decay and escape yield into vacuum,” *Applied Physics Letters*, *95*(12):124103 (September 2009).

[55] Ore, A. and J. L. Powell. “Three-Photon Annihilation of an Electron-Positron Pair,” *Physical Review*, *75*(11):1696–1699 (June 1949).

[56] Brandt, Werner and Irwin Spirn. "Positron Lifetime Spectra in Molecular Substances," *Physical Review*, *142*(1):231–237 (February 1966).

[57] Karshenboim, Savely G. "Precision study of positronium: testing bound state QED theory," *International Journal of Modern Physics A*, *19*(23):3879–3896 (September 2004).

[58] Halpern, Otto. "Magnetic Quenching of the Positronium Decay," *Physical Review*, *94*(4):904–907 (May 1954).

[59] Kim, B.H., et al. "Development of a PbWO4 Detector for Single-Shot Positron Annihilation Lifetime Spectroscopy at the GBAR Experiment," *Acta Physica Polonica A*, *137*(2):122–125 (February 2020).

[60] Hilico, Laurent, et al. "Preparing single ultra-cold antihydrogen atoms for free-fall in GBAR," *International Journal of Modern Physics: Conference Series*, *30*:1460269 (January 2014).

[61] Indelicato, Paul, et al. "The Gbar project, or how does antimatter fall?," *Hyperfine Interactions*, *228*(1-3):141–150 (February 2014).

[62] Monroe, C., et al. "Resolved-Sideband Raman Cooling of a Bound Atom to the 3D Zero-Point Energy," *Physical Review Letters*, *75*(22):4011–4014 (November 1995).

[63] Dufour, G., et al. "Shaping the distribution of vertical velocities of antihydrogen in GBAR," *The European Physical Journal C*, *74*(1) (January 2014).

[64] Thompson, Richard C. *Trapped Charged Particles*, chapter Chapter one: Penning Traps, 1–33. World Scientific (Europe), 2016.

[65] Dubin, D. H. E. *Trapped Charged Particles*, chapter Chapter nine: Plasmas in Penning Traps, 179–193. World Scientific (Europe), 2016.

[66] Malmberg, J. H. and T. M. O'Neil. "Pure Electron Plasma, Liquid, and Crystal," *Phys. Rev. Lett.*, *39*:1333–1336 (November 1977).

[67] Isaac, Christopher Aled. *Axialisation of particles in a penning-type trap by the application of a rotating dipole electric field and its application to positron accumulation*. PhD dissertation, Swansea University, 2010.

[68] Huang, X.-P., et al. "Steady-State Confinement of Non-neutral Plasmas by Rotating Electric Fields," *Physical Review Letters*, *78*(5):875–878 (February 1997).

[69] Gould, R. W. "Wave angular momentum in non-neutral plasmas," *AIP Conference Proceedings*, *498*(1):170–175 (1999).

[70] Clarke, J., et al. "Design and operation of a two-stage positron accumulator," *Review of Scientific Instruments*, *77*(6):063302 (June 2006).

[71] Murphy, T. J. and C. M. Surko. "Positron trapping in an electrostatic well by inelastic collisions with nitrogen molecules," *Phys. Rev. A*, *46*:5696–5705 (November 1992).

[72] Marler, J. P. and C. M. Surko. "Positron-impact ionization, positronium formation, and electronic excitation cross sections for diatomic molecules," *Phys. Rev. A*, *72*:062713 (December 2005).

[73] Dahl, David A. "SIMION for the personal computer in reflection," *International Journal of Mass Spectrometry*, *200*(1-3):3–25 (December 2000).

[74] BV, Delta Elektronika. *SM1500-Series 1500 Watts DC Power Supplies*. https://www.delta-elektronika.nl/upload/DATA_SHEET_SM1500_V201801.pdf.

[75] Creux, Léon. *Rotary Engine*. Technical Report, European Patent Office, June 1905.

[76] Ushimaru, Kenji. *Japanese and American competition in the development of scroll compressors and its impact on the American air conditioning industry*. Technical Report, Office of Scientific and Technical Information (OSTI), February 1990.

[77] Iqbal, Munawar, et al. "Design modification in rotor blade of turbo molecular pump," *Nuclear Instruments and Methods in Physics Research Section A: Accelerators, Spectrometers, Detectors and Associated Equipment*, *678*:88–90 (June 2012).

[78] Tait, P. G. and James Dewar. "4. Preliminary Note "On a New Method of obtaining very perfect Vacua."," *Proceedings of the Royal Society of Edinburgh*, *8*:348–349 (1875).

[79] Baechler, Werner G. "Cryopumps for research and industry," *Vacuum*, *37*(1-2):21–29 (January 1987).

[80] Hall, Lewis, et al. *Electrical vacuum pump apparatus and method*. Technical Report, European Patent Office, Jul 1961.

[81] Agilent. *Agilent Ion Pumps*. http://www.ccsservices.ru/upload/banners/IonPumps.pdf.

[82] Berman, Armand. *Vacuum Engineering Calculations, Formulas, and Solved Exercises*. Saint Louis, US: Elsevier Science & Technology, 1992.

[83] *Variant, Inc. Vacuum Technologies*. https://www.agilent.com/cs/library/catalogs/Public/Training.pdf.

[84] Zheng, Sanyi. *Conductance Calculation - Molecular Flow, Long Tube of Circular Cross Section*. Technical Report, EFD Vacuum Group, April 1993.

[85] Systems, Stanford Research, "Gas Correction Factors for Bayard-Alpert Ionization Gauges." https://www.thinksrs.com/downloads/pdfs/applicationnotes/IG1BAgasapp.pdf.

[86] Horiba, "High Performance Mass Flow Controller, SEC-Z500x." https://www.horiba.com/fileadmin/uploads/Semiconductor/Photos/applications/Products/Digital_Mass_Flow_Controller_SEC-Z500X_Series.pdf.

[87] Wiza, Joseph Ladislas. "Microchannel plate detectors," *Nuclear Instruments and Methods*, *162*(1-3):587–601 (June 1979).

[88] Bolton, P.R., et al. "Instrumentation for diagnostics and control of laser-accelerated proton (ion) beams," *Physica Medica*, *30*(3):255–270 (May 2014).

[89] de Haas, J. T. M. and P. Dorenbos. "Advances in Yield Calibration of Scintillators," *IEEE Transactions on Nuclear Science*, *55*(3):1086–1092 (2008).

[90] Kim, Han Soo, et al. "Fabrication and performance characteristics of a CsI(Tl)/PIN diode radiation sensor for industrial applications," *Applied Radiation and Isotopes*, *67*(7-8):1463–1465 (July 2009).

[91] coolfet, "A250CF CoolFET Charge Sensitive Preamplifier." https://www.amptek.com/products/charge-sensitive-preamplifiers/a250cf-coolfet-charge-sensitive-preamplifier.

[92] Mohamed, T., et al. "Comparison of non-neutral electron plasma confinement in harmonic and rectangular potentials in a very dense regime," *Physics of Plasmas*, *20*(1):012502 (January 2013).

[93] Yokogawa. *Programmable DC source, Model 7651*. https://cdn.tmi.yokogawa.com/IM7651-01E.is.pdf.

[94] Advanced Energy. *Ultravolt HVA Series, Precision High Voltage Amplifier*. https://www.advancedenergy.com/globalassets/resources-root/data-sheets/ultravolt-hvaseries-data-sheet.pdf.

[95] Kimball, KPI. *ES-535W Y2O3 Disc Cathode Care and Operating Instructions*.

[96] BV, Delta Elektronika. *ES150 - series*. Models used: ES015-10 and ES0300-0.45.

[97] Malmberg, J H, et al. "Experiments With Pure Electron Plasmas," *Physica Scripta*, *T2B*:288–292 (January 1982).

[98] Fajans, J. and C. M. Surko. "Plasma and trap-based techniques for science with antimatter," *Physics of Plasmas*, *27*(3):030601 (March 2020).

[99] Higaki, Hiroyuki, et al. "Accumulation of LINAC based low energy positrons in a buffer gas trap," *Applied Physics Express*, *13*(6):066003 (May 2020).

[100] Störmer, J, et al. "Silicon carbide: a new positron moderator," *Journal of Physics: Condensed Matter*, *8*(7):L89–L94 (February 1996).

[101] Frisbee, Robert and Stephanie Leifer. "Evaluation of propulsion options for interstellar missions." *34th AIAA/ASME/SAE/ASEE Joint Propulsion Conference and Exhibit*. American Institute of Aeronautics and Astronautics, July 1998.

[102] Frisbee, Robert. "How to Build an Antimatter Rocket for Interstellar Missions - Systems Level Considerations in Designing Advanced Propulsion Technology Vehicles." *39th AIAA/ASME/SAE/ASEE Joint Propulsion Conference and Exhibit*. American Institute of Aeronautics and Astronautics, July 2003.

[103] Frisbee, Robert. "Optimization of Antimatter Rocket Performance." *44th AIAA/ASME/SAE/ASEE Joint Propulsion Conference and Exhibit*. American Institute of Aeronautics and Astronautics, July 2008.

[104] Sutton, George. *Rocket propulsion elements*. Hoboken, New Jersey: John Wiley & Sons Inc, 2017.

[105] Bade, W. L. "Relativistic Rocket Theory," *American Journal of Physics*, *21*(4):310–312 (April 1953).

[106] Walter, Ulrich. "Relativistic rocket and space flight," *Acta Astronautica*, *59*(6):453–461 (September 2006).

[107] Vulpetti, GIOVANNI. "Antimatter propulsion for space exploration," *Journal of the British Interplanetary Society*, *39*(9):391–409 (1986).

[108] Morgan, D.L. "Concepts for the design of an antimatter annihilation rocket," *J. British Interplanetary Soc.*, *35*(NASA-CR-168660):405–412 (1982).

[109] Forward, R.L., "Antiproton AnnihilationPropulsion," 1985. http://www.dtic.mil/dtic/tr/fulltext/u2/a160734.pdf.

[110] Keane, Ronan and Wei-Ming Zhang, "Beamed Core Antimatter Propulsion: Engine Design and Optimization," 2012.

[111] Agostinelli, S., et al. "Geant4—a simulation toolkit," *Nuclear Instruments and Methods in Physics Research Section A: Accelerators, Spectrometers, Detectors and Associated Equipment*, *506*(3):250–303 (July 2003).

[112] Duerr, Hans-Peter and Edward Teller. "Interaction of Antiprotons with Nuclear Fields," *Physical Review*, *101*(1):494–495 (January 1956).

[113] Klempt, Eberhard, et al. "The antinucleon–nucleon interaction at low energy: Annihilation dynamics," *Physics Reports*, *413*(4-5):197–317 (July 2005).

[114] Hori, M., et al. "Analog Cherenkov detectors used in laser spectroscopy experiments on antiprotonic helium," *Nuclear Instruments and Methods in Physics Research Section A: Accelerators, Spectrometers, Detectors and Associated Equipment*, *496*(1):102–122 (January 2003).

[115] Zyla, P A, et al. “Review of Particle Physics,” *Progress of Theoretical and Experimental Physics*, *2020*(8) (August 2020).

[116] Simpson, James, et al., “Simple Analytic Expressions for the Magnetic Field of a Circular Current Loop.” https://ntrs.nasa.gov/archive/nasa/casi.ntrs.nasa.gov/20010038494.pdf.

[117] Ribon, A., et al. “Status of Geant4 hadronic physics for the simulation of LHC experiments at the start of LHC physics program,” *CERN* (2010).

[118] Gourgoulhon, E. *Relativité restreinte: Des particules à l’astrophysique*. Savoirs actuels, EDP Sciences, 2010.

université
PARIS-SACLAY

ÉCOLE DOCTORALE
Particules, hadrons, énergie et noyau :
instrumentation, imagerie, cosmos
et simulation (PHENIICS)

Title: Optimisation of positron accumulation in the GBAR experiment and study of space propulsion based on antimatter.

Keywords: Antimatter, Penning-trap, positrons, rocket, beam-cored engine

Abstract: The goal of the GBAR experiment is to determine the effect of gravity on antihydrogen atoms. The antihydrogen atoms are created by neutralising antihydrogen ions using laser pulses. The antihydrogen ions are produced after two positrons capture by antiprotons flying through a positronium cloud. In this scheme, to produce one single antihydrogen atom, 10×10^{10} positrons have to be beamed on a nanoporous silica to yield the positronium cloud. The positrons are produced by a 9 MeV LINAC accelerating electrons into a tungsten target equipped with a mesh moderator. In this thesis, we have studied and optimised the accumulation and trapping of positrons in two subsequent trapping devices.

The LINAC-based source provides 3×10^7 positrons per second, which have to be accumulated. They are first accumulated into a Buffer Gas Trap (BGT), a Penning trap, divided in 3 stages, with N_2 and CO_2, leading to inelastic collisions which insure the trapping and the cooling of the positrons. The positrons are then slowed in the first stage and accumulated in the second stage for 100 ms with a trapping rate of about 1.7×10^6 positrons per second, then they are transferred into the BGT's third stage. This accumulation and transfer procedure is repeated 10 times to finally provide a bunch of 1.5×10^6 positrons every 1.1 s (a loss happens during this stacking operation and 100 ms are added for a final radial compression using the Rotating Wall technique, the trapping efficiency is then 5%). This new bunch is then ready to be sent and re-trapped into the High Field Trap.

The High Field Trap is a 5 T multi-ring Penning trap allowing to trap large amounts of charged particle for hours. We first tested this trap with electrons by trapping about 5×10^9 of them. The experiments on the electrons lead to the conclusion that a better alignment of the electrodes with respect to the magnetic field still needs to be performed. However, an acceptable situation has been found allowing to re-trap the positrons with 66% efficiency. Then, accumulating the positrons bunches coming from the BGT, it was possible to accumulate 1×10^9 positrons in 1100 s. This is a really promising result for the GBAR experiment. For the future, it is about to do 10 times more, 10 times faster to collect the desired amount of positrons each time the ELENA decelerator provides a bunch of antiprotons (every 100 s).

We also studied how it could be possible to use antimatter to propel a rocket. Indeed, the energy resulting from the antimatter-matter annihilation reaction has a higher intrinsic efficiency than any other propellant. In our study, we focused on the proton-antiproton annihilation reaction in a high magnetic field in order to have the annihilation products aligned with the direction of the thrust. The theoretical model is named the beam cored engine. A simulator has been developed using GEANT4 to evaluate some parameters such the intensity of the field. According to our simulation, it is possible to get a rocket with a specific impulse of about $0.5c/g$ i.e., 1.5×10^7 s (with c the speed of light and g the earth's gravitational acceleration), which is huge if it is compared to the most modern rocket (434 s for Vulcain, propelling Ariane 5). However, this model assumes the capability to produce and store a macroscopic number of antiprotons, which might be an insurmountable show-stopper. Also, with this model, a large amount of gamma rays are produced and a solution to evacuate their energy has to be found.

Université Paris-Saclay
Espace Technologique / Immeuble Discovery
Route de l'Ôrme aux Merisiers RD 128 / 91190 Saint-Aubin, France

université
PARIS-SACLAY

ÉCOLE DOCTORALE
Particules, hadrons, énergie et noyau :
instrumentation, imagerie, cosmos
et simulation (PHENIICS)

Titre : Optimisation de l'accumulation de positons dans l'expérience GBAR et étude de la propulsion spatiale à antimatière

Mots clés : Antimatière, piège de Penning, positons, fusée, beam-cored engine

Résumé : Le but de l'expérience GBAR est de déterminer l'effet de la gravité sur des atomes d'anti-hydrogène. Les atomes d'anti-hydrogène sont créés en neutralisant des ions anti-hydrogène grace à un faisceau laser. Un ion d'anti-hydrogène étant produit par la capture de deux positons par un antiproton volant dans un nuage de positronium. Pour cela, 10×10^{10} positons doivent être envoyés sur une cible de silicate nanoporeuse de laquelle va ressortir le nuage de positronium.

Les positons sont produits par un LINAC (accélérateur linéaire), accélérant des electrons à 9 MeV sur une cible de tungsten. Ce processus fournissant 3×10^7 positons par seconde, les positons doivent être accumulés. Ils sont dans un premier temps accumulés et refroidis dans un Piège à Gas Tampon. Il s'agit d'un piège de Penning divisé en 3 étages, dans lequel de faibles pressions de gas (N_2 et CO_2) on été insérés, permettant la perte d'énergie des positons incidents par collisions inélastiques. Ils sont d'abord accumulés, dans le second étage pendant 100 ms avec un taux de piégeage d'environ 1.7×10^6 positons par seconde. Après quoi, ils sont transférés dans le troisième étage du piège. Cette opération de piégeage-transfert est répétée 10 fois ce qui fournit en sortie de ce premier piège 1.5×10^6 positon chaque 1.1 s (il y a une perte de positons pendant cette opération de stockage et 100 ms sont ajoutées pour une compression radiale en fin de processus). Ce nouveau paquet de positons est donc prêt à être transféré dans le second piège de l'expérience.

Ce second piège est un piège de Penning munit d'un électro-aimant de 5 T, permettant de piéger de grande quantités de particules chargées sur une période de plusieurs heures. Ce piège a d'abord été testé avec des électrons, en confinant des plasmas allant jusqu'à 5×10^9 particules. Ces expériences nous ont amenés à comprendre qu'il y avait un problème quant à l'alignement des électrodes avec le champ magnétique. Problème qui n'a pas pu être résolu jusqu'à présent. Cependant, une situation acceptable a été trouvée, permettant ainsi de repiéger les positons venant du premier piège avec une efficacité de 66%. Ainsi, 1×10^9 positons ont pu être piégés en 1100 s. Il s'agit un résultat très prometteur pour l'expérience GBAR. A présent, il s'agit de faire 10 fois plus et 10 fois plus vite, pour accumuler assez de positons chaque fois que le décélérateur ELENA fournit un paquet d'antiprotons (chaque 100 s).

Nous avons aussi étudiés la possibilité de propulser une fusée en utilisant de l'antimatière. En effet, la réaction d'annihilation matière-antimatière fournit une quantité d'énergie par unité de masse défiant toute concurrence. Nous avons particulièrement étudié le cas de la réaction proton-antiprotons en présence d'un fort champ magnétique. Le champ magnétique ayant pour but de diriger les particules chargées pour créer une force de poussée, fournissant alors un carburant quittant la fusée à une vitesse proche de celle de la lumière. Pour cette étude, un simulateur se basant sur la bibliothèque GEANT4 a été développé. D'après nos simulation, il est alors possible d'obtenir un moteur donnant une impulsion spécifique d'environ $0.5c/g$, c'est-à-dire, 1.5×10^7 s (avec c la vitesse de lumière et g l'accélération de pesanteur terrestre), ce qui est démesuré comparé à l'impulsion spécifique des moteurs propulsant les fusées les plus récentes (434 s pour Vulcain, propulsant Ariane 5). Cependant, ce modèle suppose la possibilité de produire et stocker des quantités macroscopiques d'antiproton, ce qui demeure une limite qui se pourrait être infranchissable. Également, ce modèle engendre une grande quantité de rayon gamma et il reste à trouver une solution pour évacuer leur énergie.

Université Paris-Saclay
Espace Technologique / Immeuble Discovery
Route de l'Ôrme aux Merisiers RD 128 / 91190 Saint-Aubin, France